

# Zinc Oxide Surfaces and Interfaces: Electronic Structure and Dynamics of Excited States

vorgelegt von  
Diplom-Physiker  
Jan-Christoph Deinert  
geboren in Dannenberg (Elbe)

von der Fakultät II – Mathematik und Naturwissenschaften  
der Technischen Universität Berlin  
zur Erlangung des akademischen Grades  
Doktor der Naturwissenschaften  
Dr. rer. nat.

vorgelegte Dissertation

Promotionsausschuss:

Vorsitzender: Prof. Dr. Andreas Knorr  
Gutachter: Prof. Dr. Martin Wolf  
Gutachter: Prof. Dr. Mario Dähne  
Gutachterin: Dr. A. Julia Stähler

Berlin 2016





This work has been performed in the electron dynamix group  
at the Physical Chemistry department  
of the Fritz Haber Institute of the Max Planck Society.



## Abstract

Hybrid systems consisting of electrically conducting, transparent inorganic materials combined with optically active molecules may potentially surpass current optoelectronic systems, e.g., LEDs or photovoltaic cells, in functionality and efficiency. However, this requires a profound understanding of the elementary electronic processes, such as charge or energy transfer, at the interface between the two material classes.

The aim of this work is to explore and understand these processes at successively more complex model hybrid interfaces in order to improve the incomplete conventional description of those systems, which mainly focuses on electrostatics. For this, the method of time-resolved two-photon photoemission spectroscopy allows the precise analysis of interfacial electronic structures and the relevant electron and quasiparticle dynamics on femto- to picosecond timescales.

In this work, zinc oxide (ZnO) serves as inorganic substrate material. It is a prototypical transparent conductive oxide, where a semiconductor-to-metal transition is observed at the surface after hydrogen adsorption. This process is comprehensively explained from an atomic perspective. The hydrogen-induced changes to the surface initially lead to strongly localized potential wells at which the energy of the conduction band bottom is lowered below the Fermi level. By selective dosing of hydrogen, the charge carrier density  $N_e$  and, thus, the metallic character of the surface can be tuned precisely.

The dynamics of photoexcited electrons at the ZnO surface is, initially, dominated by the ultrafast relaxation in the ZnO conduction band, caused by strong electron–phonon coupling. The underlying Coulomb interaction can be screened by the increase of  $N_e$ , which leads to a significant slowing down of the dynamics. In addition, the formation of an excitonic state is observed within the first 200 fs after excitation. The exciton is localized at the hydrogen-induced potential wells and exhibits an initial decay time of hundreds of picoseconds. Further, it remains detectable even after exposing the sample surface to air and at room temperature. Hence, this exciton state may be highly relevant for energy transfer processes at hybrid interfaces.

A first hybrid system to analyze ZnO surface modifications by organic molecules is the pyridine/ZnO(10 $\bar{1}$ 0) interface. The drastic reduction of the work function by 2.9 eV can be explained by the collaborative effect of the static molecular and bond-induced dipoles. The underlying mechanism potentially enables the creation of highly efficient transparent cathodes.

As a next step, charge transfer processes at the 5-phenyl-pyridine/ZnO interface were examined. Similar to pyridine, the molecules supposedly bind to the ZnO substrate via their nitrogen end atom. Here, electrons can be excited from an occupied interfacial state to an unoccupied molecular state, where presumably polaron formation competes with the ultrafast back-transfer (90 fs) to the ZnO substrate.

This work provides a novel detailed view on model ZnO-based interfaces, as it clearly illustrates the correlations between the microscopic properties and the complex dynamical processes. The obtained detailed understanding of prototypical hybrid systems answers a number of fundamental questions regarding the dynamics of excited states and it may serve as a basis for further studies.



## Deutsche Kurzfassung

Hybridsysteme aus elektrisch leitfähigen, durchsichtigen anorganischen Materialien in Kombination mit optisch aktiven organischen Molekülen haben das Potenzial, die Funktionalität und Effizienz heutiger optoelektronischer Systeme – wie LEDs oder Solarzellen – deutlich zu übertreffen. Voraussetzung hierfür ist jedoch ein tiefgreifendes Verständnis der zugrunde liegenden elementaren elektronischen Prozesse: Transfer von Ladung und Energie oder Bildung von Quasiteilchen wie Polaronen und Exzitonen an der Grenzfläche zwischen den Materialklassen.

Das Ziel dieser Arbeit ist es, diese grundlegenden Prozesse an Modellgrenzflächen, deren Komplexität schrittweise erhöht wird, zu verstehen und damit die unvollständige konventionelle, vornehmlich elektrostatische Beschreibung solcher Systeme zu erweitern. Die Methode der zeitaufgelösten Zweiphotonen-Photoemissionsspektroskopie ermöglicht hier sowohl die Untersuchung der elektronischen Struktur von Grenzflächen als auch der relevanten dynamischen Prozesse auf Femto- bis Pikosekunden-Zeitskalen.

Die betrachteten Modellsysteme basieren auf Zinkoxid (ZnO), einem prototypischen transparenten leitfähigen Material, an dessen Oberfläche bei Adsorption von Wasserstoff der Übergang von einem Halbleiter zu einem Metall beobachtet wird. Die wasserstoffinduzierten Veränderungen der Oberfläche führen anfänglich zu stark lokalisierten Potentialmulden, an denen die Energie des Leitungsbandbodens unter die Fermi-Energie sinkt. Die Ladungsträgerdichte  $N_e$  an der Oberfläche lässt sich somit durch Wasserstoffadsorption gezielt beeinflussen.

Die Dynamik angeregter Elektronen an der ZnO-Oberfläche wird zunächst durch ultraschnelle Relaxationsprozesse im ZnO Leitungsband dominiert, bedingt durch effiziente Elektron-Phonon-Streuung. Die zugrunde liegende Coulomb-Wechselwirkung kann durch Erhöhung von  $N_e$  abgeschirmt werden, sodass der Relaxationsprozess signifikant verlangsamt wird. Zusätzlich wird die Bildung eines oberflächennahen exzitonischen Zustands innerhalb von 200 fs beobachtet. Dieser zeigt eine Zerfalldynamik auf einer Zeitskala von hunderten Pikosekunden und bleibt auch nach Kontakt der ZnO-Oberfläche mit Luft und bei Raumtemperatur detektierbar. Damit ist dieses Exziton möglicherweise äußerst relevant für Energietransferprozesse an Hybridgrenzflächen.

Als erstes Hybridsystem zur Untersuchung von Oberflächenmodifikationen durch organische Moleküle dient Pyridin/ZnO(10 $\bar{1}$ 0). Die beobachtete deutliche Reduktion der Austrittsarbeit um 2.9 eV kann durch das Zusammenwirken von statischem und bindungsinduziertem Dipol erklärt werden. Der zugrunde liegende Mechanismus ermöglicht potentiell die Herstellung hocheffizienter transparenter Kathoden.

Im nächsten Schritt wurden Ladungstransferprozesse an der 5-Phenyl-Pyridin/ZnO-Grenzfläche analysiert. Ähnlich dem Pyridin bindet dieses Molekül wahrscheinlich mit dem endständigen Stickstoff-Atom ans ZnO. Elektronen können hier von einem besetzten Grenzflächenzustand in einen unbesetzten Molekülzustand angeregt werden, wo offenbar die Bildung eines Polarons mit dem ultraschnellen (90 fs) Rücktransfer ins ZnO-Substrat konkurriert.

Diese Arbeit zeigt deutlich die Zusammenhänge zwischen mikroskopischen Materialeigenschaften und den komplexen dynamischen Prozessen an Grenzflächen. Das gewonnene detaillierte Verständnis elementarer Prozesse in prototypischen Hybridsystemen klärt fundamentale Fragen der Dynamik angeregter Zustände und kann als Grundlage für weitere Studien dienen.

# Contents

<b>Abstract</b>	<b>v</b>
<b>Deutsche Kurzzusammenfassung</b>	<b>vii</b>
<b>List of Figures</b>	<b>xii</b>
<b>I Introduction</b>	<b>1</b>
<b>II Fundamentals</b>	<b>7</b>
1 Basic Principles of Hybrid Inorganic/Organic Systems . . . . .	7
2 The Traditional Description of the Energetics of HIOS – Concepts and Limitations . . . . .	9
2.1 An Introduction to Interfacial Energy Barriers and Level Alignment . . . . .	9
2.2 Open Questions and Limitations . . . . .	10
3 Energy Levels of Excited Systems and Hybrid Interfaces . . . . .	11
4 Electrostatic Aspects of Energy Level Alignment . . . . .	14
4.1 Surface Dipoles and Work Function Tuning . . . . .	14
4.2 The Limits of Work Function Tunability . . . . .	16
4.2.1 Pyridine as Prototypical Work Function Modifier . . . . .	17
4.3 Interface and Gap States in Hybrid Systems . . . . .	18
5 Electron and Quasiparticle Dynamics in Semiconductors and at Hybrid Interfaces . . . . .	19
5.1 Electronic Scattering Processes at Surfaces and Interfaces . . . . .	19
5.1.1 Overview on Hot Electron Scattering and Decay Mechanisms . . . . .	20
5.2 Excitonic Processes . . . . .	22
5.2.1 Exciton Formation and Excitonic Mott Density . . . . .	24
5.3 Interfacial Charge and Energy Transfer . . . . .	25
5.3.1 Charge Transfer . . . . .	26
5.3.2 Förster resonant energy transfer (FRET) . . . . .	27
5.3.3 Hybrid Charge Transfer States . . . . .	27
6 Zinc Oxide: Electronic Structure and Surface Morphology . . . . .	29
6.1 General Properties of Bulk ZnO . . . . .	29
6.1.1 Electronic Structure and Related Properties . . . . .	29
6.1.2 The Debated Source of Conductivity in ZnO and <i>n</i> -TCOs . . . . .	31
6.1.3 The Role of the Charge Neutrality Level in Doping . . . . .	32
6.2 Geometric Structures of ZnO Surfaces . . . . .	33
6.2.1 The Mixed-Terminated (10 $\bar{1}$ 0) Surface . . . . .	33
6.2.2 The O-Polar 000 $\bar{1}$ Surface . . . . .	34

6.3	The ZnO Surface Electronic Structure . . . . .	34
6.3.1	Surface States and Space Charge Layers . . . . .	34
6.3.2	Surface Charge Accumulation Layers and Surface Conductivity . . . . .	36
6.3.3	ZnO Surface Electronic Structure – Band Bending and CAL formation . . . . .	37
6.4	Hydrogen in Zinc Oxide . . . . .	38
6.4.1	Hydrogen as Adsorbate on ZnO . . . . .	38
6.5	The Work Function of ZnO Surfaces . . . . .	40
6.6	Concluding Remarks on Defects at Zinc Oxide Surfaces . . . . .	40
7	Excited States and Dynamics in Zinc Oxide . . . . .	42
7.1	Excitons in Zinc Oxide . . . . .	42
7.1.1	Bulk Excitonic Spectrum of ZnO . . . . .	42
7.1.2	The ZnO Surface Exciton . . . . .	43
7.2	Electron-Phonon Scattering in ZnO . . . . .	44
<b>III Experimental Techniques and Setup</b>		<b>47</b>
1	Experimental Techniques . . . . .	47
1.1	A Brief Introduction to Surface Science . . . . .	47
1.2	Photoelectron Spectroscopy – Basics . . . . .	48
1.2.1	The Three-Step Model . . . . .	49
1.2.2	The One-Step Model . . . . .	51
1.2.3	The Mean Free Path of Photoelectrons . . . . .	51
1.3	Emission Angles and Momentum Conservation . . . . .	52
1.4	Two-photon Photoemission . . . . .	54
1.4.1	Time-Resolved Two-Photon Photoemission . . . . .	56
1.4.2	Charge Injection in Two-Photon Photoemission . . . . .	57
2	Experimental Setup . . . . .	60
2.1	Laser Light Source . . . . .	60
2.1.1	Photon Energy Tuning . . . . .	61
2.2	Photoelectron Detection Using a Hemispherical Analyzer . . . . .	62
2.3	Ultrahigh Vacuum: A Brief Introduction . . . . .	64
2.3.1	The UHV System . . . . .	65
2.4	Sample Preparation . . . . .	65
2.4.1	Pristine ZnO Surface Preparation . . . . .	65
2.4.2	Adlayer Preparation – Overview . . . . .	67
2.5	Layer Thickness Determination . . . . .	67
2.5.1	Thermally Programmed Desorption . . . . .	67
2.5.2	Quartz Crystal Microbalance . . . . .	68
<b>IV Results</b>		<b>71</b>
1	Experimental Characterization of Pristine Zinc Oxide Surfaces . . . . .	73
1.1	The Geometric and Electronic Structure of the ZnO(10 $\bar{1}$ 0) Surface . . . . .	73
1.1.1	The Valence Band Maximum . . . . .	75
1.1.2	The Work Function . . . . .	75

	1.1.3	The Stability of the Surface Electronic Structure . . . . .	76
	1.2	Geometric and Electronic Structure of the Pristine ZnO(000 $\bar{1}$ ) Surface . . . . .	77
	1.3	Band Bending at the Pristine (10 $\bar{1}0$ ) and (000 $\bar{1}$ ) Surfaces . . . . .	79
2		Hydrogen-Induced Surface Metallization . . . . .	80
	2.1	Preparation of Hydrogen-Covered ZnO Surfaces . . . . .	81
	2.2	Emergence of Metallicity in Photoemission Spectra . . . . .	81
	2.3	Bond Energies and the Competition Between O–H and Zn–H Bonds . . . . .	84
	2.4	The Localized Character of the Hydrogen-Induced Potential Changes . . . . .	88
	2.4.1	Calculation of the Average Change $\Delta U$ along the z-Axis . . . . .	89
	2.4.2	A Microscopic View on the Strong Lateral Potential Variations . . . . .	91
	2.4.3	Quantized Subbands in the Surface Potential Well? . . . . .	92
	2.4.4	Angular Dependence of the CAL Signature at the (10 $\bar{1}0$ ) Surface . . . . .	94
	2.4.5	The High Coverage Regime: Band Gap Reopening and Surface Etching . . . . .	95
	2.5	Hydrogen-Induced Metallization at the (000 $\bar{1}$ ) Surface . . . . .	96
	2.6	Conclusion . . . . .	98
3		Electron and Quasiparticle Dynamics at the ZnO Surface . . . . .	101
	3.1	Ultrafast Dynamics of Electrons in the ZnO(10 $\bar{1}0$ ) Conduction Band . . . . .	101
	3.1.1	Temperature Dependence of CB Dynamics . . . . .	106
	3.1.2	Screening of the Electron–Phonon Scattering by Hydrogen Doping? . . . . .	107
	3.2	The ZnO Surface Exciton . . . . .	110
	3.2.1	Measuring of the Excitonic Signature and its Dynamics . . . . .	110
	3.2.2	The Surface Exciton Revealed . . . . .	112
	3.2.3	Surface Exciton Formation Dynamics . . . . .	114
	3.2.4	The Surface Exciton as a Probe for the Local Potential . . . . .	117
	3.2.5	Hydrogen-Induced Screening of the SX . . . . .	120
	3.2.6	Stability of the Surface Exciton . . . . .	121
	3.2.7	Cooling of Hot Excitons . . . . .	123
	3.2.8	Surface Exciton Lifetimes . . . . .	125
	3.3	Conclusion . . . . .	127
4		Hybrid Interfaces Based on ZnO(10 $\bar{1}0$ ) . . . . .	129
	4.1	Pyridine as Model $\pi$ -Conjugated Surface Modifier . . . . .	130
	4.1.1	Pyridine Layer Preparation and Characterization of the Adsorption Geometry . . . . .	130
	4.1.2	Giant Work Function Reduction . . . . .	133
	4.1.3	Modifications to the Electronic Structure: The In-Gap State . . . . .	136
	4.1.4	Conclusion . . . . .	137
	4.2	The 5-Phenyl-Pyridine/ZnO(10 $\bar{1}0$ ) Interface – Level Alignment and Ultrafast Charge Transfer Dynamics . . . . .	138
	4.2.1	Preparation and Thickness Characterization of 5P-Py Adlayers . . . . .	138
	4.2.2	Complex Adsorption Geometry, Work Function Changes and In-Gap State . . . . .	139

4.2.3	Optical Properties and Electronic Structure of 5P-Py . . . . .	142
4.2.4	Charge Transfer Excitation and Electronic Coupling Across the Hybrid Interface . . . . .	148
4.2.5	Conclusion . . . . .	152
<b>V Conclusion and Outlook</b>		<b>155</b>
<b>Appendices</b>		<b>161</b>
A	Data Analysis for 2PPE . . . . .	161
A.1	How Electron Energies Are Determined . . . . .	161
A.2	How 2PPE Spectra are Generated . . . . .	161
B	Time-Resolved 2PPE on ZnO – Technical Details and Challenges . . . . .	163
C	The UHV System in Detail . . . . .	164
C.1	UHV Chamber . . . . .	164
C.2	Sample Holder . . . . .	165
C.3	The Gas System and Pump Setup . . . . .	167
<b>Bibliography</b>		<b>169</b>
<b>Acronyms</b>		<b>188</b>
<b>Acknowledgements</b>		<b>193</b>
<b>List of Publications</b>		<b>197</b>
<b>Academic Curriculum Vitae</b>		<b>199</b>

## List of Figures

II.1	Basic macroscopic building blocks of a layered optoelectronic device. . . . .	8
II.2	Relevant energy levels at a HIOS interface and traditional schematic energy level diagram of a single layer OLED. . . . .	10
II.3	Single-particle energy diagram for electron transfer processes at a semiconductor interface and corresponding scheme of TR-2PPE. . . . .	12
II.4	Work function tuning by adsorption. . . . .	15
II.5	Scheme of Fermi level pinning for adsorption of molecules with positive electron affinity $\chi$ compared to molecules with $\chi < 0$ , such as pyridine. . . . .	16
II.6	Representation of a pyridine molecule with its static dipole moment. . . . .	17
II.7	Characteristic timescales of elastic and inelastic quasiparticle processes in metals. . . . .	20
II.8	Classical representation of Mott–Wannier and Frenkel exciton in a semiconducting crystal. . . . .	23
II.9	Schematic representation of an exciton gas below and above the Mott density. . . . .	24
II.10	Scheme of a HIOS interface that shows the interfacial electronic transfer and coupling mechanisms. . . . .	26
II.11	Schematic picture of the bound charge transfer (CT) exciton formation at a hybrid interface. . . . .	27
II.12	Geometric structure of the ZnO nonpolar, O- and Zn-polar surfaces. . . . .	30
II.13	Calculated ZnO band structure. . . . .	30
II.14	Typical optical reflection, transmission and absorption spectra of a ZnO thin film on glass. . . . .	31
II.15	Schematic representation of the formation energy of donor and acceptor type defects as a function of the Fermi level. . . . .	32
II.16	Structure of the mixed-terminated ZnO(10 $\bar{1}$ 0) surface. . . . .	33
II.17	Schematic surface band structure for a conventional <i>n</i> -doped semiconductor in case of a depletion layer. . . . .	35
II.18	Electronic structure of the ZnO(10 $\bar{1}$ 0) surface at the $\Gamma$ -point displaying downward surface band bending after hydrogen adsorption. . . . .	37
II.19	Calculated distribution of electron densities and potential curves of the 2DEG subbands in the CAL at the ZnO surface. . . . .	39
II.20	Calculated relaxation and energy-loss time of excited electrons in the ZnO bulk conduction band. . . . .	44
III.1	Basic scheme of the photoemission process at a metallic surface. . . . .	49
III.2	Schematic representation of a photoemission process in the three-step model. . . . .	50
III.3	Inelastic mean free path of electrons depending on their energy. . . . .	52

III.4	Schematic illustration of the conservation of $k_{\parallel}$ during the photoemission process.	53
III.5	Overview of excitation schemes in the 2PPE process.	55
III.6	Role of the sequence of pump and probe pulses in time-resolved photoemission.	56
III.7	Excitation pathways for the transient population of intermediate and final electronic states and related electron transfer processes.	58
III.8	Time-dependent relaxation and population decay of a transiently populated state in the energy domain, monitored by 2PPE.	59
III.9	Schematic overview of the femtosecond laser setup.	60
III.10	Schematic drawing of OPA and THG/FHG setup.	61
III.11	Schematic illustration of the hemispherical analyzer.	63
III.12	Pressure dependency of characteristic quantities of molecular nitrogen at 300 K derived from kinetic theory.	64
III.13	Photograph of ZnO(10 $\bar{1}$ 0) crystal.	66
III.14	Exemplary photoemission spectrum of ZnO(10 $\bar{1}$ 0) demonstrating the determination of the work function $\Phi$ .	66
IV.1	Exemplary LEED image of the ZnO(10 $\bar{1}$ 0) surface.	73
IV.2	Characterization of the pristine ZnO(10 $\bar{1}$ 0) surface.	74
IV.3	Stability of VBM position and work function of the pristine ZnO(10 $\bar{1}$ 0) surface with time and varying fluence.	76
IV.4	Exemplary LEED image of the ZnO(000 $\bar{1}$ ) surface.	78
IV.5	The VBM signature of the O-terminated ZnO(000 $\bar{1}$ ) surface measured with 2PPE.	79
IV.6	Surface and bulk CB and VB energies for the pristine ZnO(10 $\bar{1}$ 0) and (000 $\bar{1}$ ) surfaces.	80
IV.7	Measurement of the sample work function using PES.	82
IV.8	Schematic energy level diagram of ZnO(10 $\bar{1}$ 0) after exposure to hydrogen.	83
IV.9	UPS spectra of the ZnO(10 $\bar{1}$ 0) surface around $E_F$ .	84
IV.10	(4 × 4) ZnO(10 $\bar{1}$ 0) supercell with 25% O-H pre-coverage.	85
IV.11	Relative formation energy for the formation of O-H and Zn-H bonds and resulting work function changes.	87
IV.12	Plane-averaged potential change at the ZnO(10 $\bar{1}$ 0) surface for two different coverage geometries.	89
IV.13	Hydrogen adsorption-induced potential change for OH <sub>3</sub> ZnH <sub>1</sub> adsorption geometry.	90
IV.14	Position of the CAL peak maximum derived from a Gaussian fit to the background-corrected data.	93
IV.15	Angle-resolved spectrum of the CAL signature of the ZnO(10 $\bar{1}$ 0) surface after exposure to a 100 L dosage of hydrogen.	94
IV.16	PES of the hydrogen-covered ZnO(000 $\bar{1}$ ) surface for various dosages.	97
IV.17	Comparison of the hydrogen-induced work function change and intensity of the charge accumulation layer signature between the (10 $\bar{1}$ 0) and (000 $\bar{1}$ ) surfaces of ZnO.	98

IV.18 Photoinduced 2PPE signal showing the ultrafast charge carrier dynamics above $E_F$ at the $H_2/ZnO(10\bar{1}0)$ surface. . . . .	102
IV.19 Detailed overview of the hot electron dynamics in the $ZnO(10\bar{1}0)$ conduction band. . . . .	104
IV.20 Schematic representation of the influence of surface downward band bending on the relaxation pathways of excited electrons at the $ZnO$ surface. . . . .	105
IV.21 Temperature dependence of the hot electron relaxation in the CB of $ZnO(10\bar{1}0)$ . . . . .	107
IV.22 Hydrogen dosage-dependent time constant of hot carrier relaxation in the $ZnO(10\bar{1}0)$ CB. . . . .	108
IV.23 Schematic representation of the influence of band bending on the photoelectron energies that refer to an excitonic state with energy $E_X$ . . . . .	110
IV.24 Photoinduced 2PPE signal showing the exciton formation dynamics at the $H_2/ZnO(10\bar{1}0)$ surface. . . . .	111
IV.25 Scheme of fluence dependent effects at the $ZnO$ surface: surface photovoltage vs. exciton formation. . . . .	112
IV.26 2PPE spectra for different excitation densities after background subtraction. . . . .	113
IV.27 Formation dynamics of the surface exciton signature measured with two-photon photoemission spectroscopy. . . . .	115
IV.28 Schematic model of the transfer of electronic population from CB states to the SX, which is used as basis for rate equations. . . . .	116
IV.29 SX signatures for H dosages from 3 to 44 L . . . . .	118
IV.30 Schematic illustration of the localization of the SX in the subsurface region of the $ZnO(10\bar{1}0)$ surface. . . . .	118
IV.31 Exemplary two-dimensional plots of the charge carrier dynamics at the $ZnO(10\bar{1}0)$ surface for hydrogen dosages of 3 L and 150 L. . . . .	119
IV.32 Dependence of the SX peak shape and position on hydrogen dosage. . . . .	121
IV.33 TR-2PPE measurements of the $ZnO(10\bar{1}0)$ surface showing the effect of exposing the sample to air. . . . .	122
IV.34 Normalized XC traces of the SX signature for different temperatures. . . . .	124
IV.35 Normalized XC trace of the SX signature for pump-probe delays up to 200 ps. . . . .	126
IV.36 TPD trace of the pyridine adsorbed at the $ZnO(10\bar{1}0)$ surface. . . . .	131
IV.37 Pyridine adsorption geometry resulting from PBE+vdW calculations . . . . .	131
IV.38 Calculated absorption energy (PBE+vdw) per unit area as a function of the ratio between pyridine and surface Zn atoms. . . . .	132
IV.39 Plot of the PES signal of pyridine/ $ZnO(10\bar{1}0)$ during sample heating and, thus, evaporating of the pyridine adlayer. . . . .	133
IV.40 Work function of the pyridine/ $ZnO(10\bar{1}0)$ surface as a function of temperature. . . . .	134
IV.41 Comparison of the experimentally determined work function and the calculated work function shift at the pyridine/ $ZnO(10\bar{1}0)$ surface. . . . .	135
IV.42 Photoelectron signature of the pyridine in-gap state. . . . .	136
IV.43 Representation of an isolated 5-phenyl-pyridine molecule. . . . .	139
IV.44 Representative TPD trace of $\approx 10$ nm 5-phenyl-pyridine on $ZnO(10\bar{1}0)$ . . . . .	140

---

IV.45	Photoelectron spectrum of the 5P-Py/ZnO( $10\bar{1}0$ ) interface measured with $h\nu = 6.2$ eV photons showing the change of the spectrum with temperature. . . . .	141
IV.46	Artistic representation of the heat-induced reordering of the 5-phenyl-pyridine molecules on the ZnO( $10\bar{1}0$ ) surface. . . . .	142
IV.47	Normalized fluorescence excitation and emission spectrum of 5-phenyl-pyridine in chloroform at 25 °C . . . . .	143
IV.48	Energy level alignment at the $p$ -6P/ZnO( $10\bar{1}0$ ) interface. . . . .	144
IV.49	Energy levels and excitation scheme for single-color 2PPE experiments at the 5P-Py/ZnO( $10\bar{1}0$ ) interface. . . . .	144
IV.50	Photoelectron signatures of 5P-Py on ZnO( $10\bar{1}0$ ) measured with 6.2 eV and 2.5 eV photon energy. . . . .	146
IV.51	2PPE excitation scheme and resulting 2D plot of the charge carrier dynamics at the 5-phenyl-pyridine/ZnO( $10\bar{1}0$ ) interface. . . . .	147
IV.52	2PPE spectrum of the transient charge transfer state and its energetic position with respect to the pump-probe delay. . . . .	149
IV.53	Relaxation dynamics of the charge transfer state at the 5-phenyl-pyridine/ZnO( $10\bar{1}0$ ) interface. . . . .	150
IV.54	Amplitudes of the slow decay component associated with the charge transfer state as a function of excess energy. . . . .	151
IV.55	Overview of the experimental results regarding the 5-phenyl-pyridine/ZnO( $10\bar{1}0$ ) interface. . . . .	153
A.1	Scheme of the determination of photoelectron kinetic energies with the hemispheric analyzer. . . . .	162
A.2	Exemplary 2PPE spectra demonstrating the extraction of the pump-induced changes to the photoelectron signal. . . . .	163
C.3	Detailed overview of the UHV setup. . . . .	164
C.4	Drawing of the sample holder. . . . .	166
C.5	Photograph of the ZnO sample mounted in the sample holder. . . . .	166
C.6	Scheme of the gas system and attached vacuum parts. . . . .	168



# I Introduction

Zinc oxide is an interesting material, mostly because it is *transparent* to light in the regime of visible wavelengths and, at the same time, it is an electrical *conductor*. As a prototypical **transparent conductive oxide (TCO)** material, ZnO is a promising part of optoelectronic devices which convert light into electrical energy and vice versa, for example **organic light emitting diodes (OLEDs)** and **organic photovoltaic cells (OPVCs)**. A particularly auspicious approach is the merge of the inorganic semiconductor ZnO with optically active organic molecules into a **hybrid inorganic/organic system (HIOS)**, in order to combine the advantages of both material classes while compensating for their deficits, which is expected to result in functionality superior to that of current technologies.

As intriguing as the use of ZnO in novel optoelectronics may be, the material has not achieved a commercial breakthrough yet. This is surprising, since research on ZnO as optoelectronic material dates back more than half a century and it also has seen a vivid renaissance in the last ten years [KFZ<sup>+</sup>10]. One reason for the apparent lack of fundamental understanding might be that the physical properties of ZnO differ in many respects from those of the established semiconductor materials, such as silicon or gallium arsenide. For example, ZnO favors the formation of *n*-type defects, and it is natively *n*-type conductive – the microscopic origin of which is still debated [KVM<sup>+</sup>10].

The ZnO *surface* is the key element from the perspective of both fundamental research and device design, because any transfer of charges or energy between ZnO and a functional molecular adlayer is determined by the elementary processes which occur across the two surfaces, i.e., the *hybrid interface*. To describe such an interface, one cannot simply add up the properties of each of the two different materials, such as the positions of the respective energy levels. Instead, the hybrid interface forms a separate entity which eventually governs the functionality of HIOS [Koc07, BGS<sup>+</sup>10]. This functionality depends on two main aspects:

**The energy level alignment** across the interface determines the energetic barriers, e.g., for the interfacial charge transfer. It strongly depends on the formation of *surface* and *interface dipoles* and new hybrid electronic states.

**The electron and quasiparticle dynamics**, i.e., the elementary scattering and relaxation processes, determine the efficiency of any interfacial charge or energy transfer process. The respective timescales are largely defined by the strength of the electronic coupling of states across the interface.

Controlling and understanding these properties requires knowledge about the microscopic characteristics of the surfaces and interfaces and the resulting consequences for the elementary interactions between electrons, holes and the crystal lattice. Regarding the ZnO surface, this

concerns, in particular, the mechanisms behind surface metallization. The established model of the hydrogen-induced formation of a [charge accumulation layer \(CAL\)](#), a few nanometers thin, laterally delocalized region of high electron density [EMG76, Lüt10] has only recently begun to be understood on a microscopic level [WMY<sup>+</sup>05, OM11].

The ambivalent character of ZnO as band gap material with partly metallic character raises many questions regarding the excited charge carrier dynamics, especially the interaction of hot electrons and excitons with free carriers at the ZnO surface: Which elementary scattering processes dominate the non-equilibrium dynamics, and is it possible to change the characteristics or timescales of these dynamics by changing the surface properties of ZnO? Further, the general formation dynamics of excitons and the exciton cooling processes that precede their radiative recombination are still debated [SKB<sup>+</sup>04, DSO<sup>+</sup>90, HKB07, KKKG06]. The introduction of hybrid interfaces further raises the complexity, because of the unknown interplay between the adsorption geometry of the organic molecules, interface dipole formation and the electronic coupling across the interface [SPN<sup>+</sup>14, Zhu04b].

Thus, to tackle these basic questions regarding ZnO-based surfaces and interfaces, it is necessary to analyze and understand well-defined model systems on a fundamental level, and probably only then it will be possible to advance the knowledge of realistic and functional [HIOS](#).

Any experimental method used to address these questions has to fulfill a number of requirements: Surface and interface sensitivity, a sufficient temporal resolution to monitor the processes, and the ability to access both occupied and *unoccupied* electronic states. Time-resolved [Two-photon photoelectron spectroscopy \(2PPE\)](#) experiments in conjunction with [ultraviolet photoelectron spectroscopy \(UPS\)](#) measurements fulfill these requirements. [Time-resolved 2PPE \(TR-2PPE\)](#) enables probing of the non-equilibrium electronic structure of surfaces on a timescale of femto- to nanoseconds, which are the timescales of the relevant elementary excitation and decay processes [BMA15].

To approach and control the notoriously unstable ZnO surface properties [JZG84, Wöl07, TMN<sup>+</sup>08], single crystalline samples were prepared and characterized using a number of [ultra-high vacuum \(UHV\)](#) and surface science techniques which ensured high reproducibility and reliability of the experiments. A first step was the characterization of the *pristine* ZnO(10 $\bar{1}$ 0) surface using photoelectron spectroscopy in conjunction with [density functional theory \(DFT\)](#) calculations<sup>1</sup> to pinpoint its fundamental properties.

The thereby gained knowledge was then expanded by successively increasing the complexity of the examined system: from hydrogen-induced modifications of the surface electronic structure to hybrid interfaces with organic molecules. The brief overview of the achieved milestones towards the comprehensive description of the electronic structure and charge carrier dynamics at prototypical model surfaces and interfaces is given in the following:

**The local aspects of hydrogen-induced metallization of the ZnO(10 $\bar{1}$ 0) and (000 $\bar{1}$ ) surfaces** At the mixed-terminated (10 $\bar{1}$ 0) surface, a complex adsorption behavior caused by a strong coverage dependence of the H adsorption energies is found: Initially, O–H bond formation is energetically favorable and leads to the electron donation to the ZnO substrate and a

---

<sup>1</sup>The calculations were part of a joint project on hybrid inorganic/organic systems (Sfb 951) and were carried out by Oliver Hofmann et al. in the former group of Patrick Rinke at the [Fritz Haber Institute \(FHI\)](#) Berlin.

---

significant work function reduction by  $\Delta\Phi \approx 0.7$  eV and  $\Delta\Phi \approx 1.8$  eV at the  $(10\bar{1}0)$  and  $(000\bar{1})$  surfaces, respectively. The increase of the number of O–H bonds leads to a reversal in adsorption energies at  $\approx 18$  % coverage such that Zn–H bonds become favored at sites close to existing O–H bonds. Because Zn–H bonds have an opposite effect on the surface electronic structure, the metallic character of the ZnO( $10\bar{1}0$ ) surface is gradually extenuated for high dosages. The potential wells at the surface caused by the O–H bonds are locally restricted to the binding site. The resulting strong lateral corrugation of the potential is transformed into a rather delocalized state which corresponds to the established view of the CAL only for sufficiently high hydrogen coverages. This confirmation of the complex role of hydrogen may explain many of the inconsistencies regarding the surface properties, especially the work function, of supposedly pristine ZnO surfaces which can be found in the literature [JZG84, TMN<sup>+</sup>08, KBH<sup>+</sup>14, SBB<sup>+</sup>15].

In addition, the possibility to tune the surface properties – in particular the *screening* of the Coulomb interaction – via hydrogen adsorption enables experiments that demonstrate the complex interplay of excited charge carriers with the lattice and amongst each other.

**Ultrafast hot electron relaxation and exciton formation at the zinc oxide surface** The TR-2PPE experiments show that charge carrier dynamics upon above-band gap excitation of ZnO span timescales from the femtosecond to the nanosecond regime. The decay of hot electrons in the ZnO conduction band (CB) is found to occur on an ultrafast, few ten femtosecond timescale, which is attributed to the strong electron–phonon (e–ph) interaction with longitudinal optical (LO) phonons via Fröhlich coupling. It is shown that the e–ph interaction can be significantly screened by hydrogen-induced free electrons in the CAL, leading to a doubling in decay time constants above a critical charge density of  $N_C \approx 6 \times 10^{19} \text{ cm}^{-3}$ . For intermediate states close to the Fermi level, the dynamics slow down considerably with time constants on the order of hundreds of femtoseconds. The reason for this is the excess energy being too small to excite further LO phonons.

The excitonic signature of the ZnO surface forms within 200 fs after photoexcitation – clearly visible as an increase of electronic population *below* the Fermi level. The cooling of hot excitons into the emissive ground state then occurs within tens of picoseconds. This surface exciton (SX) species remains present even after exposing the sample to air, indicating that it is located in a sub-surface layer. Further, it persists at room temperature and shows an overall lifetime of nanoseconds, which makes it a very relevant species for interfacial processes at hybrid interfaces, in particular regarding Förster resonant energy transfer (FRET).

The presence of the exciton is intimately linked to potential wells at the ZnO surface. Its formation probability can be enhanced by adsorbing hydrogen at the ZnO surface. On the other hand, a quenching of the excitonic state due to screening of the Coulomb interaction is observed when the charge carrier density is increased above the Mott limit.

**Strong vacuum level shift by adsorption of a molecule with negative electron affinity: Pyridine on ZnO( $10\bar{1}0$ )** The pyridine ( $\text{C}_5\text{H}_5\text{N}$ )/ZnO( $10\bar{1}0$ ) interface is a first hybrid model system to study the formation of interface dipoles and the resulting consequences for the energy level alignment, as the underlying microscopic mechanisms and the influence of adsorption geometry and charge transfer upon adsorption are *per se* unknown [ISIS99].

To correlate photoemission data with the microscopic properties of the interface, experiments are again complemented by DFT calculations, performed by Oliver Hofmann et al. Experimentally, it was found that a full monolayer of pyridine causes a huge reduction of the work function, from 4.5 eV for the pristine ZnO(10 $\bar{1}0$ ) surface to 1.7 eV. There is an excellent agreement of this shift with theoretical calculations, which show a corresponding adsorption geometry where the pyridine molecules bind to every second surface Zn atom via their nitrogen atom. Pyridine as a model system, thus, shows how injection barriers at hybrid interfaces can be drastically reduced by molecular layers with strong dipole moments.

The surface electronic structure is additionally modified by the adsorption of sub-monolayer pyridine films: a new interfacial state forms below the Fermi level, which may play a role as initial state in charge or energy transfer processes [WSC<sup>+</sup>14, RKM15].

**Charge transfer excitation across the interface between 5-phenyl-pyridine and the ZnO(10 $\bar{1}0$ ) surface** A more complex hybrid system that allows studies of interfacial charge transfer processes is the novel nonsymmetrical adsorbate molecule termed 5-phenyl-pyridine (5P-Py) adsorbed on ZnO(10 $\bar{1}0$ ). The molecule consists of five phenyl rings connected to a pyridine end group [GSH<sup>+</sup>14].<sup>2</sup>

It is found that by thermal annealing at least part of the 5P-Py grows in an upright standing geometry, similar to pyridine. This coincides with a work function reduction by up to 1.9 eV and the formation of an occupied interface state below  $E_F$ . Furthermore, an unoccupied state with a vertical binding energy of 0.8 eV is observed, which presumably originates from the molecular lowest unoccupied molecular orbital (LUMO).

In a first experiment on the interfacial charge transfer dynamics, electrons were injected from the interface state into the molecular LUMO, i.e., a charge transfer excitation process is induced. The excited electrons in the LUMO exhibit an ultrashort lifetime of 90 fs before they are transferred back into the ZnO CB, indicating a strong electronic coupling across the interface. Further, an energetic relaxation of the excited electron is observed, which indicates a rearrangement of the surrounding molecules, i.e., polaron formation.

This ultrafast process is strikingly different from charge transfer processes in which the hole is located not in an interface state but inside the molecular layer. Here, the electron-hole (e-h) interaction has been found to slow down the interfacial electron transfer to picosecond timescales [SPN<sup>+</sup>14].

In summary, this thesis aims at giving a comprehensive and detailed insight into the electronic structure and dynamics at ZnO surfaces and model hybrid interfaces. These systems are both promising and challenging due to the rich physics that occur at such interfaces, which manifests itself in the diversity of approaches and descriptions which can be found in literature. These focus on a range of separate aspects, from an electrostatic treatment of energy level alignment to the quantum mechanical quasiparticle species.

To reach a *complete* description it is, thus, necessary to explore fundamental processes in highly-controlled model systems to pinpoint the essential correlations between the static and

---

<sup>2</sup>The molecule was synthesised by Y. Garmshausen et al. in the group of S. Hecht at the Humboldt Universität, Berlin as part of the joint project on hybrid inorganic/organic systems (Sfb 951).

---

dynamic electronic properties and interface morphology. The capability of this approach is exemplified by the finding of the intricate interplay between surface metallicity, hot electron relaxation and exciton formation probability. Further, 5P-Py is identified as highly interesting model system for analyzing both strong surface modifications as well as charge transfer dynamics. Thereby, this work makes substantial contributions to long standing questions regarding ZnO-based interfaces and hybrid systems in general.



## II Fundamentals

The dominating topic in current materials science is functionality and control on the molecular or atomic scale, which is the prerequisite for **hybrid inorganic/organic system (HIOS)** as will be explained in Section 1. A major difficulty is the accurate description and the assignment of the physical properties and processes at hybrid interfaces, which is still afflicted with confusion. This confusion is, to some extent, due to the interdisciplinary nature of **HIOS** research, which requires a combination of the languages of physics, chemistry, and engineering. The conventional approach to treat **HIOS** and the resulting limitations and questions are briefly introduced in Section 2. What follows in Section 3 is the description of a comprehensive concept of energy level assignments for excited states at interfaces, which is closely related to the experimental method of **TR-2PPE**.

With these basics in mind, Section 4 discusses the possibilities of electrostatic surface modifications focusing on the role of the work function and interfacial electronic states. Section 5 is then devoted to the dynamics of excited states in solids and especially at hybrid interfaces, encompassing processes such as hot electron relaxation, exciton formation and the dynamics of interfacial charge transfer excitons.

The discussions of surface properties and electronic processes is followed in Section 6 by a description of the main material of interest: zinc oxide. Here, the main focus is on the unusual features of the ZnO surface: its metallicity and the formation of a **CAL**, which concerns **TCO** materials in general. Finally, Section 7 introduces the current knowledge on the dynamical processes at ZnO surfaces.

### 1 Basic Principles of Hybrid Inorganic/Organic Systems

The creation of sustainable sources of electrical energy and the efficient use of this energy is one of the key technological challenges of the 21st century. At the heart of these challenges are devices, such as photovoltaic cells or **light emitting diodes (LEDs)**, which transform light into electrical energy and vice versa. The fundamental physical principles that enable optoelectronic functionality in all these devices are essentially identical: the absorption of photons in an optically active material creates **e-h** pairs that form an *exciton* via their mutual Coulomb interaction. If the exciton is split, both charge carriers can be extracted, which results in an electric current. The reversal of this photovoltaic process leads to the emission of light and represents the basic working principle of an **LED**. A schematic model representing this generalized optoelectronic device is shown in Fig. II.1. The main components are (i) the optically active layer where photon absorption and emission takes place, and (ii) the electrodes which are needed for the transfer of both photons and charge carriers between outside world and active layer. Furthermore, the *interfaces* between the two dissimilar components require special

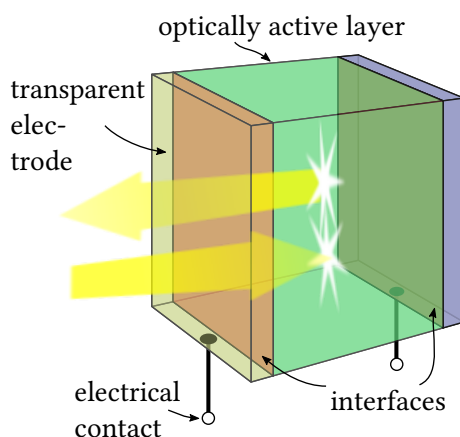


**Figure II.1:** Basic macroscopic building blocks of a layered optoelectronic device. The transformation of light into electrical energy and the reverse process inside the optically active layer requires the transfer of photons and charge carriers through the electrodes and various interfaces.

attention, since they largely govern the functionality and efficiency of the device, as will be explained below.

One promising approach for finding materials best suited to fulfill these “tasks” is the combination of inorganic materials, usually TCOs such as ZnO, with conjugated organic molecules into a **hybrid inorganic/organic system (HIOS)**. These heterostructures are intended to utilize the strengths of each material class while compensating for its deficits. From these characteristics, the role of the HIOS components in a device (see Fig. II.1) can be inferred directly:

**Conjugated organic material** It is responsible for the actual transformation of photons into electron-hole pairs, i.e., excitons, or vice versa, because of the usually strong light-matter coupling. The absorption and emission characteristics can be easily tuned by, e.g., varying the size of the molecule. On the downside, the electrical conductivity in these materials is usually low.

**Inorganic semiconductor** It acts as substrate material responsible for electron or hole transport to and from the optically active molecular layer. This is supported by the comparably fast charge delocalization and high charge carrier mobility in this material. Further requirements are transparency in the visible range of the spectrum and electrical conductivity. Here, light-matter coupling is usually weak and the tunability of the band gap is restricted.

**Hybrid interface** The elementary processes of charge or energy transfer, exciton separation or trapping, which occur at the interface, largely define the functionality of the whole system. These processes and the timescales on which they occur strongly depend on the interfacial electronic coupling and, thus, the alignment of energy levels at the interface.

The intrinsically microscopic nature of the interface and the resulting challenges in producing and analyzing well-defined systems are most probably the main reason, why viable HIOS devices are rare and the vast potential of this approach [Koc07] has not been exploited so far.

Apparently, the prevailing descriptions of HIOS which rely on a macroscopic, area-averaged view [ISIS99, Koc07, SBB<sup>+</sup>15], cannot completely account for the quantum effects and microscopic inhomogeneities which occur at hybrid interfaces. Thus, the understanding of the complexity of the hybrid interface, from its electronic structure to its multiscale morphology and a truly comprehensive picture of the microscopic mechanisms that determine the characteristics of such interfaces is still lacking [Koc12, ZT15, RL96].

## 2 The Traditional Description of the Energetics of HIOS – Concepts and Limitations

Very briefly, the functionality of hybrid interfaces generally depends on several factors: (i) the alignment of the interfacial energy levels, (ii) the resulting electronic coupling between states across the interface and (iii) the characteristics of the actual elementary electronic processes.

The traditional description of these strongly intertwined interfacial properties mostly focuses on the first point, the energy level alignment, as hybrid interfaces are usually characterized by their electronic structure [ISIS99, Koc07]. The knowledge of the interfacial electronic structure is, thus, a prerequisite to estimate the functionality and efficiency of a hybrid system. However, it is not sufficient to fully understand HIOS and their rich physical properties [RKM15], which are discussed in the following sections.

### 2.1 An Introduction to Interfacial Energy Barriers and Level Alignment

As an example, the efficient transfer of charges or energy between two materials, as it occurs at the hybrid interface, requires energetic resonance between the involved states. Thus, large interfacial energy barriers are detrimental to device performance [Koc12]. To illustrate these barriers, the simplified energy level scheme of an exemplary HIOS device – an OLED – is shown in Fig. II.2(a). The first step of its basic working principle is the injection of electrons and holes from the electrodes into the electronic bands derived from the **lowest unoccupied molecular orbital (LUMO)** and **highest occupied molecular orbital (HOMO)**, respectively. Within the organic layer, the **e–h** pair may form a **singlet exciton (SE)** which can recombine via the emission of a photon (see Section 5.2).

A common, simple approach to estimate the electron (hole) injection barrier is to take the difference between the electrode work function  $\Phi$  and the energetic position of the **LUMO (HOMO)** of the organic material [CGC<sup>+</sup>02]. The positions of the latter can be measured as the electron affinity  $\chi$  in inverse **photoelectron spectroscopy (PES)** or the ionization energy  $E_{\text{ion}}$  in **UPS**, as illustrated in Fig. II.2(b) [ISIS99, Koc07]. For this procedure, a common energetic reference between inorganic substrate and organic layer is needed: the vacuum level  $E_{\text{vac}}$ . This “vacuum level alignment”, also termed Anderson’s rule [And60], describes the construction of the energy level diagram of heterojunctions between two different semiconductor materials and is analogous to the Schottky–Mott rule for metal-semiconductor interfaces. It assumes that the equality of the vacuum levels, which is the case for large separations, is retained when the hybrid interface is formed.<sup>1</sup>

---

<sup>1</sup>The vacuum level is an intrinsic property of a material’s surface. Nevertheless, it is extended to the bulk in the

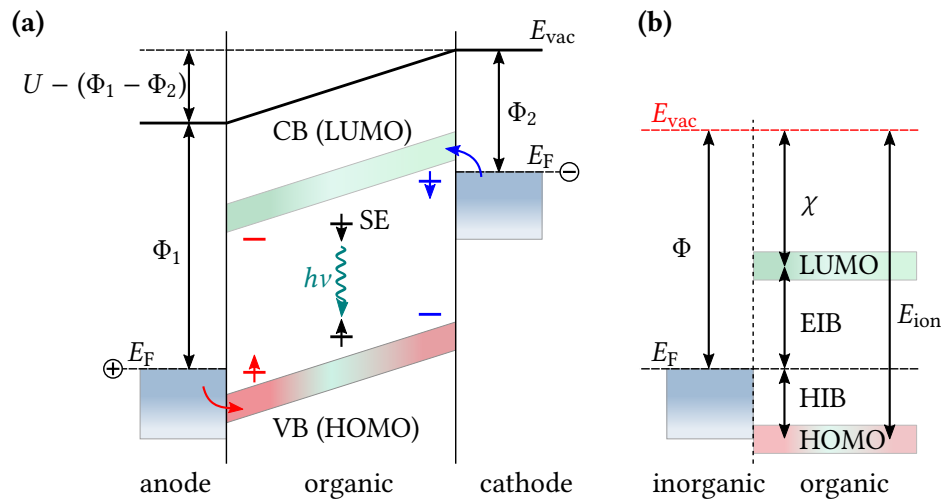


**Figure II.2:** (a) Traditional energy level diagram of a single layer OLED, adapted from Ref. [Koc07]. An external driving voltage  $U$  leads to injection of electrons (blue) and holes (red) from the electrodes into the organic layer, where they exhibit polaronic character. Exciton formation and subsequent radiative recombination in case of SEs results in the emission of a photon with energy  $h\nu$ . (b) Relevant energy levels at a hybrid interface consisting of a metallic substrate and an organic material with vacuum level alignment at the interface. The hole injection barrier (HIB) and electron injection barrier (EIB) result from the energetic offset of the bands relative to  $E_F$ .

This concept of interfacial energy level alignment has led to the idea of shifting the energy levels with respect to each other by tuning of the substrate work function which can be done by inducing changes to the electrostatic dipole at its surface. This may be achieved by the adsorption of suitable molecules which change the potential barrier at the interface, e.g., by adding a static dipole moment [CRZ<sup>+</sup>96, ISIS99, Koc07]. There are a number of studies that demonstrate the validity of this approach, i.e., the shifting of molecular levels at hybrid interfaces using interface dipole layers, in certain well-defined systems [KYY<sup>+</sup>04, FKK<sup>+</sup>07]. However, there appears to be no common way of improving interface functionality at hybrid systems in general.

## 2.2 Open Questions and Limitations

Although it has been shown that interface functionality can in principle be improved by this concept [SBB<sup>+</sup>15], this traditional characterization of the interface by the electronic structure is incomplete in several different ways and, thus, does often not facilitate the understanding of the underlying processes. As discussed in Section 4, some of the shortcomings of the simple model of vacuum level alignment can be overcome by considering the complex rearrangement of charges upon bond formation at the interface which leads to effective interface dipoles [ISIS99, CGC<sup>+</sup>02].

A more substantial deficiency of this traditional concept, which is reflected in the way energy

---

figures shown in this section in order to represent the hypothetical position of  $E_{vac}$  in the case of truncation at the respective position.

diagrams of interfaces are usually drawn, is its reliance on laterally averaged, effective energy values. In reality the electronic structure at the interface may be laterally inhomogeneous with variations of the electrostatic potential even between neighboring lattice sites which has strong impact on the elementary processes depending on the degree of localization of the relevant charge carrier or exciton [Tun92, RGW92]. This is especially true for the complex mixed-terminated surfaces found in **transparent conductive oxides (TCOs)**, in particular the ZnO(10 $\bar{1}$ 0) surface (see Section 6.2). In general, the respective role of short- and long-range effects and the influence of quantum mechanical considerations strongly depend on the characteristics of the hybrid systems [NKHT07], which complicates the finding of common design principles.

What is also not covered by this *static* description of interfacial energy levels is the intrinsically *dynamical* character of relevant interfacial processes, usually involving excitons, polarons and other quasiparticle species. This involvement of quasiparticles often results in ambiguities and confusion in the assignment of energy levels in the literature, because of the mixing of single-particle energy levels with quasiparticle energy levels in the same diagram [Zhu14, Bré14]. The role of elementary, dynamical processes at hybrid interfaces is discussed in Section 5. Before that, the next section presents a method to assign energy levels corresponding to complex interfacial processes in a physically meaningful and accurate way, which is directly related to the main experimental method used in this work: time-resolved two-photon photoemission spectroscopy TR-2PPE.

### 3 Energy Levels of Excited Systems and Hybrid Interfaces

As introduced in the previous section, the energetic positions of the molecular **HOMO** and **LUMO** at a hybrid interface are typically determined experimentally in **UPS** and inverse **PES**, respectively. These measurements yield the *vertical* single-particle energy levels, i.e., the energy difference between initial and final states with the coordinates of the nuclei fixed at the positions of the initial state [Zhu14]. The difference between these measured single-particle energies,  $E_{\text{ion}} - \chi$ , constitutes the *fundamental* gap of a semiconducting material.

To be more precise, the energy levels of charge carriers inside a semiconducting material, e.g., the electrons and holes that have been injected into the molecular layer as shown in Fig. II.2(a), are those of *polarons*. The dressing of the free charges by polarizations in the nuclear coordinates leads to an energy reduction relative to the measured vertical energies by the polaron stabilization energy. While this energy is negligible for inorganic semiconductors, it may be large (few hundreds of meV) for molecular materials [Zhu14, SC94, JMFH10], so that the *transport* gap may vary from the fundamental gap depending on material parameters.

*Excitons* are two-body quasiparticles which differ conceptually from the independent polaronic charge carriers. This correlated pair of electron in the **conduction band (CB)** or **LUMO** and hole in the **valence band (VB)** or **HOMO** has an internal energetic reference [MZ10]: The Coulomb interaction between electron and hole reduces the energy of the exciton compared to the free charge carriers by an amount called the exciton binding energy.<sup>2</sup> This energy depends on the screening of the Coulomb interaction in a material, i.e., it is inversely proportional to the

<sup>2</sup>For a more comprehensive discussion of excitons, see Section 5.2.

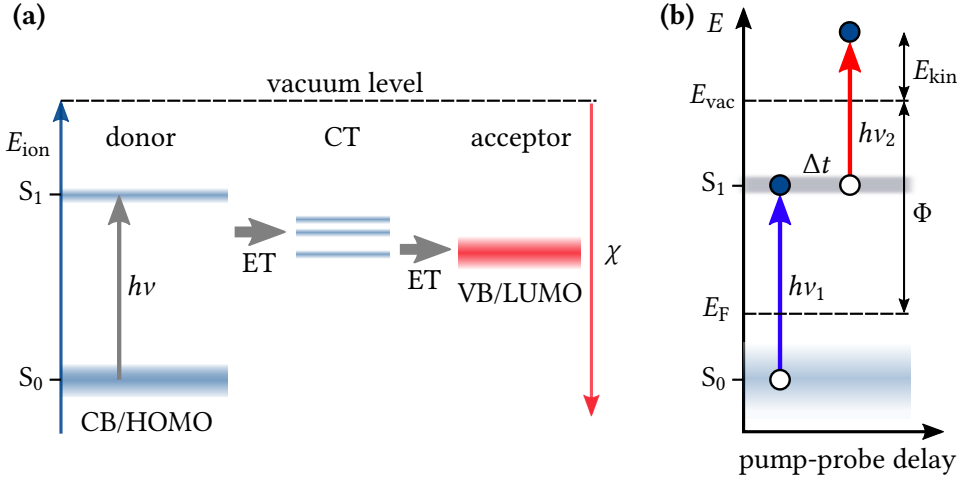


**Figure II.3:** Single-particle energy diagram for electron transfer processes at a semiconductor interface and corresponding scheme of TR-2PPE. (a) The initial optical excitation of the donor material is followed by **electron transfer (ET)** and the formation of **charge transfer (CT)** states and charge separation that leads to an electron located in the acceptor. The blue levels are ionization energies and the red level marks the electron affinity of the accepting state. (b) Schematic illustration of a **TR-2PPE** measurement which directly yields the ionization energies and the temporal evolution of the population of the involved states. Modified from Ref. [Zhu14].

dielectric constant  $\epsilon$ . As a result, excitons are the primary product of photoexcitation in low  $\epsilon$  materials, such as molecular solids [MZ10]. The energy gap associated with the formation of excitons (*optical* gap) is lower than the transport gap by the exciton binding energy [Bré14].

Energy diagrams of hybrid interfaces, thus, have to include both single-particle and exciton energies. This can be done in a physically accurate way by including ionization energies and electron affinities of both ground states and excited (excitonic) states, as has been shown for organic donor/acceptor interfaces [Zhu14, ST11, RSA<sup>+</sup>12].

The ionization energy  $E_{\text{ion}}$ , is the energy change for the process  $M \rightarrow M^+ + e$ , where a system in its neutral ground state  $M$  with energy  $E_0$  is excited to a final state with energy  $E_+$ . The latter corresponds to a hole in the **VB** or **HOMO** of the material and an electron with zero kinetic energy at the vacuum level. This is exactly the description of a conventional **UPS** experiment. For the ionization energy the following equation holds:

$$E_{\text{ion}} = E_+ - E_0. \quad (\text{II.1})$$

This relation can be generalized to accurately assign single-particle energies to all transport states *and* excitonic states, not only to the ground state. The reason is that  $E_{\text{ion}}$  is always referenced to a common final state, that is, a hole in the **VB** or **HOMO** and an electron at rest at the vacuum level. For the generalized initial state  $X$  Eq. II.1 is modified to give the corresponding generalized ionization energy

$$E_{\text{ion}}^X = E_+ - E_X \quad (\text{II.2})$$

where  $E_X$  is the energy of any single-particle or excitonic state. The assignment of generalized electron affinities  $\chi^X$  can be done analogously (see Ref. [Zhu14]).

An example of the usefulness of ionization energies to describe complex processes at interfaces between different materials is shown in Fig. II.3(a), where the blue energy levels are the ionization energies as defined by Eq. II.2. This energy diagram shows an interfacial charge separation process which starts with an optical excitation in the donor material which leaves the donor in an excited state  $S_1$ . What follows is an **electron transfer (ET)** that results in an interfacial **charge transfer (CT)** state where the hole is retained in the donor. Finally, the separation of the excitonic CT state leads to a hot electron in the acceptor.<sup>3</sup>

The presented assignment of energy levels of excited states is not only a theoretical proposal. These states, which are relevant to describe the electron dynamics in HIOS, can be accessed directly using a pump-probe technique called time-resolved two-photon photoemission spectroscopy **TR-2PPE** as has been demonstrated for a variety of systems, from inorganic semiconductors to organic donor/acceptor interfaces [WKFR04, DQLZ05, MZ10, CGLI<sup>+</sup>10, CLJ<sup>+</sup>11]. Figure II.3(b) schematically shows a **TR-2PPE** experiment in which the absorption of the pump laser pulse  $h\nu_1$  excites the sample to a, possibly excitonic, state  $S_1$ . A second pulse with energy  $h\nu_2$  then ionizes the excited state after a controlled time delay  $\Delta t$  and the photoelectron is detected with energy resolution. The measured kinetic energy of the photoelectron then directly gives the ionization energy of the excited state

$$E_{\text{ion}}^X = h\nu_2 - E_{\text{kin}}^X. \quad (\text{II.3})$$

The knowledge of the sample work function  $\Phi$  then enables an assignment of all excited intermediate states either with respect to the vacuum level or the Fermi level of the sample. The variable time delay between pump and probe pulse yields additional information about the changes of the population of the excited states, which makes **TR-2PPE** suitable for the analysis of the dynamics of elementary electronic processes at hybrid interfaces. The experimental details of **TR-2PPE** experiments and the working principle of the photoelectron detector can be found in Chapter III.

<sup>3</sup>An in-depth discussion of interfacial charge and energy transfer processes can be found in Section 5.3.

## 4 Electrostatic Aspects of Energy Level Alignment

One of the major strategies to control the functionality of hybrid surfaces is the control of the alignment of the energy levels across the interface. Although this approach is severely limited, as discussed above, the minimization of EIBs and HIBs or the creation of suitable gradients of the electrostatic potential is one of the main goals in applied HIOS research. This necessitates an in-depth microscopic understanding of the origins of these energy barriers, which is the main topic of this section. In particular, the direct connection of the energetic barriers to the work function  $\Phi$  of the inorganic substrate, as well as the limitations of this approach, are discussed.

### 4.1 Surface Dipoles and Work Function Tuning

The injection of an electron from a cathode into an organic material, or even into the vacuum requires the electron to overcome a potential barrier. In the latter case, the minimum barrier is identical to the work function  $\Phi$  of the surface which is defined as the electrostatic potential difference between the Fermi and Vacuum level:  $\Phi = E_{\text{vac}} - E_{\text{F}}$ . The origin of this potential at solid surfaces is, apart from the average electrostatic potential of a material, the surface dipole created by the slight spill-out of electrons into the vacuum relative to the static ion cores [LK71].

Any change to the surface morphology, and especially adsorption of new species, may change the spatial distribution of the electronic density at the surface, which leads to a modification of  $\Phi$ . This, of course, allows the intentional *tuning* of the work function by the controlled absorption of molecules with, e.g., a static dipole moment, as shown schematically in Fig. II.4. This energy level diagram shows the change to the effective electrostatic potential  $U(z)$  along the surface normal by a molecular dipole  $\mu_{\text{mol}}$ , which results in a change of the work function. This established way of work function tuning by creating a well-defined periodic array of dipoles at the surface [ISIS99] is described by the Helmholtz equation

$$\Delta\Phi = \frac{-q_e \mu}{\epsilon_0 A}, \quad (\text{II.4})$$

where  $q_e$  is the elementary charge,  $\epsilon_0$  is the vacuum dielectric constant, and  $\mu/A$  is the surface dipole density. Here, the effective  $\mu$  does not only consist of the static molecular dipole, but includes a number of contributions which are a result of interface formation. To be precise, the electron density tail of the substrate surface is perturbed by the presence of the chemisorbed or physisorbed molecules. Chemisorption, i.e., formation of covalent bonds between substrate and molecules [SG71], which is accompanied by an electron density flow through the atoms involved in the bond, results in interfacial charge transfer which further modifies the dipole [CGC<sup>+</sup>02]. Finally, the depolarization effects which result from the interaction between different individual molecular dipoles, have to be included in  $\mu$ . The sum of these contributions is what is commonly called the *interface dipole* at hybrid interfaces, which is a part of the traditional concept of interfacial energy level alignment (see Section 2.1).

What has to be kept in mind is that the above description of the surface or interface dipole and the use of the Helmholtz equation are only valid for homogeneous, macroscopic surfaces and interfaces. The work functions that result from Eq. II.4 refer to an area-averaged potential which is found at a certain distance away from the sample (typically on the order several Angström,

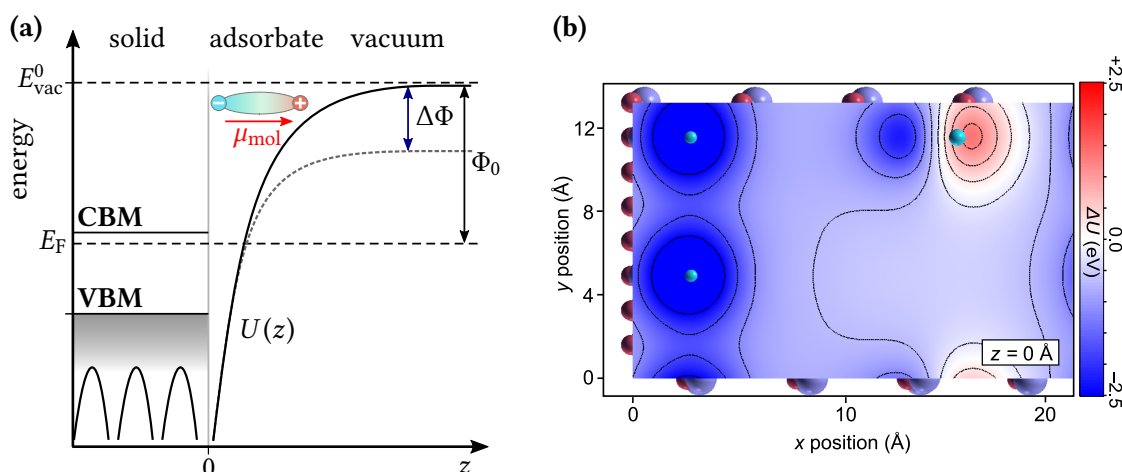


**Figure II.4:** Work function tuning by adsorption. (a) Diagram of the energy levels along the surface normal in case of ordered adsorption of dipolar molecules. The electrostatic potential  $U(z)$  is lowered by the additional surface dipole which causes a work function change  $\Delta\Phi$ . (b) Calculated change to  $U$  induced by hydrogen adsorption at the ZnO( $10\bar{1}0$ ) surface (see Section 2.4.2 of Chapter IV). These significant lateral variations of the potential directly at the surface ( $z = 0 \text{ \AA}$ ) are not considered in the diagram shown in (a). Figure courtesy of O. Hofmann.

see Section 2.4.2 of Chapter IV and Ref. [HDX<sup>+</sup>13]). What is measured in experiment is usually exactly this averaged potential, because PES and traditional Kelvin probe experiments [Lüt10] only offer limited spatial resolution, typically in the range of micrometers or more.<sup>4</sup> For this reason, work function measurements conducted by PES usually show a smooth gradual change of the work function of hybrid interfaces when the surface density of an adsorbate is increased up to a full monolayer [IOH<sup>+</sup>01, KBH<sup>+</sup>14, LRP<sup>+</sup>14].

Nevertheless, the basic idea of tuning the energy levels and thereby optimizing the functionality of interfaces remains valid, and there are several studies that clearly show . However, it has to be kept in mind, that the elementary processes at hybrid interface may predominantly depend on the microscopic characteristics of these potential changes, and a measured change in the work function may not correspond to the potential changes  $\Delta U$  that are induced at the position of the adsorbed molecule. An example of these possibly strong microscopic variations at the mixed-terminated ZnO( $10\bar{1}0$ ) surface<sup>5</sup> is shown in Fig. II.4(b). It displays the calculated change  $\Delta U$  to the surface potential induced by adsorption of *hydrogen* atoms (the detailed discussion of these results can be found in Section 2.4.2 of Chapter IV). According to the DFT calculations,  $\Delta U$  varies by several eV on distances on the order of a few Angström. The energy levels of any molecular adsorbates would, thus, differ strongly depending on the exact adsorption position. It can then be assumed that charge or energy transfer processes occur with different probabilities and efficiencies at different surface sites. What also plays an important role is the degree of localization of the quasiparticles that are involved in these elementary processes, which has

<sup>4</sup>Using Kelvin probe force microscopy, sub-nanometer resolution can be achieved, which usually reveals strong microscopic work function variations on surfaces with sum-monolayer adsorbate coverages [MSKL11].

<sup>5</sup>See Section 6.2 for a description of the surface terminations of ZnO.



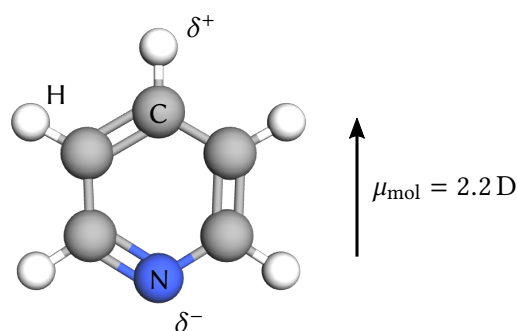


**Figure II.6:** Representation of a pyridine molecule with its static dipole moment  $\mu_{\text{mol}}$  along its symmetry axis.

which originate from the energetic position of the molecular HOMO/LUMO at the interface [ERR<sup>+</sup>10]. This is illustrated schematically in Fig. II.5: in (a) an energy diagram of a molecule with arbitrary positive electron affinity  $\chi$  is shown before adsorption to the inorganic substrate. When these molecules adsorb as an ordered layer, the assumed dipole leads to a shift of the molecular levels to lower energies, according to Anderson's rule (see Section 2.1). This shift is limited, though, as soon as the LUMO comes into resonance with the Fermi level as shown in (b). At this point, electrons are transferred from the substrate into the empty molecular state, leading to a CT-induced dipole that cancels the molecular dipole, effectively pinning the LUMO to  $E_F$ . This so called "Fermi-level pinning" can be overcome with molecules that exhibit a negative electron affinity. As schematically shown in Fig. II.5(c) and (d), the energetic location of the LUMO above the vacuum level prevents Fermi-level pinning as the LUMO approaches  $E_F$ . Assuming a high surface dipole density, this makes extremely small work functions possible, which might only be limited by the fact that the vacuum level cannot cross  $E_F$  in thermodynamic equilibrium.

#### 4.2.1 Pyridine as Prototypical Work Function Modifier

A molecule that exhibits the above-mentioned properties to cause strong work function reductions is pyridine, which is shown in Fig. II.6. Pyridine, as a prototypical heterocyclic organic compound, consists of a benzene ring where one carbon atom is replaced by a nitrogen atom, resulting in a static dipole moment of the overall molecule of  $\mu_{\text{mol}} = 2.2 \text{ D}$  [DWG54]. It was already shown by near edge X-ray absorption fine structure (NEXAFS) measurements that pyridine binds to the ZnO(10 $\bar{1}$ 0) surface in an upright standing geometry with the nitrogen atom pointing towards the ZnO substrate [WDM<sup>+</sup>93]. Further, adsorption experiments on different metal surfaces have shown drastic work function shifts with  $\Delta\Phi = -2.5 \text{ eV}$  for pyridine on Pt(111), and  $\Delta\Phi = -2.3 \text{ eV}$  for pyridine on Cu(111) surfaces [GS73, ZGW02, HRZB07]. In case of pyridine, the LUMO is located 0.62(5) eV above the vacuum level [Nen75], which makes Fermi-level pinning impossible. In addition, it was demonstrated that the use of pyridine as docking group improves the stability and electron transport properties of organic electronic devices [WBB<sup>+</sup>09], which further justifies the use of pyridine as a modifier of ZnO surfaces.

For these reasons, pyridine was chosen as model adsorbate to analyze its influence on the

electronic structure and work function of the mixed-terminated ZnO(10 $\bar{1}$ 0) surface, the results of which are presented in Section 4.1 of Chapter IV.

### 4.3 Interface and Gap States in Hybrid Systems

The electronic structure at interfaces between different materials, such as organic molecules and metal-oxide semiconductors, are not only defined by the already existing electronic levels that align in a certain way upon adsorption. It has been shown that *new* interface electronic states may occur which might play an important role for the alignment of energy levels and as pathways for relaxation processes of the excited system [WSC<sup>+</sup>14, RKM15].

The complex nature of these states and their origins makes a general description difficult (see Ref. [Lüt10]), however, it has been found that defects are a driving force for the occurrence of an *in-gap state* (IGS) at ZnO-based interfaces. At the interface between ZnO and the charge acceptor PTCDI, the presence of shallow donor-type defect states at the ZnO surface is found to lead to a charge transfer to the molecular acceptor which is accompanied by the appearance of an occupied state  $\approx 1$  eV below  $E_F$  [WSC<sup>+</sup>14]. The authors conclude that such charge transfer processes might lead to the occurrence of new states at hybrid interfaces in general, which eventually determine the interfacial energy level alignment [RKM15].

Further, the important role of structural imperfections on the energy level alignment has also been shown for organic films on metal substrates [HMG<sup>+</sup>11]. Disorder of the molecular layer was shown to cause the energetic broadening of the HOMO, which strongly influences the level alignment due to a bending of the molecular HOMO toward the Fermi level. Annealing the sample and thereby ordering the molecular film suppresses this effect, as the density of gap states that originated from the broadened HOMO is reduced.

## 5 Electron and Quasiparticle Dynamics in Semiconductors and at Hybrid Interfaces

The main functional role of a hybrid interface is to transfer charge carriers or energy from one material to the other, which naturally involves excited electronic states, e.g., polarons and excitons. Generally, the efficiency of these transfer processes is determined by the electronic coupling strength across the interface, the coupling of electronic degrees of freedom to nuclear coordinates and the thermal bath [Zhu04b] – apart from the electrostatic barriers and the resulting level alignment that were discussed previously.

In an excited system the “useful” transfer processes are only a small part of the rich relaxation dynamics that occur at interfaces. In semiconductors, particularly **electron–phonon (e–ph)** scattering or exciton recombination lead to the dissipation of energy and a deterioration of interface functionality. Their efficiency and the timescales of these competing loss channels, which eventually lead to a heating of the lattice or emission of photons, are defined by the detailed electronic properties of the interface.

Despite all these elementary electronic processes in such materials being essentially known, they cannot easily be observed in experiment or even predicted by theory [ZT15]. Thus, to understand hybrid interfaces one of the main challenges is to disentangle the individual processes and the influence of interface morphology and electronic structure. For this, well-defined model systems are required, where the elementary excitations can be studied in detail, which is the main theme of this work.

Within the following sections these elementary processes and their role in charge transfer at hybrid interfaces are discussed. Section 5.1 introduces the major scattering channels for hot electrons in solids, which is followed by a description of excitonic states and the corresponding quasiparticle dynamics in Section 5.2. Finally, Section 5.3 presents an overview on interfacial charge transfer processes.

### 5.1 Electronic Scattering Processes at Surfaces and Interfaces

The elementary relaxation processes at surfaces and interfaces have been a topic of intense studies for many years because they are of fundamental interest [Hai95]. At the same time the understanding of these processes gives insight into the ultrafast energy dissipation processes that are relevant for many different fields of novel functional optoelectronic systems [BMA15], including **HIOS**. The elementary relaxation processes determine on what pathways an excited system goes back to its ground state. Basically, electrons can scatter amongst themselves, with phonons, plasmons, or lattice imperfections, and they can diffuse laterally or perpendicular to a surface or interface. The exact details and ratios of these scattering processes determine the timescales on which systems approach their equilibrium state, which usually results in femto- to picosecond lifetimes of excited electronic states in metals, whereas the presence of an energy gap and the possibility of the formation of long-lived excitonic states can lead to slower and more complex dynamics in semiconducting materials.

One of the key differences between metals and semiconductors, the presence of a high density of delocalized free electrons in the former, determines the character of excited states and their

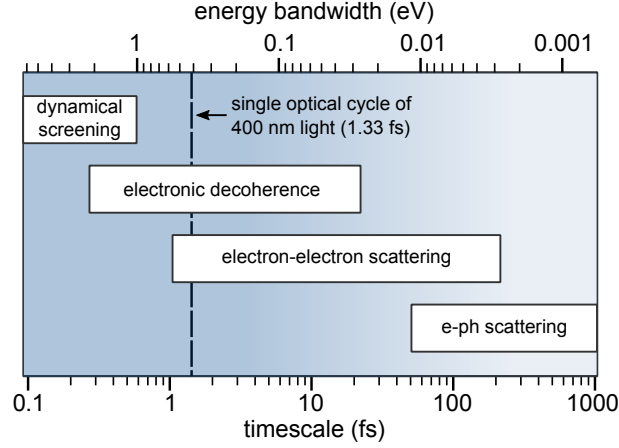


**Figure II.7:** Characteristic timescales of quasiparticle processes in metals. Adapted from Ref. [BMA15].

dynamics. While in metals electron–electron scattering is the dominating relaxation channel for excitation energies in the energy range  $E \gg k_B T$ , excited electrons in semiconductors favor different relaxation channels, mainly *e–ph* scattering, because of the overall lower density of free electrons. The high free electron density in metals is also the reason why exciton formation and recombination is usually not observed there, since the Coulomb interaction between electron and hole is efficiently screened by the electron cloud (see Section 5.2).<sup>6</sup> On the other hand, it may be asked what influence the high achievable charge carrier densities at doped semiconductor surfaces have on these relaxation processes, in particular in case of the formation of a *two-dimensional electron gas (2DEG)* at TCO surfaces [KVM<sup>+</sup>10], which has also been also observed at ZnO surfaces (see Section 6.4 and Ref. [OM11]).

### 5.1.1 Overview on Hot Electron Scattering and Decay Mechanisms

The relaxation of excited (“hot”) electrons to lower energy levels is a result of the interaction with its environment. For excitation densities which are sufficiently low, the relaxation process, which can be described by a characteristic decay rate  $\Gamma$ , is governed by a number of inelastic scattering processes [BMA15]. The most prominent ones, scattering with “cold” electrons and with phonons, are listed with other ultrafast processes in Fig. II.7. The often complex relaxation dynamics which may involve several processes may then lead to an effective scattering rate  $\Gamma_{\text{eff}}$ . Thus, the analysis of experimental data often requires the disentangling of the different decay processes, as

$$\Gamma_{\text{eff}} = \Gamma_{e-e} + \Gamma_{e-ph} + \Gamma_{e-h} + \dots \quad (\text{II.5})$$

where  $\Gamma_{e-h}$  is the population decay due to *e–h* recombination and the dots symbolize further scattering processes, such as defect scattering, that are not considered here (see Refs. [PZK<sup>+</sup>04] and [BMA15] for more details). The physically accurate assignment of the decay processes in the

<sup>6</sup>However, it has been experimentally demonstrated that excitons are actually forming in metals and precede the screening of the Coulomb interaction which happens on a few femtosecond timescale [CWA<sup>+</sup>14].

analysis of the experimentally observed population decay necessitates general knowledge about the characteristics of the different processes, which is presented in the following paragraphs.

**Electron–Electron Scattering** After excitation of a population of electrons, **electron–electron (e–e)** scattering, which randomizes both energy and momentum of the electrons, usually causes a rapid thermalization of the population. Thermalization refers to the evolution of the electron gas to a state in which the energetic distribution of electrons can be characterized by a temperature. In systems with high surface electron densities  $n \gtrsim 10^{17} \text{ cm}^{-2}$  this process dominates [Hai95] and results in a Fermi–Dirac distribution with elevated temperature  $T_{\text{el}} > T_0$ . In semiconductors, such as ZnO, **e–e** scattering is normally not the most efficient decay mechanism for hot electrons due to the lower electron densities. Even in hydrogen-doped ZnO these surface electron densities are on the order of  $10^{13} \text{ cm}^{-2}$  [OM11].

A theoretical framework for **e–e** scattering in systems with high electron density is based on **Fermi-liquid theory (FLT)** and yields an inverse quadratic energy dependence of the inelastic lifetime  $\tau_{\text{e-e}}$  on the energy of the excited intermediate state  $E_i$  relative to  $E_F$  [QF58]:

$$\tau_{\text{e-e}} \propto (E_i - E_F)^{-2}. \quad (\text{II.6})$$

Obviously, the energy of the total electronic system is not reduced by **e–e** scattering. For this, energy and momentum have to be transferred away from the electrons, e.g., to the lattice by scattering with phonons.

**Electron–Phonon Scattering** Excess energy of the electronic system can be transformed to heat in the lattice by **e–ph** scattering, which is the interaction between the electron and the quantized motion of the crystal ions. This process has decisive influence on electric and thermal resistivity in metals [Gri80].

The two main mechanisms of energy transfer between excited electrons and the lattice are (i) deformation-potential scattering in homopolar solids and (ii) Fröhlich interaction in polar materials, such as ZnO [Hai95]. The latter describes the interaction between excited electrons and polarization waves that are associated with **LO** phonons [Frö37, YC10]. Since **LO** phonons lead to a relative displacement of the oppositely charged atoms inside the unit cell, a long-range electric field  $E_{\text{LO}}$  is generated that can interact efficiently with electrons. In systems with comparably strong ionic character, such as ZnO, these fields are stronger than those originating from transversal modes, which results in the very effective interaction with the excited electrons. In addition, the energy of these phonon modes can be comparably high, e.g.,  $\hbar\omega = 72 \text{ meV}$  in case of ZnO [DPT66], compared to metals with energies absorbed per scattering event on the order of  $10 \text{ eV}$  [BMA15].

Fröhlich interaction favors scattering with phonons of small phonon wavevectors  $q$ , due to its  $q^{-1}$  dependence [YC10]. As a result, the changes in electron momentum for this type of interaction are predominantly small, as it is the case for intravalley decay of hot electrons.

Another **e–ph** scattering mechanism is the interaction with low-energy acoustic phonons, which is usually limited to energies in the few meV range. This scattering channel is, thus, only favorable in polar materials when the electron excess energies are below those of the **LO** phonons.

In the high temperature limit ( $k_B T \gg \omega_{\max}$ ,  $\omega_{\max}$  is the high frequency cutoff of the phonon spectrum) the scattering rate  $\Gamma_{e\text{-ph}}$  can be shown to scale linearly with temperature [Ski88]:

$$\Gamma_{e\text{-ph}}(T) = 2\pi\lambda_{e\text{-ph}}k_B T, \quad (\text{II.7})$$

where  $\lambda_{e\text{-ph}}$  denotes the e-ph coupling parameter. This dependency has often been used to identify the contribution of e-ph processes to the overall dynamics at metal surfaces [MBJ95, MMG93, KLI04]. For the high LO-phonon energy in ZnO, Eq. II.7 requires temperatures well above 800 K. It has been shown, that for such systems the corresponding hot electron lifetime can be approximated within the parabolic and isotropic band approximation [Bre99]

$$\Gamma_{e\text{-ph}} \propto n_{\text{BE}}(\omega t) + 1 = \frac{1}{\exp(\frac{\hbar\omega}{k_B T}) - 1} + 1. \quad (\text{II.8})$$

This temperature dependence leads, as in Eq. II.8, to a “freeze-out” of phonons for low  $T$ , which results in a slowing of the decay rate at low temperatures. This behavior has been found experimentally for a semiconducting Ge(111) surface [BH91].

**Electron-Defect Scattering** Electrons can also scatter with imperfections of the crystal structure, e.g., at impurities and corrugations at surfaces and interfaces. The scattering with defects corresponds approximately to a quasi-elastic redistribution of momenta [Kir08]. This means that usually only the phase of the electronic excitation is affected, not the energy [BMA15].

## 5.2 Excitonic Processes

In semiconductors, the excitation of the electronic system above the band gap, e.g. by the absorption of a photon, is usually followed by the formation of a quasiparticle consisting of electron ( $e^-$ ) and hole ( $h^+$ ) which are bound together by the Coulomb interaction [Lia70]:

$$h\nu \longrightarrow h^+ + e^- \xrightarrow{F_{\text{Coulomb}}} \text{exciton} \quad (\text{II.9})$$

This quantum of electronic excitation called *exciton* can transport energy, but not charge, through the semiconductor and across interfaces, and, consequently, it is an integral part of optoelectronic device functionality.

It can be classically depicted as a two-body system bound by the attractive Coulomb force (see Eq. II.9). In this respect, for many semiconductor materials it can be treated analogously to the hydrogen atom with the hole playing the role of the proton, as schematically shown in Fig. II.8(a). The exciton energies  $E_n$  thus form a series according to Bohr’s quantum theory

$$E_n = E_\infty - \frac{R}{n^2}, \quad (\text{II.10})$$

where  $n = 1, 2, \dots$  and  $R = m^* e^4 / 2\hbar^2 (4\pi\epsilon_0)^2 \epsilon^2$  [Lia70]. The binding energy  $R$  in semiconductors is significantly smaller compared to the hydrogen atom, which is because of the screening of the Coulomb force by the dielectric background of the crystal. This background consists of all atoms

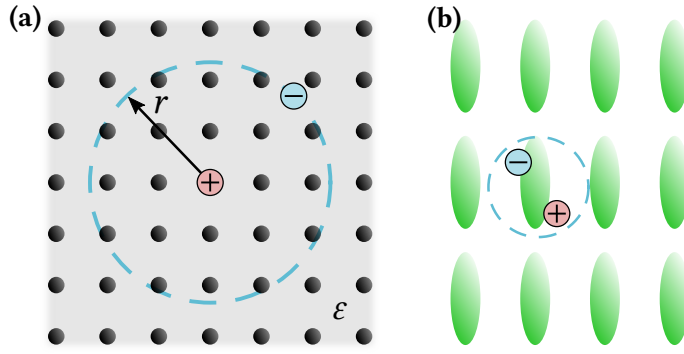


**Figure II.8:** Classical representation of (a) Mott–Wannier exciton as hydrogen-like quasiparticle with radius  $r$  in an inorganic crystal with static dielectric constant  $\epsilon$ , and (b) Frenkel exciton which is localized at a single site of an organic lattice (see text).

and free electrons and the resulting screening effect is summarized by the dielectric constant  $\epsilon$  of the material. It leads to a modification of the Coulomb potential energy, which becomes  $-e^2/(4\pi\epsilon_0\epsilon r)$ . If free electrons are present in the material, a more precise representation of the more strongly screened Coulomb potential is given by [Lia70]

$$-\frac{1}{4\pi\epsilon_0} \frac{e^2}{r} \exp\left(-\frac{r}{\lambda}\right), \quad (\text{II.11})$$

where  $\lambda$  is the screening length that defines the distance beyond which the potential rapidly approaches zero. Furthermore, the reduced effective mass  $m^*$  of the  $e$ - $h$  system leads to an additional reduction in binding energy with respect to the hydrogen atom.

The above description of the exciton as a hydrogen-like particle in a dielectric medium is, strictly speaking, only one of the two main limiting cases of excitonic species – the Mott–Wannier exciton. The other limiting case is the so-called Frenkel exciton which is characterized by its localization to one distinct lattice site, as shown in Fig. II.8(b). The character of the exciton and the determining properties of the medium can be described as follows:

**Mott–Wannier excitons** appear in semiconducting solids with covalently bound constituents, such as Si or GaAs. The generally large dielectric constant  $\epsilon$  of these materials results in comparably strong screening of the Coulomb interaction. As a result, the exciton binding energy is relatively small, according to Eq. II.10 on the order of 10 meV, and the corresponding exciton radius is significantly larger than the lattice spacing, which allows the substitution of the periodic crystal by a continuous dielectric medium. Mott–Wannier excitons can diffuse through the lattice as quasiparticles with an associated kinetic energy, as long as they are not trapped at defects.

**Frenkel excitons** are found in solids in which the neighboring atoms or molecules do only weakly interact, i.e., there is little overlap between the valence band electrons. As a consequence, excited electron and hole are localized at a single lattice site consisting of an ion or a molecule. The resulting binding energies are on the order of 0.1 eV to 1 eV with effective masses  $m^*$  that far exceed those of Mott–Wannier excitons. Energy transfer

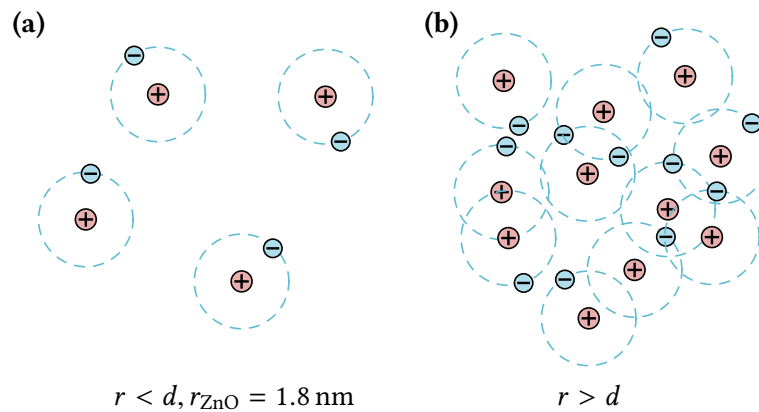


**Figure II.9:** Schematic representation of an exciton gas (a) below and (b) above the Mott density. The Mott transition of the exciton is defined by the density, at which the exciton radius  $r$  equal to the exciton-exciton distance  $d$ .

via Frenkel excitons then happens by the passage of the exciton between neighboring molecules through nonradiative dipole-dipole coupling, a process termed **Förster resonant energy transfer (FRET)** (see Section 5.3.2).

The decay of excitons, i.e., the dissipation of the energy of excitation, may happen via three main ways: By conversion to heat through collision with the lattice, by ionization that leads to free electron and hole, and by radiative recombination into the electronic ground state accompanied by the emission of a photon. This radiative recombination usually requires the exciton to be in its singlet ground state (e.g.,  $S_1$ ). Similar to the hydrogen atom, excitons can assume excited (“hot”) states that can relax internally. Further, the spin state of the exciton may change between singlet and triplet leading to interesting and technologically relevant effects, such as exciton fission [CLJ<sup>+</sup>11]. The fundamentally different physics of excitons compared to hot charge carriers results in decay dynamics that are significantly slower: in direct-gap semiconductors exciton lifetimes are on the order of nanoseconds [KKKG06], compared to the femto- to picosecond dynamics that result from  $e-e$  and  $e-ph$  scattering of hot electrons.

The bosonic character of excitons as quasiparticles with overall integer spin allows the “condensation” of an ensemble of excitons into a single quantum state – a **Bose–Einstein condensate (BEC)** [Per02]. Yet, providing the conditions for BEC formation, temperatures in the mK range, lowest exciton momentum, and a sufficiently high density of long-lived excitons, has proven challenging. Consequently, experimental evidence for excitonic condensates is scarce [ABL<sup>+</sup>14].

### 5.2.1 Exciton Formation and Excitonic Mott Density

The formation of an excitonic population after above-band gap excitation in semiconductors, such as ZnO, happens in a two-step process: first the plasma of excited electrons and holes thermalizes; thereby hot excitons are formed with an excess center of mass momentum ( $\mathbf{K} \neq 0$ ) [Per75]. Secondly, the excitons relax to the emissive ( $\mathbf{K} = 0$ ) state via the emission of phonons

[HKB07]. Timescales on which exciton formation happens, are still a heavily debated topic, especially since one has to distinguish between the complex-valued optical semiconductor polarization that determines linear absorption, transmission and reflection properties, and real-valued genuine *populations* of electrons, holes or excitons [KKKG06]. Furthermore, it is still an open question whether exciton populations are necessary for the observation of photoluminescence (PL), as PL at the exciton energy occurs at times that are much shorter than theoretical predictions [SKB<sup>+</sup>04].

It is clear, however, that the screening of the Coulomb interaction reduces the exciton formation probability. This screening due to a large number of free charge carriers may be due to (i) doping and/or related charge accumulation, or (ii) by the excited electron-hole plasma itself. In the classical description of the exciton as hydrogen-like quasiparticle with Bohr radius  $r$  there exists a critical exciton density at which the excitons would classically overlap. This so-called exciton Mott density  $n_M$  is defined by the point at which the inter-excitonic distance  $d$  is equal to the exciton Bohr radius, as depicted in Fig. II.9.

In an experiment that measured the photoconductivity of bulk ZnO with an optical pump-THz probe method it has been shown that  $n_M$  is on the order of  $2 \times 10^{24} \text{ m}^{-3}$  to  $3 \times 10^{24} \text{ m}^{-3}$  [HKB07], which roughly corresponds to the exciton Bohr radius of 1.8 nm for ZnO [KHFK07]. Above this density the electron-hole plasma decays via Auger annihilation within  $\approx 1.5$  ps, thereby depopulating the ZnO CB. For optical excitation below the Mott density, the authors observe a decay of conductivity on a timescale of 10 ps to 100 ps after excitation, which is attributed to the formation of excitons.

As indicated above, the excitonic Mott transition can not only be induced by creating a sufficiently high density of electron-hole pairs, but also by the screening of already present free carriers, e.g., in degenerately  $n$ -doped systems or 2DEGs at surfaces. In these systems, optical excitation is believed to lead to complex many-body processes that are hard to quantify experimentally. In a recent theoretical study [SRF<sup>+</sup>11] on exciton formation in degenerately doped ZnO the authors deduce a Mott density of  $n_M = 5.94 \times 10^{24} \text{ m}^{-3}$ . They conclude, however, that an actual Mott transition does *not* take place in degenerately doped ZnO, despite the fact that bound excitonic states seem to vanish in experiment and the exciton binding energy is drastically reduced. Instead, the authors suggest that Mahan-type excitons [Mah67] are formed, where an ensemble of excited CB electrons form bound states with localized holes in the VB.

These recent findings illustrate that excitonic effects in degenerate semiconductors and 2DEGs involve complex many-body physics that are far from being fully understood. The scarcity of data on exciton formation processes in ZnO, and in particular at its surface, makes further studies on this subject highly desirable.

### 5.3 Interfacial Charge and Energy Transfer

At hybrid interfaces there are different transfer mechanisms which either lead to a transfer of the excitation energy or the charge carriers, depending on the screening of the Coulomb interaction across the interface and the coupling between electronic states in the different materials. In the following, some of these processes that are relevant for HIOS and which are schematically illustrated in Fig. II.10, will be discussed.

At hybrid interfaces the distinction between “pure” excitonic or charge transfer (CT) processes

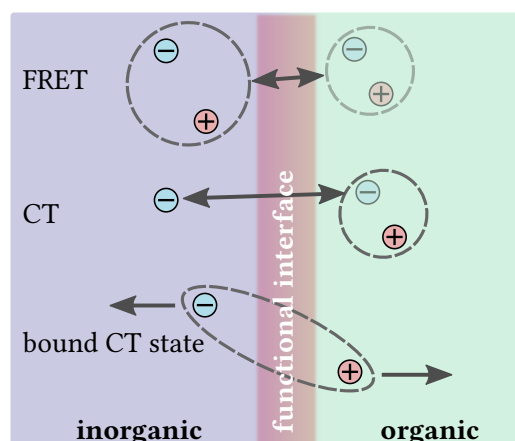


**Figure II.10:** Scheme of a HIOS interface that shows the interfacial electronic transfer and coupling mechanisms. The resonant transfer of energy via FRET competes with the transfer of charges across the interface. The CT process may be slowed down considerably by the formation of bound CT states that are localized across the interface.

cannot generally be drawn clearly. The presence of the interface may lead to the formation of bound excitonic CT states which reside in both materials. These bound hybrid states are suggested to play an important role in the charge separation process at hybrid or organic heterostructure photovoltaic cells [ZYM09, SPN<sup>+</sup>14].

Particularly, in the case of CT processes the current knowledge is largely based on studies on metal–organic interfaces, most probably because these interfaces prevail in, e.g., OLED and photovoltaics applications. For contacts between inorganic semiconductors, such as ZnO, with organic molecules further complications occur because of different, often doping-dependent, screening of the Coulomb interaction, and the generally less understood surface properties of TCO materials (see Section 6).

### 5.3.1 Charge Transfer

A comprehensive satisfactory theory of CT at hybrid interfaces, i.e., the transfer of an excited charge carrier from one material to the other, does not exist so far and all current theories rather treat different limiting cases [Sco03]. From a macroscopic perspective, the CT process is governed by the interfacial energy barriers, i.e., the electrostatic properties of the interfaces, as introduced in Section 2.1. The process of overcoming these barriers is then described within the framework of Schottky thermal injection or Fowler–Nordheim tunneling [AT04]. Descriptions that capture the microscopic character of the functional interface are derived from those of tunneling processes through molecular junctions [Zhu04a] or they make use of the formalism of heterogeneous electron transfer [MS85, SPSZ12]. This lack of a general theory makes CT processes at interfaces a topic of fundamental interest. A description of CT that refers to a 2PPE experiment can be found in Section 1.4 of Chapter III.

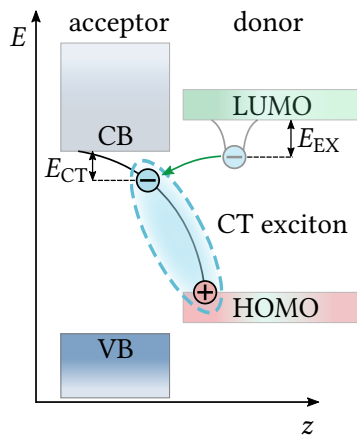


**Figure II.11:** Schematic picture of the bound charge transfer (CT) exciton formation at a hybrid interface. At the interface, the purely molecular exciton is separated by the energy offset between donor and acceptor states at the interface. Further dissociation is then inhibited by the Coulomb interaction.

### 5.3.2 Förster resonant energy transfer (FRET)

A fundamentally different way of exchanging energy in form of an electronic excitation is **Förster resonant energy transfer (FRET)** [För48], which is the primary energy transfer mechanism in photosynthesis [vGDGS94]. This potentially highly efficient (100% theoretical limit [HIM<sup>+</sup>06]) interfacial transfer of excitons is a resonant dipole coupling process between singlet states, conserving the spin states of donor and acceptor. **FRET** can, as an example, be employed to transfer an excitation from an inorganic material to an organic emitter, thereby ensuring that energy is only transferred to singlet states which can then decay radiatively [NHF<sup>+</sup>14]. Furthermore, because of its high efficiency, **FRET**-based hybrid systems may overcome the poor transport properties of organic materials [HIM<sup>+</sup>06].

The measured overlap between emission and absorption spectra of donor and acceptor, respectively, can be used as an indicator for the Coulomb interaction between donor and acceptor dipole. The rate  $k_{ET}$  of Förster transfer is given as [För48]

$$k_{ET} = \frac{1}{\tau_D} \left( \frac{R_0}{R} \right)^6, \quad (\text{II.12})$$

where  $\tau_D$  is the natural lifetime of the donor excitation and  $R_0$  is the so-called Förster radius, defined as the distance at which the energy transfer rate equals the rate of natural exciton decay. Values of  $R_0$  are on the order of 3 nm for a hybrid interface between ZnO and POPOP molecules<sup>7</sup> with a maximum efficiency of  $\eta_{ET} = 0.5$  [BSX<sup>+</sup>06]. The authors also found a radiative transfer of energy for large donor-acceptor distances ( $L_S = 50$  nm), where photons emitted from from the ZnO are reabsorbed by the organic layer, albeit with a rate that is an order of magnitude lower than the rate of radiationless **FRET**.

### 5.3.3 Hybrid Charge Transfer States

The harvesting of solar energy in organic heterostructure solar cells relies on the *dissociation* of a bound **e-h** pair (exciton) at the interface [MYTZ08], as shown in Fig II.10. The driving force

<sup>7</sup>POPOP, which is short for 2,2-*p*-phenylenebis-(5-phenyloxazol), is a highly fluorescent scintillator and laser dye, see Ref. [BSX<sup>+</sup>06] for details.

for charge separation at the interface is the energetic offset between the acceptor and donor electronic levels. This is depicted schematically in Fig. II.11, where an electron is transferred from the molecular donor LUMO to the CB of an inorganic semiconductor, while the hole remains located at the donor. The comparably low dielectric constants of both materials may then prevent the sufficient screening of the Coulomb interaction between electron and hole. As a result, they form a bound CT exciton which exhibits a binding energy  $E_{CT}$  [VBGF12] (see Section 3 for energy assignments).

This species is detrimental to interface functionality, because it inhibits the extraction of charges. The long-lived character of the CT excitons may lead to decay via different radiative and non-radiative channels, which drastically reduces the quantum yield.

There are several factors which allow the charges to overcome the “Coulomb trap” at the interface [MYTZ08, RKK<sup>+</sup>15, ZYM09]:

1. The excess energy of the e–h pair at CT exciton formation may leave the exciton in a *hot* state, i.e., a high quantum number and/or high  $k$  states, which translates into additional kinetic energy. This can be experimentally studied by re-exciting the cooled CT excitons into delocalized hot states with an infrared (IR) pulse (“pump-push” spectroscopy) [BRP<sup>+</sup>12].
2. A high extent of delocalization supports separation due to the higher effective charge mobility. This aspect is of special interest in hybrid systems where the exciton has Mott–Wannier character (see Section 5.2) in the inorganic component [ZMG<sup>+</sup>15].
3. The occurrence of electric fields across the interface may drive the charges apart. This can be achieved by doping, which results in a  $p$ – $n$  junction [LZR<sup>+</sup>08]. As an alternative, the interfacial field may come from charge redistribution and polarizations [AHB03].
4. Charges can be trapped in intermediate states, e.g., at impurity sites, which lead to a cascaded dissociation process with high probability of hot CT exciton formation, as it is observed in photosynthesis [GMM01].

Bound e–h pair states have only recently been identified at the interface between ZnO and optically active dyes [SBS<sup>+</sup>13, SPN<sup>+</sup>14, RKK<sup>+</sup>15], causing an estimated reduction of the photo-generated charges by 50% in P3HT/ZnO and F8TBT/ZnO heterostructures (see Ref. [VBGF12] for details on the chemical structures). The occurrence of species are believed to be responsible for the low performance of ZnO–dye-based photovoltaic cells, which exhibit significantly lower efficiencies compared to cells with ITO or TiO<sub>2</sub> as contact layers. This low performance is reflected in the dynamics of charge injection processes, which range from few femtoseconds for charge injection from the “N3” dye into TiO<sub>2</sub> [SBP<sup>+</sup>02] to hundreds of picoseconds at ZnO-based interfaces [SPN<sup>+</sup>14, VBGF12]. The microscopic origins for the high yield of bound CT excitons at hybrid molecule/ZnO interfaces is still unclear, however, a joint experimental and theoretical study by Siefermann et al. suggest the *intrinsic* character of a long-lived interfacial CT state at the N3/ZnO interface [SPN<sup>+</sup>14].

## 6 Zinc Oxide: Electronic Structure and Surface Morphology

Zinc oxide is a prototypical representative of the still poorly understood class of **transparent conductive oxides (TCOs)** [KV11, GHP11], which makes it a promising candidate as transparent electrode material in **HIOS**. It exhibits a large band gap of 3.4 eV and shows a distinct propensity for *n*-type conductivity [KFZ<sup>+</sup>10, ÖAL<sup>+</sup>05], which is exemplified by its native unintentional *n*-type doping. The comparably high bulk exciton binding energy of 60 meV in ZnO [Tho60] makes excitonic emission possible even above room temperature.<sup>8</sup> Further, the radiation hardness of ZnO makes it suitable for applications in extreme environments [KIA<sup>+</sup>05].

ZnO cannot be described as a *novel* material, since extended research for several decades has revealed many of the optical and electronic properties of this material [KFZ<sup>+</sup>10]. This knowledge is reflected in the various suggested applications for ZnO apart from **HIOS**, e.g., as medium for random lasing in the UV regime [CZH<sup>+</sup>99, DHH14], as sensor for hydrogen and hydrocarbons [Göp85] or as transparent semiconducting material in thin-film transistors [SS05]. In addition, the ease with which ZnO can be grown in complex self-organized shapes, such as nanorods with huge surface areas, has spurred much interest [KFZ<sup>+</sup>10].

This section focuses mainly on the surface properties of ZnO, due to their essential role in **HIOS**. Because the quality of sample surfaces has significantly evolved in recent decades, the understanding of complex morphology and electronic structure of the various ZnO surface terminations has improved drastically. However, the microscopic origin of surface conductivity and the detailed characterization of ZnO surfaces and interfaces that enables a fundamental insight into the elementary processes that happen at ZnO-based interfaces are still lacking.

### 6.1 General Properties of Bulk ZnO

Zinc oxide is a binary compound II<sup>b</sup>-VI semiconductor which predominantly crystallizes in a tetrahedrally coordinated wurtzite-type crystal structure, as shown in Fig. II.12. Although this structure is characteristic for covalent *sp*<sup>3</sup>-hybridized bonds, the bond between the Zn<sup>2+</sup> and O<sup>2-</sup> components has a substantial ionic part [Kli07]. Wurtzite crystals exhibit four most prominent surface terminations: the mixed-terminated (10 $\bar{1}$ 0) and (11 $\bar{2}$ 0) surfaces and the polar oxygen-terminated (000 $\bar{1}$ ) and zinc-terminated (0001) surfaces. The characteristic properties of these markedly different terminations will be discussed in Section 6.2, focusing on the (000 $\bar{1}$ ) and the thermodynamically most stable (10 $\bar{1}$ 0) surface.

#### 6.1.1 Electronic Structure and Related Properties

Zinc oxide shares its propensity for *n*-type doping with other binary **TCOs**, such as In<sub>2</sub>O<sub>3</sub>, SnO<sub>2</sub>, CdO (termed *n*-**TCOs** in the following). The comparably high electronic conductivity of ZnO can be traced back to the partly ionic nature of the bonds between its constituents. It causes the almost exclusive Zn<sup>2+</sup> 4s character of the **CB**, and for the same reason the **VB** is essentially formed by the 2*p* orbitals of O<sup>2-</sup>. While the former *s* states are delocalized and, thus, exhibit a high free carrier mobility, the latter *p* states show the contrary behavior, which

<sup>8</sup>Room temperature corresponds to  $k_B T = 25 \text{ meV}$ . As a comparison, the exciton binding energy in GaN is below 30 meV [KPD<sup>+</sup>05].

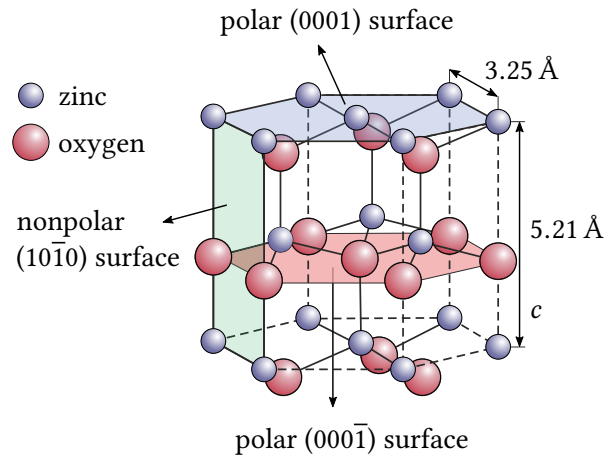


**Figure II.12:** Geometric structure of wurtzite ZnO. The nonpolar (10 $\bar{1}0$ ), (000 $\bar{1}$ )-O-polar and (0001)-Zn-polar surfaces are indicated. The direction of the  $c$ -axis is perpendicular to the polar surfaces. Modified from Ref. [GPIR82].

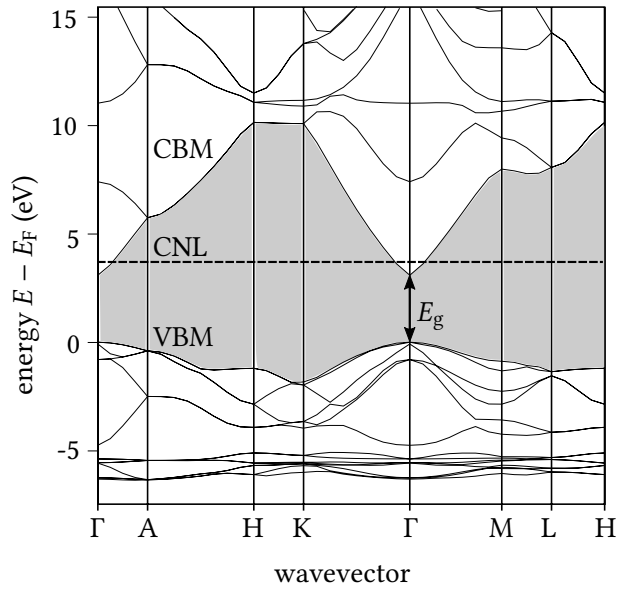


**Figure II.13:** Calculated wurtzite ZnO band structure. The striking feature is the distinct **conduction band minimum (CBM)** at the  $\Gamma$ -point and the otherwise comparably broad gap. Modified from Ref. [MOI99].

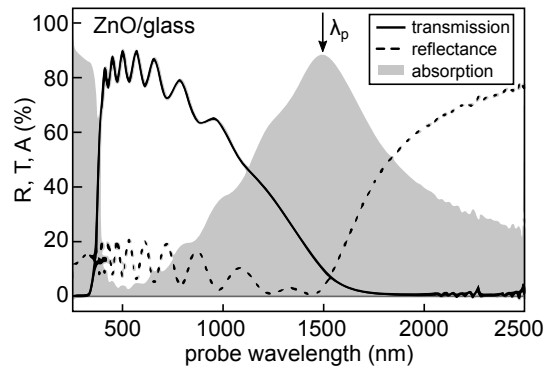


**Figure II.14:** Typical optical reflection, transmission and absorption spectra of a ZnO thin film on glass. The oscillations in transmission and reflectance spectra are due to thin film interference effects. Adopted from Ref. [GHP11], with kind permission from Springer Science and Business Media.

leads to high electron and low hole mobilities [GHP11]: For *p*-doped ZnO, hole mobilities of a few  $\text{cm}^2 \text{V}^{-1} \text{s}^{-1}$  have been reported [EKR08], while the electron mobilities can reach values of  $5000 \text{ cm}^2 \text{V}^{-1} \text{s}^{-1}$  in thin undoped films at 100 K [TOO<sup>+</sup>04].

From the calculated bulk band structure of wurtzite ZnO, shown in Fig. II.13 [GHP11], one can directly conclude its hallmark optical properties. The direct gap of  $\approx 3.4 \text{ eV}$  (wavelength of 365 nm) – located at the  $\Gamma$ -point without any subsidiary CB minima – is responsible for the optical transparency, which can be seen in the transmission and absorption spectra of typical commercial ZnO on glass, shown in Fig. II.14 [GHP11]. The sharp high energy cutoff of transmission at  $\approx 350 \text{ nm}$  is due to interband absorption by excitation across the gap. On the low energy side of the transmission window, the gradual decrease in transmission starting at  $\approx 1000 \text{ nm}$  and the simultaneous increase of reflectance from  $\approx 1500 \text{ nm}$  onwards is due to collective excitations of electrons (plasmons) in the CB. These oscillations have a characteristic plasma wavelength  $\lambda_p$  that depends on the density of electrons in the CB and which is marked by the maximum of light absorption at about 1500 nm for this apparently highly *n*-doped sample.

### 6.1.2 The Debated Source of Conductivity in ZnO and *n*-TCOs

The strong tendency of ZnO and the other *n*-TCO materials to exhibit high *n*-type conductivity distinguishes them from conventional semiconductors, such as Si or GaAs. In particular, the question on the origin of the native *n*-type doping of these materials and the apparent difficulties in producing commercially viable *p*-doped variants has led to continuous debates.

Among the candidates that have been proposed as being responsible for the *n*-type characteristics and conductivity, the oxygen vacancy  $V_O$  is of particular importance [Sam73]. However, so far experimental and theoretical studies on ZnO do not yield conclusive results, as the  $V_O$  appears to be a deep donor with an energy far below the CBM [JdW05, MJ09]. According to experiments, significant  $V_O$  concentrations in ZnO are either present natively [SWSL07], or need to be introduced intentionally by particle irradiation [VW05]. Similar findings on the role of the  $V_O$  have been made for the other *n*-TCOs with strong variations depending on growth conditions, temperature and further parameters.

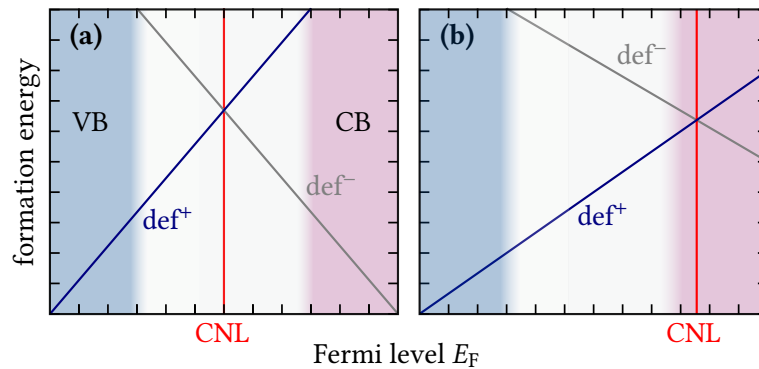


**Figure II.15:** Schematic representation of the formation energy of electron donor ( $def^+$ ) and acceptor ( $def^-$ ) type defects as a function of the Fermi level. (a) Conventional semiconductor with **charge neutrality level (CNL)** in the mid gap position. (b) *n*-TCO with **charge neutrality level (CNL)** located above the CBM. Adapted from Ref. [KVJ<sup>+</sup>09].

In brief, the role of – usually *unintentional* – native defects in ZnO and TCOs in general is still largely unclear. It was concluded, that there is no type of defect which is *solely* responsible for the *n*-type behavior of the *n*-TCO materials, but there is obviously an intricate interplay of different mechanisms [KV11]. Furthermore, unintentional impurity doping, especially with ubiquitous *hydrogen*, is suggested to play a decisive role for the conductivity in *n*-TCOs, as will be discussed in detail in Section 6.4.

### 6.1.3 The Role of the Charge Neutrality Level in Doping

Using the macroscopic concept of the **charge neutrality level (CNL)** one may deduce the doping properties of TCO materials from their band structure [KVJ<sup>+</sup>09]. It defines the energetic “branching point” above (below) which a defect assumes predominantly electron acceptor (donor) characteristics. As a result, the formation of defects with electron donor character ( $def^+$ ) is energetically favorable if  $E_F$  is located below the CNL. This is especially relevant for amphoteric defects,<sup>9</sup> such as hydrogen. The position of the CNL is given by the mid gap energy *averaged* across the Brillouin zone [KV11, KVJ<sup>+</sup>09].

In ZnO the pronounced low lying CBM at the  $\Gamma$ -point consequently leads to a comparably high energetic position of the CNL at  $\approx 0.2$  eV above the CBM [SFR<sup>+</sup>09], as indicated in Fig. II.13.

Fig. II.15 schematically compares the formation energies for donor and acceptor type defects CNL in conventional semiconductors, such as, Si, or GaAs, with those of *n*-TCOs, both with respect to the position of the Fermi level. In the former, the CNL lies in the center of the energy gap, while in the latter it is close, or above the CBM. As a consequence, the formation of *n*-type defects ( $def^+$ ) is much higher in *n*-TCOs, even when the Fermi level is already located close to the CBM, i.e., even in already *n*-doped systems. An analogous argument shows, that any shift of  $E_F$  towards the **valence band maximum (VBM)**, as it happens in *p*-doping, will energetically

<sup>9</sup>In the context of semiconductors, amphoteric means that a defect can act either as electron donor or acceptor, leading to either *n*- or *p*-type doping.

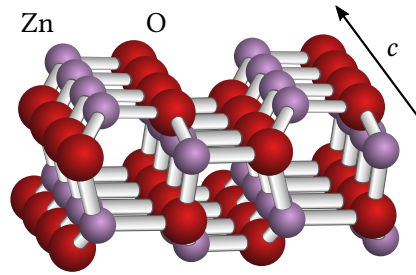


**Figure II.16:** Structure of the mixed-terminated  $\text{ZnO}(10\bar{1}0)$  surface. The Zn (violet) and O (red) atoms form rows and valleys along the  $c$ -axis of the crystal with a rectangular unit cell.

favor the formation of compensating donor-type defects in a much stronger way compared to conventional semiconductors, thus, strong  $p$ -doping in ZnO is inhibited.

## 6.2 Geometric Structures of ZnO Surfaces

The breaking of chemical bonds at a surface usually has significant consequences for the surface morphology and, in particular, for the electronic structure which is markedly different at or near the surface compared to the bulk crystal [Lüt10]. The probably most debated point in current ZnO materials research is the bridging between the exact microscopic structure of ZnO surfaces and the consequences of these geometric properties for the electronic structure. Here, the distinctly different characteristics of the examined ZnO  $(10\bar{1}0)$  and  $(000\bar{1})$  surface terminations are briefly discussed.

### 6.2.1 The Mixed-Terminated $(10\bar{1}0)$ Surface

The non-polar  $\text{ZnO}(10\bar{1}0)$  surface termination with its rectangular surface unit cell (see Fig. II.16) is the energetically most favorable surface of ZnO [MMD<sup>+</sup>04]. Consequently, this termination forms the dominating portion of surfaces in nanoscale structures, such as hexagonal rods, where the outer sides predominantly exhibit the  $(10\bar{1}0)$  termination (cf. Fig. II.12). It exhibits no electrostatic instabilities – in contrast to the polar terminations – which is corroborated by **low-energy electron diffraction (LEED)** and **scanning tunneling microscopy (STM)** measurements of pristine  $\text{ZnO}(10\bar{1}0)$  surfaces [DBD02, DKD04] that show the bulk truncated and unreconstructed rectangular surface structure. In addition to its intrinsic stability, this surface termination has been found to exhibit only few point defects, such as oxygen vacancies, in its pristine state [YBH<sup>+</sup>06]. Despite this preservation of stoichiometry, **STM** measurements revealed that the surface is comparably strongly corrugated, exhibiting many steps and terraces [?].

The electrostatic stability of this surface makes it comparably tractable for theoretical modeling. Together with the fact that this surface dominates in nanostructures this is one major reason why this surface termination was chosen as a starting point in this work.

### 6.2.2 The O-Polar $000\bar{1}$ Surface

The  $000\bar{1}$  surface exhibits a hexagonal surface structure (see Fig. II.12) that is exclusively terminated by oxygen atoms. Assuming that all ions are in their formal bulk oxidation state, each ZnO double layer carries a dipole moment which diverges with the thickness of the ZnO slab. As a consequence, the surface energy will diverge with sample size, and, thus the bulk truncated polar structure is not stable [Mey04]. To diminish the dipole between the two layers, there has to be a redistribution of charges, which usually happens by either by structural rearrangement or the loss of ions at the surface.

It is a surprising fact that there is no consensus on the structure of the clean surface, as mostly no reconstructions are found and LEED measurements usually show clear hexagonal diffraction patterns without any overstructures [Wöl07]. However, there is one study that suggests a  $(1 \times 3)$  reconstruction of the clean surface [KGGB<sup>+</sup>02]. In this work it is argued that the bulk-truncated  $(1 \times 1)$  structure can only exist with *hydrogen* adsorbed on the surface, which is corroborated by DFT calculations [Mey04]. As a consequence, the majority of all studies that report on unreconstructed surfaces would have actually measured a surface which has been stabilized by hydrogenation.

Summing up, hydrogen is a clear candidate as stabilizing agent at zinc oxide (and possibly other *n*-TCO) surfaces, apart from its role in *n*-doping of bulk ZnO. A discussion of the role of hydrogen as defect in ZnO can be found in Section 6.4.

## 6.3 The ZnO Surface Electronic Structure

### 6.3.1 Surface States and Space Charge Layers

The breaking of the translational symmetry at the surface of a solid leads to the occurrence of electronic states which have no analog in the crystal bulk.<sup>10</sup> In semiconductors, unlike in metals, these states can lead to so-called *space-charge* layers, where the concentration of carriers varies significantly with the distance relative to the surface, causing electric fields with strengths on the order of  $10 \text{ MV cm}^{-1}$  [YOY<sup>+</sup>15]. Considering these space charge layers in models of energy level alignment and charge transport is, thus, of utmost importance for the understanding of hybrid interfaces.

Space charge layers have their origin in the charge that is added to the surface by a surface state. These states have either electron donor or acceptor character and, depending on their occupancy, are either charged positively or negatively: empty donor states carry a positive charge, while occupied acceptor states carry a negative charge. Any neighboring charge will then act to minimize the energy of the system by rearrangement, which leads to *screening* of the surface charge. The efficiency, and thus the range over which charges have to rearrange to cause sufficient screening, depends on the density of electrons close to the surface. The higher the density of electrons, the shorter the so-called Thomas–Fermi screening length

$$L_{\text{Th-F}} = \left[ \frac{e^2}{\varepsilon_0} D(E_F) \right]^{-1/2}, \quad (\text{II.13})$$

<sup>10</sup>For an extensive treatment of surface states at solid surfaces, see Refs. [Lüt10, Mön01].

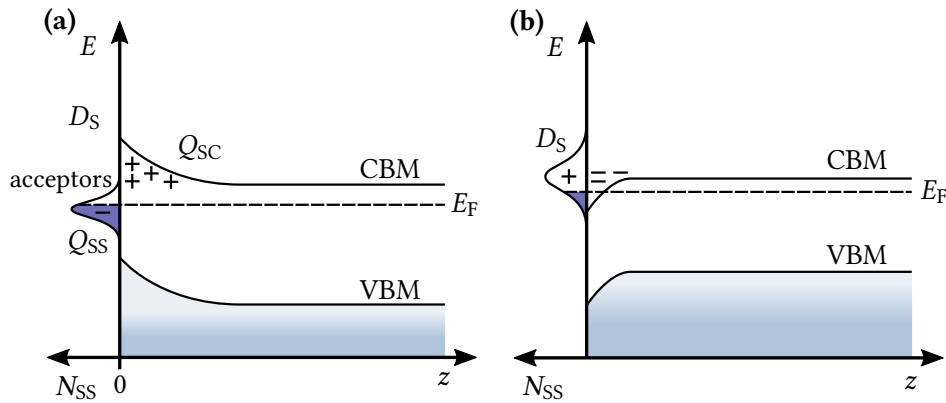


**Figure II.17:** Schematic surface band structure (band energy  $E$  with respect to  $z$  coordinate normal to the surface at  $z = 0$ ) for (a) a conventional  $n$ -doped semiconductor and (b) zinc oxide. (a) The partially occupied acceptor type surface state (density  $N_{SS}$  with charge  $Q_{SS}$ ) pins  $E_F$  close to the mid gap at the surface.  $Q_{SS}$  is screened in the bulk by ionized donors, carrying a positive charge  $Q_{SC}$ . As a result, the electronic bands bend upward at the surface and a depletion layer forms. (b) A surface donor state  $D_S$  with density of states  $N_{SS}$ , which is mostly unoccupied, causes a positive surface charge. This charge is screened by electrons which accumulate close to the surface ( $z = 0$ ) leading to downward bending of the bands relative to  $E_F$ , and, thus, the crossing of the **CBM** with  $E_F$  close to the surface. Modified from Ref. [Lüt10].

where  $D(E_F)$  is the density of electronic states at  $E_F$  and  $e$  is the elementary charge.  $L_{Th-F}$  varies from sub-atomic distances in metals with electron densities on the order of  $10^{22} \text{ cm}^{-3}$  to tens of nanometers and more in non-degenerate semiconductors with free-carrier concentrations on the order of  $10^{17} \text{ cm}^{-3}$  [Lüt10].

In conventional  $n$ -type semiconductors such as Si or GaAs, acceptor-type surface states exist, which are energetically fixed to the **CBM** and located near the center of the band gap. As depicted in Fig. II.17(a) a filling of such a state introduces a negative charge  $Q_{SS}$  at the very surface that has to be screened and compensated to maintain charge neutrality. This also means that the Fermi energy at the surface cannot have the same position as in the bulk, where it is located close to the **CBM**. If that was the case, a considerable negative charge would build up and, thus, inhibit the formation of any compensating positive charges. Instead, the Fermi level is said to be *pinned* by the surface state at mid gap energy and an effective *upward* band bending occurs. This deformation of the surface band structure goes along with an electric field along the surface normal, which lifts bulk donor states above  $E_F$  and, thus, creates a positive space charge  $Q_{SC}$ . As a consequence, free negative charge carriers are pushed away from the surface and the space charge layer is therefore called a *depletion layer*.

It appears to be a universal feature of  $n$ -TCOs to behave in the *opposite* way: The position of the **CNL** right at, or even above the **CBM** favors the formation of mostly unoccupied donor-type surface states at energies close to the **CBM**. Again, the Fermi level is pinned by these states, which, due to their electron donating character, now carry a positive charge. Accordingly, as depicted in Fig. II.17(b), this leads to a *downward* band bending at the surface accompanied by negatively charged space charge layer. Since the shape of the bands at the surface now attracts

electrons that accumulate until charge neutrality is reached, this characteristic configuration is called *accumulation layer*.

### 6.3.2 Surface Charge Accumulation Layers and Surface Conductivity

Electrical conductivity is one of the two hallmark features of TCOs and the understanding of its origin in these materials is a vital step towards the design of novel devices. A considerably basic description of the conductivity  $\sigma$  in solids is given by the Drude model [Dru00]:

$$\sigma = en\mu, \quad (\text{II.14})$$

with  $e$  the elementary charge,  $n$  the density and  $\mu$  the mobility of charge carriers. According to this model, the charge carrier density  $n$  directly defines  $\sigma$ , and, thus, the strong variations in  $n$  due to CAL formation at the surface of TCO materials are expected to have a pronounced influence on the overall conductivity.

In the case of accumulation layers on  $n$ -type semiconductors the Fermi level  $E_F$  is located close to the CBM. If the downward surface band bending (SBB) is sufficiently strong the CBM bends below  $E_F$ , such that the accumulation layer contains a degenerate free-electron gas. This free electron gas is then confined perpendicular to the surface by a nearly triangular potential well with a width defined by the energetic position of the CBM and the field strength, as schematically depicted in Fig. II.17(b).<sup>11</sup> The resulting quantum confinement is expected to lead to a quantization of the 2DEG inside the potential well [Lüt10]. Because of the quantum nature of these states, their wave function exhibits a node at the edge of the potential well at  $z = 0$ . For this reason, the charge density distribution  $n(z)$  exhibits its maximum not directly at the surface, but slightly below, depending on the shape of the potential well (cf. Section 6.4.1).

In the typical  $n$ -TCO materials, considerably strong CALs have been observed, however, their microscopic origins are not entirely clarified. In  $\text{In}_2\text{O}_3$  oxygen vacancies acting as doubly ionized shallow donors have recently been identified as main provider of free electrons [ZEO<sup>+</sup>13], while in CdO, several types of surface states and defects have been recognized as source of CAL formation [KVJ<sup>+</sup>09]. Also the other two  $n$ -TCOs,  $\text{SnO}_2$  and ZnO exhibit electron accumulation at their surfaces, and the origin of this effect has been attributed to either adsorbates and defects [FDG83], or it was considered an “intrinsic” property of the respective surface [NBW<sup>+</sup>10, SKdW<sup>+</sup>05, ASM<sup>+</sup>10].

It has to be added, that a complete *microscopic* description of CAL formation in TCO materials has not been achieved. The layer is generally treated as a macroscopic quantity and its *averaged* properties are usually derived from a combination of electrostatics and quantum mechanics (Poisson–Schrödinger equations, see Refs. [Duk67, YOY<sup>+</sup>15]). Experimentally, charge carrier densities are commonly determined using Hall-effect measurements [Loo08] or they are estimated from the band structure measured in angle-resolved photoelectron spectroscopy (ARPES) [KVM<sup>+</sup>10, OM10].

---

<sup>11</sup>Typical depths of strong CALs in TCO materials are on the order of few 10 Å [Lüt10], which can be attributed to the very short Thomas–Fermi screening lengths (see Section 6.3.1) in the highly doped CAL.

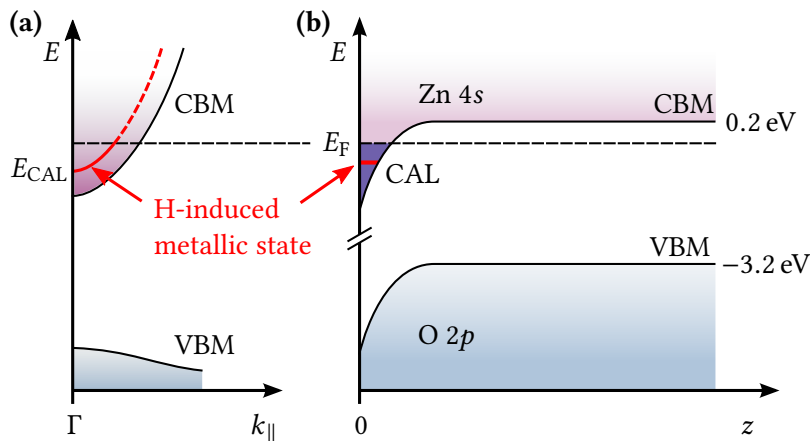


**Figure II.18:** Electronic structure of the ZnO(10 $\bar{1}0$ ) surface at the  $\Gamma$ -point displaying downward SBB after hydrogen adsorption. (a) Surface band structure along  $k_{||}$  showing the CBM below  $E_F$  around the  $\Gamma$ -point. Within the CAL a single metallic band (red) can form (see Section 6.4.1). (b)  $z$ -dependence of the CAL showing strong confinement perpendicular to the surface at  $z = 0$ .

### 6.3.3 ZnO Surface Electronic Structure – Band Bending and CAL formation

Figure II.18 shows the electronic structure of the ZnO(10 $\bar{1}0$ ) surface at the  $\Gamma$ -point with respect to (a) the wave vector  $k_{||}$ , and (b) the distance from the surface at  $z = 0$  (cf. Fig. II.13 for the bulk electronic structure). In the bulk the CBM is located about 0.2 eV above the Fermi level because of the unintentional native doping in ZnO. The surface electronic structure of ZnO(10 $\bar{1}0$ ) is, except for very clean surfaces under UHV conditions, dominated by downward bending of the electronic bands with respect to the bulk. As explained in Section 6.3.1, this is due to the occurrence of unoccupied donor-type surface states.

These states induce a negatively charged layer which compensates the positively charged surface donors. The resulting electric field perpendicular to the ZnO surface goes along with a downward bending of the electronic bands, so that the CBM can actually cross  $E_F$ . Consequently, a confining potential well at the surface is created, as shown in Fig. II.18(a) for the case of hydrogen adsorbed on ZnO. This charge accumulation layer (CAL) at the ZnO surface has been known for long, due to the observation that the surface charge density can be increased by hydrogen adsorption [HK69]. As a side note, it is surprising that despite clear experimental evidence, which will be presented in Section 6.4.1, many authors neglect the peculiar surface band structure of ZnO and treat it as a conventional semiconductor [TMN<sup>+</sup>08, SGH<sup>+</sup>13]. One possible reason for this might be that only after the “re-discovery” of the role of hydrogen as dopant in ZnO in the year 2000 (see next section), the prevalence of electron accumulation layers at ZnO surfaces was recognized.

CAL formation at ZnO surfaces was also found after exposure to He ions, irradiation with electrons, or ultraviolet (UV) light [SKdW<sup>+</sup>05], as well as the adsorption of water and methanol [OM10]. Thus, it appears likely that there are several ways to introduce surface donors on ZnO as they play a role in surface stabilization and their formation is energetically favorable. As a consequence, unless great care is taken to prevent formation of these surface donors, the

most abundant impurity will dominate. Under the conditions under which ZnO and other TCO samples are produced and examined, in particular in vacuum environments, there is one dominating contaminant: *hydrogen* [Red03].

## 6.4 Hydrogen in Zinc Oxide

In recent years, hydrogen has been recognized as the most probable dominant donor in zinc oxide and other *n*-TCO materials. Despite the fact that hydrogen diffusion was found to drastically increase the conductivity of ZnO as early as in the 1950s [TL56], not until 50 years later its role as major (unintentional) *n*-type donor in ZnO was re-discovered in a DFT study [Van00] and experimentally verified by electron paramagnetic resonance shortly afterwards [HHL<sup>+</sup>02]. One of the many proposed origins of stable *shallow* bulk donor centers is substitutional hydrogen in an oxygen vacancy [JdW06, SWSL07]. The explanation for this role of hydrogen in ZnO and *n*-TCOs in general can be given using the concept of the CNL (see Section 6.1.3):

Hydrogen has amphoteric character, that means that it usually forms acceptor-type defects ( $H^-$ ) in *n*-type materials and donor-type defects ( $H^+$ ) in *p*-type materials [VN03]. In ZnO it is predicted, though, that hydrogen *solely* acts as donor. As shown in Fig. II.15(b) the formation energy for  $H^+$  must be favorable despite the *n*-type nature of ZnO, because the CNL in ZnO lies well above the CBM. Hence, it can be concluded that hydrogen directly contributes its electron into the *bulk* ZnO CB.

What is not entirely clear yet, is the microscopic character of the hydrogen defect, as many different sites and bond configurations have been proposed, one of which is the highly stable substitutional hydrogen in an oxygen vacancy [JdW06, SWSL07]. Other configurations, such as interstitial hydrogen, have been found to be highly mobile due to low migration barriers of less than 0.5 eV, rendering interstitial hydrogen unstable at elevated temperatures [WGB06]. On the other hand, the low diffusion barrier would aid hydrogen incorporation after hydrogen exposition and adsorption at the crystal surface.

### 6.4.1 Hydrogen as Adsorbate on ZnO

Although hydrogen has been unambiguously confirmed as surface donor leading to CAL formation in ZnO, little is known about the exact bonding mechanisms, bond energies and microscopic changes to the surface electronic structure. Only recently the research focus has shifted from hydrogen in the bulk to hydrogen adsorbed at the ZnO surface. In particular, due to the studies of Wöll, Meyer and co-workers, it appears certain that atomic hydrogen predominantly binds to surface oxygen atoms to form O–H species. At the Zn-terminated (0001) surface a sticking coefficient below  $10^{-6}$  was found [BHK<sup>+</sup>01]. It was further shown that the mixed-terminated (10 $\bar{1}$ 0) ZnO surface becomes metallic in case of a fully hydroxylated surface and loses metallic character when the free surface Zn atoms form *additional* Zn–H bonds [WMY<sup>+</sup>05]. Thus, apparently, the O–H bonds at the ZnO surface are responsible for the additional donated electron that results in CAL formation and surface metallicity.

The first direct spectroscopic evidence of hydrogen-induced CAL formation on the mixed-terminated (10 $\bar{1}$ 0) surface was published by Ozawa and Mase [OM10, OM11], who observed occupied electronic states in the vicinity of the  $\Gamma$ -point using ARPES. They observe a downward

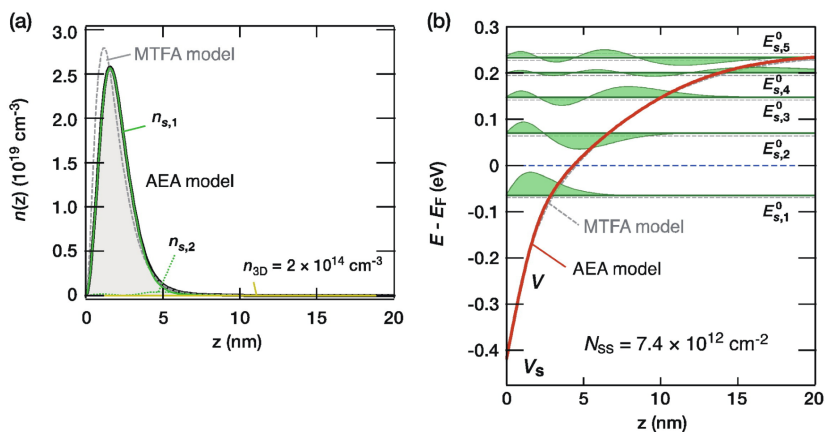


**Figure II.19:** Calculated distribution of (a) electron densities and (b) potential curves of the 2DEG subbands in the CAL at the ZnO surface. Calculations were based on anisotropic effective-mass approximation (AEA) and modified Thomas–Fermi approximation (MTFA) approximations with initial band bending  $V_s$  of  $-0.42$  eV relative to  $E_F$  (see Ref. [YOY<sup>+</sup>15] for details). The electron density of the first subband  $n_{s,1}$  is located at  $-0.065$  eV below  $E_F$  and confined within the first few nanometers from the surface. Reprinted from Ref. [YOY<sup>+</sup>15], with permission from Elsevier.

SBB on the order of  $-0.4$  eV on the mixed-terminated, and  $-0.65$  eV on the O-terminated surface for a hydrogen dosage of 200 langmuir (L).<sup>12</sup> At the Zn-terminated surface the SBB is not pronounced enough to form a CAL.

Consequently, in ARPES a single broad metallic band can be observed at the  $(10\bar{1}0)$  and  $(000\bar{1})$  surfaces is observed, which is confined in the potential well between CBM and surface. For the mixed-terminated surface this band is located at  $E_{\text{CAL}} = 0.16(3)$  eV below  $E_F$ , as schematically shown in Fig. II.18. The data show that the bound metallic state, which is attributed to a laterally delocalized 2DEG, exhibits a (hardly recognizable) parabolic dispersion. From this, a surface charge density on the order of  $10^{13}$   $\text{cm}^{-2}$  was concluded, which is slightly higher than, but comparable to results deduced from Hall-effect measurements [Loo08]. Further, the authors observe a reduction of the CAL signal intensity for dosages exceeding 200 L, which they attribute to hydrogen-induced etching and a resulting roughening of the surface which then leads to a quenching of the 2DEG.

Recent calculations based on the Poisson-Schrödinger equations [YOY<sup>+</sup>15] corroborate the occurrence of a single bound metallic band in the CAL, as shown in Fig. II.19. Using different approximations and assuming a comparably low bulk donor density of  $N_D = 2.0 \times 10^{14}$   $\text{cm}^{-3}$  the authors derive a binding energy of the bound band of  $E_{s,1}^0 \approx -0.065$  eV. This does not agree well with the results determined experimentally (see above), and the authors consent that further systematic studies on ZnO surfaces are required.

An aspect of hydrogen adsorption on ZnO surfaces that has not been treated sufficiently so far was the electronic structure of the ZnO surfaces for comparably low amounts of adsorbed hydrogen. This coverage regime, which does not fit in with the concept of the homogeneous CAL,

<sup>12</sup>This is the dosage at which the CAL signature intensity is at its maximum. For details on dosing hydrogen and the role of dosing atomic vs. molecular hydrogen, see Section 2.1 in Chapter IV.

is expected to be of interest from a both fundamental, as well as a device-centric perspective, due to the drastic changes in the surface potential, screening, and electronic coupling that can be expected even for low hydrogen coverages. This question is directly connected to a *microscopic* description of how exactly hydrogen atoms bind to these surfaces. The main reason for this deficit, from a theoretical viewpoint, is the challenge of calculating various surface structures that deviate from an ideal surface [YOY<sup>+</sup>15]. Experimentally, the formation of hydrogen overlayers cannot be detected using LEED, and methods such as STM and helium atom scattering (HAS) on ZnO surfaces are challenging [Wöl07]. A further experimental evidence for the metallicity of the ZnO surface after hydrogen adsorption was the observation of an ohmic surface contact in scanning tunneling spectroscopy (STS) [WMY<sup>+</sup>05].

### 6.5 The Work Function of ZnO Surfaces

The work function is a measure for the electric field at a solid surface, and as such it often drastically changes when a pristine surface is covered with adsorbates. This potential tunability of surface electronic levels can be exploited technologically to reduce interfacial energy barriers, as described in Section 4. However, for unstable or reactive surfaces, such as zinc oxide, this sensitivity to contaminants can also lead to apparently unreliable values given in literature.

In their Kelvin-probe studies, Moormann et al. find work functions of freshly cleaved ZnO single crystals of 4.64 eV for the (10 $\bar{1}$ 0) surface and 4.95 eV for the O-terminated (000 $\bar{1}$ ) surface [MKH79]. They also find that treatment of the oxygen-terminated face with hydrogen leads to downward band bending and a work function reduction to  $\Phi = 4.26$  eV.

A few years later, Jacobi et al. used PES to determine the work functions of ZnO single crystal faces. Sample preparation was done by AR<sup>+</sup> sputtering and annealing cycles [JZG84]. Interestingly, the measured values of  $\Phi$  were highly unstable, all reduced on a few ten minute timescale. This was most apparent for the oxygen-terminated face, where the work function shifted from 6 eV to 4.3 eV within two hours. The measured values after a few minute wait are nevertheless comparable to those given in the earlier work [MKH79].

If one compares work function values in recent literature, one often finds strong variations and values which often lie below those given above. This indicates that the examined sample surfaces were most likely not pristine, but exhibit a certain amount of defects and adsorbates. For high quality hydrothermally grown samples cleaned in UHV by sputtering and annealing cycles work function of  $\Phi = 4.5$  eV for ZnO(10 $\bar{1}$ 0) [OM11, TMN<sup>+</sup>08] and  $\Phi = 5.1$  eV for ZnO(000 $\bar{1}$ ) [OM11] appear to be the gold standard, which is routinely reproduced also in this work.

### 6.6 Concluding Remarks on Defects at Zinc Oxide Surfaces

Zinc oxide, and *n*-TCOs in general, exhibit electronic and optical properties that highly remarkable – *n*-type conductivity, high sensitivity to hydrogen – yet there appears to be no *sole* microscopic source responsible for this. A reason for this seems to be the richness of defect physics in these materials with a plurality of possible intrinsic and extrinsic defects. The role of both types of defects in the ZnO bulk, or at its surface, respectively, has been subject to many debates. Hydrogen, as an interstitial, trapped, or adsorbed at the surface, has become the main contender for a microscopic donor in ZnO. Still, it was shown that conductivity exists even

when hydrogen is annealed out or absent [LZ07], which indicates that defects such as oxygen vacancies cannot be completely neglected.

It has to be stated here, that the established concept of the CAL as shown in Fig. II.18 only gives an *averaged* description of the surface electronic structure, assuming that the character of the confining potential at the surface is perfectly homogeneous. The situation at *realistic* ZnO surfaces with its various defect species can be expected to be different. Since the characteristics of any functional hybrid interface are essentially determined by its *microscopic* properties (see Sections 2 and 5.3), the concept of the CAL is *not* sufficient to give a comprehensive description of the zinc oxide surface. Instead, one has to focus on the *microscopic* surface properties, which prove to be extremely inhomogeneous, as will be shown in Section 2 of Chapter IV.

## 7 Excited States and Dynamics in Zinc Oxide

The previous Sections were intended to give a comprehensive overview on the properties of zinc oxide in thermodynamic *equilibrium*. However, it was made clear in Section 5.3 that device functionality is intimately linked to excited electronic states and the resulting non-equilibrium processes. This section focuses on these excited states and their dynamics in ZnO.

### 7.1 Excitons in Zinc Oxide

Excitons at zinc oxide *surfaces* naturally play an important role with regard to energetic coupling with other materials, e.g., organic dye molecules via FRET. This is especially true for nanostructured or thin film systems with large surface-to-bulk ratios, where surface excitons are the dominant species in PL studies [WVR<sup>+</sup>06, KFS<sup>+</sup>13].

From the application perspective, excitonic *recombination* is the main mechanism for light emission in semiconductors at sufficiently low temperatures. If the thermal energy  $k_B T$  exceeds the exciton binding energy, the radiationless recombination of free electrons and holes will dominate. The comparably high bulk free exciton binding energy  $E_{\text{exc}} = 60$  meV of ZnO [Tho60] is, thus, of great advantage for any applications involving excitonic processes, as 60 meV correspond to a temperature of roughly 700 K.

This high exciton binding energy is attributed mainly to the stabilization of the exciton by lattice distortions. This stabilization mechanism originates from the comparably strong coupling of carriers and excitons to the lattice in semiconductors with ionic character, such as ZnO or TiO<sub>2</sub> [ZEC10, CGLI<sup>+</sup>10, BPZ<sup>+</sup>13] (see also Section 5.1). As a result of the coupling, the exciton exhibits polaronic character (the relaxation of the ions localizes the e-h pair), leading to an increase of binding energy due to coupling with phonons [HH04].

#### 7.1.1 Bulk Excitonic Spectrum of ZnO

The intense research on the optical properties of ZnO has led to a wealth of information on the properties of bulk excitons in ZnO [KFZ<sup>+</sup>10, MAH<sup>+</sup>04]. These studies were mainly carried out using photoluminescence (PL) and cathodoluminescence (CL) measurements, thus they cannot clearly distinguish between *polarizations* of the ZnO samples and real populations of excitonic states (see Section 5.2). One important finding is the fact, that there are not only different free exciton states, due to the splitting of the valence band, but also up to eleven excitonic recombinations have been observed [MAH<sup>+</sup>04], where excitons bind to neutral donors and/or acceptors. The microscopic nature of these species is not completely clear, though, owing to the rich and complex defect physics in ZnO, as described in Section 6.2. In the luminescence spectra, emission from bound exciton recombination dominates for low cryogenic temperatures, and the free exciton emission takes over at higher temperatures. For an overview on the bulk excitonic features in ZnO and the corresponding optical material constants, see Ref. [MAH<sup>+</sup>04].

Apart from the excitonic emission with a maximum around 3.35 eV at 300 K [LPTT14], there is usually strong visible emission in the green-orange and blue spectral region, depending on sample preparation conditions. The former is attributed to transitions to and from ionized oxygen vacancies (V<sub>O</sub>) that predominantly appear at surfaces, interfaces and grain boundaries

[BM15]. Blue emission between 415 and 488 nm wavelength can be observed in samples rich in interstitial Zn defects. As a consequence, it was concluded that blue emission originates from excitonic recombinations of electrons trapped in zinc interstitial states [ZDL<sup>+</sup>10].

### 7.1.2 The ZnO Surface Exciton

From the above-mentioned luminescence studies that were mostly conducted on ZnO nanoparticles, it can be concluded that many of the emission features of ZnO do indeed originate from *surface* effects. As for the geometric properties of ZnO (see Section ??) the excitonic properties of the ZnO surfaces appear to be more complex than those of the bulk, and they are apparently less understood.

Investigations on ZnO nanostructures, predominantly nanorods and -wires, have identified a number of surface-related emission channels. Wischmeier et al. showed that a distinct PL peak at 3.367 eV, i.e. near the band edge, can be attributed to a **surface exciton (SX)** [WVR<sup>+</sup>06]. They argue that the SX signal originates from two different excitonic species, one of which is strongly localized, resulting in different decay dynamics of the two species.

Measurements on thin epitaxial ZnO(000 $\bar{1}$ ) films show that the occurrence of an SX signature can be enhanced by depositing organic molecules with a carboxylic acid anchor group onto the ZnO film [KFS<sup>+</sup>13]. The authors suggest that the SX emission is associated to defect-related localization centers which are generated through a photochemical process. The intensity of the SX signature, which competes with the emission of donor-bound excitons, can be tuned by varying the density of anchor groups on the surface.

An explanation of the microscopic origins of SX-related photoluminescence was suggested by Biswas et al. [BJK<sup>+</sup>11]. In their photoluminescence study on nanostructured ZnO samples with high surface-to-bulk ratios, the SX has only been visible for temperatures below 25 K. The conditions at the surface that are responsible for the SX signature also lead to temperature-activated nonradiative recombination processes at higher temperatures. They suggest that the defects responsible for SX formation are related to surface O–H species that can bind excitons in their vicinity. Furthermore, the surface conditions that support a strong SX signal are linked to the quenching of the overall PL intensity at higher temperatures.

Apart from these nanostructured samples with huge surface-to-bulk ratios, SX species have only once been identified at a ZnO *single crystal* surface [TFS90]. The major reason for this scarcity is the generally low surface sensitivity of PL experiments. In their paper, the authors report that the SX signature emerges only after exposure of the cleaved crystal surface to air, which indicates that the SX signal is intimately linked to adsorption of residual gases. Because of the rather undefined crystal surface, a characterization of SX under reproducible conditions is still necessary to determine the microscopic origin of this excitonic species. With regard to the role of ZnO *surfaces* in HIOS, the understanding and control of excitonic effects at surfaces and interfaces is naturally of high interest. Particularly, the energetic coupling between ZnO and other materials, e.g., organic dye molecules, in Förster-type energy transfer processes (see Section 5.3.2) depends strongly on the properties of surface-related excitonic processes.

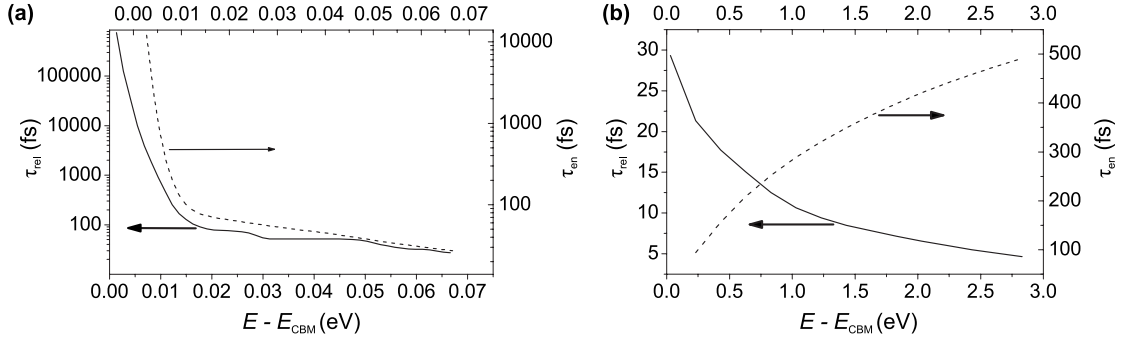


**Figure II.20:** Calculated relaxation time  $\tau_{\text{rel}}$  and energy-loss time  $\tau_{\text{en}}$  of excited electrons in the ZnO bulk conduction band for two different energy intervals (a) from zero to the maximum phonon energy, and (b) above the highest phonon energy to the energy of 3 eV above the CBM.  $\tau_{\text{rel}}$  is the inverse of the rate of e-ph relaxation at that energy, and  $\tau_{\text{en}}$  is the time necessary for an electron to relax to the CBM via repeated emission of phonons. Reprinted figure with permission from Ref. [ZEC10]. Copyright 2010 by the American Physical Society.

## 7.2 Electron-Phonon Scattering in ZnO

Phonons, the quanta of lattice vibrations, play an important role in the dissipation of energy from excited states in semiconductors. The excess energy of hot carriers in Si-based solar cells, as an example, is transferred to the lattice via phonons. The number and type of phonon bands can be calculated from the number of atoms  $s$  per unit cell which is four in case of ZnO. As a consequence, there are  $(3s - 3) = 9$  optical phonon modes in addition to the three always present acoustic modes [Kli07]. Among the optical phonon modes, the LO phonons with a comparably high energy of 72 meV play the decisive role in electron-phonon scattering [TMN<sup>+</sup>08], as will be explained below.

The interest in zinc oxide as material for optoelectronic applications the research on excited state dynamics has so far focused on excitonic processes (see Section 7.1). Only few experimental studies were devoted to the the dynamics of free electrons and holes, and there is only one study by Tisdale et al. employing 2PPE to directly observe the population dynamics of electrons in the ZnO(10 $\bar{1}$ 0) CB [TMN<sup>+</sup>08]. The authors find a very efficient relaxation of hot electrons, with relaxations times below 30 fs for electrons that are excited more than 0.1 eV above the bulk CBM.

These ultrashort relaxation times are consistent with the strong Fröhlich coupling of electrons to the LO phonons. Furthermore, the dynamics of this process shows no distinct temperature dependence, which is consistent with Fröhlich coupling mechanism. The authors calculate that hot electron lifetimes should only increase by  $\approx 6.5\%$  when the temperature is reduced from 300 K to 200 K, which is within the experimental uncertainty. For energies approaching the Fermi level, electron lifetimes increase drastically up to 1 ps. Due to the experimental design (2PPE autocorrelation with  $h\nu = 4.4$  eV at 76 MHz repetition rate), dynamics in the nanosecond regime and energies below the Fermi level cannot be addressed. Therefore, this study is not capable of giving detailed answers on excitonic processes, although it can be expected that excitonic species are present, due to above-band gap excitation (see Fig. II.18).

A theoretical study by Zhukov et al. corroborates the predominant role of e-ph coupling for the ultrafast relaxation of hot electrons in the ZnO CB [ZEC10]. The authors find ultrashort relaxation times similar to those in the 2PPE experiment, as depicted in Fig. II.20. For energies approaching the CBM, the dynamics slow down considerably until there is a divergence for vanishing excess energies. The strong increase in lifetimes in this model is readily explained by the energetic distribution of phonon modes in ZnO. As the excess electron energy gets below that of the LO mode, Fröhlich coupling can no longer occur, instead, scattering with low energy acoustic modes takes place which significantly slows down the energetic relaxation.



## III Experimental Techniques and Setup

This chapter is about the experimental methods used to characterize the electronic structure and dynamics at zinc oxide surfaces and interfaces. The foundations of the primary experimental method, [two-photon photoelectron spectroscopy \(2PPE\)](#), are the subject of Section 1. The following Sections 2 deals with the experimental setup used to conduct these studies on pristine and adsorbate-covered zinc oxide surfaces.

### 1 Experimental Techniques

The physical entities of particular interest – charge carrier dynamics at surfaces and interfaces – are obviously not directly accessible to the human observer. To analyze these properties by thorough and systematic experiments, the following basic questions have to be answered:

1. What are the physical effects and principles which enable the experimenter to gain an insight into the properties of a sample?
2. Which experimental techniques and devices are utilized to exploit these effects?

This chapter is intended to answer these questions by first giving an introduction to the primary experimental technique: photoelectron spectroscopy, from static photoemission spectroscopy to time-resolved femtosecond [2PPE](#). Subsequently, the actual experimental setup is explained, which includes the femtosecond laser system and the hemispherical two-dimensional photoelectron detector. Also, the [UHV](#) system used to prepare and further characterize the samples is described in detail. The last part of this chapter is devoted to the description of the preparation procedures and the characterization of various adlayers.

#### 1.1 A Brief Introduction to Surface Science

The importance of surfaces and interfaces in modern solid state physics and engineering cannot be overestimated. This is, to a large extent, due to the fact that material properties at surfaces and interfaces are often vastly different from those in the bulk material. Furthermore, the influence of surfaces and interfaces to the performance of any device becomes stronger in the course of device miniaturization.

Among the outstanding examples of surface effects are the occurrence of surface states, band bending and the formation of space charge layers, or, as very recent examples, superconductivity in  $\text{LaAlO}_3/\text{SrTiO}_3$  interfaces and the occurrence of topological insulators, which are highly relevant for modern and future technology.

The creation of interfaces of different materials often aims at a beneficial combination of the properties of its constituent surfaces, so that new functionality emerges. The most prominent

example might be the ubiquitous  $p$ - $n$  junction as integral part of most semiconductor devices and hybrid interfaces formed by inorganic and organic semiconductors, which are examined in this work and which are en route to become a staple of future optoelectronic devices. Hybrid devices, as explained in Section 1 of Chapter II, derive their functionality largely from the characteristics of the heterogeneous interface. Device functionality is determined by surface chemistry and physics effects which have to be tackled with surface science methods to arrive at a fundamental and quantitative understanding of the relevant characteristics.

The field of experimental surface science owes its existence mainly to two technological advances: firstly to UHV technology that enables long enough mean free paths of the probes, i.e., photoelectrons, to examine surfaces and also leads to a reduction of surface contaminants, and, secondly, the recording and processing of extremely weak electronic signals, such as single photoelectrons [HG94].

In this chapter, a description of the experimental surface science techniques which were used in this work and the underlying physical processes is given. To begin with, this section describes the physical background behind photoemission experiments, from static PES in case of photon energies higher than the sample work function to nonlinear 2PPE processes and finally time- and angle-resolved methods. A detailed account of the experimental setup with its two main parts, the femtosecond laser system and the UHV system is given in Section 2. The techniques used for sample surface preparation and adlayer characterization, such as LEED and thermally programmed desorption (TPD), among others, are given within the description of the UHV setup.

## 1.2 Photoelectron Spectroscopy – Basics

Photon-in electron-out measurements appear to be very useful in fundamental and applied materials science, since energies, wave vectors, polarization and temporal structure are well-defined quantifiable measures for both electrons and photons [SS14]. The underlying photoelectric effect originally led to the concept of photons as quantized entities by Einstein [Ein05]. Nowadays, besides its extensive use in research, the photoelectric effect is also used in, e.g., photomultipliers. The effect can be described as the absorption of photons by a single bound electron which gains enough energy to pass the work function barrier at the material's surface and, as a consequence, is emitted into the vacuum.

The spectroscopic signatures of these photoelectrons comprise a multitude of information about the sample material's properties. Therefore, a large number of experimental techniques based on photoelectron spectroscopy (PES) have emerged. What makes PES especially worthwhile is the fact, that the kinetic energies of the photoelectrons provide absolute energies of the electronic state which they emerged from. Thereby, it is possible to gain direct access to the (un)occupied electronic structure of a material. The comparably small escape depth of photoelectrons make PES experiments generally surface sensitive.

Starting from basic, angle-integrated one-photon photoelectron spectroscopy (1PPE), several techniques have emerged that additionally measure the photoelectrons' momenta  $\mathbf{k}$ , so that a direct mapping of the electronic band structure  $E(\mathbf{k})$  becomes possible. This is due to the predominantly  $\mathbf{k}$ -conserving nature of PES when *direct* transitions are excited in the solid. Additionally, multiphoton or pump-probe excitation schemes allow access to normally

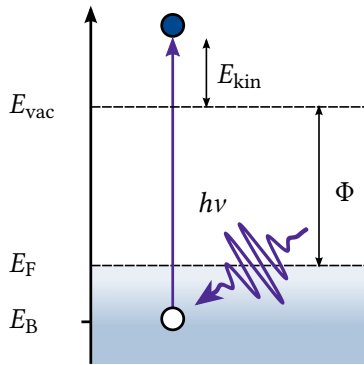


**Figure III.1:** Basic scheme of the photoemission process at a metallic surface. A photon with energy  $h\nu$  is absorbed by an electron. This energy gain of the electron is sufficient for the transition above the vacuum barrier. The kinetic energy of the photoelectron in vacuum is given as  $E_{\text{kin}} = h\nu - \Phi - E_{\text{B}}$ .

unoccupied states and thereby give an insight into *dynamical processes* of the electronic system on timescales as short as attoseconds.

The fundamental equation describing the energetics of the photoelectric effect relates the kinetic energy of the photoelectron  $E_{\text{kin}}$  to the photon energy  $h\nu$  and the initial binding energy of the electron  $E_{\text{B}}$  as follows:

$$E_{\text{kin}} = h\nu - \underbrace{(E_{\text{vac}} - E_{\text{F}})}_{\Phi} - E_{\text{B}}, \quad (\text{III.1})$$

as illustrated in Fig. III.1. Note, that  $E_{\text{kin}}$  crucially depends on the surface material parameter  $\Phi$ , the so-called work function. In a first approximation, the energetic distribution of the photoelectrons represents the [density of states \(DOS\)](#) of the corresponding electronic states in the sample.

The considerably more intricate details of the photoelectric effect and the different experimental methods to extract information about the examined sample electronic structures are briefly presented in the following Sections.

### 1.2.1 The Three-Step Model

Photoemission can be described intuitively by the *three-step* model. Despite its somewhat arbitrary character, this model gives results which are in most cases comparable to a theory which describes the photoemission process in *one-step*, i.e., an excitation from an initial state into a damped final state near the surface. The three-step model is a purely phenomenologic description of the physical processes which happen in a [PES](#) experiment. The whole photoemission process is divided into three distinct and independent parts, as shown in Fig. III.2:

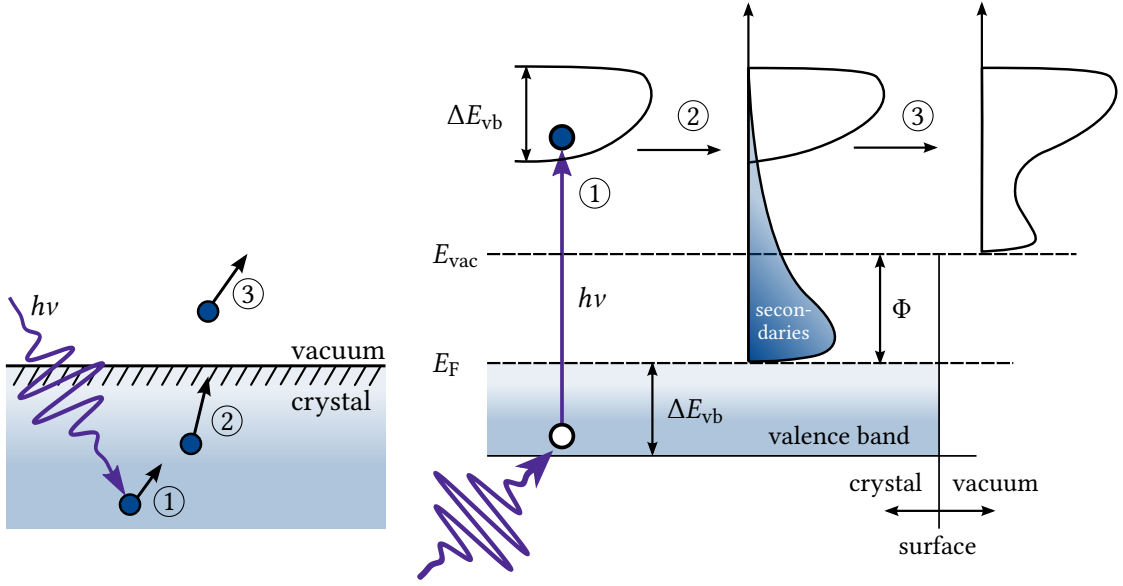


**Figure III.2:** Schematic representation of a photoemission process in the three-step model (adapted from Ref. [SS14]) in real space (left) and energy space (right). In this model, the steps are: ① the photoexcitation of the electron, ② transport to the surface, and ③ the penetration through the surface barrier and escape into vacuum (adapted from [Hüf96]).

1. Absorption of a photon with energy  $h\nu$  by an electron inside the solid, which creates a photoelectron. The probability  $w$  of the excitation of an electron in an  $N$ -electron system from an initial state  $|i\rangle$  to a final state  $|f\rangle$  is given by Fermi's Golden Rule [SS14]

$$w \propto \sum_{f,j} |\langle f | \mathbf{A} \cdot \mathbf{p}_j | i \rangle|^2 \delta(E_f(N) - E_i(N) - h\nu), \quad (\text{III.2})$$

where  $\mathbf{A}$  and  $\mathbf{p}_j$  represent the quantized vector potential of the excitation light and the momentum operator of the  $j$ -th electron to be excited.  $E_f(N)$  and  $E_i(N)$  represent the total energy in the  $N$ -electron system in the final and initial state, respectively. A comparably large energy difference between the photoexcited electron and each of the electrons in the remaining  $(N - 1)$ -electron system justifies the description of the system as an instantaneous creation of the photoelectron without any interaction with the remaining  $(N - 1)$  electrons. This assumption is called the *sudden approximation*, which is valid for photon energies  $h\nu \gtrsim 10$  eV, but debatable for the very low photon energies used in this work [SS14]. In Fig. III.2 this first step is shown for the excitation of valence band electrons.

2. The photoexcited electrons travel to the sample surface. On their way they may undergo inelastic scattering events, thereby creating secondary low-energy excited electrons. The inelastic mean free path  $\lambda_{\text{mp}}(E(\mathbf{k}))$  depends on material parameters and, most importantly, the photoelectron energy  $E(\mathbf{k})$  (see subsection 1.2.3). Because it is on the order of about

3–5 Å in the energy range of  $\approx 15$ –200 eV, photoelectron spectroscopy is mostly sensitive to the electronic structure and processes at the sample surface.

3. Transmission of the photoexcited electron through the sample surface into the vacuum followed by the propagation to the detector. As a first approximation, the photoelectrons can be treated as nearly free electrons with  $E_0$  the bottom of the nearly free electron band. These nearly free electrons experience the so-called inner potential of depth  $V_0 \equiv E_{\text{vac}} - E_0$  with the vacuum level  $E_{\text{vac}}$ . Crossing the boundary to the vacuum the kinetic energy of the photoelectron changes from  $E(\mathbf{k}) + V_0$  to  $E(\mathbf{k})$ . The potential step at the boundary is perpendicular to the surface, which is the reason for the conservation of momentum parallel to the surface  $\mathbf{k}_{\parallel}$ , but not perpendicular to the surface ( $\mathbf{k}_{\perp}$ ). This also means, that only electrons with a sufficient component of their kinetic energy normal to the surface can overcome the potential barrier.

### 1.2.2 The One-Step Model

The one-step model of photoemission is the formally correct theory of photoemission [Pen76]. It treats the photoemission process as a single coherent process which couples the exact initial and final state wave functions via the optical field. The states inside the solid are treated as Bloch waves, whereas final states in the vacuum are considered as plane waves which decay exponentially into the bulk of the crystal (cf. Fig. III.7). This damping of the final state wave function accounts for the limited escape depth of photoelectrons inside the crystal.

A complete description of the one-step process is in principle given by Fermi's Golden Rule (III.2) considering that the final state is the state of the electron after escape into the vacuum. A theoretic description of this process can be derived from the theory of LEED which is the conceptually *inverse* process of PES [Mah70, Pen76].

### 1.2.3 The Mean Free Path of Photoelectrons

To carry the desired information about their state inside a sample, the photoelectrons must not encounter any inelastic scattering during the photoemission process. Their relatively short inelastic mean free path  $\lambda_{\text{mp}} \lesssim 10$  Å over a wide  $E(\mathbf{k})$  region is the reason for the comparably high surface sensitivity of photoelectron spectroscopy. The length of  $\lambda_{\text{mp}}$  is determined by the electron transport property  $T(E(\mathbf{k}), h\nu)$  which varies with electron energy. Variations of the electron energy (by changing the excitation energy  $h\nu$ ) are thus a means to deconvolve surface, subsurface, or bulk spectral weights from the photoemission spectra [SS14]. Remarkably,  $\lambda_{\text{mp}}$  does not vary significantly for different materials, at least for high kinetic energies of the photoelectrons, as shown in Fig. III.3. This is due to the fact that high energy electrons inside a solid can be considered as quasi-free, so that the loss function is determined by the plasma frequency. The latter depends on the mean electron-electron distance, which is almost a constant for a wide range of materials. For that reason, the data shown in Fig. III.3 is often referred to as *universal curve*.

It is generally believed that  $\lambda_{\text{mp}}$  takes on larger values for very low energy photoexcited electrons  $E(\mathbf{k}) \lesssim 10$  eV, however, corresponding data in this energy range is scarce. The increase

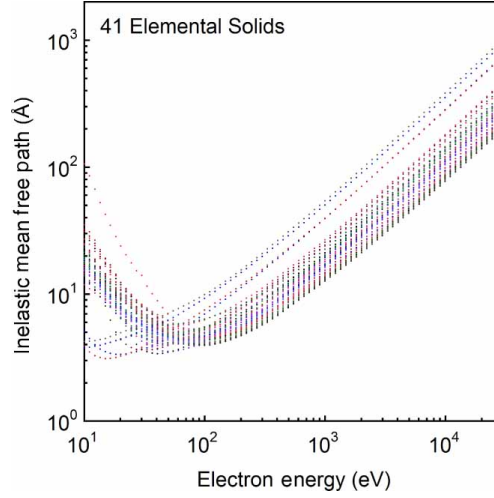


**Figure III.3:** Dependence of the inelastic mean free path  $\lambda_{\text{mp}}$  on the photoexcited electron energy for 41 different elemental solids. Values were calculated from experimental optical data using the Penn algorithm. Taken from Ref. [TPP11].

of  $\lambda_{\text{mp}}$  for low electron energies is shown in Fig. III.3, which suggests comparably high bulk sensitivity for slow electrons, i.e., low photon energies. The general character of the universal curve is in dispute, though, since very prominent surface effects such as surface states on copper [HKWE96, HSR<sup>+</sup>97], silver [MMC96], or topological insulators [RGK<sup>+</sup>14] dominate PES data also for very low energy electrons. We can safely assume that the contribution from the surface is the dominating part of the data presented in this work, as will be explained in Chapter IV. It has to be kept in mind that depth information is mainly restricted by the limited mean free path of photoelectrons in a material and not by the absorption depth of the probe photons, which is on the order of 50 nm in ZnO for above-gap photon energies.

### 1.3 Emission Angles and Momentum Conservation

A concise description of the electronic states at the sample surface requires knowledge of the electronic dispersion relation  $E(\mathbf{k})$ , i.e., the band structure of the solid. When electrons are photoemitted from a solid, they lose a part of their energy and momentum to overcome the vacuum barrier, i.e., the work function  $\phi$ . However, the component of the wave vector parallel to the sample surface  $k_{\parallel}$  is conserved in the photoemission process (cf. Section 1.2.1). At the same time, this conservation of  $k_{\parallel}$  leads to an apparent increase of the work function with increasing emission angle. This so-called escape cone results from the reduction of the perpendicular component  $k_{\perp}$ , which is needed for overcoming  $\phi$ , if  $k_{\parallel} \neq 0$  (see Section ??). [Hüf96, BNF<sup>+</sup>06]

The conservation of the momentum component of the photoelectron parallel to the surface,  $p_{\parallel} = \hbar k_{\parallel}$ , makes it possible to determine  $k_{\parallel}$  by measuring the kinetic energy  $E_{\text{kin}}$  and emission

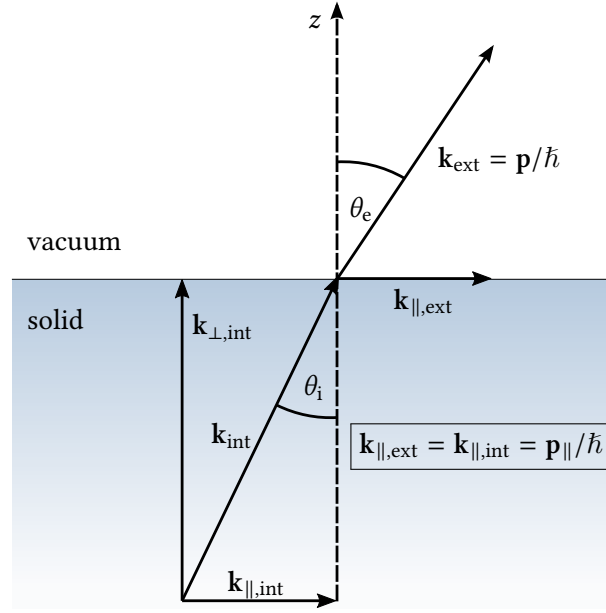


**Figure III.4:** Schematic illustration of the conservation of  $k_{\parallel}$  during the photoemission process. The perpendicular component  $k_{\perp}$  is reduced by the work function during the photoemission process (adapted from [Kir08]).

angle  $\theta_e$  of the nascent photoelectrons:

$$k_{\parallel} = \sin \theta_e \sqrt{\frac{2m_e}{\hbar^2} E_{\text{kin}}} \quad (\text{III.3})$$

$$= 0.5123 \text{ \AA}^{-1} \text{ eV}^{-1/2} \sin \theta_e \sqrt{E_{\text{kin}}}. \quad (\text{III.4})$$

This allows the complete assignment of the band structure of *two-dimensional* states, such as *surface* or *interface* states, which show no dispersion perpendicular to the surface. As a consequence, two-dimensional surface states remain at the same energetic position relative to  $E_F$  for different photon energies. Coupling of surface states to plane waves in the vacuum happens in one single step and is thus less restrictive than the bulk photoemission process. Hence, the photoelectron intensity of surface states is relatively constant when the photon energy is varied.

For the perpendicular component of the wave vector, the following relation can be derived:

$$k_{\perp} = \sqrt{\frac{2m}{\hbar^2} (E_{\text{kin}} \cos^2 \theta_e + V_0)},$$

where  $V_0$  is given by  $V_0 = E_{\text{vac}} - E_0$  with  $E_0$  the inner potential of the assumed parabolic free-electron-like final-state band. It follows, that once the inner potential is known, also the band structure of the *bulk* can be experimentally determined.

In *ARPES* experiments, the emission angles of the escaping photoelectrons can be measured directly by using an angle-resolved electron detector such as the two-dimensional detector of

a hemispherical analyzer which is described in Section 2.2. This type of analyzer enables a direct and instantaneous mapping of the dispersion relation  $E(k_{\parallel})$  without the need for sample rotation.

### 1.4 Two-photon Photoemission

The functionality of HIOS devices is determined by non-equilibrium, i.e., excited state properties of the system, as explained above. Accessing these properties in a photoemission experiment means accessing the electronic states of the system which are normally unoccupied in thermal equilibrium. This can be realized by implementing a *pump-probe* photoexcitation scheme: The system is first excited (*pumped*) into a non-equilibrium state with a first photon of energy  $h\nu_{\text{pump}}$ . Normally, the photon energy is smaller than the sample work function ( $h\nu_{\text{pump}} < \Phi$ ), so that direct photoemission processes are excluded. Instead, intermediate bound electronic states between the Fermi level  $E_{\text{F}}$  and the vacuum level  $E_{\text{vac}}$  become occupied. Absorption of a second photon  $h\nu_{\text{probe}}$  then *probes* the electronic population of the system in its excited state by promoting an electron from its intermediate state to above the vacuum level  $E_{\text{vac}}$  (see Fig. III.5(a) for an overview of different 2PPE mechanisms).

Since its first experimental realization in the 1970s,[LW77, WL77] a multitude of ways to perform 2PPE experiments has been established, some of which will be elucidated in the following text. A common prerequisite for two-photon or multiphoton photoemission experiments is the creation of very high photon fluxes to efficiently drive nonlinear optical processes,[Fau94] which has become a standard procedure since the advent of pulsed Ti:sapphire lasers in the 1990s. These lasers provide ultrashort light pulses with durations on timescales of sub-100 femtoseconds, which leads to pulse energies in the micro- to millijoule range. The femtosecond laser setup used in this work is described in Section 2.1.

The 2PPE process is defined by the absorption of two individual photons resulting in the emission of a single electron, which leaves room for different experimental implementations:

**Single-color 2PPE** The two photons are provided within a single laser pulse, which means that they have essentially the same energy  $h\nu$  and are absorbed during the duration of the single pulse, i.e., basically simultaneously. Using single-color 2PPE one can easily determine the origin of spectral signatures by a variation of the photon energy, as depicted in Fig. III.5(b). If the state that is probed in 2PPE originates from an occupied initial state then its signature shifts with *twice* the photon energy difference  $\Delta h\nu$ . An intermediate state which has to be populated by the absorption of a first photon then shifts with exactly the photon energy difference. It is also possible due to matrix element effects that energetically fixed final states occur in the 2PPE spectrum, which show no dependence on photon energy at all.

**Two-color 2PPE** Here, pump and probe photons originate from two distinct laser pulses, which may have different photon energies  $h\nu_{\text{pump}} \neq h\nu_{\text{probe}}$  and may arrive at the sample surface at different times, delayed by  $\Delta t$ . This scheme enables further insights into dynamical electronic processes via *time-resolved* measurements of pump-induced changes to the population of electronic states, as described in Section 1.4.1. Furthermore, the photon energy of one of the pulses (usually the probe pulse) may *exceed* the work function of

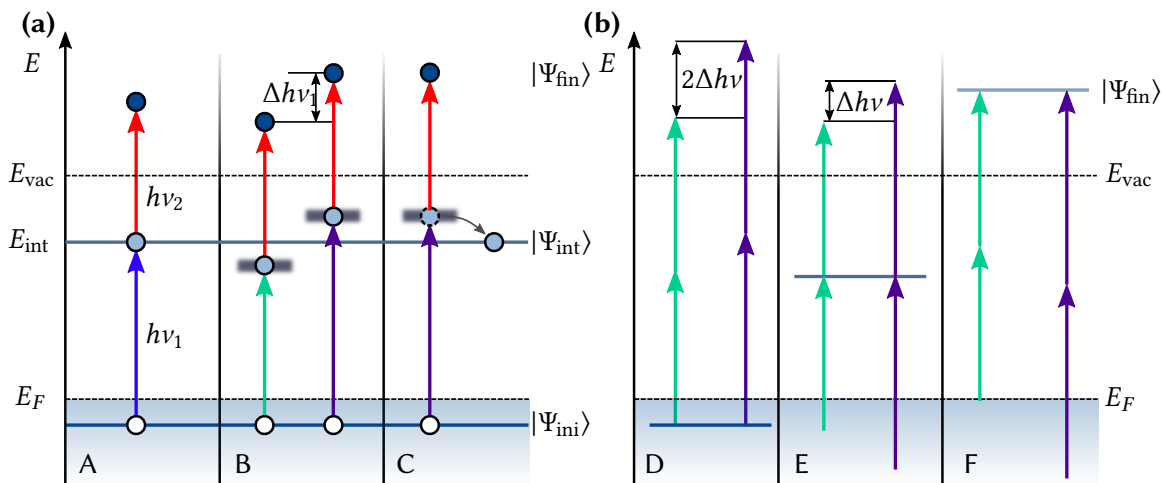


**Figure III.5:** Overview of excitation schemes in the *2PPE* process, which involves discrete initial, intermediate and final states  $|\Psi_{\text{ini}}\rangle$ ,  $|\Psi_{\text{int}}\rangle$ , and  $|\Psi_{\text{fin}}\rangle$ , respectively. (a) depicts the different excitation pathways in a pump-probe experiment, where the intermediate state is either (A) resonantly excited, (B) occurs as virtual state only, or (C) is excited non-resonantly via inelastic scattering. (b) shows how signatures in the photoelectron spectra can be characterized by varying the photon energy in a single-color *2PPE* experiment. (D) if the signature originates from an occupied initial state the change of kinetic energy equals  $2\Delta h\nu$ . (E) if a normally unoccupied intermediate state is probed, the energy shift is  $\Delta h\nu$ , (F) and no shift is observed when electrons are excited into a distinct final state.

the sample, i.e.,  $h\nu > \Phi$ . This way it is possible to observe pump-induced changes to the occupation of electronic states close to and even *below* the Fermi level  $E_F$ . This method, which is often used to examine hot electron dynamics in metals[FSTB92] or ultrafast phase transitions[PLL<sup>+</sup>06] is usually termed time-resolved ARPES.

The excitation pathways that electrons undergo in the *2PPE* process from an occupied initial state  $|\Psi_{\text{ini}}\rangle$  to a final state  $|\Psi_{\text{fin}}\rangle$  are summed up in Fig. III.5(a). The intermediate state  $|\Psi_{\text{int}}\rangle$  can (A) be populated resonantly if the pump photon energy  $h\nu_1$  equals the energy difference between the states  $|\Psi_{\text{ini}}\rangle$  and  $|\Psi_{\text{int}}\rangle$ . The resulting *2PPE* signal after photoemission by absorption of a photon with energy  $h\nu_2$  is enhanced in case of this resonance. If no energetically resonant intermediate state is available, as shown in case (B), the transition between  $|\Psi_{\text{ini}}\rangle$  and  $|\Psi_{\text{fin}}\rangle$  happens via so-called *virtual* intermediate states. These virtual states are a consequence of the second order polarization of the system by the intense light field. Non-resonant excitation may still involve *real* intermediate states if these are populated via electron scattering events, as depicted in case (C). If the energy provided by  $h\nu_1$  exceeds the difference between initial and real intermediate state, the electron can transfer its excess energy, e.g., to another electron or phonon, by an inter- or intraband scattering process. This excitation pathway predominates in case a continuous spectrum of initial states, e.g., VB states of a semiconductor.

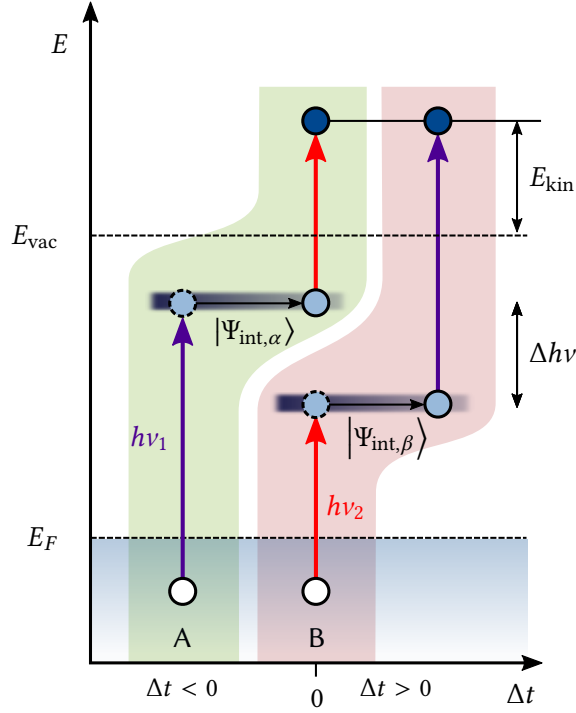


**Figure III.6:** Role of the sequence of pump and probe pulses in TR-2PPE. Two sequences of pump and probe pulse are possible: (A) system is pumped by  $h\nu_1$  and probed by  $h\nu_2$ , so here  $\Delta t < 0$ , and the intermediate state pumped by  $h\nu_1$  is  $|\Psi_{int,\alpha}\rangle$ . (B) reverses the order of pump and probe, i.e.,  $\Delta t > 0$ . The intermediate state  $|\Psi_{int,\beta}\rangle$  is shifted by  $\Delta h\nu$  relative to  $|\Psi_{int,\alpha}\rangle$ . Depending whether an intermediate state shows a distinct lifetime for either  $\Delta t < 0$  or  $\Delta t > 0$  one can unambiguously assign pump and probe pulse. As a consequence, the absolute energetic position of the intermediate state relative to  $E_F$  can be determined.

#### 1.4.1 Time-Resolved Two-Photon Photoemission

The very nature of the 2PPE process, which involves the population of normally unoccupied intermediate electronic states, makes it a convenient tool for the analysis of excited states' dynamics. The temporal resolution of a 2PPE experiment is defined by the duration of the used laser pulses, which is on the order of few tens of femtoseconds. As a consequence, the main energy loss channels of electrons, which are electron-electron and electron-phonon scattering, can be resolved, because they usually occur on similar or longer timescales [PO97]. For the same reason, also the formation of quasiparticles such as excitons or polarons can be resolved in time. On the other hand, processes like electronic decoherence or the dynamical screening of electrons inside a metal happen so quickly that they cannot be accessed with conventional 2PPE. However, recent advances in interferometric techniques enable also the analysis of screening processes on sub-ten femtosecond timescales. [CWA<sup>+</sup>14]

Experimentally, the information on the population dynamics of intermediate states is gained by varying the temporal delay  $\Delta t$  between pump and probe pulse. This is realized by changing

the optical path length of one color with respect to the other.<sup>1</sup> As soon as the pulses are delayed in time ( $\Delta t \neq 0$ ) the excited electronic distribution of the system literally has time to relax and thermalize via the above-mentioned mechanisms. By repeating this experiment for a suitable range of  $\Delta t$  values, the exact time-constants of the relaxation processes can be determined. The repetition rate of the experiment has to be chosen lower than the lowest inverse relaxation time of the system.

Furthermore, temporal changes to the *dispersion* of electronic states (see Section 1.3) can be measured directly by using an angle-resolved detector, as described in Section 2.2. Monitoring the dispersion gives insight on the degree of localization of the intermediate state. This is due to the fact that measured dispersions can often be approximated by a free electron parabola with  $E_0$  the energetic onset of the interfacial band at  $\mathbf{k}_{\parallel} = 0$  [GWH00]:

$$E(\mathbf{k}_{\parallel}) = E_0 + \frac{\hbar^2 \mathbf{k}_{\parallel}^2}{2m_{\text{eff}}}. \quad (\text{III.5})$$

$m_{\text{eff}}$  is the effective mass which increases relative to the free electron mass (see Eq. III.3) with higher degree of spatial localization. It has been demonstrated, e.g., for solvation processes [Bov05], that stronger localization results in a flattening of the bands.

The variation of the sequence of pump and probe pulse in a TR-2PPE experiment helps to assign an absolute energetic position of the transiently populated intermediate state. As the role of pump and probe pulse is not given per se, both pulses may, in principle, take either role, as depicted in Fig III.6. The figure shows the two possible sequences as a UV pulse  $h\nu_1$  is shifted in time relative to an optical pulse  $h\nu_2$ . It follows, that for  $\Delta t < 0$ ,  $h\nu_1$  arrives at the sample before  $h\nu_2$  and, thus, acts as pump and vice versa. As a consequence, the intermediate state must have been pumped by  $h\nu_1$  if it shows a finite lifetime for  $\Delta t < 0$ . One can, thus, unambiguously assign roles to the two pulses and determine the absolute energetic position of any intermediate state which exhibits a finite lifetime. More details on the assignment of energies to spectral signatures and the data analysis methods in general will be given in Section A.

### 1.4.2 Charge Injection in Two-Photon Photoemission

The 2PPE process at heterogeneous interfaces is intimately linked to interfacial charge transfer processes, (see Section 5.3 of Chapter II), which makes this method an ideal tool to study these processes. Any transition from an occupied initial state  $|\Psi_{\text{ini}}\rangle$  to a normally unoccupied state  $|\Psi_{\text{int}}\rangle$  initiated by optical pumping depends on the coupling between the two states, i.e., the non-vanishing transition dipole moment [see Eq. (III.2)]. As a result, electron transfer at a heterogeneous interface, e.g., between a semiconductor substrate and a molecular overlayer, can be directly initiated by optical excitation if there is *spatial* overlap between the involved wave functions. The possible pathways for the direct transient excitation across an interface are shown in Fig. III.7. In pathway (A), the initial state  $|\Psi_{\text{ini}}\rangle$  is a pure bulk state of the substrate; as a consequence the intermediate state  $|\Psi_{\text{int}}\rangle$  must have non-zero probability density inside the substrate, which is true for an unoccupied molecular or interface state with strong coupling to

<sup>1</sup>Here, a computer controlled linear stage is used, which offers sub-micrometer precision. A length difference in the optical path of 1  $\mu\text{m}$  corresponds to a temporal shift of  $\approx 3.3$  fs via  $t = s/c$ .

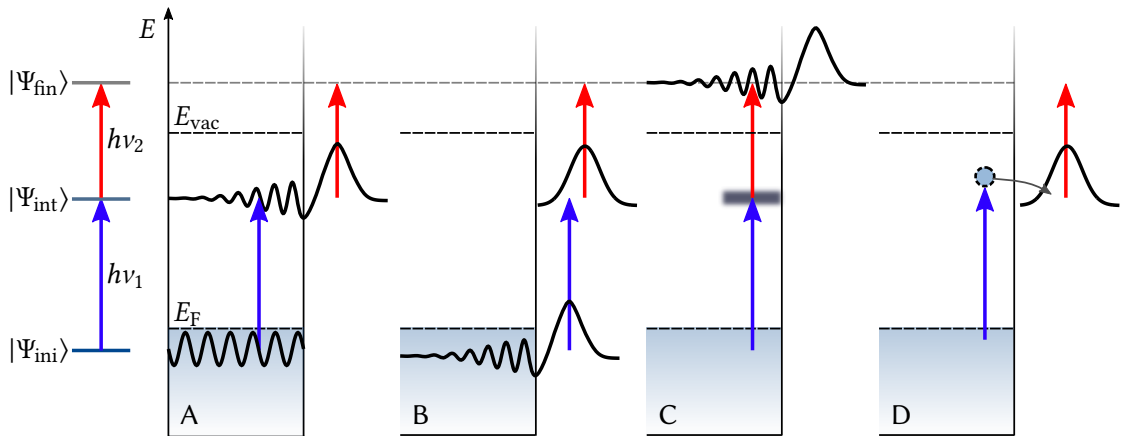


**Figure III.7:** Excitation pathways for the transient population of intermediate and final electronic states and related electron transfer processes (see text for details). Adapted from Ref. [Zhu04b].

the substrate. In pathway (B) an occupied surface or interface state with significant probability density in front of the substrate surface serves as initial state. As a consequence, molecular or interface states with significant probability density *near* the surface can be populated, however, strong electronic coupling to the bulk is not required. Similarly, final states  $|\Psi_{\text{fin}}\rangle$  of the molecule or interface states above the vacuum level with significant probability density near the surface can be excited directly via a virtual intermediate state, as depicted in mechanism (C). Again, spatial overlap of the wave functions is required in this coherent process.

Alternatively, molecular or interfacial states can be populated indirectly from hot electrons in the substrate (D). The intermediate state in the molecular layer is excited via inelastic scattering from hot electrons in the substrate. This incoherent mechanism can be distinguished from the coherent direct excitation by analyzing the dependence of the 2PPE signal on light polarizations [WHKV99].

Apparently, the 2PPE process at heterogeneous interfaces does not necessarily involve charge transfer as a first step upon optical pumping. The absorption of the pump photon can also happen purely inside the molecular layer followed by ionization of the excited molecular state by the second probe photon. As in case of light absorption inside the substrate, the intermediate state may either be an actual molecular state, or a virtual state.

In any case the substrate does not only serve as source for excited charge carriers, but also as source for competitive decay channels. This *back* transfer of the excited electron or quasiparticle populations obviously also depends on the electronic coupling, i.e., wave function overlap between the excited state and the substrate, and it often competes with the energetic relaxation due to polaron formation in polarizable environments (see, e.g., Ref. [SBW10] for a comprehensive description of this process). TR-2PPE allows a direct quantitative observation of the transfer process by probing the transiently decaying population of the intermediate state for a fixed energy, as depicted schematically in Fig. III.8. The energetic relaxation can be quantified by measuring the peak position in the spectra for different pump-probe delay times. More details on the analysis of TR-2PPE data are presented in Section A.

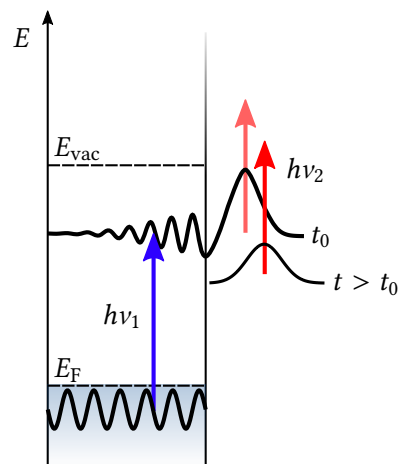


**Figure III.8:** Time-dependent relaxation and population decay of a transiently populated state in the energy domain, monitored by TR-2PPE. Adapted from Ref. [Zhu04b].

In sum, TR-2PPE is a method which is well suited for the analysis of relaxation and charge transfer dynamics at well-defined (hybrid) interfaces. It gives access to absolute energy levels of occupied and unoccupied states and its temporal resolution on the scale of elementary scattering and relaxation processes gives insight into the coupling between electronic and nuclear degrees of freedom and the coupling of electronic states across an interface.

## 2 Experimental Setup

This Section comprises the description of the experimental setup used in this work, which can be divided into two main parts:

1. The *femtosecond laser system* which generates tunable ultrashort light pulses by means of nonlinear optical effects. These pulses are used to excite and subsequently photoemit electrons at the sample surface.
2. The *ultrahigh vacuum system* which is essential for carrying out photoemission experiments on well-defined, contamination-free sample surfaces. This part includes the device for photoelectron analysis: a hemispherical analyzer equipped with a two-dimensional detector for simultaneous measurement of photoelectron energy and emission angle.

Further technical details on the setup can be found in Appendix C.

### 2.1 Laser Light Source

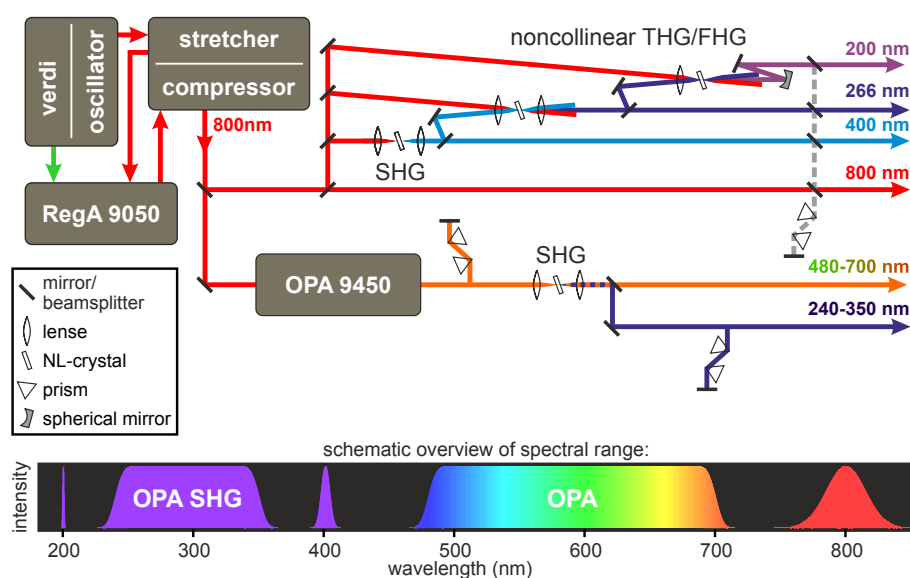


**Figure III.9:** Schematic overview of the femtosecond laser setup. The setup mainly consists of commercial laser components by *Coherent, Inc.*: A femtosecond oscillator (*Micra*, exchanged with *Vitara* in the course of this work) pumped by a diode laser (*Verdi*) provides femtosecond pulses at 80 MHz repetition rate. These pulses are amplified using a **regenerative amplifier (RegA)** (*RegA 9050*) with external stretcher and compressor. The 800 nm output of the compressor at repetition rates between 40 and 300 kHz can be converted to a wide range of photon energies. The **optical parametric amplifier (OPA)** (*OPA 9450*) covers the visible range of the spectrum, whereas a custom built setup for **third harmonic generation (THG)** and **fourth harmonic generation (FHG)** is used to produce photons with energies up to 6.2 eV. The range of photon energies covered by this setup is shown at the bottom. Modified from [Weg15].

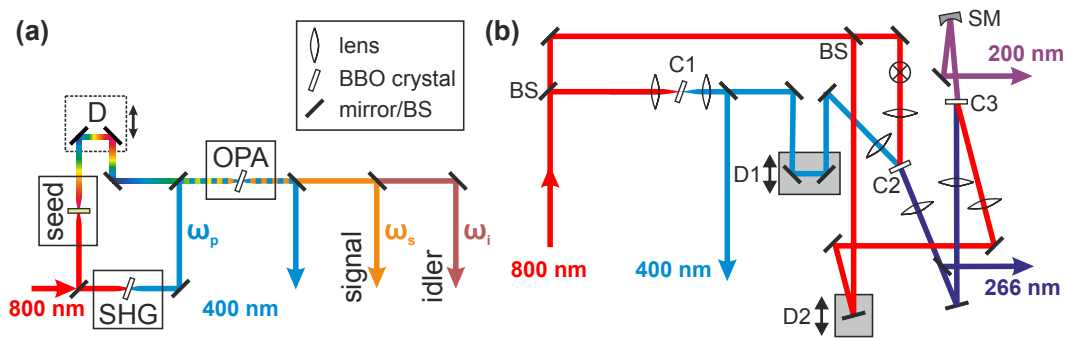


**Figure III.10:** Schematic drawing of OPA and THG-FHG setup. (a) shows the basic building blocks of an OPA, as described in the text. Part (b) shows the noncollinear THG and FHG setup for generation of photons with energies up to 6.2 eV.

The study of elementary charge carrier dynamics of surfaces and interfaces on their intrinsically ultrafast timescales requires short light pulses with durations well below 100 fs. Another basic requirement for 2PPE experiments is the energetic tunability of the light pulses. This is either for, e.g., exploiting energetic resonances or for avoiding one-photon photoemission, which can completely cover the 2PPE signal. Tuning of the photon energy is achieved by using a variety of nonlinear optical effects. These effects, on the other hand, rely on the fact that femtosecond light pulses provide extremely high light intensities with field strengths on the order of  $1 \text{ MW cm}^{-2}$ .

The source of these high intensity femtosecond pulses is a commercial laser system (*Coherent, Inc.*) mainly consisting of an oscillator (*Micra/Vitara*) and a *RegA* (*RegA9050*), as depicted in Fig. III.9. The fundamental output of the system are broadband pulses centered at a wavelength of  $\approx 800 \text{ nm}$ , i.e. a photon energy of 1.55 eV. The repetition rate of the pulses provided by the *RegA* is tunable between 40 and 300 kHz.<sup>2</sup> The resulting energy per pulse is on the order of  $9 \mu\text{J}$  at pulse durations of  $\approx 40 \text{ fs}$ . A comprehensive and detailed overview of the laser setup and its characterization can be found in Refs. [Weg15] and [Dei11].

### 2.1.1 Photon Energy Tuning

The conversion of photon energies by nonlinear optical processes happens in two different optical setups. First, a commercial optical parametric amplifier (OPA) (*OPA 9450, Coherent, Inc.*) and second, a home-built third and fourth harmonic generation setup. In the OPA the optical parametric amplification process is used to amplify a selected energy range of a broadband white light continuum by pumping with 400 nm photons [see Fig. III.10(a)]. The white light continuum is created by focusing the fundamental 800 nm beam into a sapphire crystal. At the same time pump pulses  $\omega_p$  are created in a nonlinear crystal [ $\beta$ -Barium borate (BBO)] by an second harmonic generation (SHG) process. These two pulses are overlapped in space and time in another BBO crystal. The selection of seed photon frequency  $\omega_s$  out of the white

<sup>2</sup>The repetition rate used for the bulk of experiments was 200 kHz which leads to a pulse separation of  $5 \mu\text{s}$ , if not stated otherwise.

light continuum can be done by varying the delay between the pump and the strongly chirped whitelight, so that temporal overlap between both is only given for a certain seed photon frequency  $\omega_s$ . The selection of the right phase matching angle leads to an energy transfer from the pump into the seed, i.e., signal beam. This process leads to the creation of a third beam, the so-called idler, at frequency  $\omega_i$ , which fulfills the condition  $\omega_p = \omega_s + \omega_i$ . The OPA signal wavelength can be tuned in a wide range from about 460 nm (2.7 eV) to 730 nm (1.7 eV) with resulting light intensities on the order of 40 mW at 200 kHz. After pulse compression by a prism pair compressor which introduces a negative group velocity dispersion (GVD) another BBO can be used for SHG which enables the creation of photon energies up to 5.4 eV.

An even higher photon energy of 6.2 eV (wavelength of 200 nm) can be reached by fourth harmonic generation (FHG). The principal setup is shown in Fig. III.9(b). The generation of these high energy photons happens in two consecutive sum frequency generation (SFG) processes. Again, a BBO crystal is used to first generate 400 nm photons by SHG. Two further BBOs are then utilized to create 266 nm and, finally, 200 nm photons by two successive steps of mixing with the fundamental 800 nm.

The working principle of the nonlinear optical effects described above requires the light to be linearly polarized with the appropriate orientation for optimum efficiency. The polarization of the incident light on the sample was chosen to be parallel to the plane of incidence (*p*-polarized) unless otherwise stated.

## 2.2 Photoelectron Detection Using a Hemispherical Analyzer

The photoelectron dispersion relation  $E(\mathbf{k})$  (cf. Section 1.3) can be directly measured using a hemispherical photoelectron analyzer equipped with a two-dimensional electron detector, as depicted in Fig. III.11. All PES data presented in this work was collected using this type of analyzer (*PHOIBOS 100, Specs GmbH*). Its basic working principle is the spatial separation of electrons according to their kinetic energy  $E_{\text{kin}}$  and their emission angle  $\theta_e$  (cf. Fig III.4). This is established by (i) an electrostatic lens system, which selects electrons by their emission angle and, thus, defines the mapping of emission angles along one axis of the detector, and (ii) a double hemisphere which maps photoelectrons according to their kinetic energy onto the other axis of the detector. The actual spatially resolved detection of the photoelectrons happens in three steps: First, the signal of single electrons is intensified with an MCP detector and then converted to light by accelerating the amplified electron bunches onto a phosphor screen where they generate flashes of light. As a last step the light is detected by a CCD camera (*sensicam qe, PCO AG*).

This comparably sophisticated way of detecting and analyzing photoelectrons requires considerable effort when interpreting the raw data, which is explained in Appendix A and in Ref. [Weg15]. As an example, special caution has to be taken when samples with considerably low work functions are analyzed. An extensive characterization of the basic properties of the analyzer can be found in Ref. [Dei11].

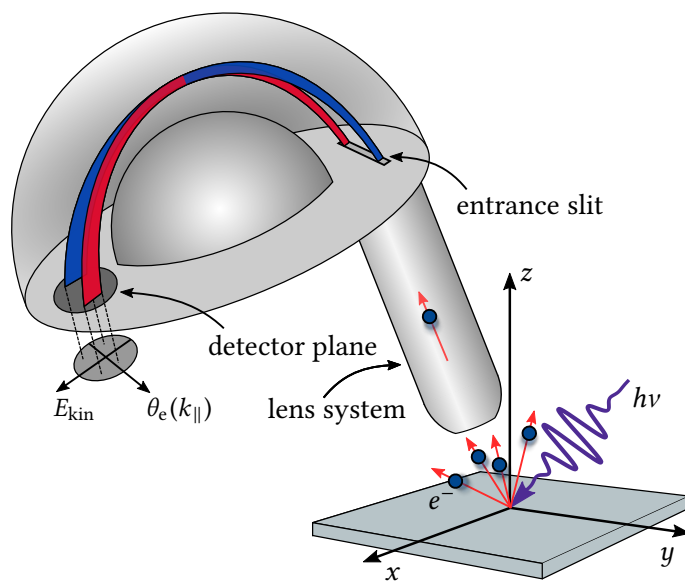


**Figure III.11:** Schematic illustration of the hemispherical analyzer. Photoexcitation with photon energy  $h\nu$  leads to emission of electrons at various angles  $\theta_e$ . A portion of these photoelectrons enters the lens system of the analyzer where they are mapped onto the entrance slit of the hemisphere according to their emission angle, as indicated by trajectories marked in blue and red. The hemisphere then disperses the electrons with respect to their kinetic energy. The separation of electrons by  $E_{\text{kin}}$  and emission angle  $\theta_e$  in space allows to determine these quantities by recording the spatial distribution of the electrons impinging on a two-dimensional [micro-channel plate \(MCP\)](#) detector.

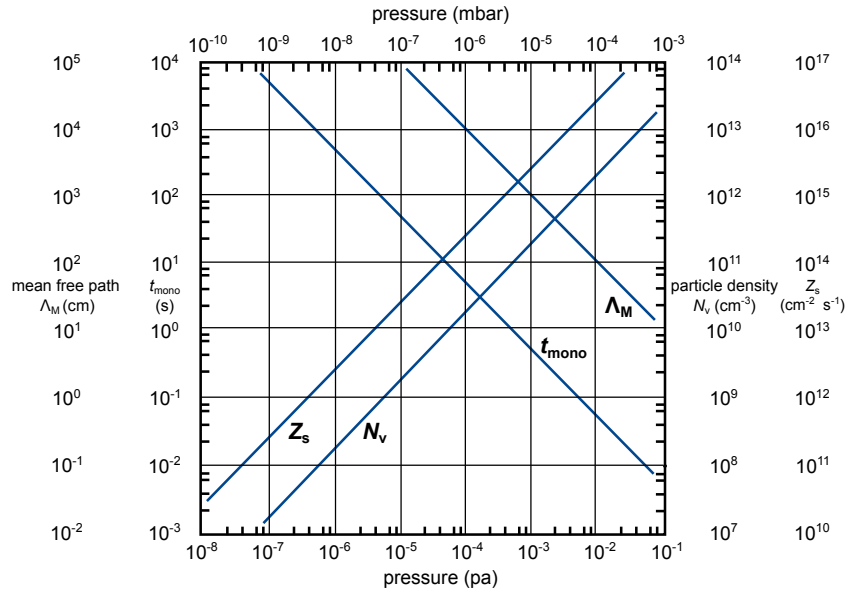


**Figure III.12:** Pressure dependency of characteristic quantities of molecular nitrogen at 300 K derived from kinetic theory: number of impinging particles per unit time  $Z_s$ , particle density  $N_v$ , time for monolayer formation  $t_{\text{mono}}$ , and mean free path  $\Lambda_M$ . Graph adapted from Ref. [HG94].

### 2.3 Ultrahigh Vacuum: A Brief Introduction

In the introduction it was mentioned that UHV conditions ( $10^{-9}$  mbar  $> p_{\text{UHV}} > 10^{-12}$  mbar) are necessary to limit surface contamination by adsorbed residual gases to a minimum, which makes measurements of well-defined surfaces over several hours possible. According to kinetic theory of gases, the number of particles impinging on a surface per unit time  $Z_s$  is given as

$$Z_s = \frac{1}{4} N_v \bar{v} \quad (\text{III.6})$$

where  $N_v = N/V$  is the particle density, which is proportional to the pressure, as  $N_v \propto p$ , and  $\bar{v}$  is the Maxwell-Boltzmann distribution for the velocity of the particles. The actual amount of adsorbed species per unit time, the adsorption rate  $R_{\text{ads}}$  is the product of  $Z_s$  with  $S$ , the sticking coefficient:

$$R_{\text{ads}} = Z_s \cdot S \quad (\text{III.7})$$

The importance of very low pressures for measuring on a well-defined sample surface can be illustrated by estimating the time needed for the formation of a full monolayer of an adsorbate at a given residual gas pressure of  $p = 1 \times 10^{-6}$  mbar. Assuming a maximum sticking coefficient of  $S = 1$  and the kinetic properties of molecular nitrogen gas, monolayer formation takes only about 1 s under these circumstances (see Fig. III.12). Naturally, the sticking coefficient  $S$  depends on the chemical (surface) properties of substrate and adsorbate and on the temperature. As an example, alkali metals will immediately react with semiconductor surfaces also at high temperatures whereas noble gases form adsorbate layers on noble metal surfaces only when the surface is cooled to temperatures of a few tens of Kelvin. This temperature dependence

of adsorption is used in TPD to determine adsorption energies and adlayer thicknesses (see Section 2.5.1).

Beside its importance for clean surfaces, low pressures are crucial for spectroscopic methods that involve electrons. Detection of photoelectron kinetic energies and momenta requires the absence of collisions with gas particles, i.e. a large particle mean free path

$$\Lambda_M = (\sqrt{2} \cdot N_v \cdot q)^{-1}, \quad (\text{III.8})$$

where  $q$  denotes the collision cross section. With  $q = 4.4 \times 10^{-19} \text{ m}^2$  of  $\text{N}_2$  at UHV pressure of  $10^{-10}$  mbar eq. III.8 results in  $\Lambda_M \approx 666 \text{ km}$ . The methods for reaching UHV conditions are described in Section 2.3.1, more details on the preparation of adlayers are given in Section 2.4. For additional details on the general topic of UHV, see Ref. [HG94].

### 2.3.1 The UHV System

A detailed overview of the UHV system and all relevant vacuum and sample preparation and characterization equipment is given in Appendix C. In the following, the basic characteristics of the UHV system are discussed together with the methods used to create well-defined sample surfaces and interfaces. To reach pressures below  $10^{-10}$  mbar for sample analysis and to prepare desired surfaces and interfaces, a multitude of mainly standard vacuum technology components was used. As shown in Fig. C.6 in the appendix, the UHV chamber is divided into two separable parts, a preparation and a spectrometer section. This separation ensures that contaminants are not present in the whole system, especially not the photoelectron analyzer, during sample preparation.

The base pressures that were routinely reached in the UHV system after bakeout were  $p_{\text{prep}} < 1 \times 10^{-10}$  mbar in the preparation chamber and  $p_{\text{spec}} < 5 \times 10^{-11}$  mbar in the spectrometer part of the chamber. These pressures are monitored using two Bayard-Alpert hot-cathode ionization gauges, as shown in Fig. C.3 in the appendix.

## 2.4 Sample Preparation

### 2.4.1 Pristine ZnO Surface Preparation

Hydrothermally grown single crystals with polished  $\text{ZnO}(10\bar{1}0)$  and  $(000\bar{1})$  surfaces (*MaTeck GmbH*) were first mounted to the sample holder. A photograph of a  $\text{ZnO}(10\bar{1}0)$  crystal with transparent, slightly yellow color is shown in Fig. III.13. The direct mount consisted of a tantalum foil which was partly wrapped around the crystal sides and front. This ensured a good thermal contact for cooling and resistive heating of the sample and an electric contact to the sample front which is crucial for defining the energy reference. The electrical contact to the sample holder was furthermore used to apply a bias voltage to the sample surface in photoemission experiments.

Clean and smooth sample surface were prepared in the UHV system by  $\text{Ar}^+$  sputtering (0.75 keV, 10 min, ion current of  $\approx 6 \mu\text{A}$ ) and annealing cycles at 750–900 K for 30 min. The annealing of the oxygen-terminated  $(000\bar{1})$  surface happened at an  $\text{O}_2$  background pressure of  $1 \times 10^{-6}$  mbar to prevent the formation of oxygen vacancies at the surface, following established

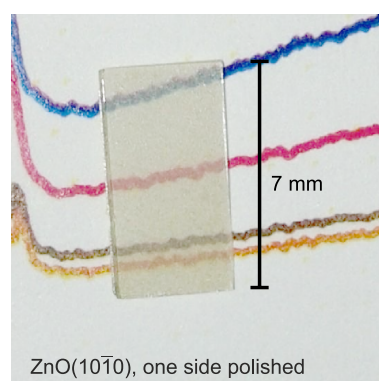


**Figure III.13:** Photograph of ZnO( $10\bar{1}0$ ) crystal after measurements, demonstrating transparency of the 0.4 mm thick single crystal.

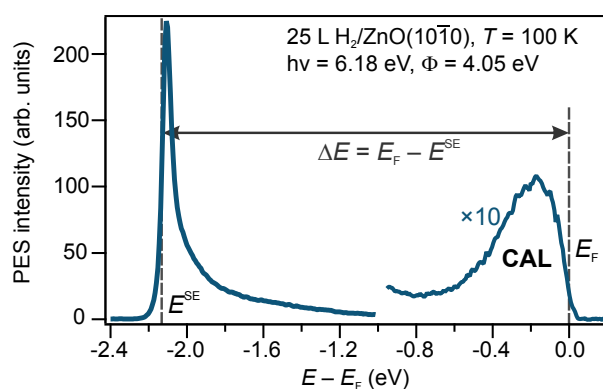


**Figure III.14:** Exemplary photoemission spectrum of ZnO( $10\bar{1}0$ ) after dosage of 25 L hydrogen. The work function  $\Phi$  can be determined by measuring the width of the spectrum  $\Delta E$ , since  $\Phi = h\nu - \Delta E$  (see text).

procedures [DKD04, DBD02]. The heating and cooling rates were kept comparably slow at  $20 \text{ K min}^{-1}$ , which ensures smooth and adsorbate free surfaces [NF03].

The quality of the pristine ZnO( $10\bar{1}0$ ) surfaces was routinely checked by measurements of the work function  $\Phi_{\text{pristine}} = 4.50(5) \text{ eV}$  and the valence band maximum (VBM) at  $E - E_F = -3.18(6) \text{ eV}$ , all agreeing well with literature values [OM10]. The work function, which is a sensitive measure of surface cleanliness (cf. Section 6.5 of Chapter II), was determined using PES by measuring the energetic position of the secondary electron cutoff  $E^{\text{SE}}$ , that is constituted by photoelectrons that barely overcome  $\Phi = h\nu - (E_F - E^{\text{SE}})$  as depicted in Fig. III.14. To achieve high quality pristine surfaces, about ten preparation cycles were necessary. The resulting surface properties were then highly reproducible (see Section 1.1 of Chapter IV). Furthermore, the structural order of the sample surface was routinely checked by recording LEED images.

### 2.4.2 Adlayer Preparation – Overview

The thorough investigation of hybrid inorganic/organic interfaces with photoelectrons depends on well-defined sample surfaces and interfaces. All samples described in this work were prepared *in situ*, usually by first creating a smooth and pristine ZnO substrate surface by means of Ar<sup>+</sup> sputtering and annealing cycles. In an optional second step, the sample substrate was exposed to adsorbate molecules via different methods which have to be chosen according to the adsorbate properties:

1. Adsorbates which are gaseous at ambient conditions, such as hydrogen, can be dosed via the chamber background pressure. For this case, a **leak valve (LV)** is used to set a specific background pressure inside the chamber. The storage and selection of the adsorbates happens within the *gas system*.
2. To minimize exposure of the **UHV** chamber walls to the adsorbates, the sample can be positioned directly in front of the pinhole doser at a distance of  $\approx 2$  mm. The molecular beam which is produced by the doser leads to a high adsorbate partial pressure at the sample surface, without significantly affecting the chamber pressure.
3. Solid substances, such as comparably high molecular weight organic molecules, have to be heated and evaporated to produce adsorbate films. For this reason, a Knudsen cell is used, which contains the solid adsorbate. Heating the adsorbates above their sublimation temperature produces a well-defined molecular beam which is directed onto the substrate surface.

Liquid adsorbates, such as pyridine, can be further purified in the gas system by freeze-pump-thaw cycles. Here, the liquid is cooled inside its reservoir (see Fig. C.6) with liquid nitrogen.

## 2.5 Layer Thickness Determination

As explained in Section 1.2.3 the photoemission experiments presented in this work are highly surface sensitive. Any PES investigations of interfaces between ZnO and an adlayer may, thus, be impeded by electron scattering and a concomitant loss of information, if the adlayer reaches a certain thickness. This also means that structures like buried interfaces, might not be accessible in experiment. As a consequence, the thickness of any adlayer has to be measurable and controllable very precisely, i.e., on a scale of single molecular layers which measure only a few nanometers.

### 2.5.1 Thermally Programmed Desorption

**Thermally programmed desorption (TPD)** is a standard method to characterize ultrathin molecular layers on single crystal surfaces. Most importantly, the absolute coverage  $\theta$  and the activation energy of desorption can be deduced from a TPD trace. The method makes use of the fact that molecules desorb from surfaces at a temperature  $T_{\text{des}}$ , which reflects their adsorption energies: the stronger the bond to the surface, the higher  $T_{\text{des}}$ . It is thus possible to determine the adsorbate

coverage  $\theta$  and the activation energy of desorption  $E(\theta)$ . Experimentally, TPD is carried out by heating the sample surface at a constant rate  $\beta = dT/dt$  and simultaneously recording the partial pressure  $p$  of the desorbing molecules with a quadrupole mass spectrometer (QMS).<sup>3</sup> If the desorbing molecules are pumped sufficiently fast, as it is the case in a UHV environment, then the partial pressure is proportional to the desorption rate  $r$  which is given as [Kin75]

$$p \propto r(\theta) = -\frac{d\theta_i}{dt} = \beta^{-1} \nu_i(\theta_i) \theta_i^{n_i} \exp\left(-\frac{E_i(\theta_i)}{k_b T}\right). \quad (\text{III.9})$$

This Arrhenius-type equation connects the activation energy of desorption to the partial pressure. Here,  $\nu(\theta)$  is the so-called frequency factor, and  $n$  is the reaction order of desorption from state  $i$ . This equation allows a detailed analysis of adsorbate layers, especially on well-defined metal surfaces, as is explained in detail in [Kin75] and carried out in [Dei11].

In this work, TPD traces are analyzed to a lesser extent. Their integral is used as a means to determine the coverage  $\theta$  and the shape and onset of the trace is interpreted as marker for multilayer formation and the thermal stability of adlayers, as demonstrated in Section 4.1 of Chapter IV.

It should be noted that the direct comparison of TPD data between different experimental setups and for different heating rates is subject to shifts the temperature axis. The measurement of the temperature does usually not happen directly at the substrate surface but, in our case, at the backside of the sample (see Appendix ?? for a drawing of the sample holder). Heating the sample with a constant rate, thus, leads to a thermal gradient between sample surface and heated backside. As a result, the offset between the actual temperature at the sample surface and the measured temperature increases with higher heating rate. A further complication are the desorption kinetics and the amount of already desorbed residual molecules that are still detected as a background signal, which can also vary with the heating rate.

### 2.5.2 Quartz Crystal Microbalance

Common functional molecules have molecular weights of hundreds of unified atomic mass units (u) and are thus hard to be detected with a QMS. Furthermore, the collimated molecular beam from the Knudsen cell (see Section 2.4.2) and the high sticking coefficient of the used molecules make it necessary to measure molecular adlayer thickness *in place*, i.e., at the position of the sample during deposition. This is done using a quartz quartz crystal microbalance (QCM) which uses the frequency shift of a quartz resonator to measure molecular mass per unit area and enables film thickness measurements with nanometer precision.

The QCM we are using consists of the UHV quartz sensor head, an oscillator (*PST GmbH*) that drives the quartz crystal at its resonant frequency and a high resolution frequency counter (*Agilent 53200A RF*). The resonant frequency  $f_0$  of the piezoelectric quartz crystal is given as

$$\nu_0 = \frac{1}{2t_q} \sqrt{\frac{\mu_q}{\rho_q}} \quad (\text{III.10})$$

<sup>3</sup>The recorded partial pressure is not necessarily the pressure of the intact adsorbate molecules. It may be advantageous with regard to signal-to-noise ratio to record the partial pressure of the dominant molecular fragment. This hold especially true if high-weight molecules are analyzed, since the performance of the QMS instrument is reduced at high molecular weights.

with  $\mu_q$  the shear modulus,  $\rho_q$  the crystal density, and  $t_q$  the crystal thickness. For our crystal  $\nu_0$  had a value of roughly 5.98 MHz. As eq. (III.10) shows, a change in crystal thickness  $t_q$  leads to a frequency shift. In the end, as the thickness  $t_q$  increases because molecules adsorb at the crystal surface, the frequency  $\nu_0$  decreases from its initial value. Under certain assumptions, this change  $\Delta\nu$  can directly be correlated to a mass change  $\Delta m$  using Sauerbrey's equation[Sau59]:

$$\Delta\nu = -\frac{2\nu_0^2}{A\sqrt{\rho_q\mu_q}}\Delta m = -\frac{2\nu_0^2}{AZ_q}\Delta m \Rightarrow \Delta m = -\frac{A\Delta\nu}{2\nu_0^2}Z_q \quad (\text{III.11})$$

where  $A$  is the piezoelectrically active crystal area and  $Z_q$  is the so-called acoustic impedance of the material, which is in our case given as  $Z_q = 8.8 \times 10^6 \text{ kg m}^{-2} \text{ s}^{-1}$ . This equation is valid under the assumptions that the frequency shift  $\Delta\nu$  is much smaller than  $\nu_0$  and the deposited molecules form a thin homogeneous film that is rigidly coupled to the quartz crystal. We can safely assume, for the molecules used in this work, that both assumptions are valid. If the mass density  $\rho_m$  of the molecular film is known, the film thickness  $t_f$  will directly be given by

$$t_f = \frac{\Delta m}{A\rho_m} = -\frac{\Delta\nu}{2\rho_m\nu_0^2}Z_q. \quad (\text{III.12})$$

Thus, eventually the quartz crystal microbalance allows a direct readout of the adlayer thickness during adlayer deposition.



## IV Results

Within this chapter the results of my experiments on ZnO-based surfaces and interfaces are presented and discussed. These experiments have been designed to answer the following fundamental questions: (i) What is the surface or interfacial electronic structure and how is this related to the microscopic structure of the surface or interface, and (ii) what are the elementary electronic and quasiparticle relaxation processes that occur after an excitation of the electronic system? The vital importance of answers to these questions for novel optoelectronics devices has been pointed out and discussed in Chapter II, and the experimental methods used to gain insight into the energy level alignment and electron dynamics have been described in Chapter III.

A part of the experimental results are complemented with theoretical work from the collaboration with Oliver Hofmann and further former members of the group of Patrick Rinke at the FHI Berlin, who conducted DFT calculations on some of the examined systems. As a result of this collaboration it was possible to achieve a deep and comprehensive understanding of the interplay between the intricate microscopic properties of ZnO surfaces and hybrid interfaces and the resulting electronic characteristics.

This chapter starts with a discussion of the properties of the pristine substrate surfaces followed by a successive increase of the complexity of the examined system. First, the focus is on the electronic structure of the pristine ZnO(10 $\bar{1}$ 0) and (000 $\bar{1}$ ) surfaces and the demonstration of reproducible, well-defined surface conditions. Section 2 presents a detailed investigation of the hydrogen-induced changes of the electronic structure which result in a metallization of the ZnO surfaces. These comparably strong and highly localized potential changes may have a distinct impact on the electronic coupling at hybrid interfaces (see Section 2 of Chapter II). The comprehensive description of the correlation between microscopic and electronic structure at H/ZnO interfaces is followed by the analysis of the excited state dynamics at pristine and hydrogen-covered ZnO surfaces in Section 3. It is demonstrated that the femtosecond dynamics in the ZnO CB are accompanied by the ultrafast formation of a sub-surface excitonic species (SX) which exhibits a lifetime of several hundred picoseconds. Interestingly, it can be shown that the electron and SX dynamics can be clearly influenced by adsorbed hydrogen. This effect can be attributed to the change in screening of the Coulomb interaction which is influenced by the charge carrier density at the ZnO(10 $\bar{1}$ 0) surface.

Results on the *hybrid* interface of ZnO(10 $\bar{1}$ 0) and pyridine (C<sub>5</sub>H<sub>5</sub>N) are presented in Section 4.1. The role of pyridine as docking group and its small size make it an ideal model system for the analysis of adsorption-induced work function changes and allows a quantitative comparison of experimental and theoretical findings. We demonstrate that pyridine forms a well-ordered monolayer on the mixed-terminated surface. The cooperative effect of static molecular dipole and the bond-induced charge redistribution results in a giant work function reduction of  $\approx 2.9$  eV, which is exactly reproduced by DFT calculations.

The complexity of the interface is further increased by replacing the pyridine with 5-Phenyl-

Pyridine, which consists of the pyridine docking group extended with five attached phenyl rings. Apart from the electronic structure of the interface, we examine the ultrafast excited state dynamics which occur upon the injection of an electron from an occupied interfacial state to the molecular LUMO, resulting in a competition between polaron formation and charge back-transfer. The results of these 2PPE experiments which show an ultrafast depopulation of the intermediate charge transfer state with a time constant of 90 fs, are presented in Section 4.2.

## 1 Experimental Characterization of Pristine Zinc Oxide Surfaces

Photoemission experiments on **transparent conductive oxide (TCO)** materials, and especially zinc oxide, pose challenges that exceed those usually encountered during experiments on metal surfaces. First, one cannot assume per se that the emission of electrons does not lead to a charging of the surface because of the low electrical conductivity. Further, band-bending related effects, such as surface photovoltage shifts [ACH90] have to be considered (or excluded). In addition, particularly the polar ZnO surfaces exhibit surface instabilities which have proven to lead to irreproducible surface properties [JZG84], which reveals itself in the often varying reported values of the ZnO work function. Interestingly, recent studies of pristine ZnO surfaces report consistent values of work functions for ZnO surfaces (see Section 6.5 of Chapter II), whereas work functions reported by studies focusing on ZnO-based interfaces often show strong deviations from the reference values [SBB<sup>+</sup>15, KBH<sup>+</sup>14, TNK<sup>+</sup>14].

This section presents the basic characterization of the pristine ZnO( $10\bar{1}0$ ) and ( $000\bar{1}$ ) surfaces using photoemission methods. It is demonstrated, that the sample surface preparation yields highly reproducible surface properties which agree well with recent results in the literature.

### 1.1 The Geometric and Electronic Structure of the ZnO( $10\bar{1}0$ ) Surface

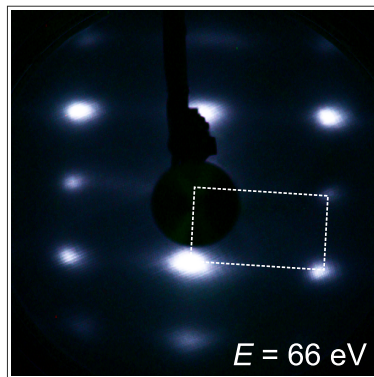


**Figure IV.1:** Exemplary ( $1 \times 1$ ) LEED image of the rectangular ZnO( $10\bar{1}0$ ) surface obtained with an electron energy of 66 eV. The rectangular unit cell is indicated by the dotted lines.

The single crystalline, polished ZnO( $10\bar{1}0$ ) samples were prepared by relatively gentle sputtering and annealing procedures as explained in Section 2.4.1 of Chapter III. An exemplary image of the rectangular diffraction pattern of the ZnO( $10\bar{1}0$ ) surface after a series of preparation cycles is shown in Fig. IV.1. This image, while not as sharp as diffraction from pristine metal surfaces, confirms the occurrence of the bulk truncated structure (cf. Fig. II.16 in Chapter II) without any visible overstructures and is comparable to results from literature [DBD02]. It should be noted that, according to previous STM experiments, the formation of vacancies and surface roughening caused by the preparation process is in any case not expected for the ( $10\bar{1}0$ ) surface [DKD04].

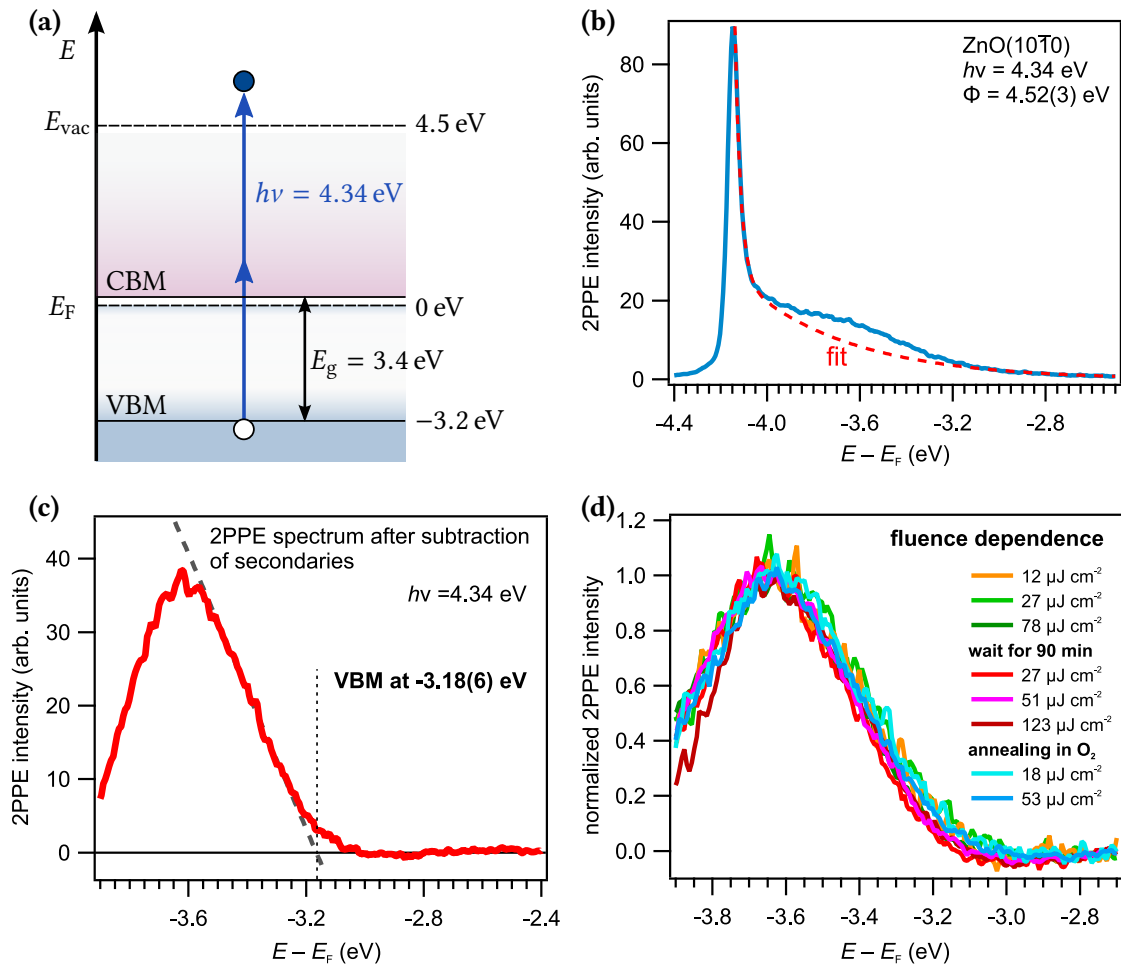


**Figure IV.2:** Characterization of the pristine ZnO(10 $\bar{1}0$ ) surface. All energies refer to the initial states' position relative to  $E_F$ . (a) Scheme of the *bulk* band structure of ZnO with energy values taken from Refs. [OM11, TMN<sup>+</sup>08]. Indicated is the excitation scheme using 4.34 eV photons in a 2PPE process to determine the VBM position and the work function. (b) A typical 2PPE spectrum of the VBM. It shows the secondary electron signal with its sharp cutoff and the high energy edge of the VB. The fit used for the subtraction of the secondary electron background is shown as dotted line. (c) The spectroscopic signature of the VBM after subtraction of the secondary electron background. The linear extrapolation of the VB edge yields a VBM position at  $-3.18(6)$  eV relative to  $E_F$ . (d) A comparison of background-subtracted VBM signatures for different laser fluences and after a waiting time of 90 min under UHV conditions at a temperature of 100 K. Furthermore, spectra are shown for sample annealing in an oxygen atmosphere. All these variations leave the VBM signature virtually unchanged.

The energetic range of the electronic structure of zinc oxide that is accessible with our comparably low energy photons is sketched in Fig. IV.2(a), showing the positions of CBM and VBM and the vacuum level  $E_{\text{vac}}$ . Measuring these features gives essential information about the surface band bending (SBB) and the alignment of energy levels at a potential hybrid interface. Most importantly, the work function  $\Phi = E_{\text{vac}} - E_{\text{F}}$  is a hallmark of the interfacial energy barriers, as explained in Section 4 of Chapter II and it serves as a sensitive indicator of surface stoichiometry and cleanliness.

### 1.1.1 The Valence Band Maximum

The VBM is the unique occupied electronic signature that we can access by a 2PPE process with  $2 \times h\nu = 4.34$  eV photons [see Fig. IV.2(a)]. A resulting, representative spectrum showing the tail of the VB at high energies and the background of secondary electrons which is cutoff at  $\approx -4.2$  eV relative to  $E_{\text{F}}$  is shown in Fig. IV.2(b), together with a fit to the background signal. After subtraction of the aforementioned background, the conventional assignment of the energetic position of the VBM – by linear extrapolation of its edge – yields a value of  $E_{\text{VBM}} = -3.18(6)$  eV relative to  $E_{\text{F}}$ , as shown in part (c) of Figure IV.2. This value is comparable to literature values given for ZnO bulk and the pristine ZnO(10 $\bar{1}$ 0) surface which range between 3.1 eV and 3.2 eV below  $E_{\text{F}}$  [OOE<sup>+</sup>09, OSS<sup>+</sup>03, TMN<sup>+</sup>08]. This means, that the bands at the pristine ZnO(10 $\bar{1}$ 0) surface cannot be bent upward, and in case of downward band bending this cannot extend deep into the bulk of the crystal.

The restricted energy range of the laser and the requirement to use photon energies  $h\nu < \Phi$  inhibit the analysis of the complete VB spectrum. The maximum of the VB peak, which is located at  $\approx 3.7$  eV below  $E_{\text{F}}$  [OSS<sup>+</sup>03], interferes with the strong secondary electron background signal and is the cut off at lower energies.

The stability and reproducibility of the measurement of the VBM was checked by variation of the laser fluence, and also by leaving the sample at 100 K under UHV conditions for about 90 min between measurements. Figure IV.2(d) shows normalized spectra of the VBM signature for different fluences and surface conditions. Obviously, there is only little variation of the energetic position of the VBM. In order to test whether the presence of oxygen would change the surface termination due to pre-existing oxygen vacancies, the sample was annealed in an oxygen atmosphere<sup>1</sup> in addition to the regular preparation procedure. As demonstrated in Fig. IV.2(d), the changes to the VBM signature are subtle. This stability is in contrast to previous measurements of cleaved ZnO(10 $\bar{1}$ 0) surfaces where strong variations of these surface properties with shifts on the order of hundreds of meV were observed with time[MKH80]. However, the slight variations presented in Fig. IV.2(d) show a systematic behavior, which will be discussed in Section 1.1.3 together with the stability of the work function.

### 1.1.2 The Work Function

The work function, which is a purely surface-related material property, in contrast to the VBM, can be derived from the position of the secondary electron cutoff in PES spectra (see Fig. IV.2

<sup>1</sup>The annealing parameters were:  $p_{\text{O}_2} = 1 \times 10^{-6}$  mbar,  $T = 500$  K,  $t = 10$  min.

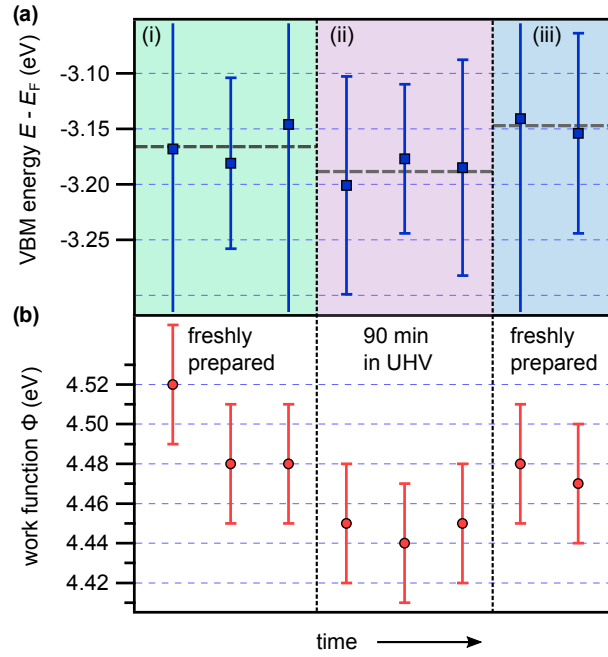


**Figure IV.3:** Stability of VBM position and work function of the pristine ZnO( $10\bar{1}0$ ) surface with time and varying fluence. (a) position of the VB edge from linear extrapolation (see text). (b) corresponding work function. Both properties were measured for three different “states” of the sample and exhibit a slight but discernible shift.

and Section 2.2 for details). The width of the secondary cutoff, or edge, is a measure of both the energetic resolution of the analyzer and the homogeneity of the surface work function. Any variation in  $\Phi$  within the laser spot causes a widening of the secondary edge. Thus, a sharp edge is generally a sign of laterally homogeneous surface conditions. In our experiments, we observe widths on the order of 50 meV, which are largely determined by the analyzer resolution (see Ref. [Dei11] for details on the photoelectron analyzer characteristics).

The work function of the freshly prepared, pristine ZnO( $10\bar{1}0$ ) surface is  $\Phi = 4.52(3)$  eV which is identical to the value of  $\Phi_{\text{lit}} = 4.5$  eV given in literature [OM10, TMN<sup>+</sup>08], which indicates a well-ordered, defect-poor surface.

### 1.1.3 The Stability of the Surface Electronic Structure

The instability of ZnO surfaces characteristics was a major issue in early ZnO studies [MKH80, JZG84]. Hence, it is advisable to study any changes to the surface electronic structure due to unintentional adsorption of residual gases photoinduced processes or of other unknown origin. A closer look at the VBM signatures shown in Fig. IV.2(d) reveals that there is no perfect overlap of these signatures, but there are slight shifts on the order of 0.1 eV, i.e., slightly above the experimental uncertainty. A thorough analysis of the VB edge by linear extrapolation results in energies which are displayed in Fig. IV.3(a). At first sight, the values are scattered

nonsystematically between 3.15 eV and 3.2 eV below  $E_F$ .<sup>2</sup> However, by considering the three “states” of the sample: (i) surface freshly prepared with the standard procedure described above, (ii) the sample has been left at a pressure of  $5 \times 10^{-11}$  mbar for 90 min at 100 K, and (iii) after preparation with additional annealing in  $O_2$  atmosphere. The mean **VBM** energies for each state, indicated by the dotted lines, show that the **VBM** bends downward slightly with time, which can be restored by another preparation cycle. There is also a minor difference on the order of 20 meV between annealing with and without additional oxygen.

In Fig. IV.3(b) the corresponding work functions are shown, which exhibit roughly the same shifts with time, indicating that the bending of the bands includes the shift of the vacuum level. Still, the absolute changes of both **VBM** energy and work function on the order of few 10 meV are far less pronounced than those of early ZnO studies [MKH80, JZG84] which are an order of magnitude stronger. Moreover, the observed unintentional reduction of the work function by  $\approx 60$  meV within 90 min is significantly smaller than that reported in a more recent work by Tisdale et al. who observed a reduction by  $\approx 300$  meV within 1 h [TMN<sup>+</sup>08]. It should be noted that there is one residual gas which is exceedingly difficult to completely remove from a **UHV** system: hydrogen. Hydrogen adsorption is the most probable cause of work function shifts observed in experimental studies and a detailed study of the hydrogen-induced effects on ZnO is given in Section 2.

As for the variation of the laser fluence, there appears to be a weak relationship between high fluence, downward band bending and work function reduction. This effect is neglected in the following due to its weakness. A discussion of photoinduced effects on the ZnO surface electronic structure can be found in the appendix.

One can, thus, conclude that our established preparation method yields reproducible surface conditions that match with previous **PES** experiments on high quality ZnO(10 $\bar{1}0$ ) samples. The changes of the surface electronic characteristics which are most likely a result of adsorption of residual gases, especially hydrogen, are negligible. This is an indication of the very low contaminant levels inside the **UHV** system.

## 1.2 Geometric and Electronic Structure of the Pristine ZnO(000 $\bar{1}$ ) Surface

The comparison between the different surface terminations of ZnO is particularly interesting because of the distinct differences of the electrostatic fields at the surface which are caused by the partly ionic bond between the  $Zn^{2+}$  and  $O^{2-}$  components (see Section 6.1 of Chapter II). The resulting dipole at the polar surfaces possibly leads to surface reconstructions, as discussed in Section ?? of Chapter II. In case of the oxygen-terminated (000 $\bar{1}$ ) surface such a reconstruction is usually not found with imaging methods like **LEED** or **STM** [DBD02]. However, this absence has been attributed to the presence of unintentionally adsorbed hydrogen which supposedly has a stabilizing effect [KGGB<sup>+</sup>02] that preserves the bulk-truncated surface.

When comparing the oxygen-terminated ZnO surface to the mixed-terminated one it is particularly interesting that both of these surfaces show the formation of a **CAL** when hydrogen is adsorbed, which is in contrast to the Zn-terminated surface [OM11]. The hydrogen-induced

<sup>2</sup>The error was derived from the uncertainty of a linear fit to the **VB** edge. It is noteworthy, that the error of this method of determining the **VB** edge is generally larger than the scatter of the data itself.

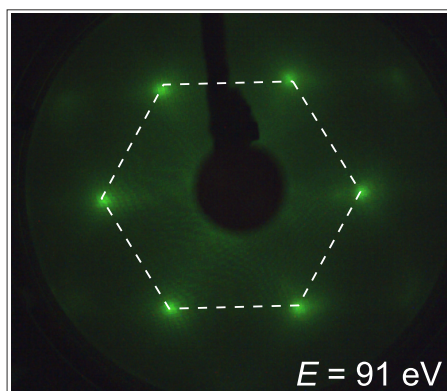


**Figure IV.4:** Exemplary  $(1 \times 1)$  LEED image of the hexagonal  $(000\bar{1})$  surface obtained with an electron energy of 91 eV. The hexagonal unit cell is indicated by the dotted lines.

effects will be discussed in Section 2.5. The measurements which are presented here have mainly been carried out by Clemens Richter as a part of his master’s thesis work.

The surface structure of the freshly prepared single crystalline  $\text{ZnO}(000\bar{1})$  samples (for details on the surface preparation see Section 2.4.1 of Chapter III) was checked routinely by LEED. Figure IV.4 shows the hexagonal  $(1 \times 1)$  pattern of the unreconstructed surface, which is comparable to earlier LEED measurements [DBD02]. The absence of overstructure patterns can be an indicator for hydrogen being already adsorbed to the surface (see above), however, this amount must be comparably small as the unintentional hydrogen dosage from the residual gas is on the order of 0.01 L per hour.<sup>3</sup> LEED images of the hydrogen-covered surface are virtually identical to those of the pristine surface (not shown).

Figure IV.5 displays a 2PPE spectrum of the VBM signature of the oxygen-terminated ZnO surface. This spectrum was recorded directly after surface preparation with a photon energy of  $h\nu = 4.65$  eV at a sample temperature of 100 K. Notably, the work function of 5.21(3) eV is  $\approx 0.7$  eV higher compared to that of the mixed-terminated surface. This is intuitively understandable when considering the surface dipole that is induced by the negatively charged oxygen atoms pointing outward from the surface (see Fig. II.12). The measured work function is marginally higher than what has been reported in literature (5.1 eV) [OM11]. However, leaving the sample at  $T \approx 100$  K under UHV conditions for several minutes leads to a reduction of  $\Phi$  by  $\approx 0.1$  eV, which is analogous to the behavior of the pristine  $(10\bar{1}0)$  surface (see Section 1.1.3). The higher magnitude of the shift in case of the polar surface indicates an overall higher reactivity of this surface. These comparably strong unintentional work function shifts have been observed before (see Ref. [JZG84]), albeit with significantly higher instability ( $\Delta\Phi = -1$  eV within 40 min).

As it is the case for the mixed-terminated surface, the slight shift of  $\Phi$  is also reflected in the energetic position of the VBM which is shown in the inset of Fig. IV.5. For the freshly prepared surface the edge is located 2.78(7) eV while it is shifted to higher binding energy at 2.99(13) eV after the  $\approx 30$  min wait. These values differ strongly from those of the pristine  $(10\bar{1}0)$  surface

<sup>3</sup>This dosage can be determined from the  $\text{H}_2$  partial pressure in the UHV chamber which is on the order of  $4 \times 10^{-12}$  mbar as measured by the QMS.

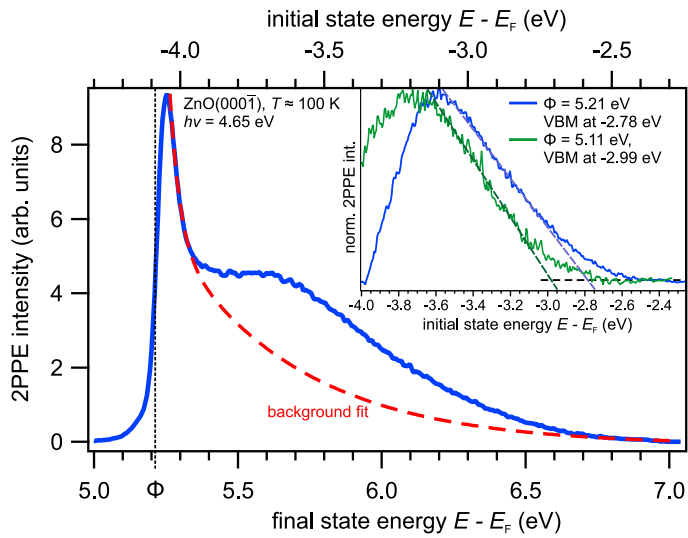


**Figure IV.5:** The VBM signature of the O-terminated ZnO(000 $\bar{1}$ ) surface measured with 2PPE. The work function  $\Phi = 5.21$  eV can be read directly from the final state energy axis. The inset shows the VB high energy edge after subtraction of the secondary electron background for two different measurements: (blue) directly after surface preparation, and (green)  $\approx 30$  min after the end of the preparation cycle. The position of the VBM is determined by linear extrapolation of the edge. Modified from Ref. [Ric14].

which exhibited a VBM of  $\approx -3.2$  eV relative to  $E_F$  which is identical to the bulk value (see Fig. IV.2). In contrast, the VB at the pristine (000 $\bar{1}$ ) surface apparently bends upwards as it is energetically located  $\approx 0.4$  eV higher at the surface compared to the bulk. Ozawa and Mase report basically the same behavior with a VBM at  $-2.9$  eV [OM11] which is between the two values found in this work.

### 1.3 Band Bending at the Pristine (10 $\bar{1}0$ ) and (000 $\bar{1}$ ) Surfaces

Figure IV.6 compares the energetic positions of bulk and surface CBM and VBM and the work functions of the two examined ZnO surfaces. In contrast to the flat bands at the mixed-terminated surface, the oxygen terminated surface exhibits upward SBB which is in agreement with the ARPES data measured with photon energies ( $h\nu$ ) from 60 eV to 70 eV [OM11]. In contrast to the strong spatial restriction of the CAL normal to the ZnO surface, which reaches only  $\lesssim 2$  nm (see Section 2.4) below the surface, any depletion layer on the oxygen-terminated surface may reach far deeper ( $\approx 1$   $\mu$ m) into the bulk of the crystal [YYO<sup>+</sup>14]. This difference in depth of the band bending is the main reason why our experiment, which samples over a certain depth below the surface of our sample, is very sensitive on upward band bending, while downward band bending in ZnO is hard to detect directly (see Section 1.2.3 of Chapter III).

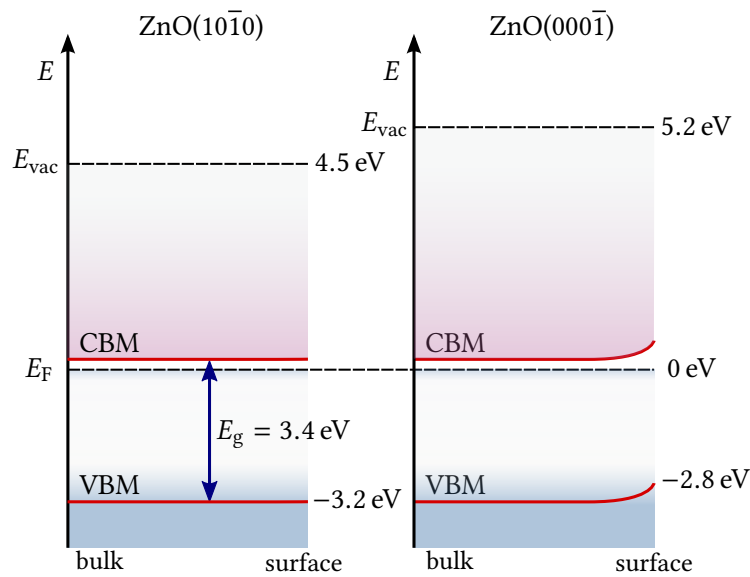


**Figure IV.6:** Surface and bulk CB and VB energies for the pristine ZnO(10 $\bar{1}$ 0) and (000 $\bar{1}$ ) surfaces. At the mixed-terminated surface the energetic positions of the bands in the bulk and at the surface are identical. The oxygen-terminated surface exhibits an upward SBB by  $\approx 0.4$  eV and a significantly higher work function of 5.21(3) eV.

## 2 Hydrogen-Induced Surface Metallization

Hydrogen has been recognized as the predominant source of conductivity and high charge carrier densities in zinc oxide (see Section 6.4 of Chapter II). The direct influence of adsorbed hydrogen on the *surface* electronic structure has recently been revealed in ARPES studies on the main ZnO surface terminations which showed the occurrence of metallicity – occupied electronic states at the Fermi level – if hydrogen is adsorbed on the O-polar and the mixed-terminated ZnO surfaces [OM11], which is accompanied by a distinct reduction of the work function.

Naturally, the electronic properties of the ZnO surface, and the methods to modify these, are of high interest for research on HIOS, because any functionality is intimately linked to the interfacial energy alignment and energy barriers. The investigation of hybrid surfaces and interfaces has so far focused mainly on *area averaged* values of energy level alignment, band bending and other interfacial properties. This averaged view is well justified as a first step in interface modeling, however, it cannot capture the actual microscopic situation at the interface when the surface potential exhibits highly localized corrugations, which is the case with the mixed-terminated ZnO surface under the influence of hydrogen. Thus, a comprehensive model of the hydrogen/ZnO(10 $\bar{1}$ 0) interface requires a detailed understanding of the adsorption process and the resulting changes to the surface electronic structure, which will be presented in this work.

For this purpose, the experimental characterization of ZnO(10 $\bar{1}$ 0) surfaces with various amounts of adsorbed hydrogen are complemented by DFT calculations carried out by Oliver

Hofmann et al. under supervision of Patrick Rinke and Matthias Scheffler at the theory department of the FHI. All DFT data and the corresponding visualizations were provided to me by Oliver Hofmann, while all experimental data, the analysis and overall interpretation of the results are my own work. The bulk of the findings presented in this section have been published in Ref. [DHM<sup>+</sup>15].

The presence of both zinc and oxygen atoms at the vacuum interface of the mixed-terminated surface makes it an interesting model system for adsorption experiments in general, as one can expect a strong site specificity. The key finding of this collaborative effort is the competition for hydrogen bonds between surface oxygen (O) and zinc (Zn) atoms, depending on how much hydrogen is offered to the surface: Initially, O-H bonds are favored, but as soon as about every fifth surface oxygen atom is covered with a hydrogen atom, Zn-H bonds start to form with ever increasing probability. This results in a complex adsorption pattern even at low hydrogen coverages and has a strong impact on the understanding of ZnO-based hybrid interfaces where residual hydrogen is usually present during interface preparation. The results on the mixed-terminated surface are compared to adsorption experiments on the oxygen-terminated (000 $\bar{1}$ ) surface which further corroborate our view on the role of hydrogen as highly potent and relevant adsorbate.

## 2.1 Preparation of Hydrogen-Covered ZnO Surfaces

Before adsorbing any hydrogen on the ZnO surfaces, the sample was cleaned by the standard procedure described in Section 2.4.1 of Chapter II. Molecular hydrogen was then offered at a constant background pressure of  $6.7(2) \times 10^{-7}$  mbar ( $0.5 \text{ L s}^{-1}$ ), at a sample temperature of 100 K for all measurements presented in this paper. Atomic H was generated using the glowing tungsten filament of the Bayard-Alpert pressure gauge at a distance of  $\approx 15$  cm in the line of sight of the sample surface. It is well known that the hot filament causes a partial cracking of the H<sub>2</sub> molecules. This procedure is analogous to that described in Refs. [OM11, WMY<sup>+</sup>05].

Because of the indeterminate portions of molecular and atomic hydrogen a quantitative determination of the hydrogen coverage is not possible. It is well-justified to assume that most molecular hydrogen impinging on the surface does not adsorb, because the sticking coefficient for H<sub>2</sub> is very small, while for atomic H it is close to one [JZG84]. Since the partial pressures of both hydrogen species at the sample surface are unknown, only the overall H<sub>2</sub> dosage in units of Langmuir can be given.<sup>4</sup> The estimated atomic hydrogen dosage is only a few percent of the measured H<sub>2</sub> dosage, which is derived from the H<sub>2</sub> cracking efficiency at a hot tungsten filament which is on that order [SOOK95].

Nevertheless, the calculations which are presented in the following make it possible to relate the hydrogen dosage to the actual coverage  $\Theta$ .

## 2.2 Emergence of Metallicity in Photoemission Spectra

The experimental characterization of the hydrogen-covered ZnO(10 $\bar{1}$ 0) surface was done using  $\approx 6.2$  eV photons to access the electronic states around  $E_F$  and to deduce the work function

<sup>4</sup>1L  $\approx 1.33 \times 10^{-6}$  mbar s.

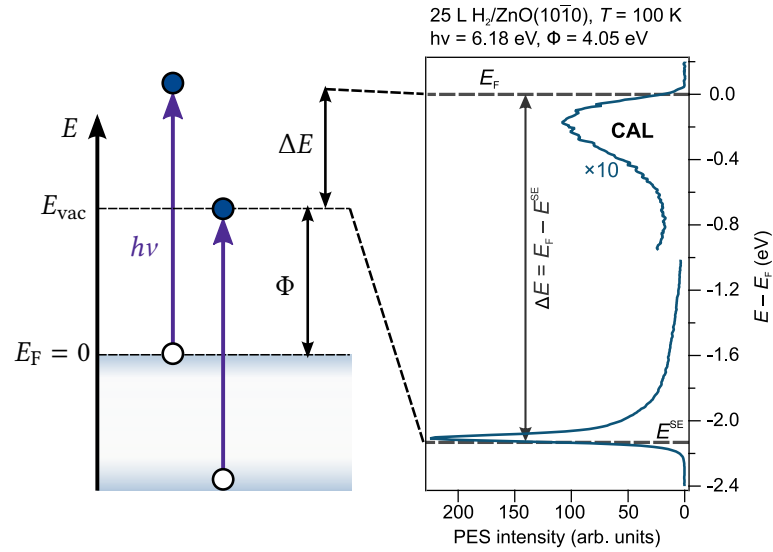


**Figure IV.7:** Measurement of the sample work function using PES. (Left) The scheme illustrates the energetic difference  $\Delta E$  between electrons originating from the CAL at  $E_F$  defined as 0 eV and electrons which barely overcome the vacuum level  $E_{\text{vac}}$ . (Right) an exemplary spectrum of the hydrogen-covered ZnO(10 $\bar{1}$ 0) surface shows the CAL signature below  $E_F$  and the signature of the secondary electrons at  $E^{\text{SE}}$ .

from the secondary electron cutoff, as indicated on the left side of Fig. IV.7. An exemplary photoemission spectrum after dosing 25 L of H<sub>2</sub> is shown on the right. At this H<sub>2</sub> dosage, we observe a reduced work function of  $\Phi = 4.03(5)$  eV and a distinct PES signal peak right below  $E_F = 0$  eV. This occurrence of an occupied state right below  $E_F$  is attributed to the formation of the well-known **charge accumulation layer (CAL)** at the ZnO(10 $\bar{1}$ 0) surface, as described in Section 6.3.3 of Chapter II. The supposition that this signature does indeed originate from an initially *occupied* electronic state could be verified by determining the CAL signal intensity for different laser fluences, which yielded a *linear* dependence (not shown).

The established explanation of the hydrogen-induced CAL formation is illustrated in Fig. IV.8. In this view, the adsorption of hydrogen reduces the net surface dipole by donating its electron, so that the average surface potential  $V(z)$  decreases. Thus, the electron donation from the adsorbed hydrogen causes an effective downward bending of the electronic bands at the surface. Because of the *n*-type character on ZnO the CBM bends below  $E_F$ , which eventually leads the occurrence of occupied electronic states in a few ten angstrom thick CAL (cf. Figs II.17 and II.18).

To quantify the H-induced changes to the surface potential, we took a series of spectra for H<sub>2</sub> dosages ranging from 0 L to 500 L and analyzed the shift of  $\Phi$  and the intensity of the CAL signature. Fig. IV.9(a) shows the respective spectra in an energy range close to  $E_F$ . The corresponding analysis is shown in Fig. IV.9(b): The blue curve depicts the dependency of  $\Phi$  on the H<sub>2</sub> dosage. The work function is continuously reduced by up to  $\Delta\Phi_{\text{max}} = -0.65(5)$  eV, as compared to the work function of the pristine surface after annealing. Clearly, the shift of  $\Phi$  occurs mainly at hydrogen dosages below 50 L, and for dosages approaching 100 L we observe a *stabilization* of the work function. A quantitatively identical dependency of  $\Phi$  on H dosage is

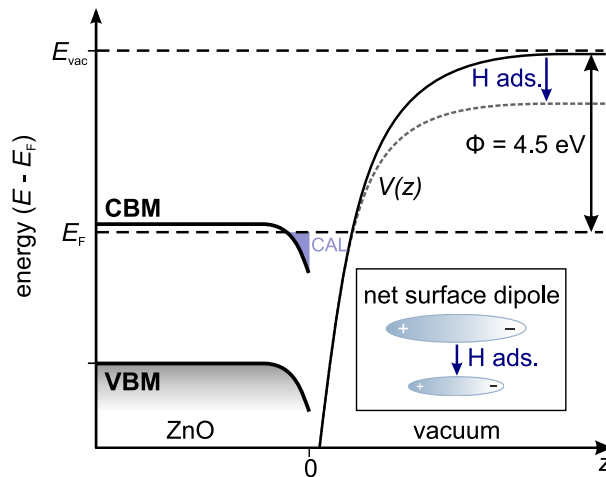


**Figure IV.8:** Schematic energy level diagram of ZnO( $10\bar{1}0$ ) after exposure to hydrogen with an average potential  $V(z)$  across the interface. The bulk CBM, which is located only 200 meV above the Fermi energy in  $n$ -type ZnO( $10\bar{1}0$ ), is bent below  $E_F$  leading to the formation of a few ten angstrom thick CAL. The net surface dipole is reduced by H adsorption, causing a downshift of the surface potential  $V(z)$ .

measured for two different samples. The reproducibility of this effect is further corroborated by the fact that our measured value of  $\Delta\Phi_{\max}$  is identical to the value for H-saturated surfaces reported in the literature [OM11].

To evaluate the effect of H adsorption on the surface electronic structure we analyzed the intensity of the CAL signature with respect to the hydrogen dosage as shown by the red squares in Fig. IV.9(b).<sup>5</sup> While the PE spectrum of the freshly prepared surface shows nearly zero intensity below  $E_F$ , the CAL intensity shows a distinct increase for hydrogen dosages up to 150 L. It should be noted that the spectral shape of the peak and its energetic position do not change significantly in this low dosage regime. The energetic position of the CAL peak maximum can be derived from a single Gaussian fit to the data. We find a peak maximum at about 0.165 eV below  $E_F$  for a dosage of 200 L, which agrees well with the position of 0.16(3) eV measured by Ozawa and Mase for the same dosage, see Ref. [OM11]. A detailed analysis of the dosage-dependent energetic position of the CAL can be found in the following Section 2.4.3. In addition, the increasing intensity of the CAL peak at  $E_F$  implies an increase of the electron density and, therewith, metallic character of the ZnO surface.

Continued dosing of hydrogen above 150 L then leads to a significant intensity *reduction* of the CAL signature, which is in contrast to the *stabilization* of  $\Phi$  for high dosages. Most notably, the characteristic change of the two H-induced effects in the dosage range between 50 and 150 L hints at a competition between two different processes: (i) the creation of DOS below  $E_F$ , i.e., metallization and a simultaneous reduction of the surface dipole for dosages  $\lesssim 150$  L and (ii) the subsequent reduction of the CAL intensity accompanied by a stabilization of the

<sup>5</sup>The intensity of the CAL signature was determined by integrating the spectra in an energy range from  $-0.74$  eV to  $0.12$  eV after subtracting the secondary electron background.

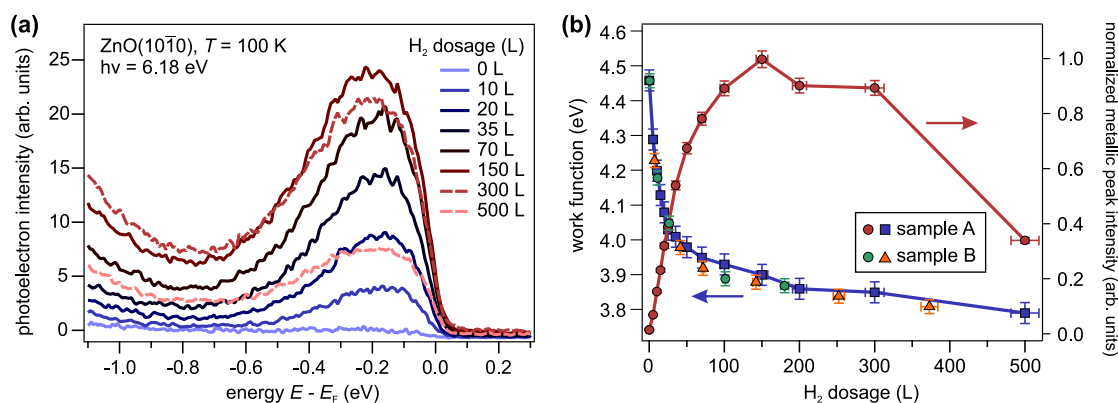


**Figure IV.9:** (a) UPS spectra of the ZnO(10 $\bar{1}$ 0) surface around  $E_F$ . The increase of hydrogen dosage causes the drastic increase of the CAL signature. (b) Dependency of the work function of different ZnO(10 $\bar{1}$ 0) samples on hydrogen dosage (blue curve) and integrated intensity of the CAL signature (red curve).

surface dipole for higher dosages. This finding of dosage-dependent changes that both exhibit a characteristic point at  $\approx 100$  L may originate from the availability of two different adsorption sites: Zn and O surface atoms. A closer look at this site specificity of hydrogen adsorption will be taken in the next Section.

### 2.3 Bond Energies and the Competition Between O–H and Zn–H Bonds

Experimentally, it is challenging to distinguish between the two possible surface species – O–H and Zn–H bonds. It was demonstrated in CO adsorption experiments by Wöll and coworkers that O–H bonds are the predominant species at room temperature, while Zn–H bonds apparently have a much lower binding energy [WMY<sup>+</sup>05]. Moreover, STM images from the same study show a distinct change in the ZnO(10 $\bar{1}$ 0) surface structure when hydrogen is adsorbed, but they do not yield certain adsorption sites. A further deficit in previous studies is the lack of information on very low amounts of adsorbed hydrogen. Instead, the majority of works focuses on hydrogen-saturated surfaces, i.e., comparably high dosages.

A comprehensive description of the hydrogen adsorption behavior at the ZnO(10 $\bar{1}$ 0) surface requires more information on the energetics of single binding sites, which can be gained from DFT calculations, the results of which are presented in the following.

The first question that Oliver Hofmann and Patrick Rinke addressed was the adsorption pattern of hydrogen, which can be deduced by calculating the Gibbs energy of bond formation  $\Delta G$  for each of the possible adsorption geometries. The ZnO(10 $\bar{1}$ 0) surface was modeled with a  $4 \times 4$  unit cell containing 16 ZnO surface dimers, with a depth of 32 single-layers (see Fig. IV.10). They found that such a slab thickness was necessary to capture the whole extent of downward band-bending in the most extreme case in which each surface oxygen is decorated by a hydrogen atom.<sup>6</sup>

<sup>6</sup>A complete account of the computational methods used in this work can be found in Ref. [DHM<sup>+</sup>15]

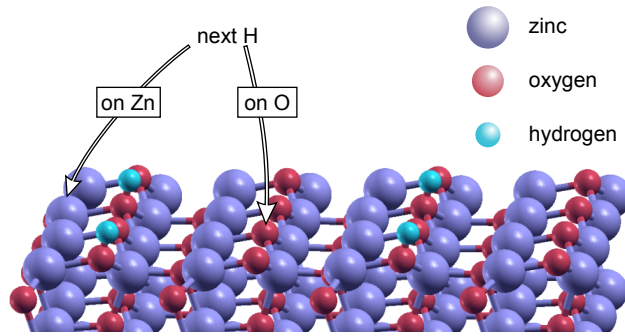


**Figure IV.10:**  $(4 \times 4)$  ZnO supercell with 25% O–H pre-coverage. In our calculations we compare the energy difference for the adsorption of an additional H atom on either an O atom or a Zn atom next to an H-pre-covered O atom, as indicated.

Strictly speaking, the correct way to determine the surface structures would be to generate *all* possible hydrogen configurations and to calculate their surface energy. The different configurations would then be populated according to Boltzmann-statistics at the experimental temperature of 100 K. The large number of possible configurations (a  $(4 \times 4)$ -supercell can represent on the order of  $2 \times 10^8$  different geometries), renders this approach intractable.

The traditional approach is to deal with this is to neglect temperature effects, i.e., to assume  $T = 0$  K. This would reduce the problem to finding the conformation with the lowest energy, which could be done by cluster expansion or genetic algorithm methods. However, picking several random configurations it was found that the energy differences are very small, on the order of 10 meV to 50 meV. Assuming  $T = 0$  K also neglects configurational entropy, which is not constant for a coverage series. Instead, configurational entropy favors submonolayers with medium coverage over almost full or empty layers. Moreover, for a given hydrogen decoration, it favors layers with mixed adsorption sites over layers with only one adsorption site. Given the small energy differences between the geometries, it was chosen to simplify the calculations by assuming that for a fixed number of O–H and Zn–H bonds all configurations are essentially degenerate. This removes the burden of finding the global minimum, and we can simply pick one arbitrary geometry as representative. Moreover, the configurational entropy  $S$  can then be expressed analytically. According to Boltzmann’s equation, it is given as

$$S = k_B \ln \left[ \binom{n_{\text{OH}}}{n_{\text{O}}} \binom{n_{\text{ZnH}}}{n_{\text{Zn}}} \right] \quad (\text{IV.1})$$

Here,  $n_{\text{O}}$  and  $n_{\text{Zn}}$  denote the number of surface O and Zn atoms, respectively, and  $n_{\text{OH}}$  and  $n_{\text{ZnH}}$  the number of O–H and Zn–H bonds.

To keep the computational effort reasonable, not all 256 calculations were performed that would be required to generate a full surface energy diagram as function of O–H and Zn–H coverage. Instead, the main question was whether at some point during the dosage of hydrogen atoms, the formation of Zn–H bonds could energetically compete with the formation of O–H bonds. As stated above, previous work from Wöll and coworkers suggested [WMY<sup>+</sup>05], that surface O–H bonds are more stable than Zn–H bonds, since the latter were not observed at high

temperatures. Furthermore, the sticking coefficient of hydrogen on the pristine Zn-terminated ZnO(0001) surface was found to be extremely small at  $< 1 \times 10^{-6}$  (Ref. [BHK<sup>+</sup>01]), which illustrates the low formation probability of isolated Zn–H bonds. Moreover, the propensity of ZnO to form donor-type defects (see Section 6.1.3 of Chapter II) is in agreement with the predominant occurrence of O–H bonds. It is noteworthy, that the theory of the [charge neutrality level \(CNL\)](#) predicts, that a high density of these donor-type defects would then promote the formation of compensating acceptor-type defects, i.e., Zn–H bonds.

Taking all this into consideration, the Gibbs energy was calculated for the formation of adding *another* hydrogen atom to a surface that is already pre-covered with a sub-monolayer of hydrogen *exclusively* adsorbed on oxygen. The pre-coverages which were explicitly considered cover a wide range from 0% to 94%, specifically one, two, three, four, six, and eight H atoms in the unit cell, which were always distributed such that the distance between them was maximized. An example of this approach is shown in Fig. IV.10 for a sample with a pre-coverage of four O–H bonds. An additional hydrogen is then adsorbed on either a Zn atom next to an O–H bond or on an additional O atom. The Gibbs energy of formation,  $\Delta G$  is calculated separately for adsorption on a surface Zn or O site as

$$\Delta G^{\text{Zn/O}} = E_{n+1} - E_n - E(\text{H}) - TS \quad (\text{IV.2})$$

where  $E_{n+1}$  is the energy of the  $(4 \times 4)$  supercell with one additional hydrogen adsorbed on either Zn or O,  $E_n$  the energy of the supercell without the additional hydrogen,  $E(\text{H})$  the energy of an isolated hydrogen atom,  $T$  the temperature in experiment (100 K) and  $S$  the configurational entropy. Note that the contribution from vibrational zero-point energies was neglected here.<sup>7</sup>

It is indeed found that with increasing (pre-)coverage of O–H bonds, the formation of further O–H bonds becomes increasingly energetically *unfavorable* with respect to the formation of Zn–H bonds. We attribute this, as indicated above, to the amphoteric character of hydrogen which acts as an electron *donor* on oxygen, but as an electron *acceptor* on Zn. Pre-covering the surface with O–H bonds reduces the work function of ZnO and thus also the ionization energy and electron affinity. Consequently, with increasing O–H pre-coverage, charge-transfer from the electron donor to ZnO becomes less favorable, while charge transfer from ZnO to the electron acceptor becomes beneficial. As Fig. IV.11(a) shows, this results in a turning point at an O–H coverage of approx. 18%, where the adsorption of hydrogen on a zinc atom next to an O–H bond becomes energetically favorable compared to the formation of another O–H bond. This argument implies that there is a critical work function at which the adsorption of H on O and Zn is nearly isoenergetic and, thus, there is no distinct energetic benefit of one bond over the other.

This work function will essentially stabilize itself, as the adsorption of H on O lowers the work function and facilitates further adsorption on Zn, while conversely, the adsorption of H on Zn increases the work function and leads to further adsorption of H on O. It would thus explain why the work function saturates before the hydrogen layer is completed. Hence, for coverages around and above 18 %, always a complex mixed monolayer with O–H and Zn–H

<sup>7</sup>To check the influence of an increase of temperature on our results we also performed calculations using the above-described method for  $T = 300$  K and find neither qualitative nor quantitative changes to our results – within the precision of the calculation.

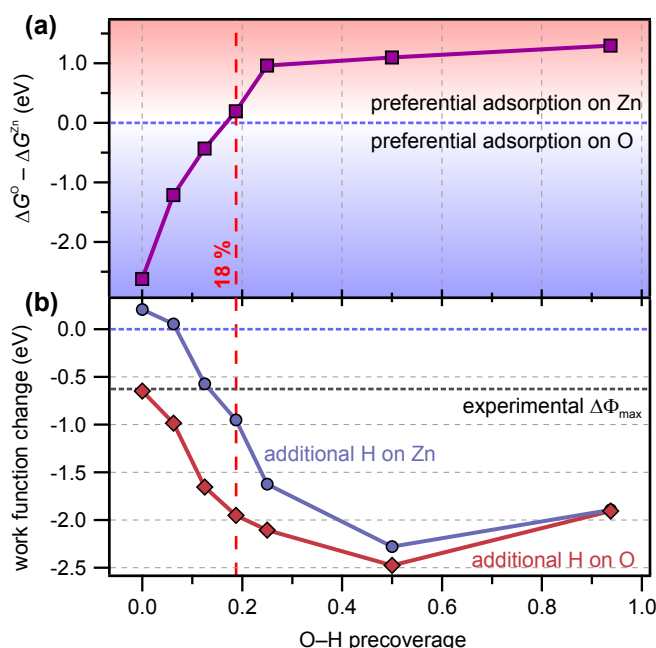


**Figure IV.11:** (a) Relative formation energy for the formation of one O-H bond ( $\Delta G^O$ ) and one Zn-H bond ( $\Delta G^{Zn}$ ) per  $(4 \times 4)$  supercell, depending on the amount of oxygen atoms pre-covered with hydrogen. Formation of O-H bonds is clearly favored for pristine ZnO(1010). The crossing of the zero line marks the O-H-bond pre-coverage at which the next H favorably adsorbs at a surface Zn atom next to an O-H bond. This coverage of 18 % is marked with a red dotted line. (b) Calculated work function change resulting from H adsorption at a surface with the same O-H pre-coverage as in (a). Diamonds and circles show  $\Delta\Phi$  for H adsorption on O or a first Zn site, respectively.

moieties will form. Therefore, it should be emphasized that for higher hydrogen coverages, the work functions calculated with the artificial adsorption scheme adopted here do not correspond to adsorption structures that will occur in experiment.

Figure IV.11(b) shows the calculated hydrogen-induced work function change  $\Delta\Phi$  for a number of different adsorption geometries. To compare the effect of O-H vs. Zn-H bond formation on surfaces with different amounts of O-H bonds already present,  $\Delta\Phi$  is plotted for an adsorption pattern where one *additional* H atom is adsorbed on either another surface O site or a first surface Zn site (red diamonds and blue circles, respectively). For the  $(4 \times 4)$  supercell this means that the work function change for a certain O-H pre-coverage corresponds to an overall hydrogen coverage which is 6.25 % higher than the given O-H *pre-coverage*, and it is always referred to the work function of the *pristine* ZnO(1010) surface. In the theoretical case of exclusive O-H bond formation, we compute a work function change of up to  $\Delta\Phi = -2.5$  eV, which corresponds to an overall O-H coverage of 56.25 %. However, in experiment this maximum theoretical  $\Delta\Phi$  cannot possibly be achieved, because Zn-H bond formation sets in well before the O-H coverage can reach such high values, as described above. We expect the stabilization of  $\Phi$  by the formation of a complex adsorption pattern of O-H and Zn-H bonds for coverages around and above 18% (see red dotted line in Fig. IV.11). This stabilization can be illustrated

quantitatively by considering the effect of a first Zn–H bond on the overall work function (blue circles). Remarkably, the difference in  $\Delta\Phi$  between H adsorption on a surface Zn vs. a surface O is as large as 1 eV in case of a 18% O–H pre-coverage, and the resulting  $\Delta\Phi = -0.95$  eV is on the same order as the experimentally determined  $\Delta\Phi_{\max} = -0.65$  eV.

Clearly, the suggested stabilization of the work function involves the formation of more than only one single Zn–H bond for coverages above 18%. As a consequence, the corresponding calculated  $\Delta\Phi$  for *realistic* mixed coverages is expected to be much closer to the experimentally determined value compared to the calculations for the hypothetical adsorption patterns shown in Fig. IV.11(b).

Although these calculations and their underlying adsorption model do not allow us to identify the exact surface structure and conformation under experimental conditions, the theoretical work unambiguously shows that the O–H monolayer does *not* complete before the Zn–H monolayer starts forming. Rather, the results indicate that both adsorption sites compete for hydrogen adsorption, which is expected to lead to a complex equilibrium between the O–H and Zn–H (sub)monolayers.

Summing up, this suggests that exposure of a pristine ZnO(10 $\bar{1}$ 0) surface to hydrogen leads, at first, to the formation of O–H-bonds along with a work function reduction and CAL formation. Further dosing of H increasingly favors the formation of Zn–H-bonds, which results in a complex adsorption behavior and a mixed adsorption pattern, which is reflected in the change of slope of the experimentally determined  $\Delta\Phi$  below 100 L. It should be noted that the experimentally determined rather moderate shift of the work function leading to saturation at  $\Delta\Phi_{\max} = -0.65(5)$  eV [see Fig. IV.11(b)] refers to the first  $\Phi_{\text{ini}}$  measured after surface preparation. Because of the slow cooling process of our sample we expect the initially measured work function  $\Phi_{\text{ini}}$  to be slightly lower than the work function of the ideal pristine surface  $\Phi_{\text{pristine}}$  and hence  $\Delta\Phi_{\text{exp}} < \Delta\Phi_{\text{theo}}$ , which is in accordance with the experimentally and theoretically determined values.

## 2.4 The Localized Character of the Hydrogen-Induced Potential Changes

As mentioned above, the properties and the functionality of interfaces between ZnO and molecular adlayers may strongly depend on the local, microscopic electronic structure. In the previous section, it was shown that hydrogen, due to its amphoteric character, acts as both electron donor and acceptor, depending on whether it forms an O–H or a Zn–H bond. As a consequence, these two types of bonds should lead to a significantly different change to the surface potential  $\Delta U$ , which is reflected in their different effect on the work function. Since both bonds are energetically expected to be located in very close proximity, the resulting  $\Delta U$  should exhibit strong variations on a microscopic scale. A complete picture of the H-induced changes at the ZnO(10 $\bar{1}$ 0) surface therefore requires a *microscopic* description of the changes to the electrostatic potential  $U$ . As a first step, the change of  $U$  is calculated as

$$\Delta U(x,y,z) = U^{\text{ZnO+H}}(x,y,z) - \left( U^{\text{ZnO}}(x,y,z) + U^{\text{H}}(x,y,z) \right) \quad (\text{IV.3})$$

where  $U^{\text{ZnO+H}}$  is the potential of the ZnO surface with adsorbed hydrogen,  $U^{\text{ZnO}}$  the surface without adsorbed hydrogen, and  $U^{\text{H}}$  the potential of a hypothetical, free-standing hydrogen

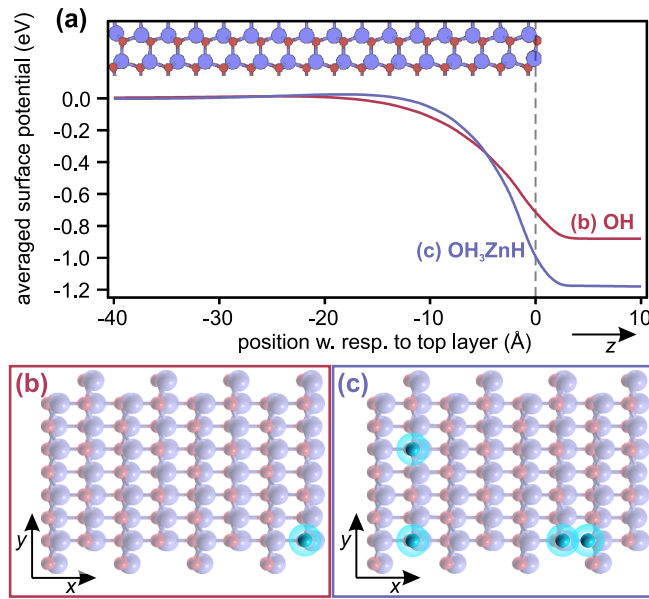


**Figure IV.12:** (a) Plane-averaged potential change at the ZnO( $10\bar{1}0$ ) surface for two different coverage geometries: a single O–H bond [red curve, (b)] and three O–H bonds and a single Zn–H bond [violet curve, (c)] per  $4 \times 4$  supercell. The location of adsorbed H is highlighted by markers in (b), (c).

layer in the same geometry as the adsorbed hydrogen atoms. The potential was calculated on a regular grid with a grid spacing of  $0.1 \text{ \AA}$  in each direction.

#### 2.4.1 Calculation of the Average Change $\Delta U$ along the $z$ -Axis

The resulting  $\Delta U$  is shown in Fig. IV.12(a) along the surface normal for two different adsorption geometries: First, OH with a single hydrogen in a  $(4 \times 4)$  supercell that is adsorbed on an oxygen atom [corresponding to a coverage of 6.25%, (red curve)], and second,  $\text{OH}_3\text{ZnH}$  which contains 3 O–H and one Zn–H bond (violet curve). The corresponding adsorption geometries are depicted in Fig. IV.12(b) and (c). The latter corresponds to a first Zn–H bond on a surface with 18.75% O–H pre-coverage and it is thus consistent with our previous calculations. For the sake of simplicity, here we averaged the potential in the  $x$  and  $y$  directions.

For both adsorption geometries, the calculated  $\Delta U$ , i.e., the H-induced downward band bending, is on the order of 1 eV. This value is comparable to earlier calculations of band bending magnitudes which were based on a simple electrostatic model [EMG76]. It is also consistent with the spectral width of the CAL peak [see Fig. IV.9(a)]. Remarkably, even for a coverage of only one hydrogen atom per 16 surface sites the band bending is already very pronounced. The increase in the number of adsorbed hydrogen atoms for the  $\text{OH}_3\text{ZnH}$  geometry then leads to a 0.3 eV higher magnitude of the bending and a further narrowing of the surface potential well.

Notably, in both cases the potential changes extend less than  $20 \text{ \AA}$  into the ZnO bulk, which makes them strongly localized along the surface normal compared to surface charge accumulation layer depths in conventional semiconductors such as GaAs or Si [KKK76, CNS<sup>+</sup>89].

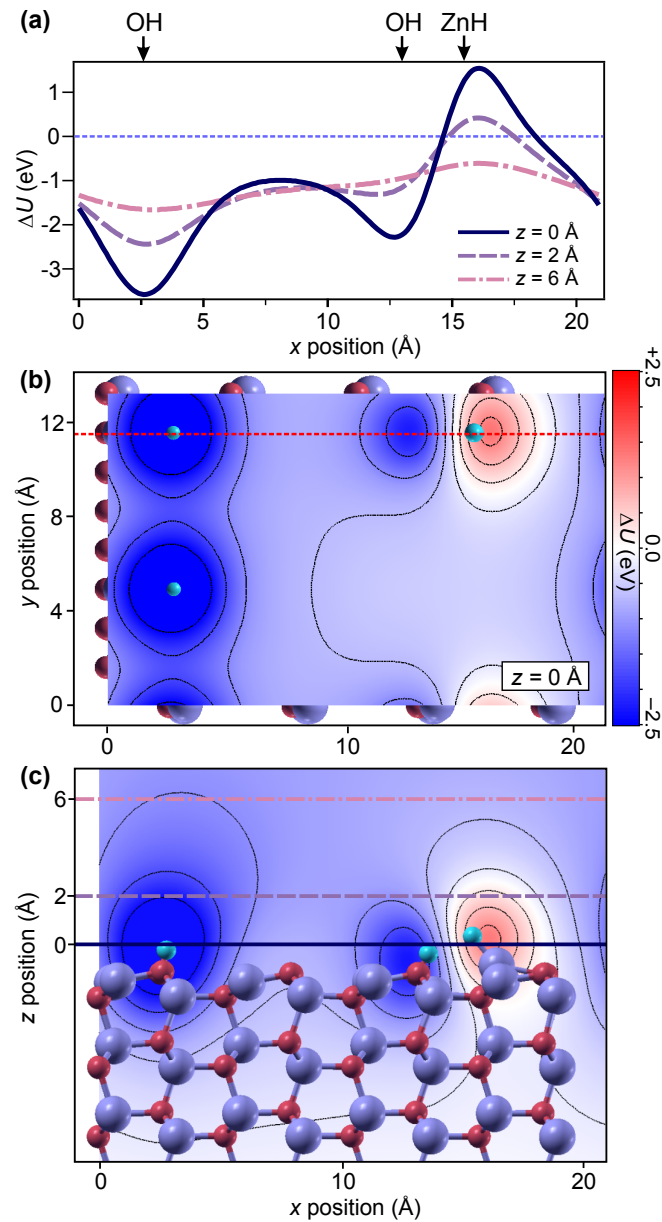


**Figure IV.13:** Hydrogen adsorption induced potential change,  $\Delta U$ , for  $\text{OH}_3\text{ZnH}_1$  adsorption geometry. (a) Dependence along the red dotted line indicated in (b) for different distances from the surface.  $z = 0$  Å corresponds to the line shown in (c). (b)  $\Delta U$  in false colors along the  $(x-y)$ -plane at  $z = 0$  Å. (c)  $\Delta U$  shown for the  $(x-z)$ -plane cut along the line indicated in (b). Isolines are drawn at 0.5 eV increments of  $\Delta U$ .

The strong confinement of the  $\text{OH}_3\text{ZnH}$  geometry leads to a band bending that extends only across the first four  $\text{ZnO}(10\bar{1}0)$  layers. To our knowledge, this is the first DFT calculation of the strongly confined surface downward band bending in such a material. It, thus, represents

the first quantitative and microscopic confirmation of the established qualitative view of the strong charge accumulation layer in  $n$ -type materials (cf. Fig. IV.8) [Lüt10]. Considering, that Ozawa and Mase conclude a maximum area surface charge density of  $1.0(2) \times 10^{13} \text{ cm}^{-2}$  for the hydrogen-doped ZnO(10 $\bar{1}$ 0) surface (cf. Section 2.4.4), confining this area density to a 1 nm thin layer results in a volume charge carrier density of  $N_{\text{ZnO}}^{\text{max}} = 1.0(2) \times 10^{20} \text{ cm}^{-3}$ .  $N_{\text{ZnO}}^{\text{max}}$  is much closer to charge carrier densities of typical metals which are on the order of  $10^{22} \text{ cm}^{-3}$  compared to the densities found for typical semiconductors.<sup>8</sup>

### 2.4.2 A Microscopic View on the Strong Lateral Potential Variations

Apart from the laterally averaged changes to the surface potential, we computed the three-dimensional changes of  $U$  with respect to the pristine ZnO(10 $\bar{1}$ 0) surface for the adsorption geometries displayed in Fig. IV.12(b,c). Hence, our DFT calculations also provide a detailed description of the *lateral* structure of H-induced modifications to the surface potential energy landscape. Figures IV.13(b) and (c) show the H-induced potential changes for the OH<sub>3</sub>ZnH adsorption geometry in the ( $x$ - $y$ )-plane at  $z = 0 \text{ \AA}$  and in the ( $x$ - $z$ )-plane, respectively. It is shown that O–H bonds lead to a pronounced reduction of  $U$  (blue) which laterally extends over roughly 5 nm. This behavior is nearly identical to the  $\Delta U$  caused by the lone O–H bond in the OH adsorption geometry (not shown). The Zn–H-induced *increase* of the potential (red) exhibits a similarly localized character. As a consequence,  $\Delta U$  is close to zero everywhere else.

Figure IV.13(a) shows  $\Delta U$  along a line that is crossing an O–H site and a neighboring pair of O–H and Zn–H adsorption sites for different distances  $z$  from the surface, as indicated in the top and side view [Fig. IV.13(b,c)]. The definition of  $z = 0 \text{ \AA}$  is shown in (c). It should be noted that  $z = 0 \text{ \AA}$  corresponds to a position slightly above the final ZnO layer and thus roughly agrees with the position of further possible adsorbates. At  $z = 0 \text{ \AA}$ ,  $\Delta U$  is strongly corrugated, varying between  $-3.58 \text{ eV}$  at the single O–H bond and  $+1.54 \text{ eV}$  at the Zn–H bond. Again, the counteracting character of O–H and Zn–H bonds becomes directly visible. As expected, for an excess of O–H bonds, and already shown in Fig. IV.12, the average  $\Delta U$  is negative for this geometry. Moving away from the surface, the corrugation of  $\Delta U$  is smoothed, which can also be seen in Fig. IV.13(c). This smeared out  $\Delta U$  is what, at even larger distances (30  $\text{\AA}$ ), defines the work function change  $\Delta\Phi$  [cf. Fig. IV.11(b)].

The microscopic perspective on the surface potential modifications obtained from the calculations reveals that, in the low coverage regime, changes to the surface electronic structure are strongly localized both laterally and along the  $z$ -axis. This corroborates our experimental finding that the intensity of the CAL peak is increasing upon H adsorption without a distinct change of its spectral shape. During the initial stages of H adsorption, the predominant formation of O–H bonds creates *localized* and independent metallic sites, supposedly by partially filling the conduction band Zn4s states which are shifted below  $E_F$ . The accumulation of these potential wells then leads to the experimentally observed increase of the CAL peak [cf. Fig. IV.29(b,c)].

The spatial extent of these wells, which are confined laterally within  $\approx 5 \text{ nm}$ , indicates at which coverages a *delocalization* of charges within the CAL is to be expected. As can be seen

<sup>8</sup>Intrinsic charge carrier densities in semiconductors are well below  $10^{15} \text{ cm}^{-3}$  at room temperature and can, of course, be strongly enhanced by doping.

in Fig. IV.13, at an O–H coverage of 18 %, the potential wells partially start to overlap. An increase of the O–H coverage to 25 % and beyond would clearly lead to significant overlap and a generally delocalized character of the reduced potential. It should be noted, however, that at these coverages, the formation of Zn–H bonds has already become favorable (cf. Fig. IV.11), which suggests that the occurrence of a laterally delocalized CAL roughly coincides with the beginning of a mixed adsorption geometry.

An *experimental* analysis of the localized character of the potential changes requires a probe with a spatial sensitivity of a few nanometers. This spatial resolution cannot be reached directly because of the laser spot size on the order of 60  $\mu\text{m}$ . However, the spectroscopy of a highly localized species which is exposed to the potential changes can reveal the desired spatial information. This species, which will be characterized in detail in Section 3.2.2, is the **surface exciton (SX)**. By analyzing the intensity of the SX signature for varying hydrogen dosages the above-mentioned findings on the degree of localization of the potential changes will be further substantiated.

Another possibility to experimentally investigate the (de)localized character of the potential changes is the analysis of the spectroscopic signature of the CAL itself. In the next section it will be demonstrated that the slight energetic shift of the CAL signature at dosages between 50 and 150 L further corroborates the transition of the potential changes from localized to delocalized characteristics in this coverage regime.

### 2.4.3 Quantized Subbands in the Surface Potential Well?

The suggested delocalization process for O–H coverages above  $\approx 25\%$  can be pictured as a transition from approximately zero-dimensional dot-like potential wells to a two-dimensional well. This process is described by the established view of homogeneous band bending at the surface [see sketches of both cases in Fig. IV.14(a)]. One may now ask, whether this change in the electron-confining potential has an effect on the energy spectrum of the CAL signature. Generally, a reduction of the confinement that is expected to happen during the transition to the two-dimensional case results in a lowering of the energy  $\varepsilon_i$  of the subbands.

Thus, it is worth examining the energetic position of the CAL signature as a function of hydrogen dosage. This position supposedly corresponds to the energy  $\varepsilon_0$  of the lowest energy subband state in a potential well (see below). Figure IV.14(b) shows the dosage-dependent position as determined by fitting a Gaussian function, with a different **full width at half maximum (FWHM)** for each side of the peak, to the spectra after subtraction of the secondary electron background. An exemplary fit after multiplication with a Fermi-Dirac distribution is shown in the inset. Remarkably, the overall, shift of the peak is comparably small with  $\approx -35$  meV for hydrogen dosages from 0 L to 500 L. This small shift is consistent with the alleged absence of a gradual, homogeneous downward bending of the CB with increasing hydrogen dosage. Instead, the potential wells appear to have similar characteristics for a wide range of dosages. Upon closer inspection of the data, it becomes visible that there are two different regimes of the energetic position. For dosages up to  $\approx 100$  L the position is slowly shifting, but reaches a constant value of  $\approx -170$  meV for higher dosages. Interestingly, dosages on the order of 100 L to 150 L most probably correspond to O–H coverages on the order of 25 %, as for these dosages formation of Zn–H bonds has just set in which corresponds to a coverage of  $\approx 18\%$ . The data

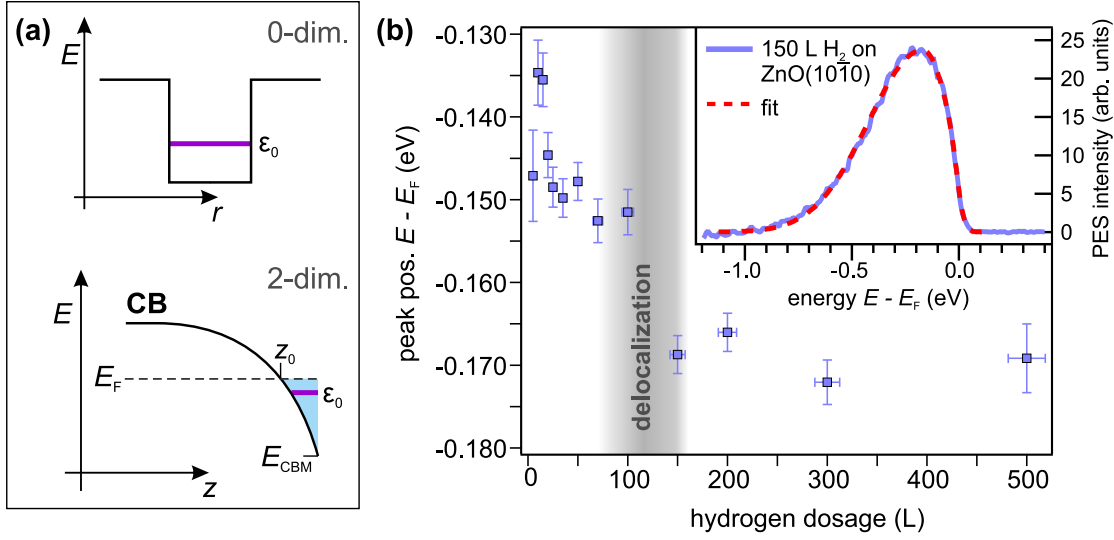


**Figure IV.14:** (a) Schematic representations of the zero-dimensional and the two-dimensional potential wells (see text). In case of the approximately triangular potential well formed by the CBM, the energetic position of the lowest energy quantized subband  $\epsilon_0$  is given by the magnitude and spatial extent of the band bending. (b) Position of the CAL peak maximum derived from a Gaussian fit to the background-corrected data. An exemplary fit is shown in the inset. The data shows a weak shift ( $\Delta E \approx -35$  meV) of the peak maximum for  $H_2$  dosages up to 150 L and a constant position for higher dosages.

thus suggests that at these coverages indeed a change in the character of the potential wells occurs which may be associated with a higher degree of delocalization. On the other hand, the relatively weak shift of the CAL signature during the first 50 L indicates that there is very little change happening to the actual band bending, despite the fact that the major shift of the work function happens exactly in this coverage regime [(see Fig. IV.9(b)]. Additionally, the strong increase of the CAL signature [cf. Fig. IV.9(a)] without a distinct change of the spectral shape hints at an *additive* buildup of the CAL from constituents with identical characteristics which scales with the amount of adsorbed hydrogen atoms.

In case of high hydrogen coverages, where the CAL might actually be best described by the established band bending picture, it is possible to estimate the energetic position of the subband states inside the two-dimensional potential well [cf. [Fig. IV.14(a)]. Within the two-dimensional well one would expect the electronic states to form quantized subbands with energetic positions according to the shape of the potential (for a detailed discussion, see Ref. [Lüt10]). The exact solution of the Schrödinger equation for subband states  $i = 1, 2, 3, \dots$  in such a triangular well is given as

$$\epsilon_i = \left(\frac{3}{4}he\right)^{(2/3)} \frac{|\mathcal{E}_{sc}|^{(2/3)}}{(2m_{\perp}^*)^{(1/3)}} \left(i + \frac{3}{4}\right)^{(2/3)}, \quad i = 0, 1, 2, 3, \dots \quad (\text{IV.4})$$

with the space charge field  $\mathcal{E}_{sc} = E_{CBM}/z_0$ , the elementary charge  $e$ , and the principal effective mass normal to the surface  $m_{\perp}^*$ . Thus, it is possible to estimate the energetic positions  $\epsilon_i$  of the subband states relative to the CBM only if the shape of the CBM, i.e.  $\mathcal{E}_{sc}$ , is known. From the

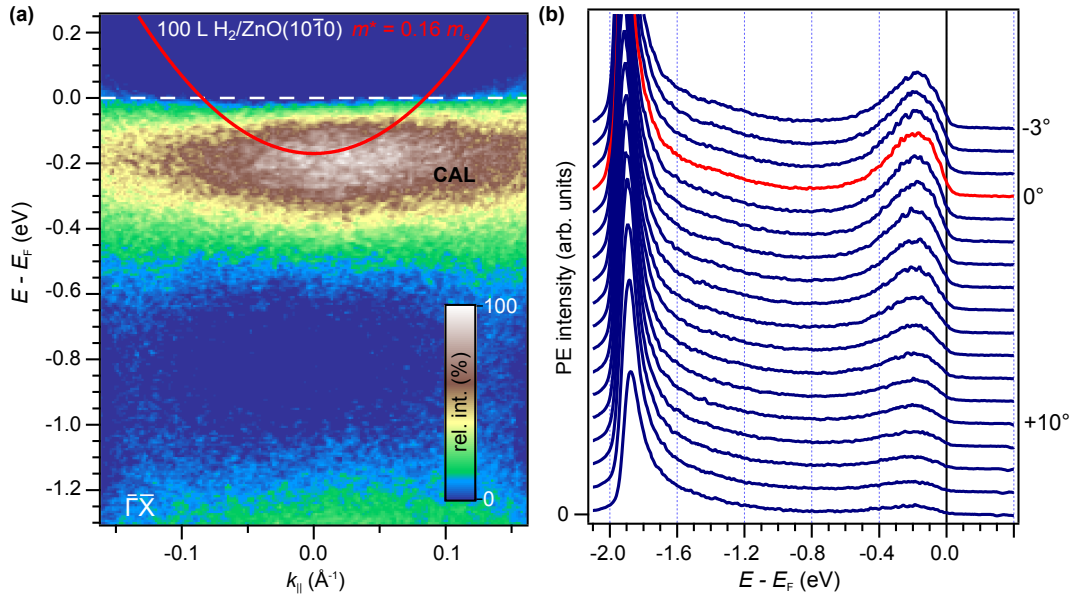


**Figure IV.15:** (a) Angle-resolved spectrum of the CAL signature of the  $\text{ZnO}(10\bar{1}0)$  surface after exposure to a 100 L dosage of hydrogen. The maximum intensity is found at the  $\bar{\Gamma}$  point. The photoelectrons are detected along the  $\bar{\Gamma}\bar{X}$  axis of the crystal. The red solid line represents the dispersion of a nearly free electron-like state with an effective mass of  $m^* = 0.16m_e$ . (b) Angle-dependent energy distribution curves (EDCs) also show the photoelectron intensity distribution for a range of emission angles.

DFT calculations of the hydrogen-induced potential changes (for details, see Fig. IV.12) a value of  $\mathcal{E}_{sc}$  on the order of  $10^7 \text{ V cm}^{-1}$  can be estimated, which corresponds to a CBM that is 1 eV below  $E_F$  at the surface. With an effective mass of  $m_1^* = 0.28$  [Eli01] the energetic position of  $\varepsilon_0$  is on the order of 1 eV above the CBM bottom at the surface. This means that the lowest subband is energetically located very close to the Fermi level, as it is observed in experiment. Only this single bound subband state should occur: Due to the extraordinarily high space charge field  $\mathcal{E}_{sc}$  in the CAL the next higher subband lies at  $\varepsilon_1 \approx 2 \text{ eV}$  which is well above the bulk CBM and, thus, outside of the potential well. Thus, the energetic position of the CAL signature is generally consistent with the band bending parameters that result from the DFT calculations (see Fig. IV.12).

#### 2.4.4 Angular Dependence of the CAL Signature at the $(10\bar{1}0)$ Surface

The degree of (de)localization can further be inferred from the dispersion  $E_{k_{\parallel}}$  of an electronic state. In case of the formation of a delocalized free electron-like state one would expect to observe a band with a parabolic dispersion, as sketched in Fig. II.18(a). A corresponding measurement for a hydrogen coverage of 100 L on  $\text{ZnO}(10\bar{1}0)$  is depicted in Figure IV.15(a). The two-dimensional intensity distribution shown in (a) was recorded with the wide angle mode of the electron analyzer and covers emission angles of up to  $15^\circ$ . In (b) the corresponding EDCs with respect to the emission angle are shown. The intensity distribution of the CAL signature reflects the shape of the CBM with its maximum at the  $\bar{\Gamma}$  point (cf. Fig. II.13). These spectral representations of

the CAL bear close resemblance to those measured by Ozawa and Mase [OM11].

In case of the formation of a delocalized free electron-like state one would expect to observe a band with a parabolic dispersion, as sketched in Fig. II.18(a). However, fitting the CAL signature with the procedure described in the previous section yields *no* angular dependence for the energetic position, i.e., a flat dispersion indicative of laterally localized states. This finding holds true for all examined hydrogen dosages from 100 L to 200 L. Interestingly, this is in contrast to the measurements of Ozawa and Mase, who derived a parabolic dispersion of the CAL signature that corresponds to an effective electron mass  $m^*/m_e$  of 0.16(5) using a fitting procedure where the Fermi cutoff was “eliminated” by dividing the whole spectrum by a suitably widened Fermi-Dirac distribution. The resulting parabola is added to Fig. IV.15 as a red solid line, and it clearly does not represent our data. Still, one may argue that the analysis of an energetically broad and weakly dispersing state which is located very close to the Fermi level is at least challenging. The raw data shown by Ozawa and Mase show the dispersion much less clearly than the fit results suggest.

Furthermore, it is still possible that despite the suggested overlap of the potential wells for dosages of  $\approx 100$  L the majority of the electrons in the CAL is still localized, so that the purported two-dimensional electron gas at the ZnO(10 $\bar{1}$ ) surface does not exhibit a perfectly delocalized character. This idea is corroborated by the fact that hydrogen has the tendency to etch ZnO surface and, thereby, induces surface defects [OM11] (see Section 2.4.5). On a rough, defect-rich surface the translational symmetry is reduced and, as a consequence,  $k_{\parallel}$  is no longer a good quantum number [OM11]. Thus, the suggested roughening of the ZnO(10 $\bar{1}$ ) surface may be a reason for the hard-to-detect dispersion of the CAL state, since the formation of a standing wave within the potential well is partly suppressed.

The inconclusiveness of these results calls for further angle-resolved photoemission studies of zinc oxide with adsorbed hydrogen surfaces that use light sources with higher photon energies and lower bandwidth, such as UPS.

#### 2.4.5 The High Coverage Regime: Band Gap Reopening and Surface Etching

For even higher hydrogen coverages well above 200 L we expect a significant difference between the adsorption patterns that are considered in the DFT calculations and the actual situation in the experiment. This is, because high hydrogen coverages were shown to lead to drastic changes in the surface geometric structure of various ZnO surfaces [Wöl07] that cannot be accounted for in our model adsorption geometries. Diffusion of hydrogen into the ZnO bulk may increase defects and lead to substantial changes in the (near-)surface electronic structure [WGB06]. Eventually, this means that at these high hydrogen dosages the surface will start to differ significantly from the ideal bulk-truncated structure. In particular, it was found for the Zn-terminated ZnO surface that hydrogen at high dosages forms bonds with initially sub-surface O atoms, indicating a complex reconstruction behavior at this surface. This restructuring is suggested as the main stabilization mechanism for the Zn-terminated surface [BHK<sup>+</sup>01, DDK03].

What is found in experiment for hydrogen dosages above 200 L on the mixed-terminated surface is a *reduction* of the intensity of the CAL, as shown in Fig. IV.9(b). This behavior is consistent with the experimental study by Ozawa and Mase [OM11] who also observed a maximum intensity for a dosage of 200 L and a subsequent intensity reduction.

There exist different explanations for this behavior in literature. The loss of metallic character can be associated with the re-opening of the band gap and the restoration of the semiconducting state. If one assumes a bulk-truncated ZnO(10 $\bar{1}$ 0) surface with hydrogen adsorbed on all surface O and Zn atoms the DFT calculation do indeed show this gap re-opening. An intuitive explanation for this behavior, as given in Ref. [W<sup>MY</sup>+05] is that the even number of additional electrons per surface unit cell leads to the complete filling of electronic states which suppresses the previous metallic character that occurs when only O–H bonds are formed and only one electron is added to the surface unit cell.

Experimentally, however, we never observe a complete quenching of the CAL, even for H<sub>2</sub> exposures up to 500 L. This inability to return to a truly semiconducting surface is concordant with the previous study which reports a weak but present signature at a dosage as high as  $2 \times 10^4$  L [OM11]. The reason for this might be the complex surface stoichiometry induced by surface etching which is not covered by the calculations, which results in a preservation of metallic character for parts of the surface. It is further still possible that a complete saturation of all surface O and Zn sites does actually occur for the conditions in our experiments, due to energetic restrictions. Further, both experimental and theoretical studies of the high hydrogen coverage regime at different ZnO surface terminations are, thus, highly desirable.

## 2.5 Hydrogen-Induced Metallization at the (000 $\bar{1}$ ) Surface

The unique effect of a competition between the O–H and the Zn–H bonds can – in principle – not occur on the oxygen-terminated surface. Instead, it can be expected that only effects related to the formation of O–H bonds are observed. In Section 1.2 it was suggested that the pristine (000 $\bar{1}$ ) surface is more reactive with respect to residual gases compared to the mixed-terminated surface, and that the unintentional adsorption leads to donor-type states at the surface. The resulting effects, especially regarding the formation of a CAL when hydrogen is adsorbed are qualitatively identical to those observed at the (10 $\bar{1}$ 0) surface, as was reported by Ozawa and Mase [OM11] (cf. Section 6.4.1 of Chapter II). Hence, also the ZnO(000 $\bar{1}$ ) can be rendered metallic by hydrogen adsorption. This section compares the hydrogen-induced effects between the (000 $\bar{1}$ ) and (10 $\bar{1}$ 0) surfaces quantitatively in order to further clarify the processes that occur at these surfaces.

As before, hydrogen was dosed by backfilling the UHV system with H<sub>2</sub> which was partially dissociated using a glowing tungsten filament (see Section 2.1). The intensity of the CAL and the work function were then measured using  $h\nu = 6.19$  eV photons.

Figure IV.16(a) shows an exemplary spectrum of the ZnO(000 $\bar{1}$ ) surface for a hydrogen dosage of 96 L. The work function has been reduced by  $\Delta\Phi \approx -0.9$  eV to  $\Phi = 4.3$  eV and occupied electronic states which are attributed to CAL formation appear below  $E_F$ , which is in accordance with literature. Additionally, there is another occupied electronic state which appears clearly at a binding energy of  $\approx 1.4$  eV after subtraction of the secondary electron background. This state, which is formed within the band gap of ZnO, probably originates from defects, such as oxygen vacancies  $V_O$  and missing OH groups  $V_{OH}$ . In such vacancies, electrons can be captured and thus bound with a characteristic binding energy. The well-known  $V_O$  and  $V_{OH}$  defects, which play an important role as F centers in catalytic processes, are located  $\approx 1.6$  eV below

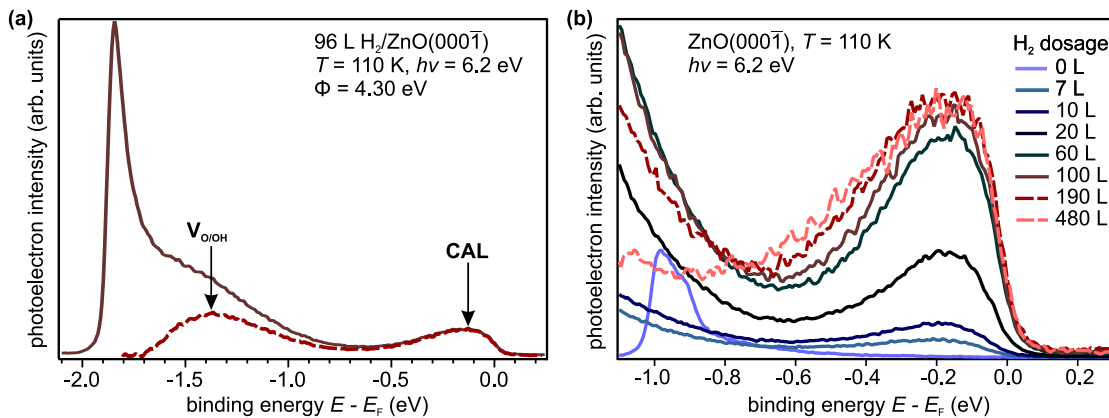


**Figure IV.16:** PES of the hydrogen-covered ZnO(000 $\bar{1}$ ) surface for various dosages. (a) Exemplary spectrum for a hydrogen dosage of 96 L. Apart from the CAL signature an in-gap state  $V_{O/OH}$  occurs  $\approx 1.4$  eV below  $E_F$  which is attributed to oxygen vacancies. (b) The CAL signature for hydrogen dosages from 0 L to 480 L. In analogy to the mixed-terminated surface, the signal is strongly enhanced by hydrogen adsorption. Modified from Ref. [Ric14].

the CBM according to DFT calculations [Fin06]. Thus, the observed feature in our spectrum agrees reasonably well with the calculations. Please note that under certain circumstances at mixed-terminated surface an occupied state at the same binding energy can be observed (not shown). Its significantly lower intensity can be attributed to the higher stability and lower density of oxygen atoms at the (10 $\bar{1}0$ ) surface, which reduces the formation probability of  $V_O$  and  $V_{OH}$  defects.

The CAL intensity at the ZnO(000 $\bar{1}$ ) surface for hydrogen dosages from 0 L to 480 L is depicted in Fig. IV.16(b). The increase of the signal intensity for higher hydrogen dosages occurs analogously to the mixed-terminated surface [see Fig. IV.9(a)]. This can be seen in Fig. IV.17 where dosage-dependent CAL intensities and work functions are compared. For dosages up to  $\approx 50$  L the intensity increases linearly at both surfaces. However, there is clearly no comparable signal reduction observed in case of the oxygen-terminated surface for very high dosages approaching 1000 L.

The comparison of the work function changes shows that both are significantly reduced for dosages below 50 L and, despite the strongly differing  $\Phi$  of the pristine surfaces, they saturate at a similar value with a minimal work function of the (000 $\bar{1}$ ) surface of  $\Phi_{\min} \approx 3.6$  eV.

Comparing the hydrogen-induced effects at the two surfaces corroborates the finding of the decisive role of the O–H bond for the surface electronic structure of ZnO, which will be explained in the following. Regarding the surface stoichiometry, the oxygen-terminated surface exhibits no surface Zn atoms and almost double the amount of oxygen atoms per unit surface (see Fig. II.12).<sup>9</sup> Thus, one would intuitively expect that in case of a saturation of all O–H bonds at both surfaces, the work function reduction at the (000 $\bar{1}$ ) surface is roughly twice as strong as the reduction observed at the (10 $\bar{1}0$ ) surface. As Fig. IV.17 demonstrates, this is indeed the case

<sup>9</sup>The comparison of the density of surface oxygen atoms  $\rho^O$  between the two unreconstructed surfaces gives  $\rho_{(000\bar{1})}^O = 1.85\rho_{(10\bar{1}0)}^O$ .

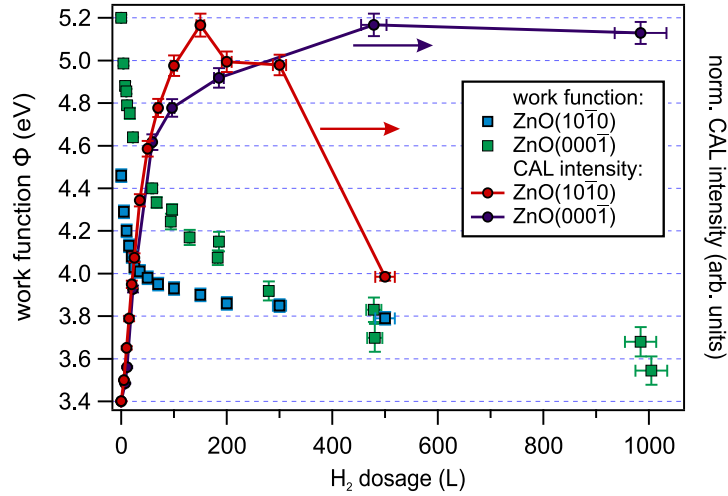


**Figure IV.17:** Comparison of the hydrogen-induced work function change and intensity of the CAL signature between the  $(10\bar{1}0)$  and  $(000\bar{1})$  surfaces of ZnO. Modified from Ref. [Ric14].

with  $\Delta\Phi_{(10\bar{1}0)} \approx -0.7$  eV and  $\Delta\Phi_{(000\bar{1})} \approx -1.8$  eV. However, the shift is even stronger than what is implied by this naive model. This may be due to the fact, that the adsorption energies have not been considered. As shown before, the formation of Zn–H bonds at the mixed-terminated surface has a strong effect on the work function, effectively compensating for the O–H-induced reduction. This can be a reason for the stronger than expected work function reduction at the oxygen-terminated surface.

The comparison between the hydrogen-induced effects at the mixed- and oxygen-terminated surfaces of ZnO further substantiates the previous findings on the role of surface Zn–H and O–H bonds: (i) When no surface Zn atoms are present there is no reduction of the CAL signature. (ii) For the surface termination with an approximately twice as high surface density of oxygen atoms, the hydrogen-induced work function shift is stronger by a factor of  $\approx 2.6$ . This is clearly consistent with the assumption that O–H bond formation causes electron donation into the ZnO and results in the reduction of the work function and the formation of the CAL, whereas Zn–H bonds counteract both these defects, because in this bond hydrogen acts as electron acceptor.

## 2.6 Conclusion

The focus of this section was the presentation of the detailed microscopic view of hydrogen adsorbed on the mixed- and oxygen-terminated surfaces. Therewith, it also provided a general understanding of the ZnO surface electronic structure which can serve as solid foundation for the following experiments of electron and quasiparticle dynamics at ZnO surfaces and interfaces. The findings presented here go beyond the established view of the **charge accumulation layer (CAL)** as a macroscopic area-averaged entity. Our comprehensive model of the CAL has been developed using surface-sensitive photoemission experiments in conjunction with DFT calculations and the presented results underline the significant influence of hydrogen adsorbed on ZnO surfaces on the surface electronic structure and possibly the excited state dynamics

on a microscopic level. In case of low hydrogen dosages, the highly localized character of the potential changes  $\Delta U$  has to be considered when energy level alignment and electronic coupling across a hybrid interface are discussed. Here, adsorbed hydrogen may lead to laterally inhomogeneous surface properties.

Nevertheless, adsorbed hydrogen does not only increase the complexity of ZnO surfaces, but it can possibly be used to intentionally tune the surface properties, particularly the surface conductivity and electronic band positions. The significance of hydrogen doping is illustrated by the high attainable charge carrier densities of  $\approx 1 \times 10^{20} \text{ cm}^{-3}$  at the ZnO(10 $\bar{1}$ 0) and (000 $\bar{1}$ ) surfaces, which are confined within the few nanometers thin surface layer.

It was clearly shown that the mechanism behind the hydrogen-induced changes, work function reduction and metallisation, originates from the O–H bond where hydrogen acts as electron donor and forms the positively charged end of a surface dipole. Using this mechanism, the work function of the mixed-terminated surface can be reduced from 4.5 eV to 3.8 eV, whereas at the oxygen-terminated surface a reduction from 5.2 eV to 3.6 eV is possible. It is noteworthy, that the surface properties in our experiments can be controlled in a highly reproducible and stable manner, which is an ideal starting point for further experiments focusing on charge carrier dynamics and increasingly complex interfaces. The observed instabilities and shifts of work function and band edge positions for the pristine surface most probably originate from the unintentional adsorption of residual hydrogen. The inconsistencies regarding these characteristics which can be found in literature might thus be related to this unintentional adsorption of residual hydrogen or water.

The next question is, if and how the – intentionally tunable – surface properties of ZnO influence the *dynamics* of excited states. Especially the strongly varying charge density at the ZnO surface and the precisely confined band banding may have a significant influence on the Coulomb-mediated interactions between charge carriers and excitonic quasiparticles. Thus, the dynamics of hot electron relaxation, e.g., due to the changes in electrostatic screening (see Section 7 of Chapter II).



### 3 Electron and Quasiparticle Dynamics at the ZnO Surface

The previous section presented a comprehensive description of the *static* electronic properties of the ZnO(10 $\bar{1}$ 0) surface. This sets a solid basis for the investigation of *dynamic* processes such as the relaxation of excited charge carriers at the surface. The understanding of these processes is of utmost importance for the functionality of HIOS devices, because all relevant interfacial processes such as charge or energy transfer involve *excited* charge carriers, as was discussed in Section 7 of Chapter II. The aim of the experiments is to directly determine the timescales of the energetic relaxation of these species, which contain detailed information about the fundamental scattering processes that occur at the sample surface or interface.

One important class of excited species in semiconductors are excitons. It was shown in Section 7.1.2 of Chapter II that, in ZnO, these do not only occur in the bulk, but that surface-related excitonic species dominate in samples with large surface-to-bulk ratios. These spatially confined species are of special importance for Förster-type energy transfer processes between ZnO nanostructures and its direct surroundings, e.g., adsorbed molecules, because of the strong characteristic  $r^{-6}$  distance dependence of FRET (see Section 5.3.2 of Chapter II). The origin and character of the SX have yet to be fully understood, and particularly the influence of the unique surface electronic structure and CAL formation at ZnO surfaces on the SX have not been examined yet. The interactions between hot electrons, excitons and the tunability of the electron density in the background might enable fundamental insights into the complex many-body processes in such degenerate semiconductor systems.

In this section, the excited charge carrier dynamics of the pristine and hydrogen-covered ZnO(10 $\bar{1}$ 0) surface are examined by femtosecond TR-2PPE experiments. First, Section 3.1 focuses on the ultrafast relaxation of excited electrons in the ZnO CB and the influence of the tunable electron density in the CAL. In Section 3.2 the formation and decay dynamics of the sub-surface bound excitonic species (SX) are discussed in detail. The crucial influence of hydrogen-induced surface modifications is analyzed in detail. An essential part of these findings has been published in Ref. [DWM<sup>+</sup>14]. While this work focuses on the mixed-terminated (10 $\bar{1}$ 0) surface, first experiments which examine the oxygen-terminated (000 $\bar{1}$ ) surface show qualitatively identical results, as discussed in Refs. [Ric14, Bog15].

#### 3.1 Ultrafast Dynamics of Electrons in the ZnO(10 $\bar{1}$ 0) Conduction Band

The relaxation dynamics of free excited carriers in the ZnO conduction band give insight into the interaction of hot electrons with its surroundings. The timescales on which relaxation to the CBM occurs may also determine the efficiency of interfacial charge transfer processes between the ZnO CB and adsorbate states at a hybrid interface. In a first 2PPE study by Tisdale et al. [TMN<sup>+</sup>08] it was found that the relaxation time constants for energies above the bulk CBM are on the order of few ten femtoseconds, which is remarkably short compared to the picosecond dynamics observed in conventional semiconductors, such as silicon [WKS<sup>+</sup>05] (see Section 7.2 of Chapter II). This was attributed to the extraordinarily strong coupling of hot electrons to LO phonons, which is also termed Fröhlich coupling. A recent theoretical study by Zhukov et al. [ZEC10] corroborated the experimental findings, showing that in pristine ZnO the e-ph scattering via LO phonons dominates and leads to the stated ultrashort timescales.

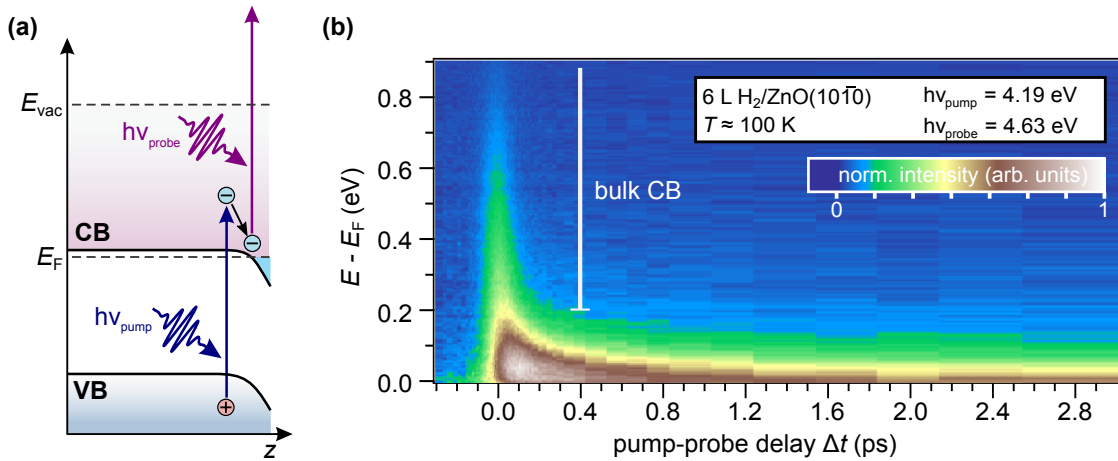


**Figure IV.18:** 2PPE signal showing the ultrafast charge carrier dynamics above  $E_F$  at the  $\text{H}_2/\text{ZnO}(10\bar{1}0)$  surface. (a) Excitation scheme for TR-2PPE experiments of ZnO surfaces. The pump laser pulse excited electrons above the band gap and, thus, creates a non-equilibrium distribution of hot electrons in the ZnO CB which is photoemitted by a subsequent probe pulse. (b) False-color plot of the photoinduced changes to the electronic population at the ZnO surface for energies *above* the Fermi level. It displays the ultrafast charge carrier dynamics in the ZnO( $10\bar{1}0$ ) CB, which occur on a femtosecond timescale for energies above the bulk CBM and slows down significantly at lower excess energies.

What is not addressed in the previous studies is the role of the ZnO surface, in particular the CAL with its possibly high electron densities, which has a drastic effect on the surface electronic structure, as shown in the previous sections. Because the relaxation processes of the excited electrons are mediated via the Coulomb interaction, any variation of the electrostatic screening by tuning the electron density in the CAL may have a significant influence on the relaxation timescales.

The 2PPE excitation scheme that is used to access and analyze the dynamics of hot electrons in the ZnO( $10\bar{1}0$ ) CB is schematically shown in Fig. IV.18(a). Electrons are excited above the band gap by absorption of 4.19 eV photons. The non-equilibrium distribution of electrons in the CB is then probed with the time-delayed probe laser pulse with a photon energy of 4.63 eV. For this experiment, the freshly prepared ZnO sample was exposed to a small dose of 6 L of hydrogen before the measurement of the dynamics. This was done in order to stabilize the surface properties and to reduce the slow shifts that occur because of the adsorption of residual hydrogen (see Section 1.1.3 and Appendix B for more details).

To access and record the population dynamics of the excited states, spectra of the pump-induced changes to the electron distribution are measured for different delays  $\Delta t$ , as explained in Appendix A.2. The result of this procedure is a two-dimensional dataset that can be visualized as demonstrated in Fig. IV.18(b): the photoinduced 2PPE intensity is shown in false colors both with respect to the initial state energy  $E - E_F$  and the pump-probe delay  $\Delta t$ . This representative measurement was carried out with a maximum excitation density of  $1.45 \times 10^{18} \text{ cm}^{-3}$ ,<sup>10</sup> which is *below* the Mott density, i.e., no e-h plasma is expected to form (see Section 5.2.1 of Chapter II).

<sup>10</sup>This corresponds to a laser fluence of  $10 \mu\text{J cm}^{-2}$ .

The sample temperature was held at 100 K during the measurement and the cross correlation between the pump and probe pulses had a temporal width of  $\approx 65$  fs. The resulting maximum charge carrier density in the CAL for those small dosages is on the order of  $1 \times 10^{18} \text{ cm}^{-3}$ , according to Ref. [OM11].

The quantitative analysis of the population dynamics presented in Fig. IV.18(b) can be done by examining the XC traces at different excess energies. Thereby, it is possible to assign characteristic relaxation timescales to certain energetic positions which are one of the keys to unraveling the scattering processes in this system. Figure IV.19(a) shows XC traces for excess energies between 60 meV (dark blue circles) and 650 meV (yellow circles) above  $E_F$ . Additionally, the result from an empirical fitting procedure is shown (solid lines), which accurately reproduces the measured data.

At first glance, these XC traces illustrate the ultrafast character of the relaxation dynamics of the CB electrons. For a quantitative analysis these dynamics were fitted by a double exponential decay

$$I_{XC}(t) \propto A_1 \exp(-t/\tau_1) + A_2 \exp(-t/\tau_2) \quad (\text{IV.5})$$

for delays  $\Delta t > 0$  fs, which is convolved with the laser pulse XC at time zero, i.e.,  $\Delta t = 0$  (green dashed curve). In addition, a single exponential decay towards negative delays includes all processes that are triggered by the reversed pump-probe scheme, i.e., pumped with 4.63 eV and probed with 4.19 eV pulses.

For the decay dynamics ( $\Delta t > 0$  fs) this means that there is a fast component  $\tau_1$  and a slower component  $\tau_2$ . The resulting  $\tau_1$  from the fitting procedure are shown in Fig. IV.19(b) overlaid with a 2PPE spectrum at  $\Delta t = 0$  fs (red curve) illustrating the initial continuous electronic energy distribution induced by the pump pulse. For highly excited electrons, 0.75 eV above  $E_F$ , the decay constant  $\tau_1$  is as low as 10(4) fs. There is a slow increase of  $\tau_1$  towards the bulk CBM, located at 0.2 eV above  $E_F$ , to  $\tau_1 = 74(4)$  fs at  $E = 0.225$  eV. These comparably fast relaxation times, which are among the fastest observed in any semiconductor material [TMN<sup>+</sup>08], can be attributed to the strong Fröhlich coupling between the excited electrons and the LO phonons of the surrounding polar crystal environment, as described in detail in Section 7.2 of Chapter II. Essentially, Fröhlich coupling is the dominant scattering channel in ZnO because of the comparably ionic character of the crystal. Because of this, the LO phonon mode, with its relatively high energy of  $\hbar\omega = 72$  meV, leads to a strong distortion of the electric field, considerably stronger than in case of transversal phonons and acoustic phonons. For other polar semiconductors, such as GaAs and InP, it has been shown that Fröhlich interaction is indeed the dominating scattering mechanism [Noz01, Kit05].

Further validation whether the scattering with LO phonons is indeed the dominant process can be derived from measurements at various temperatures, which are discussed in Section 3.1.1. It should be noted, that the charge density at the small hydrogen dosage of 6 L is not sufficient to assume efficient electron–electron scattering, so that this process may be neglected, as discussed in Section 5.1 of Chapter II.

At excess energies below the bulk CBM, shown as violet and blue circles in Fig IV.19(a), there is a significant increase in relaxation times which reach values of hundreds of femtoseconds. The main reason for this increase of the population lifetimes is the reduction of scattering channels for low excess energies at which the excitation of LO phonons with their energy of

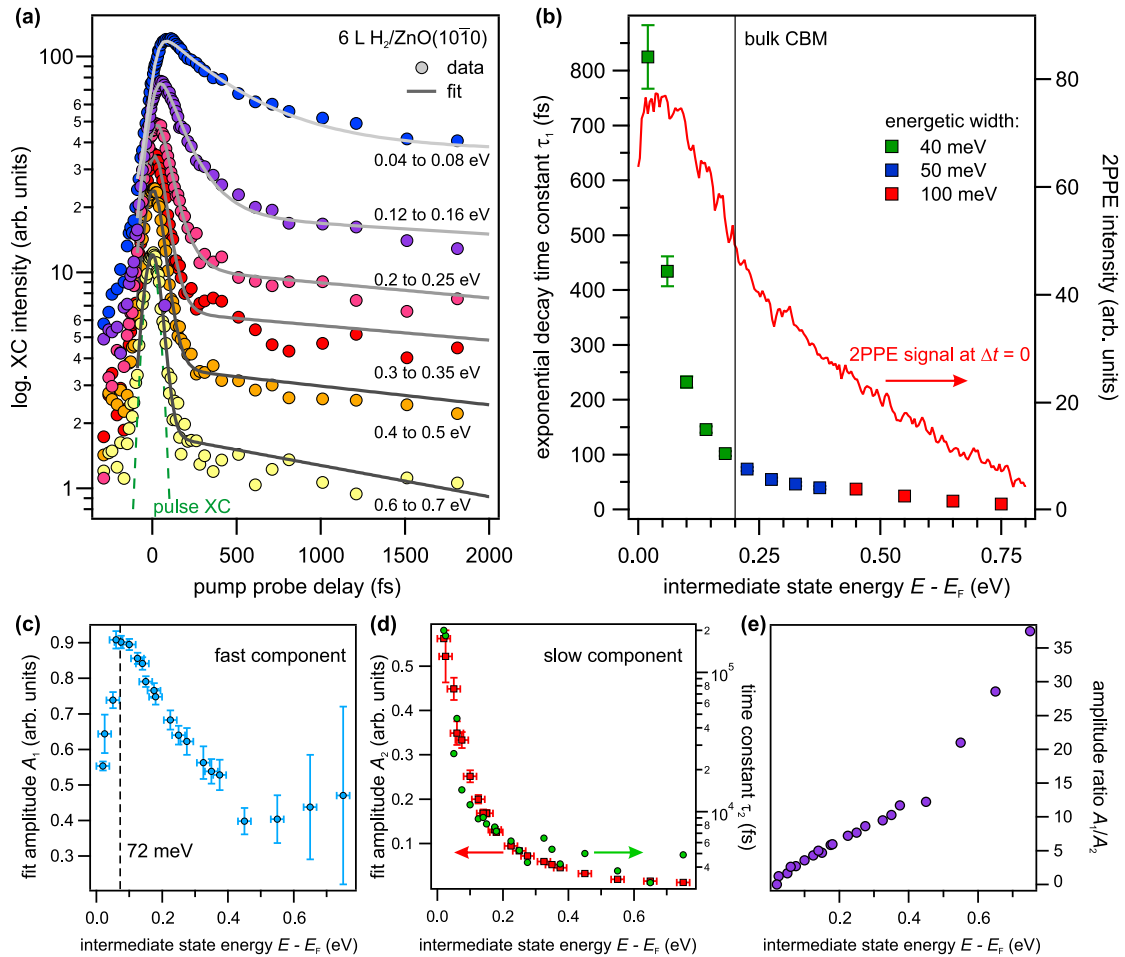


**Figure IV.19:** Detailed overview of the hot electron dynamics in the ZnO(10 $\bar{1}0$ ) CB. (a) Exemplary cross correlation (XC) traces for a range of energies with corresponding double exponential fits (see text). (b) Resulting time constants for fast decay component  $\tau_1$  ranging from 825(60) fs at 20 meV above  $E_F$  to 10(4) fs at 0.75 eV. The red curve is the corresponding 2PPE signal at  $\Delta t = 0$  fs. (c) The amplitude of the fast ( $A_1$ ) component of the decay dynamics taken from the fit exhibiting a distinct maximum between 50 meV and 100 meV. (d) Amplitude of the slow component  $A_2$  (red squares) and corresponding time constant  $\tau_2$  (green circles). (e) The ratio  $A_1/A_2$  shows that the fast component  $A_1$  dominates for high energies, making the decay dynamics quasi single-exponential.

72 meV is no longer possible. The scattering with lower-frequency acoustic phonon modes results in growing hot electron lifetimes, because of the characteristically slower scattering rates, as will be discussed in detail in the following.

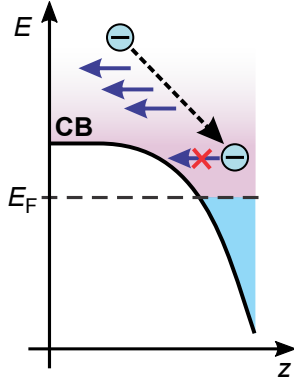


**Figure IV.20:** Schematic representation of the influence of surface downward band bending on the relaxation pathways of excited electrons at the ZnO surface. The crossing of CBM and  $E_F$  close to the surface allows relaxation to energies below the bulk CBM, albeit with a reduced number of scattering channels (see text).

This overall behavior of excited electrons in the ZnO(10 $\bar{1}$ 0) CB agrees very well with previous experiments [TMN<sup>+</sup>08] (see Section 7.2 of Chapter II) and also with the theoretical work by Zhukov et al., as shown in Fig. II.20. However, it must be noted, that in previous work the characteristic surface band bending of ZnO is *not* considered. In the calculations, this leads to the divergence of decay time constants at the bulk CBM, which is considered constant. Instead, at the ZnO surface the CBM is not located at a constant energy, as shown schematically in Fig. IV.20, and the downward SBB provides additional DOS down to the Fermi level, as schematically shown in Fig. IV.20. This means, that the theoretically predicted “phonon bottleneck” does only occur for excess energies very close to  $E_F$ , i.e., for energies less than  $E - E_F = 72$  meV. This energetic threshold for LO phonon scattering becomes apparent in the behavior of the amplitude  $A_1$  of the fast decay component. As shown in Fig. IV.19(c),  $A_1$  exhibits a characteristic reduction for energies below  $\approx 75$  meV which coincides with the energy of the LO phonon.

Further, the SBB may lead to increased relaxation times at energies below the CBM, because bulk states cannot contribute as final states in scattering or diffusion processes, as they are energetically “forbidden” (see Fig. IV.20). Eventually, the concurrence of all the described effects leads to the smooth increase of the hot electron relaxation dynamics at low energies which are represented by  $\tau_1$  in Fig. IV.19(b).

It was found in the work of Tisdale et al. [TMN<sup>+</sup>08] on the relaxation dynamics of excited electrons in the ZnO(10 $\bar{1}$ 0) CB, that the dynamics exhibit a *single* exponential behavior regardless of excess energy. This behavior even considers the repopulation of low-energy states by decay from higher lying levels. The authors also demonstrated that the resulting time constant  $\tau$  shows an exponential dependency with respect to the excess energy below the bulk CBM [cf. Fig. IV.19(b)]. This was shown under the assumption that there is *upward* band bending at the ZnO surface and additional DOS below the CBM is provided by a continuum of acceptor-type surface states. Notably, this view of the ZnO surface electronic structure is often found in literature prior to the “re-discovery” of the surface CAL (see Section 6.3.3 of Chapter II). However, the findings presented in previous sections and recent literature unambiguously validate the occurrence of (unintentional) downward band bending at the ZnO(10 $\bar{1}$ 0) surface.

In contrast to the previous study, we found that approximating the decay dynamics by a *double* exponential function, i.e., including an additional slow component, results in the best fit to our data. The slow time constant  $\tau_2$  (see Eq. IV.5) is plotted as green circles in Fig. IV.19(d) as a function of excess electron energy. Its values span a wide range of timescales, from below ten picoseconds for excess energies on the order of 0.5 eV to more than 100 ps close to  $E_F$ . We compare the amplitudes of both components,  $A_1$  and  $A_2$ , to analyze their role and importance in the decay process, as shown in Fig. IV.19(c)–(e). Plotting only  $A_1$  and  $A_2$  in (c) and (d) shows essentially an intensity reduction with higher excess energies, which reflects the overall lower 2PPE intensity at higher energies [see (a), (b)]. The ratio  $A_1/A_2$  between both amplitudes is plotted in (e), showing a distinct increase from  $\approx 1$  at 20 meV above  $E_{\text{ext}F}$  to  $\approx 30$  for excess energies exceeding 0.6 eV. Thus, the ratio  $A_1/A_2$  clearly shows that the dynamics at high excess energies exhibit a predominantly single exponential behavior which becomes less dominant at lower energies.

The increasing addition of a slower decay process with time constant  $\tau_2$  indicates that a complete description of the charge carrier dynamics at the ZnO(10 $\bar{1}$ 0) surface becomes increasingly complex for lower excess energies, especially below the bulk CBM. It also means, that the used fitting procedure is most likely not able to completely disentangle the different contributions to the decay dynamics, especially for the slow component  $\tau_2$ . This component might be partially associated to the scattering with acoustic phonons, which exhibit a characteristic time constant a timescale of 1 ps to 2 ps close to  $E_F$ , as measured in recent optical experiments [Fog15]. Since the values of  $\tau_2$  in the experiment are higher by two orders of magnitude, the slow component of the decay may be associated to another comparably slow process: the decay of *excitonic* states, which will be discussed in detail in Section 3.2.

### 3.1.1 Temperature Dependence of CB Dynamics

Temperature plays a role in the occupation of phonon states and, thus, a variation of temperature in the experiment may allow the distinction between different scattering mechanisms, i.e., phonon modes. Generally, the phonon emission rate  $\Gamma_{\text{e-ph}} = 1/\tau_{\text{e-ph}}$  in Fröhlich scattering depends on the temperature via the Bose–Einstein occupation probability  $n_{\text{BE}}(\omega t)$  of a phonon with energy  $\hbar\omega$  at temperature  $T$  (see Section 5.1.1 of Chapter II). As a consequence, an increase in temperature results in a reduction of decay times. However, regarding the proposed Fröhlich scattering mechanism in ZnO with comparatively large LO phonon energies  $\hbar\omega$ , only a weak dependence of decay rate on temperature is expected: a reduction in temperature from 300 K to 100 K should, according to Eq. II.8, lead to an increase of the hot electron lifetimes by less than 10% [TMN<sup>+</sup>08], which is on the order of the experimental uncertainty.

Figure IV.21 shows the experimentally determined fast decay time constant  $\tau_1$  for temperatures ranging from 50 K to 300 K. As discussed in the previous section,  $\tau_1$  is expected to account for the dynamics of e–ph scattering at the ZnO surface. Within the error bars, there is no significant dependence of  $\tau_1$  on the temperature within this range. This finding is in accordance with the assumption that hot electron decay happens via scattering with LO phonons.

The time constant  $\tau_2$  of the slow decay component shows also no distinct temperature dependence and its values are comparable to those shown in Fig. IV.19(d). The lower signal-to-noise ratio in the temperature-dependent measurements hampers any precise quantitative

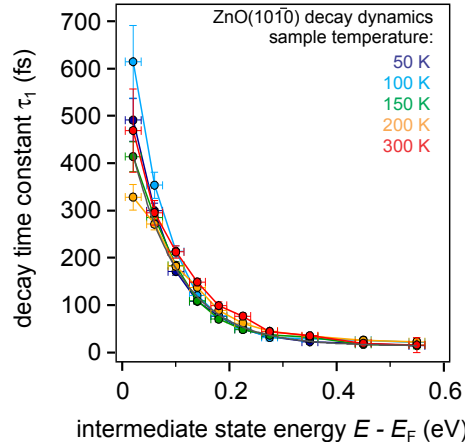


**Figure IV.21:** Temperature dependence of the hot electron relaxation in the CB of ZnO(10 $\bar{1}0$ ). Within the examined range of temperatures from 50 K to room temperature (300 K) we do not observe any significant variation of the relaxation time constant  $\tau_1$  with temperature. This behavior is expected for the LO phonon-assisted relaxation (see text).

comparison, though.

### 3.1.2 Screening of the Electron–Phonon Scattering by Hydrogen Doping?

Another aspect in e–ph interaction is its *screening* by charge carriers: The Fröhlich coupling in ZnO is based on the strong electric field induced by the ionic motion in case of LO phonons. The range of this field depends on the compensating polarization of the surrounding mobile charge carriers which is in this case defined by the *density*  $N$  of free electrons. There are two ways to influence  $N$ , either by changing the density of excited electrons in the CB via the laser power, or by chemically doping the system. The latter is possible, as shown in Section 2, by the addition of electrons to the ZnO surface by hydrogen adsorption.

Calculations by Yoffa [Yof80, Yof81] show that the relaxation time  $\tau_c$  increases quadratically with the charge density  $N$ , namely [SPD98]

$$\tau_c = \tau_0 \left[ 1 + (N/N_c)^2 \right], \quad (\text{IV.6})$$

where  $\tau_0$  is the relaxation time without carrier density dependence and  $N_c$  is the critical charge carrier density above which the relaxation time increases sharply. An experimental proof of this relation has been found for silicon surfaces where a critical density of  $N_c = 6.0(7) \times 10^{20} \text{ cm}^{-3}$  was deduced [SPD98]. In contrast to this study,  $N$  was varied by changes to the laser intensity.

An estimate value of  $N_c$  for any material can be deduced from a known value of  $N_c$  of a different material. This is because of the proportionality relation

$$N_c \propto \varepsilon_s m_{\text{eff}} \omega^3, \quad (\text{IV.7})$$

with  $\varepsilon_s$  the static dielectric constant,  $m_{\text{eff}}$  the effective electron mass, and  $\omega$  the phonon frequency [TMN<sup>+</sup>08]. Because those constants are known for ZnO, and using the known  $N_c$  of GaAs

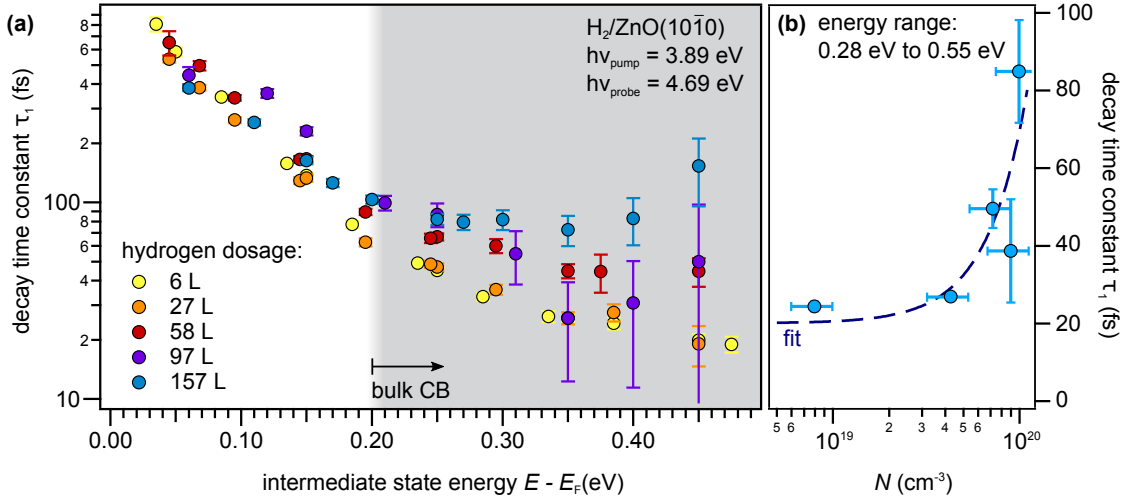


**Figure IV.22:** Hydrogen dosage-dependent time constant of hot carrier relaxation in the ZnO(10 $\bar{1}0$ ) CB. (a) Time constant  $\tau_1$  determined from fits to the XC of the 2PPE signal for different hydrogen dosages, from 6 L (yellow) to 157 L (blue). There is a clear increase of  $\tau_1$  with increasing dosage for high excess energies  $E \gtrsim 0.1$  eV. (b) Time constants  $\tau_1$  extracted from XC traces integrated over a wide energy range from 0.28 eV to 0.55 eV plotted versus the hydrogen-induced charge carrier density  $N$  (see text). The quadratic fit to the data is done according to Eq. IV.6.

( $N_c^{GaAs} = 5 \times 10^{17} \text{ cm}^{-3}$ ), Eq. IV.7 results in a calculated  $N_c^{ZnO} = 1 \times 10^{19} \text{ cm}^{-3}$  which is one order of magnitude above the maximum excitation densities used in the presented experiments, which range from  $1.4 \times 10^{18} \text{ cm}^{-3}$  to  $1.6 \times 10^{18} \text{ cm}^{-3}$ .<sup>11</sup> On the other hand, the maximum hydrogen-induced charge density at the ZnO surface is on the order of  $1 \times 10^{20} \text{ cm}^{-3}$  (cf. Section 2.4.1). While, in our experiment, surpassing the calculated  $N_c$  by means of high laser intensities is not possible, hydrogen doping can easily induce charge carrier densities which are well above  $N_c$ .

Thus, it is within the realm of possibility that an increase of the decay time constant is observed for strongly hydrogen-doped samples. Starting with low hydrogen dosages one would expect a dosage-independent value of  $\tau_1$  which increases sharply when the critical carrier density  $N_c$  is surpassed.

The main experimental difficulty lies in the variation of one parameter (hydrogen dosage, i.e., charge carrier density) while the excitation density should remain constant. The hydrogen-induced change of the work function and the increase of the CAL signature result in significantly lower signal-to-background ratio. As a consequence, the experimental results for high hydrogen coverages exhibit more scatter and larger errors.

Figure IV.22(a) shows the fast time constant  $\tau_1$  of hot electron relaxation in the ZnO(10 $\bar{1}0$ ) CB for a wide range of excess energies and varying hydrogen dosages (cf. Fig. IV.19). As discussed in the previous sections, in the energy range above the bulk CB at  $E = 0.2$  eV, e-ph scattering via Fröhlich coupling is the dominant relaxation process. Please note that this does not imply

<sup>11</sup>The experimentally attainable excitation density has a practical upper limit which is given by either the maximum laser power or the limit of the dynamic range of the photoelectron analyzer. Further, excitation densities above the exciton Mott limit are avoided.

that the observed relaxation processes occur within the bulk, but rather at the region of the surface CAL, due to the surface sensitivity of 2PPE (see Section 1.2.3 of Chapter III). Despite the visible scatter of the data there is a clear trend towards increasing relaxation time constants  $\tau_1$  with increasing hydrogen dosage. For dosages of 6 L and 27 L,  $\tau_1$  is on the order of 20 fs to 40 fs in the high energy range. Further increase of the hydrogen dosage results in an approximate doubling of  $\tau_1$  for 58 L, and for 150 L values close to 100 fs are found.

To account for the uncertainties at high dosages, XCs for a wider energy range that spans values from 0.28 eV to 0.55 eV were analyzed, i.e., the values shown in (a) were averaged over the respective energy range. The resulting  $\tau_1$  are displayed in Fig. IV.22(b) with respect to the hydrogen-induced charge carrier density  $N$ . Since  $N$  could not be measured directly, it was estimated from the intensity of the CAL signature for each dosage: Ozawa and Mase determined the maximum electron density in the CAL at the ZnO(10 $\bar{1}$ 0) surface as  $N_{\max} = 1.0(2) \times 10^{20} \text{ cm}^{-3}$  [OM11]. This value was determined from ARPES measurements that resulted in a model of the CAL as 2DEG, which eventually lead to the stated  $N_{\max}$ . This  $N_{\max}$  was then assigned to the maximum CAL intensity in our experiments. The densities corresponding to the respective dosages could then be extrapolated from the CAL intensities corresponding to the respective dosage.

The resulting plot of  $\tau_1$  as a function of  $N$  exhibits a sharp increase of the relaxation times for densities between  $10^{19} \text{ cm}^{-3}$  and  $10^{20} \text{ cm}^{-3}$ . This data can be approximated reasonably well by Eq. IV.6, as shown in Fig. IV.22(b). The fit yields a carrier density-independent time constant  $\tau_0 = 20(12) \text{ fs}$  and a critical density  $N_c = 6(3) \times 10^{19} \text{ cm}^{-3}$ . Compared to the value of  $N_c^{\text{est}} = 1 \times 10^{19} \text{ cm}^{-3}$  that was estimated based on literature, the measured  $N_c$  is clearly higher, but is still of the same order of magnitude.

Summing up, our data strongly indicates that the addition of free charge carriers in the CAL by hydrogen adsorption at ZnO surfaces can drastically slow down the hot electron dynamics – approximately by a factor of five for highly doped surfaces. This effect can be expected to be even more pronounced on the oxygen-terminated (000 $\bar{1}$ ) surface, where higher electron densities might be achieved, as  $N_{\max} = 2.3 \pm 1.2 \times 10^{20} \text{ cm}^{-3}$  [OM11]. This makes additional measurements, which might also consider variations in the laser intensity, highly desirable. Furthermore, the tunability of the dynamic screening at ZnO surfaces, which occurs in the spatially highly restricted surface region, might be of interest for other types of surface and interface processes, such as energy or charge transfer at HIOS interfaces. Eventually, this potentially strong dependence of the relaxation timescales on screening effects may also explain the strong variations found in previous experiments (see Ref. [ZEC10] for an overview), in which either comparably high excitation densities are reported, or unintentional surface doping might be present.

### 3.2 The ZnO Surface Exciton

The excitation of electrons across the semiconductor band gap creates **electron–hole (e–h)** pairs that may form bound excitonic states via the Coulomb interaction. This further fundamental non-equilibrium process is strongly influenced by charge carriers which may screen the **e–h** interactions. As a consequence, the presence of the tunable **CAL** at the ZnO surface can be expected to affect excitonic processes at the ZnO surface. The excitons which are present at the surface of ZnO may play an important role in interfacial energy transport via Förster transfer, as introduced in Section 7.1 of Chapter II.

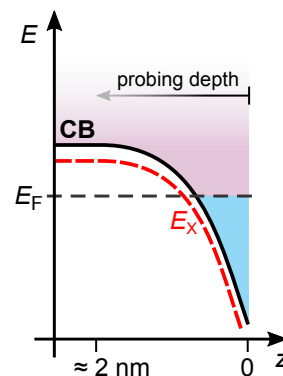
These **surface excitons (SXs)** in ZnO are the dominant species in **PL** studies in nanostructured systems, due to the systems' characteristically large surface-to-bulk ratio [WVR<sup>+</sup>06, KFS<sup>+</sup>13, SLMF14]. However, despite the great scientific attention devoted to **SX**, detailed understanding of this species is still missing, also because the systematic modification and characterization of nanoparticles is very challenging. At *single crystal* surfaces, **SX** were only identified once [TFS90] (see Section 7.1.2 of Chapter II for details). As the sample was exposed to air before measuring the **SX** in that experiment, no observation and systematic characterization of this excitonic species under highly reproducible **UHV** conditions exists to date, so that its origin and characteristics remain vague.

In this section, it will be shown that the **SX** at the ZnO(10 $\bar{1}$ 0) surface can be identified and characterized in a **2PPE** experiment. Thereby, its formation and decay dynamics can be analyzed which yields to new insight into the fundamental properties of this relevant species. In particular, it is suggested that the presence of potentially hydrogen-induced potential wells at the surface is a prerequisite for **SX** formation, which results in a complex interplay between excitons and free electrons at the ZnO surface.

#### 3.2.1 Measuring of the Excitonic Signature and its Dynamics

The detection of excitonic states in semiconductor materials by means of **2PPE** is comparably straightforward: The photoemitted electrons that originate from an exciton in its ground state are expected to appear in the spectra *below* the **CBM**, with an energy difference that is the excitonic binding energy (cf. Fig. II.11) [WKFR04, Zhu14]. The energy of the photoelectron then corresponds to the ionization energy of the excitonic state, as explained in Section 3 of Chapter II, which justifies drawing the exciton energy into the single particle band structure.

**Figure IV.23:** Schematic, area-averaged representation of the influence of band bending on the photoelectron energies that refer to an excitonic state with energy  $E_X$ .



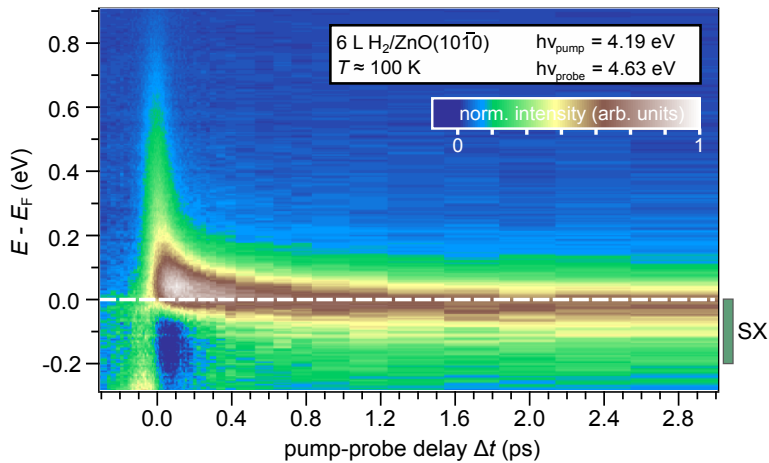


**Figure IV.24:** 2PPE signal. False-color plot of the photoinduced changes to the electronic population  $\text{H}_2/\text{ZnO}(10\bar{1}0)$  surface, showing the ultrafast charge carrier dynamics. The ultrafast relaxation of hot electrons in the CB slows down significantly at lower excess energies. For energies below  $E_F$  there is a comparably slow increase of the photoinduced signal which is attributed to the formation of the long-lived SX (see text).

For the very strong downward SBB at  $\text{ZnO}(10\bar{1}0)$  and  $(000\bar{1})$  surfaces this means that 2PPE probes a spatial region of the sample in which there are strong energetic variations to the band edges. In the area-averaged description of the surface band structure, which is sketched in Fig. IV.23, this would mean that the absolute energetic position of the SX is strongly widened by this band bending.<sup>12</sup> What is more, it can be concluded from this scheme that any electron that is emitted from an excitonic state energetically located very close, or even below, the Fermi level.

Figure IV.24 shows the pump-induced changes to the photoelectron signal, i.e., after subtraction of the equilibrium background (cf. Fig. A.2), in false colors as a function of pump-probe delay and energy with respect to  $E_F$ . The corresponding excitation scheme is sketched in Fig. IV.18(a), and the excitation density was below the Mott limit (max.  $1.45 \times 10^{18} \text{ cm}^{-3}$ ). This characteristic measurement was already presented and discussed regarding energies above  $E_F$  in Section 3.1 (see Fig. IV.18). Below  $E_F$  there is first an initial drop of intensity, which is because of the bleaching of the CAL by  $h\nu_{\text{pump}}$ . This drop is then followed a signal increase above the equilibrium value on a sub-picosecond timescale. This increase is striking, because the Fermi level is defined as the energy up to which all electronic states are filled at  $T = 0 \text{ K}$ , and an addition of electrons, as presumably observed here, would violate the Pauli exclusion principle. As a consequence, pumping the system above the band gap must create additional states below  $E_F$ , leading to an increase in the 2PPE signal. Such photoinduced creation of states could be caused by (i) small polaron formation, (ii) photoinduced changes to the surface electronic structure like surface photovoltage (SPV) shifts [ACH90], heating or bleaching of the CAL, or (iii) exciton formation.

<sup>12</sup>A discussion of the microscopic properties of the SX that go beyond this simple scheme can be found in Section 3.2.4.

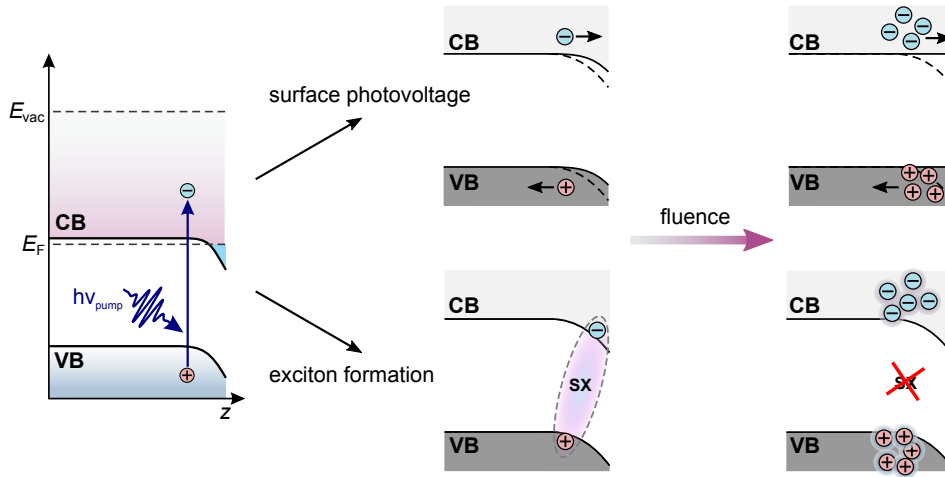


**Figure IV.25:** Scheme of fluence dependent effects at the ZnO surface: surface photovoltage (top) vs. exciton formation (bottom). The SPV effect leads to an accumulation of negative charge at the surface resulting in a change of the band bending. Increasing the fluence results eventually in flat bands at the surface. In case of excitons, the increase of the fluence is expected to reduce the exciton formation probability, due to enhanced screening in the  $e-h$  plasma above the Mott limit.

### 3.2.2 The Surface Exciton Revealed

The natural question now is, how the signal increase below  $E_F$  can be unambiguously assigned to the formation of the SX, i.e., how the alternative scenarios can be excluded.

The formation of polarons is connected to the distortion of the ZnO lattice. It is well known, that excitons in ZnO have partly polaronic character, which contributes to the large bulk exciton binding energy of 60 meV (see Section 7.1 of Chapter II). The formation of *separate* polarons of electron and hole is thus unlikely. In addition, no experimental evidence was found for small polaron formation in a time-resolved THz study [HKB07], which rules out scenario (i).

Scenarios (ii) and (ii) can be tested by varying the excitation density. The dependence of the SPV effect on the excitation density in comparison to exciton formation is shown schematically in Fig. IV.25. In general, any changes due to the occurrence of light-induced effects that lead to a change in band positions, e.g., SPV or band gap renormalization (BGR), or occupational changes induced by laser heating should be more pronounced with increased pump fluence. In case of SPV, the shift of the bands becomes more pronounced with excitation density, until flat band conditions are reached. For excitonic states the signal intensity should also increase with the number of excited  $e-h$  pairs. However, this behavior is expected to change as soon as the density of the photoexcited  $e-h$  plasma is high enough to screen the Coulomb interaction of the  $e-h$  pairs. As a result, above this Mott limit, the exciton formation probability should indeed be *reduced* when the excitation density increases (see Section 5.2.1 of Chapter II).

Figure IV.26(a) compares the 2PPE signatures measured with different excitation densities for different pump-probe delays. The excitation densities were varied by changing the pump laser fluence while keeping the probe fluence constant. The value of  $1.7 \times 10^{18} \text{ cm}^{-3}$  was selected to be as low as possible while providing sufficient statistics, whereas the high excitation density

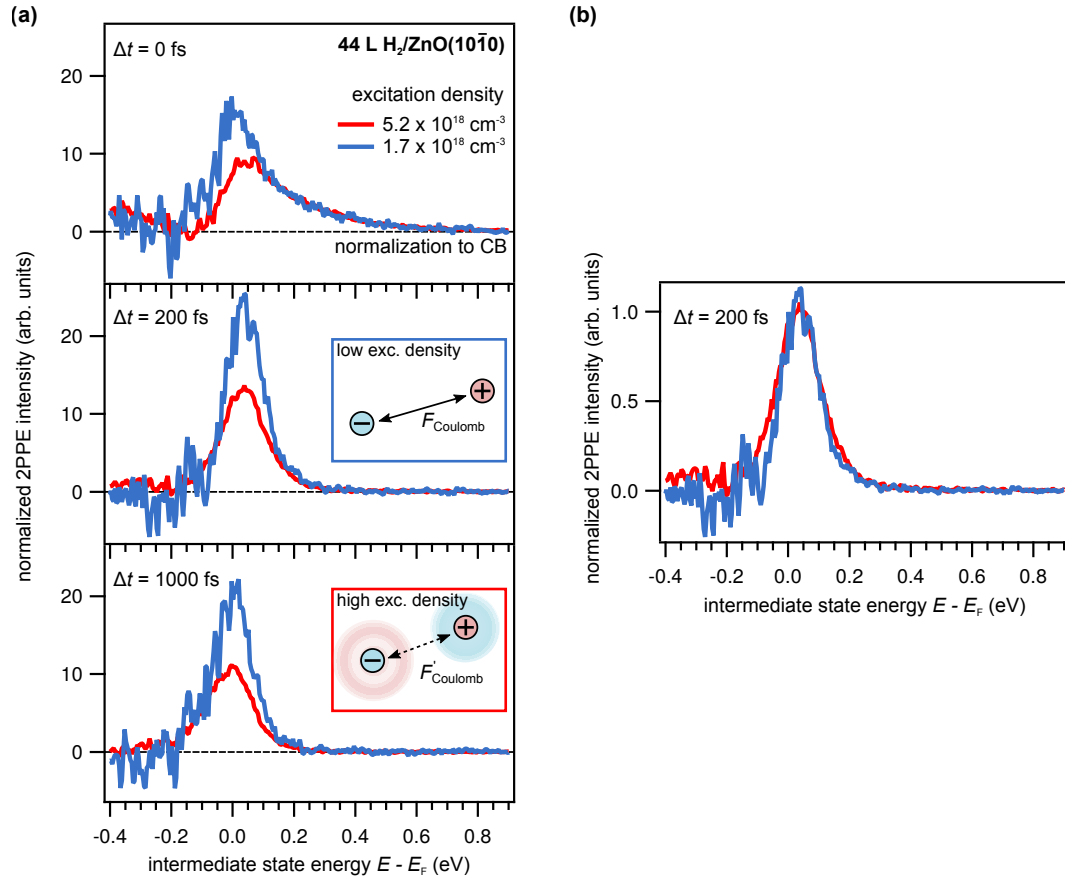


**Figure IV.26:** 2PPE spectra of 44 L  $\text{H}_2/\text{ZnO}(10\bar{1}0)$  for different excitation densities after background subtraction. (a) Signal normalized to the electron population in the CB at  $\Delta t = 0$  fs in order to compare changes relative to the excitation density of single particles. Higher excitation density reduces the formation probability of the SX due to sufficiently strong screening of the Coulomb interaction by the  $e-h$  plasma in the background (see schematic illustration in the insets). (b) Signal intensity normalized for both excitation densities to show that there is no perceptible energetic shift.

of  $5.2 \times 10^{18} \text{ cm}^{-3}$  should be well above the Mott limit without inducing any space charge effects [HRMBK09]. While there is no significant overall change to the charge carrier dynamics, the intensity of the spectral signature located at  $E_F$  is *reduced* upon *increasing* the excitation density. According to the argument given above, this behavior unambiguously shows that (ii) photoinduced processes that change the SBB and occupation of the CAL cannot be the reason for the observed signal. Instead, the observed behavior of the peak matches with that of an excitonic state which is subject to the screening of the e–h interaction above the Mott limit. Thus, it can be concluded that the increase of 2PPE intensity below  $E_F$  corresponds to the formation of a new excitonic state, which creates additional DOS.

The observation that an excitonic state is still visible despite the surpassing of the Mott limit can be understood when considering that the Mott transition occurs smoothly across a range of e–h pair densities [YJLH<sup>+</sup>12]. It should be mentioned, that also at lower excitation densities the dynamics are qualitatively identical (not shown).

Further, Fig. IV.26(b) shows that the energetic position of the observed peak is independent of excitation density within the experimental precision. This corroborates the conclusion that there are no dynamic changes to the band bending by the SPV effect. Additional test measurements on the oxygen-terminated (000 $\bar{1}$ ) surface showed an identical dependence of the SX signature on excitation density [Ric14]. This underlines the similarities of the surface electronic band structures of both terminations, as discussed in Section 1.2.

Thus, it can be concluded that the observed spectral feature is indeed the signature of an excitonic species SX which resides close to the ZnO(10 $\bar{1}$ 0) surface and which is subject to the strong downward SBB. This band bending results in the high binding energy of the SX of  $\approx 0.25 \text{ eV}$  relative to the bulk CBM. However, the energetic position relative to the local CBM at the surface is expected to be significantly lower (see Fig. IV.23). The energetic position of the SX signature below the Fermi level strongly suggests that there is an intimate connection between the downward SBB and the occurrence of SX species. In Section 3.2.4, the interplay between hydrogen-induced potential changes  $\Delta U$  and the SX will be discussed, which not only further elucidates the nature of the SX, but also gives experimental evidence for the localized character of  $\Delta U$ . Before that, the next section focuses on the formation dynamics of the SX, which may shed light onto the debated topic of exciton formation processes in general.

### 3.2.3 Surface Exciton Formation Dynamics

The exact description of electron–hole (e–h) interactions leading to exciton formation and relaxation to thermal equilibrium in ZnO are not yet fully understood and there appears to be no consensus in literature about the timescales of exciton formation in typical semiconductors.<sup>13</sup> This is partly due to the fact that most methods for examining exciton dynamics do not directly measure the excitonic *population*, but optical properties, such as photoluminescence (PL) which are only indirectly related to exciton formation [BvHS<sup>+</sup>93]. In particular, these optical methods are most sensitive to the excitonic ground state with  $\mathbf{K} = 0$  (see Section 5.2.1 of Chapter II) [CS01, SKB<sup>+</sup>04]. As a consequence, reported values of experimentally determined exciton formation times range from below 10 ps up to 1 ns [SKB<sup>+</sup>04]. Interestingly, the onset of

<sup>13</sup>The major part of experimental studies is about GaAs and related materials.

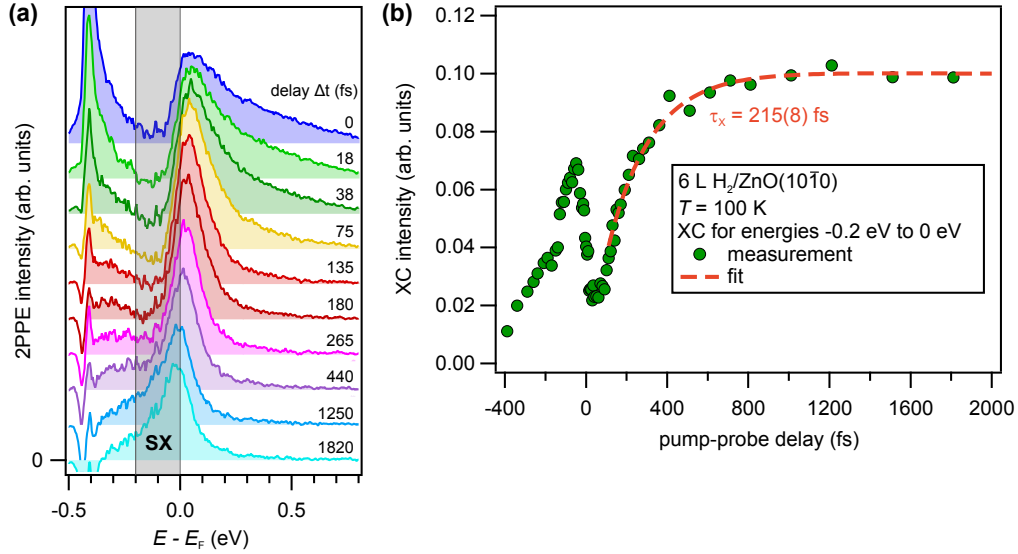


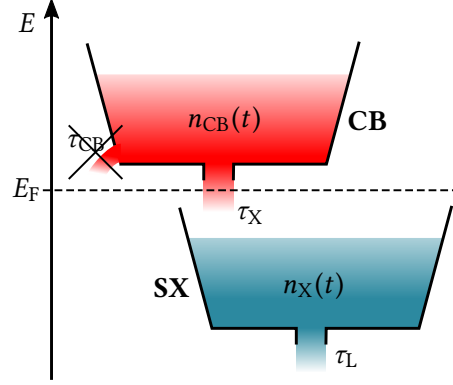
**Figure IV.27:** Formation dynamics of the SX signature measured with 2PPE (cf. Fig. IV.18). (a) 2PPE spectra of 6 L  $\text{H}_2/\text{ZnO}(10\bar{1}0)$  for comparably short delays. The spectra change their energetic position and shape by shifting towards lower energies, whereas the population above  $E_F$  decays on a short timescale. The shadowed area indicates the energy area used to analyze the dynamics of the excitonic signature. (b) XC trace showing the comparably low rise of the excitonic signature below  $E_F$  including a fit to the data which is based on a rate equation model (see text). The peak around  $t = 0$  fs results from the signal of hot electrons pumped by the 4.63 eV photons.

photoluminescence is often observed on timescales shorter than the stated timescales of exciton formation [DSO<sup>+</sup>90, SKB<sup>+</sup>04]. These complications in the description of excitonic processes on ultrashort timescales are reflected in the lack of a comprehensive theoretical model of exciton formation and luminescence. A major question here is the role of exciton versus e-h plasma contributions to the PL at the exciton energy [HGB00, CEM<sup>+</sup>04].

In contrast to optical methods, 2PPE accesses the actual electronic population and should, thus, be able to directly detect electrons that were part of either an e-h plasma or exciton in their initial state. Further, the pump-probe scheme of 2PPE enables a femtosecond temporal resolution that is ahead of typical time-resolved PL experiments, in which the time between sample excitation and the arrival of an emitted photon can be determined on timescales on the order of tens of picoseconds [WVR<sup>+</sup>06]. However, with the downside that the energy resolution is fairly broad compared to PL experiments and only states at or very close to the surface are accessible.

Figure IV.27(a) shows exemplary spectra from the 2PPE measurement presented in Fig. IV.24. What can be seen there is that spectra at very early delays  $\Delta t \lesssim 200$  fs are cut off at their lower energy edge by the Fermi level, i.e., the SX signature is not yet visible. Any signal below  $E_F$  for

**Figure IV.28:** Schematic model of the transfer of electronic population from **CB** states  $n_{CB}$  to the **SX** population  $n_{SX}$ , which is used as basis for rate equations (see text).



these delays originates from electrons which were emitted due to a reversed excitation scheme (pumped by 4.6 eV and probed by 4.2 eV). What is also visible below  $E_F$  is an initial drop of intensity during the first  $\approx 100$  fs induced by bleaching of the **CAL** by  $h\nu_{\text{pump}} = 4.2$  eV. This bleaching occurs due to the direct excitation of electrons in the **CAL** by  $h\nu_{\text{pump}}$  and its intensity is significantly lower than those of the signatures which result from pumping across the gap.

For  $\Delta t \gtrsim 200$  fs the spectral shape of the **2PPE** signal changes significantly: The hot electrons above  $E_F$  have decayed (see Section 3.1) and instead the lower energy edge has broadened towards lower energies, so that the majority of the signal originates from electrons in an intermediate state with an energy below  $E_F$  – these electrons originate from the **SX**.

Apparently, the **SX** state is not populated *directly* by  $h\nu_{\text{pump}}$  but it forms after hot electrons and holes have been created. To quantify the dynamics, **XC** traces can be analyzed, which display the time-dependent **2PPE** signal integrated over an energy range from  $-0.2$  eV to  $0.0$  eV [see shaded area in Fig. IV.27(a)].<sup>14</sup>

Because of the indirect formation process of the **SX**, which does apparently not depend on the pulse durations, the **XC** trace, which is depicted in Fig. IV.27(b), cannot be approximated by a fit consisting of a convolution of the two-pulse **XC** and a sufficiently complex decay with characteristic time constants. Instead, one can make use of *rate equations* which model the transfer of electronic population between different reservoirs, i.e., electronic states.

Figure IV.28 shows a schematic model of the transfer of electronic population into the excitonic state. The population  $n_X(t)$  of the **SX** is given by the time constant  $\tau_X$  which defines the rate of exciton formation from formerly separate electrons and holes. The population of electrons, that is located at the **CBM** and, thus, available for forming excitons is denoted by  $n_{CB}$ . As lifetimes at the **CBM** become exceedingly long compared to the formation time of the **SX** [ZEC10], alternative decay channels with time constant  $\tau_{CB}$  may be excluded.

The rate equations which govern **SX** formation and their subsequent decay with a time constant  $\tau_L$  then read:

$$\dot{n}_{CB} = -\frac{1}{\tau_X}n_{CB}(t) \quad (\text{IV.8})$$

<sup>14</sup>The energy region used for the analysis of the **SX** was always chosen from  $-0.2$  eV to  $0$  eV to ensure that hot electrons at the **CB** bottom and any artifacts from secondary edge shifts are *not* included in the data.

and

$$\dot{n}_X = \frac{1}{\tau_X} n_{CB}(t) - \frac{1}{\tau_L} n_X(t). \quad (\text{IV.9})$$

The solution to these simple coupled equations is

$$n_X(t) = n_X^0 \cdot e^{-t/\tau_L} + n_{CB}^0 \frac{\tau_X^{-1}}{\tau_X^{-1} - \tau_L^{-1}} \left( e^{-t/\tau_L} - e^{-t/\tau_X} \right). \quad (\text{IV.10})$$

The rate equation IV.10 for the population of the SX can be fit to the XC trace, which is shown in Fig. IV.27(b). With the assumption that the initial population of the excitonic state is zero ( $n_X^0 = 0$ ) the resulting characteristic time constant of exciton formation at the ZnO(10 $\bar{1}$ 0) surface is  $\tau_X = 215(8)$  fs.

This sub-picosecond timescale of exciton formation is an order of magnitude faster than what has previously been determined for different systems, all using alternative methods (see Section 5.2.1 of Chapter II).

The presented results are, thus, indicative of an exciton formation process that is characterized by an ultrafast formation of potentially hot, i.e. excitons which further relax to the optically active  $\mathbf{K} = 0$  state on a slower picosecond timescale, as was suggested in earlier studies on exciton formation [KAV<sup>+</sup>96]. The cooling dynamics of the excitonic state, which fit to the experimentally-determined occurrence of PL from the SX [WVR<sup>+</sup>06] are discussed in Section 3.2.7.

### 3.2.4 The Surface Exciton as a Probe for the Local Potential

The interplay of the SX with its surrounding mainly depends on both the dielectric function of the surrounding material and the local electrostatic potential (see Section 7.1 of Chapter II). Both are effectively changed when hydrogen adsorbs at the ZnO(10 $\bar{1}$ 0) and (000 $\bar{1}$ ) surfaces by the addition of free charge carriers (CAL formation) and the formation of laterally localized potential wells (see Section 2.4.2) together with a work function reduction by hundreds of meV.

The SX could, thus, serve as an experimental probe of the potential change  $\Delta U$  and vice versa. Hence, the measurement of the behavior of the SX for different hydrogen dosages may expand on the area averaged measurements discussed in Section 2. As mentioned before, the SX must be connected to regions with downward surface band bending, i.e., where the CBM is located very close to, or below,  $E_F$ . This connection between H-induced surface band bending and the SX makes the latter a sensor for the strength and degree of the *localization* of the surface potential changes: An increase of the H coverage, i.e., an enhancement of the number of potential minima and, therefore, the number of SX sites can be expected lead to an increase of the SX photoemission intensity. On the other hand, the free carriers which are introduced by hydrogen adsorption may also reduce the exciton formation probability when a sufficiently high electron density is reached (see Section 3.2.5).

The change in SX photoemission intensity with the amount of adsorbed hydrogen is shown in Fig. IV.29(a). For the depicted, comparably low dosages ranging from 3 L to 44 L a clear SX signal increase is observed. This finding is in agreement with the localized and non-interacting character of the potential wells created by O–H bond formation, which was found in the

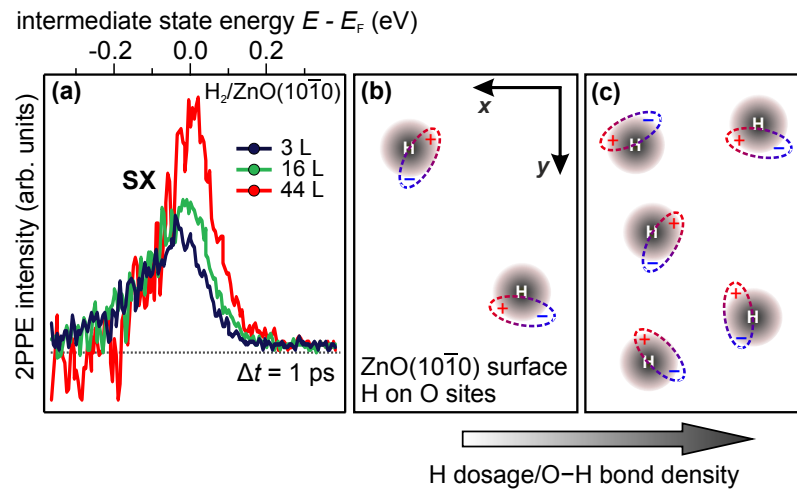


**Figure IV.29:** (a) SX signatures at a pump-probe delay of 1 ps for H dosages from 3 to 44 L. Intensities are normalized to the number of electrons excited from the valence into the conduction band by the pump pulse (cf. Section 3.2.2). (b)-(c) Strongly simplified scheme of the ZnO surface showing the correlation of H dosage and the resulting density of potential wells with SX density for low coverages.

calculations (cf. Fig. IV.13). In this low coverage regime, these wells accumulate *without* leading to a spatial overlap of the SX species, as schematically depicted in Fig. IV.29(b)–(c). Hence, these experimental findings confirm the strongly localized character of the potential change  $\Delta U$ , as predicted by our calculations.

At the same time these findings are a sign for the stability and localization of the SX: It remains largely unperturbed by significant changes to the *macroscopic* properties of the sample surface caused by H dosing: The work function for the presented H dosages changes by  $\Delta\Phi = -250$  meV and at the same time the CAL intensity increases by a factor of about ten [cf. Fig. IV.9(a)]. One can conclude that the SX is *not* localized directly at the vacuum interface or within the first ZnO double layer, but in the *subsurface* region where the static screening of the Coulomb interaction

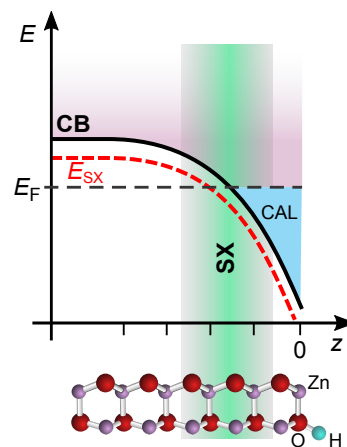


**Figure IV.30:** Schematic illustration of the localization of the SX in the subsurface region of the ZnO(10 $\bar{1}$ 0) surface (cf. Fig. IV.12).

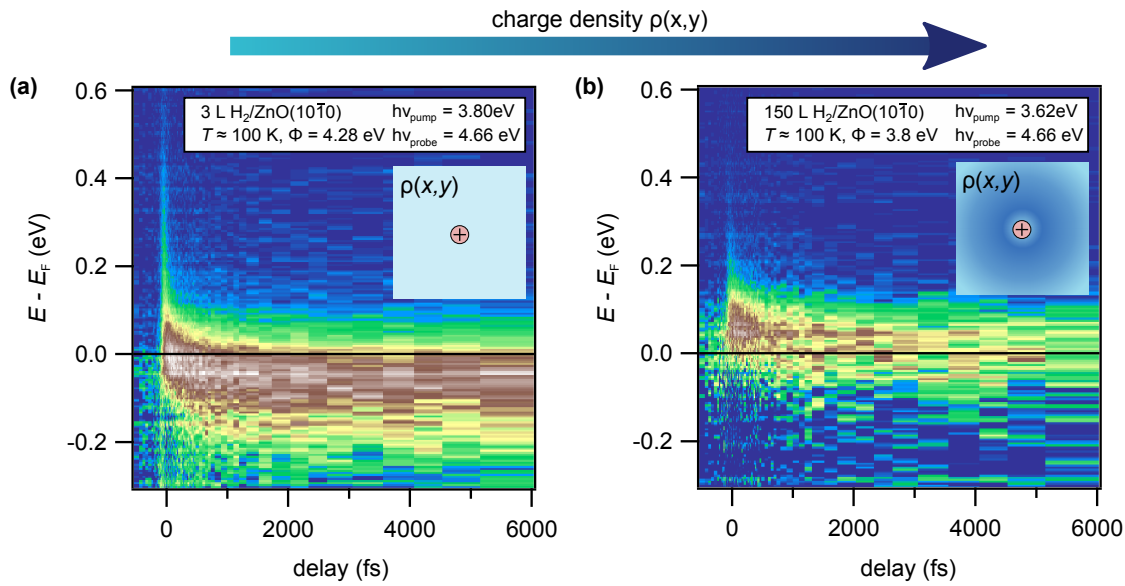


**Figure IV.31:** Exemplary background-subtracted two-dimensional plots of the charge carrier dynamics at the ZnO(10 $\bar{1}0$ ) surface for hydrogen dosages of 3 L and 150 L. (a) At a low dosage of 3 L the SX signature is very pronounced and located below  $E_F$ . (b) Increasing the hydrogen dosage to 150 L leads to a significantly lower signal-to-noise ratio and the quenching of the SX signature below  $E_F$ , because of screening effects (see text).

is comparably weak, as schematically sketched in Fig. IV.30 (cf. Fig. IV.12). This would also explain, why changes of the work function have no apparent influence on the energetic position of the SX signature, which would be expected for true surface excitons where the excited electron resides above the surface in the vacuum [RWKP03]. The exact position of the exciton may then be influenced by the charge density distribution along the surface normal of the CAL, as discussed in detail in the next section.

In addition to the study of the SX in the low H coverage regime, we also examined the limiting case of high H dosages where the distance between H adsorption sites is greatly reduced and the surface electron density is at its maximum due to formation of the CAL. Both effects are expected to reduce the SX intensity because of (i) spatial overlap and resulting mutual screening of the electron-hole pairs and (ii) screening by the increased amount of charge carriers in the CAL. Indeed, by increasing the H<sub>2</sub> dosage to 150 L, where the CAL intensity is at its overall maximum [see Fig. IV.9(b)], the SX signal is quenched, i.e., we observe barely any 2PPE signal below  $E_F$ , as shown in Fig. IV.31. The comparison between the dosages of 3 L and 150 L shows a significant reduction of the long-lived SX signature, in particular at energies below  $E_F$ . This reduction of the signal from the strongly bound SX species, thus, appears in the spectra as a shift to higher energies and a reduction of the SX peak width.

This observation suggests that in the hydrogen dosage regime between 44 L and 150 L, there is a transition of  $\Delta U$  from the strongly localized character to a laterally smeared out CAL which results in the formation of a two-dimensional electron gas at the surface as suggested for a comparable coverage by Ozawa and Mase [OM11]. In conjunction with our theoretical

results which suggest an enhanced overlap of potential wells for O–H coverages above  $\approx 25\%$ , we conclude from this measurement that the delocalization of the surface charge is reached between 44 and 150 L. This is, again, in accordance with our previous findings regarding the delocalization of the potential wells (see Section 2.4.1), and also coincides with the coverage regime below 100 L at which isoenergetic Zn–H bond formation sets in (at 18% O–H coverage), as deduced from the work function change further above.

Apart from the quenching of the SX signature for high hydrogen dosages, our measurements show more subtle changes to its spectral shape with varying, comparably low dosages: There is an apparent shift of the peak to higher energies relative to  $E_F$  accompanied by a slight reduction of signal intensity at energies below  $-0.2$  eV, as can be recognized in Fig. IV.29(a) upon closer inspection. This effect is discussed in detail in Section 3.2.5, where it is shown that screening of the Coulomb interaction influences the SX signature even for comparably low hydrogen dosages.

### 3.2.5 Hydrogen-Induced Screening of the SX

In the previous section it was shown that very high charge densities quench the formation of the SX (see Fig. IV.31). It may now be asked whether it is possible to transiently change the screening of the Coulomb interaction between e–h pairs by comparably small hydrogen dosages, as it was possible to do this by changing the excitation density (cf. Section 3.2.2).<sup>15</sup> The reason for this is, that the charge carrier densities which can be attained by hydrogen doping are sufficiently high to surpass the Mott limit:  $\approx 1 \times 10^{20} \text{ cm}^{-3}$  for maximum CAL intensity at  $\approx 150$  L hydrogen dosage (see Section 3.1.2). On the other hand, it was found that for comparably low dosages the SX intensity is actually increased by increasing the amount of hydrogen, because of the intimate connection between hydrogen-induced potential wells and the presence of SX species.

Summing up, the interplay between hydrogen-induced charge carriers and the presence of SX is very complex, in particular, because of the pronounced field and charge density gradients at the ZnO surface which makes it difficult to assign an exact spatial distribution to the charge carriers.

Nevertheless, the influence of a change in charge density in the CAL on the SX properties may be extracted from the 2PPE data and a thorough analysis of the spectral shape and position of the SX signature may help to further specify the nature of the SX.

Figure IV.32 shows the position of the SX peak maximum for different, comparably low hydrogen dosages and at different delays  $\Delta t$ , measured on the ZnO(10 $\bar{1}$ 0) surface. The exemplary normalized spectra for  $\Delta t = 1$  ps shown in (a) indicate that by increasing the hydrogen dosage there is a slight shift of the SX signature to higher energies relative to  $E_F$ . Again, this behavior corroborates the finding that an increase of the amount of adsorbed hydrogen does *not* lead to an increase of the magnitude of the SBB, which expectedly shift the signatures to lower energies. Instead, it leads to the increase of the number of potential wells, as discussed in Section 2 (cf. Fig. IV.29).

A precise analysis of the dosage-dependent shift of the peak maxima is shown in (b). The analysis was conducted by using a fit function that consists of a Gaussian peak which possessed

<sup>15</sup>For a brief discussion of screening in space charge layers, see Section 6.3.1 of Chapter II.

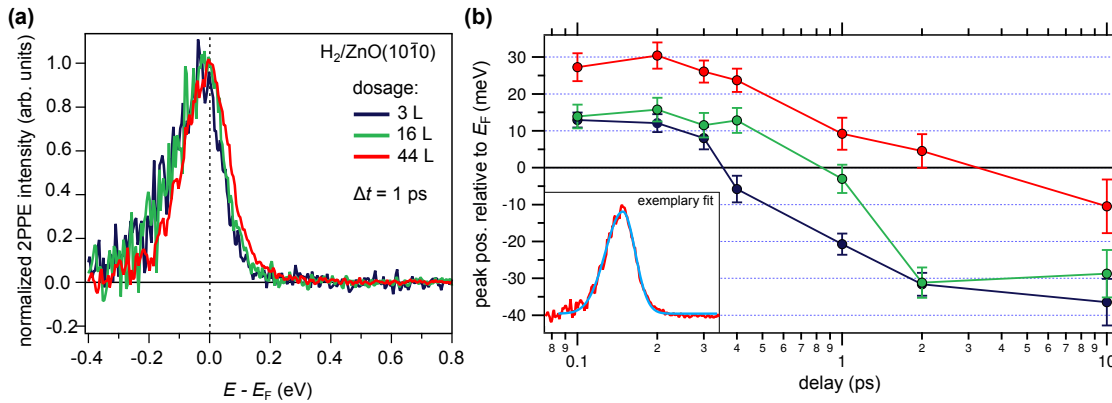


**Figure IV.32:** Dependence of the SX peak shape and position on hydrogen dosage. (a) SX signatures for a delay of 1 ps and dosages from 3 L to 44 L, normalized to the peak maximum. With increasing dosage the peak tends to shift to higher energies relative to  $E_F$ . (b) Energetic positions of the peak maxima for different hydrogen dosage at various delays, determined by fitting a Gaussian with different widths for each side to the spectra (see inset). The difference in peak position averages out at  $\approx 30$  meV and remains present for all delays.

different peak widths for each side. An example of this fitting procedure is shown in the inset. The resulting values show a clear dependency of the peak position on the hydrogen dosage. By increasing the hydrogen dosage from 3 L to 44 L the position of the SX peak maximum is shifted to higher energies by  $\approx 20$  meV to 30 meV for all observed delays. This change of the SX energy is supposedly caused by the enhanced screening of the Coulomb interaction with increasing dosage, which reduces the exciton binding energy.

In summary, it could be shown that the SX formation probability can be influenced by both the variation of the excitation density and the charge carrier density in the CAL. The mechanism behind the quenching of SX formation is the screening of the Coulomb interaction by the free charge carrier density in the background leading to a reduction of the exciton formation probability. For carrier concentrations below this limit, a reduction of the exciton binding energy is observed.

An exact quantification of these processes remains a difficult task, though, because the link between hydrogen-induced potential wells and the presence of the SX complicate any analysis. This complex role of the hydrogen-induced CAL for any HIOS employing FRET or other transfer processes that include the SX, has to be borne in mind: The presence of the CAL is necessary for the formation of SX species, but an increasingly high charge density at the surface may screen the SX from the (hybrid) interface. Obviously, rigorous experimental testing of these suggestions at realistic interface is highly desirable.

### 3.2.6 Stability of the Surface Exciton

The suggested important role of the SX for interfacial electronic processes in ZnO-based hybrid systems requires stability with respect to surface contaminants, since industrial production processes do not reach the level of cleanliness that is present in a UHV system. The supposed

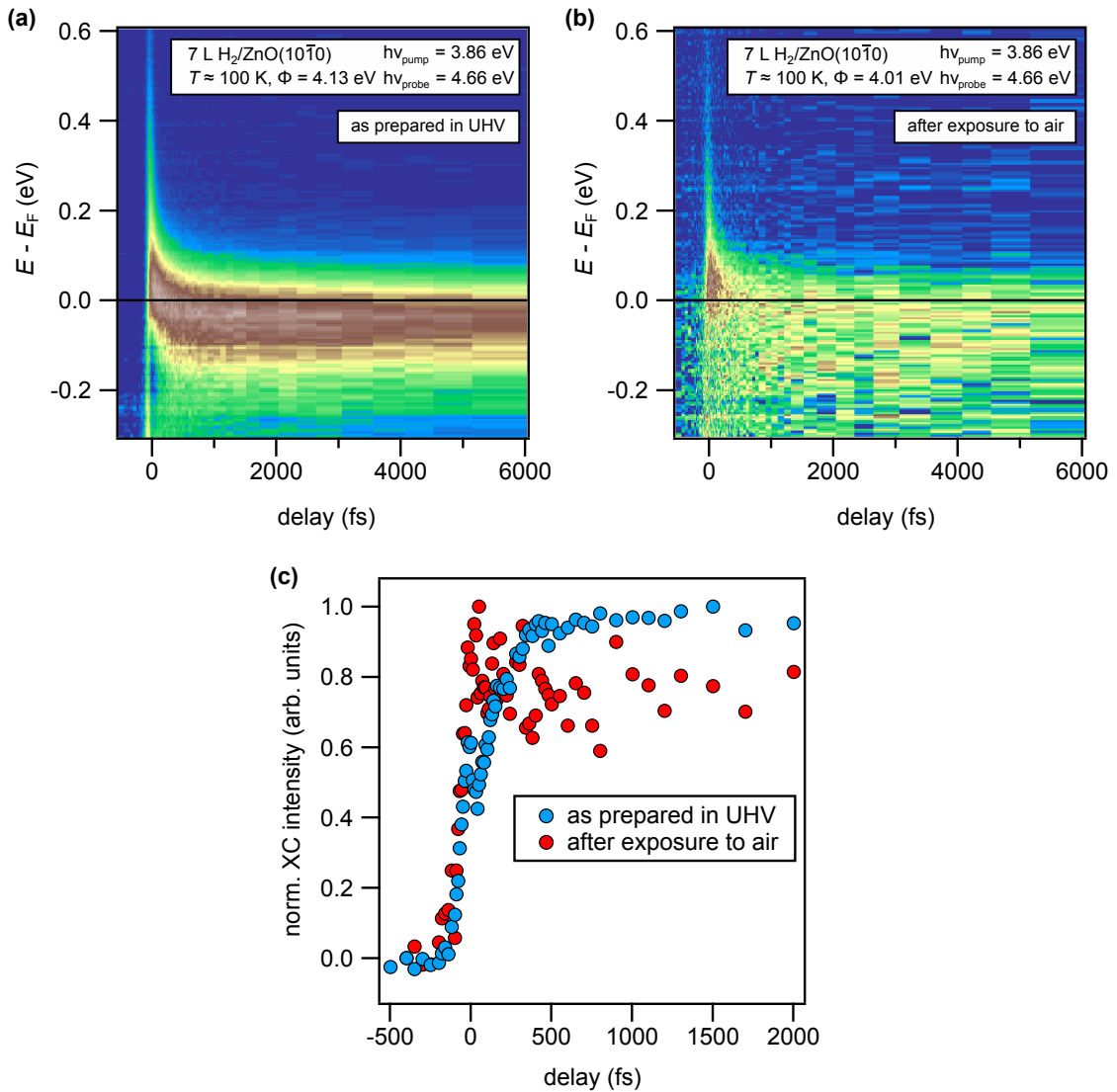


**Figure IV.33:** TR-2PPE measurements of the  $ZnO(10\bar{1}0)$  surface showing the effect of exposing the sample to air. (a) Two-dimensional plot of a reference measurement of 7 L  $H_2/ZnO(10\bar{1}0)$ , measured at 100 K. (b) Plot of a measurement taken with the same parameters as in (a), but after exposing the sample to air outside the UHV system for  $\approx 1$  min. The typical SX signature below  $E_F$  is still present, however, the signal-to-noise ratio is drastically reduced. (c) XC traces of the exciton signature showing the increase of the 2PPE signal in the energy range between 0 eV and  $-0.2$  eV relative to  $E_F$ .

location of the **SX** below the ZnO surface (see Section 3.2.4) may have a “protective” effect. However, the dependence of the **SX** on the local potential and the related complex interplay with hydrogen adsorbed at the ZnO surface may strongly influence the **SX** formation probability, also in case of other contaminants. In order to test the tolerance of the **SX** for the presence of such surface contaminants, the sample was exposed to the laboratory atmosphere by removing it from the **UHV** system for approximately one minute.

Before that, the freshly prepared ZnO(10 $\bar{1}$ 0) sample was exposed to a dose of 7 L hydrogen and a reference **TR-2PPE** measurement of the electron dynamics was taken, which is shown in Fig. IV.33(a). After exposure to atmosphere, the measurement was then repeated under identical conditions and laser fluences. The resulting two-dimensional plot of the **TR-2PPE** data after subtraction of the static background is shown in (b). As a consequence of the adsorption of surface contaminants, the work function of the sample was further reduced from  $\Phi = 4.13$  eV for the reference measurement to 4.01 eV after exposure to air. Another consequence of the presence of contaminants is a distinctly enhanced signal at the secondary electron cutoff (not shown) in the static spectra, indicating that the photoexcited electrons are subject to a high number of scattering events before emission. This high **PES** intensity at the secondary electron cutoff is generally a marker for rough and defective surfaces.

However, after subtraction of the strong background signal, the **SX** signature remains clearly visible, albeit with a drastically reduced signal-to-noise ratio. A closer analysis of the **XC** traces of the **SX** signature is depicted in (c). As done previously, the **XC** traces are averaged over the energy range from 0 eV to  $-0.2$  eV relative to  $E_F$ . The temporal evolution of the trace after exposure to air shows a more abrupt increase of the signal, however considerable noise obstructs a clear judgment. The comparably fast rise of the signal may also be due to the comparably strong signal of the ultrafast dynamics measured with the inverted order of pump and probe pulses (cf. Section 3.2.3). Eventually, this measurement shows that the **SX** species is present even at a contaminated or poorly prepared ZnO(10 $\bar{1}$ 0) surface that was subject to ambient conditions. This finding further corroborates the notion that the **SX** is located *below* the ZnO surface and, thus, it is separated from surface contaminants.

### 3.2.7 Cooling of Hot Excitons

After the discussion of **SX** formation and the interaction with free carriers the focus is now on the decay dynamics of the excitonic species. Here, we have to distinguish between the relaxation of “hot” excitons, which does not change the overall **SX** population, and excitonic decay via luminescence and radiationless processes which reduce the population.

Figure IV.34 shows **XC** traces measured at the ZnO(10 $\bar{1}$ 0) surface with a hydrogen dosage of 5 L and at temperatures ranging from 50 K to 300 Ks. The **SX formation** (left) shows no immediately visible change with temperature and a quantitative analysis of  $\tau_X$  reveals no discernible temperature dependence, either, yielding a time constant on the order of 200 fs at any temperature (cf. Section 3.2.3). However, regarding longer timescales on the order of a few ten picoseconds there is a clear dependency of the **SX** population on temperature. With increasing temperature the reduction of the **SX** signature with time becomes more pronounced. While for temperatures of 50 K and 100 K the signal reduction from 1 ps to 80 ps is on the order of 20 %, there is a distinct additional decay process visible for 200 K and 300 K. The quantitative

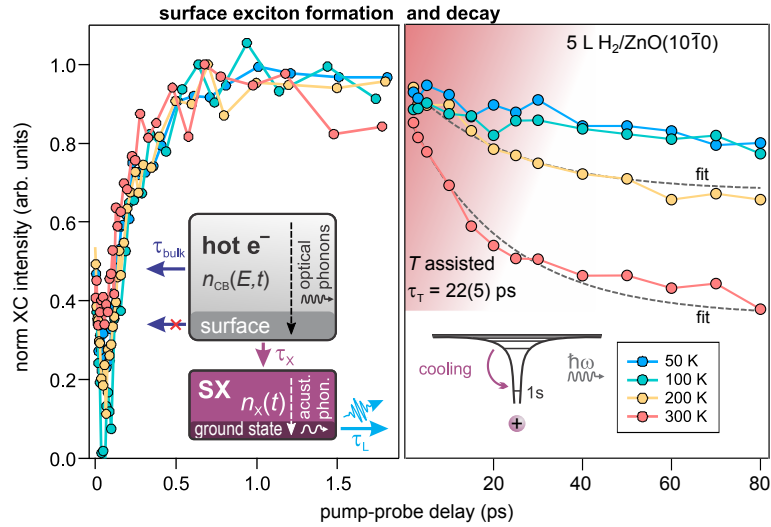


**Figure IV.34:** Normalized XC traces of the SX signature for different temperatures. Temperature variations between 50 K and 300 K do not lead to changes in the formation dynamics of the SX. For timescales exceeding tens of picoseconds a comparably slow decay of the excitonic population can be observed, which appears to be thermally activated. For temperatures above 100 K the SX population shows a pronounced decay with a time constant of  $\approx 22$  ps, which is further intensified when the sample is heated to 300 K.

analysis of the decay timescales is hampered by the comparably low quality and limited temporal range of the data. To compare the temperature-assisted decay with later measurements, a single exponential decay was used as fit function for delays between 1 ps and 100 ps, as plotted in the figure. This procedure results in a time constant of 22(5) ps for the temperature-assisted decay for  $T = 200$  K and  $T = 300$  K. Remarkably, after the initial population decay, the SX shows a lifetime exceeding hundreds of picoseconds even for a temperature of 300 K (cf. Section 3.2.8). Apparently, exciton binding energy is high enough to prevent the thermally induced exciton dissociation also for the SX species. However, an analysis of the overall SX lifetime as a function of temperature requires further measurements.

The timescale of few ten picoseconds of the thermally activated population decay hints at a process which is based on phonon scattering: The cooling of “hot” excitons to the ground state via the emission of phonons. As discussed above in Section 3.1.1 there is strong Fröhlich coupling between excited electrons and LO phonons, and the same mechanism was found to be responsible for the relaxation of electrons to their emissive 1s, i.e.,  $\mathbf{K} = 0$  ground state in GaN [KAV<sup>+</sup>96] (cf. Section 5.2.1 of Chapter II). However, the slower scattering with acoustic phonons appears to be the overall rate determining process for reaching the excitonic ground state [HKB07, KAV<sup>+</sup>96], leading to picosecond dynamics. It must be clarified at this point, that a relaxation of excitons into the ground state does not reduce the overall population of the SX, but shifts its energies to lower values. The population reduction over tens of picoseconds observed in experiment can, thus, originate from exciton recombination processes, or, possibly, the exciton diffusion. The radiative recombination of excitons, i.e., luminescence, requires the

excitons to be in its ground state. As a consequence, it can be assumed that the observed decay is related to the thermalization of the **SX** which is assisted by higher temperatures. This is further corroborated by the coincidence of the thermalization time constant of  $\tau_T = 22(5)$  ps found in our experiments with the temporal onset of **PL** from the excitonic ground state: a **PL** rise time of  $\tau_R = 20$  ps was found by Wischmeyer et al. for surface-related excitons in ZnO nanowires [WVR<sup>+</sup>06].

However, the near-identical time constants (within a large  $\approx 25\%$  error) of the picosecond dynamics for the different temperatures measured in our experiment do not clearly imply a certain model of the exciton relaxation process. Furthermore, the fact that at the end of this relaxation process a different plateau of population is reached for different temperatures hints at separate populations that undergo different relaxation or diffusion processes. This is a particularly important issue for the **2PPE** experiments presented here since the spectral features of hot electrons and excitons smoothly meld due to their energetic overlap and the limited energetic resolution of the experiment. In earlier experiments on similar systems, often nontrivial exciton formation and relaxation/thermalization dynamics were found indicating the complexity of excitonic processes especially in spatially restricted systems [DSO<sup>+</sup>90, YJLH<sup>+</sup>12, TKK<sup>+</sup>15].

As a consequence, complementary experiments using optical techniques, such as **electronic sum frequency generation (eSFG)** [Fog15], and also optical pump and terahertz probe spectroscopy are highly desirable in order to fully unravel the complex electron and quasiparticle thermalization processes at the ZnO(10 $\bar{1}0$ ) and ZnO(000 $\bar{1}$ ) surfaces.

### 3.2.8 Surface Exciton Lifetimes

This section focuses on the comparably slow decay of the overall excitonic population, i.e., the **SX** lifetime which is beyond the sub-100 ps timescale examined in the previous sections. A first hint that there is a long-lived feature which is energetically consistent with the exciton in ZnO was given by Tisdale et al. [TMN<sup>+</sup>08]. The authors concluded that above-gap optical excitation leads to an *indirect* population of an excitonic state close to  $E_F$  with lifetimes  $> 100$  ps. However, the used photon energy of  $\approx 4.4$  eV and the high repetition rate of the laser of 76 MHz prohibited any further insights into the characteristics of the excitonic species.

In our experiments, the **SX** signature could be detected for delays as large as 500 ps.<sup>16</sup> This makes it necessary to test whether the **SX** population has decayed before the experiment is repeated, i.e., the next sequence of pump and probe laser pulses arrives at the sample, and it was found, that the **SX** population has completely decayed after a time 5  $\mu$ s.

To access and quantify the **SX** lifetime more precisely, pump-probe delays of up to 200 ps were used to record **XC** traces. An exemplary trace measured at the H<sub>2</sub>/ZnO(10 $\bar{1}0$ ) surface at  $T = 100$  K is depicted in Fig. IV.35. The data was fitted over the whole delay range to a modified version of Eq. IV.10: The delay was separated into two components which describe (i) the thermalization time constant  $\tau_T$  and (ii) the time constant comprising all other excitonic decay processes  $\tau_L$ .

<sup>16</sup>The experiment is limited to comparably short sub-nanosecond timescales, because of the length of the used delay stages.

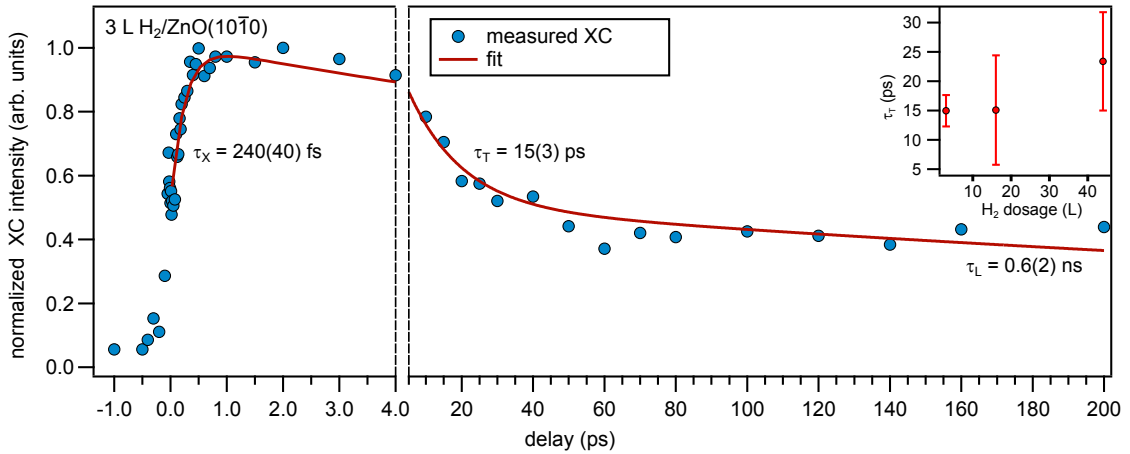


**Figure IV.35:** Normalized XC trace of the SX signature for pump-probe delays up to 200 ps. A fit to the data based on Eq. IV.10 yields a time constant of  $\tau_T = 15(3)$  ps for the comparably fast decay. For delays  $> 100$  ps an apparent plateau of the SX population is reached. The inset shows  $\tau_T$  for varying hydrogen dosages.

The characteristic delayed rise of the SX population with a time constant of  $\tau_X = 240(40)$  fs is followed by the comparably fast decay  $\tau_T = 15(3)$  ps which was attributed to the cooling of hot excitons, as discussed in the previous section. As a result the overall SX population is reduced approximately by half. Subsequently, the decay dynamics almost come to a halt on the timescale accessible by the experiment. From the fitting procedure, the time constant of this slow decay process which defines the lifetime of the SX is determined as  $\tau_L = 0.6(2)$  ns. Thus, the dynamics of the SX span timescales differing by more than three orders of magnitude, which illustrates the diversity of the occurring elementary processes (cf. Section 5.1 of Chapter II). It is noteworthy, that the time constant  $\tau_L$  in this experiment is comparable to the slow decay component of the PL of SX in ZnO nanowires, which amounts to 0.55 ns at a sample temperature of 50 K [WVR<sup>+</sup>06]. This corroborates the assignment of  $\tau_L$  to the radiative recombination of the SX species in our experiment.

It was also tested, whether both the thermally activated decay with time constant  $\tau_T$ , as well as  $\tau_L$  show a distinct dependence on hydrogen dosage. Concerning  $\tau_T$ , the resulting values show no dependence on hydrogen dosage for the comparably low dosages between 3 L and 44 L, as depicted in the inset of Fig. IV.35. Within the experimental uncertainty, these values are identical or compatible with those derived by a single exponential fit in the previous section. For  $\tau_L$  the values vary between 0.2 ns and 2 ns, which is a testament to the uncertainty of the fit over the limited range of pump-probe delays. In sum, the longevity and prevalence of the SX species make it an important participant in many kinds of electronic processes at the ZnO surface and at functional interfaces. A complete assessment of its lifetime requires additional experiments, preferentially with surface sensitive optical techniques.

### 3.3 Conclusion

The previous sections give a comprehensive overview of the electron and quasiparticle dynamics at the ZnO(10 $\bar{1}$ 0) surface which exhibit relaxation processes that comprise timescales from the femtosecond to the nanosecond regime. It was shown that these dynamics are particularly complex, because different electronic and excitonic species coincide both energetically and locally in the ZnO(10 $\bar{1}$ 0) surface region. The resulting interplay between the free carriers in the CAL, the hot electrons in the ZnO CB and the long lived surface exciton (SX) could be described with the available experimental tool: TR-2PPE. However, a complete theoretical description of the many-body physics occurring at the ZnO surface after optical excitation is still highly desirable, in particular to understand the manifold of charge and energy transfer processes which occur at the interfaces of HIOS.

The measurements presented here show that the dynamics of hot electrons in the ZnO CB are determined by the ultrafast scattering with LO phonons via Fröhlich coupling. Due to the strength of the e-ph coupling the timescales of electron relaxation are among the fastest observed in semiconductors, taking on values on the order of 10 fs for sufficient excess energies. This finding is in accord with previous results from 2PPE measurements [TMN<sup>+</sup>08]. In addition, the effect of charge screening on the CB dynamics was examined. Utilizing the findings presented in Section 2, the carrier density in the CAL was increased by hydrogen adsorption. As a result, the e-ph coupling was reduced which manifested itself in a significant increase of the decay times of the hot electrons.

Apart from the relaxation pathways of hot electrons it was possible to identify and characterize an excitonic species – the SX – at the ZnO(10 $\bar{1}$ 0) and (000 $\bar{1}$ ) surfaces. This species is located in the sub-surface region of the ZnO, making it comparably insensitive to surface contamination and, possibly, to intentionally adsorbed molecular layers. Again, the interplay between the SX and the charge carriers in the CAL was examined. It was found that the presence of the SX is strongly connected to the occurrence of surface potential wells, which can be created intentionally by the adsorption of electron donors, such as hydrogen. This way, we were able to experimentally corroborate the strongly localized character of these wells, which adds a microscopic and, thus, more precise view to the description of band bending at surfaces. As expected, the free carriers in the CAL modify the SX formation process, as the Coulomb interaction between excited electron and hole is screened and a quenching of the SX signature is observed.

Formation of the SX is observed on a timescale of 200 fs, which is considerably shorter than previously reported values which showed a wide range of values ranging from few picoseconds to tens of picoseconds. Since our experiments measures the actual population of electronic states in contrast to purely optical techniques, this work may, thus, contribute to the long standing debate of exciton formation mechanisms in semiconductor materials, especially TCOs. Nevertheless, the special properties of the ZnO surfaces have to be kept in mind, which might lead to different relaxation dynamics in the bulk of the material compared to the surface.

It was found that the decay dynamics of the SX population happen on two different timescales: A comparably fast process which is enhanced by an increase in temperature and which exhibits a time constant  $\tau_T$  on the order of 20 ps and a significantly slower decay attributed to mainly radiative recombination with a time constant  $\tau_L \approx 0.5$  ns. These characteristic time constants

**Table IV.1:** Characteristic time constants of *SX* formation and decay at the ZnO(10 $\bar{1}0$ ) surface.

type of process	symbol	timescale
formation	$\tau_X$	200 fs
thermalization/thermal dissociation	$\tau_T$	20 ps
decay/luminescence	$\tau_L$	0.5 ns

of the *SX* are summarized in Table IV.1, and for an overview in literature values of excitonic processes in ZnO see Ref. [Fog15].

The experimental results presented in this work may, thus, stimulate further further experimental and theoretical endeavors towards a complete description of the complex many-body electronic and excitonic processes at ZnO and TCO surfaces in general.

## 4 Hybrid Interfaces Based on ZnO(10 $\bar{1}0$ )

The understanding of the pristine ZnO surfaces with respect to their surface electronic structure and the excited states' dynamics is a first step towards the fundamental understanding of hybrid interfaces. The *next* step comprises the analysis of a model hybrid interfaces with a  $\pi$ -conjugated molecule adsorbed on the well-defined ZnO(10 $\bar{1}0$ ) surface. Pyridine (C<sub>5</sub>H<sub>5</sub>N) is an ideal candidate, as it is already used as docking group in metal–organic interfaces [HRZB07, WBB<sup>+</sup>09] with the potential to create very low work function electrodes [ZFHS<sup>+</sup>12]. Furthermore, it is computationally tractable because of its comparably small size.

Section 4.1 focuses on the effects of pyridine adsorption on the ZnO(10 $\bar{1}0$ ) surface with respect to the changes of the surface electronic structure, in particular the surface dipole. These changes have significant impact on the interfacial energy level alignment and the resulting device efficiency, as explained in Section 4 of Chapter II. DFT calculations, which were carried out by Oliver Hofmann et al., complement the experimental results. The results, which demonstrate that pyridine adsorption leads to an extraordinarily strong work function reduction of  $\approx 2.9$  eV, were published in Ref. [HDX<sup>+</sup>13]. This effect can be linked to the negative electron affinity  $\chi$  of the molecules, which prevents any Fermi level pinning effects.

On the path towards more realistic and functional interfaces, the complexity of the adsorbate molecule was increased by using a novel molecular species, which features five additional phenyl rings attached to the pyridine docking group, termed **5-phenyl-pyridine (5P-Py)**. Thereby, the energy gap of the molecule was significantly reduced compared to pyridine and the thermal stability was enhanced. The **5P-Py** exhibits an alignment of the frontier orbitals relative to the ZnO bands which corresponds to the adsorption-induced surface dipole, i.e., it follows Anderson's rule. The absolute energy of the **LUMO** can be measured using **2PPE**. Further, the transient population of the **LUMO** by injection of electrons from the ZnO substrate and the subsequent decay of this excited state through charge transfer from the molecule to the ZnO **CB** are demonstrated. The resulting dynamics of the transient state resulting from this **charge transfer (CT)** excitation process gives insight into the electronic coupling strength across the hybrid interface.

## 4.1 Pyridine as Model $\pi$ -Conjugated Surface Modifier

The alignment of energy levels at a hybrid interface crucially determines the efficiency of charge transfer by influencing the electronic coupling of energy levels. Furthermore, the barriers for charge injection and extraction are essentially determined by the energetic position of the molecular frontier orbitals relative to the Fermi level, as described in Section 4 of Chapter II. As a consequence, low work functions are desirable for any layer that either injects electrons into or collects electrons from the LUMO of the active layer.

In this work pyridine molecules, which were introduced in Section 4.2.1 of Chapter II are used to tune the work function  $\Phi$  of the ZnO(10 $\bar{1}$ 0) surface. As depicted in Fig. II.6, these molecules consist of a benzene ring where one carbon atom is replaced by a nitrogen atom, resulting in a static dipole moment of the overall molecule of  $\mu_{\text{mol}} = 2.2$  D [DWG54]. The electron affinity of pyridine is negative with  $\chi = -0.62(5)$  eV [Nen75], which should inhibit any Fermi-level pinning (see Section 4.2 of Chapter II).

Under the assumption of a homogeneous, ordered growth of the adlayer, the adsorption-induced work function change is determined by the area density of dipoles  $\mu$  and their individual strength. It should be noted that  $\mu$  does not consist only of the static dipoles, but includes further effects such as bond dipole formation, depolarization and band bending. These effects are not known a priori and have to be measured or computed for every individual interface.

In this section it is demonstrated that a single monolayer (ML) of pyridine adsorbed on freshly-prepared ZnO(10 $\bar{1}$ 0) surfaces leads to a work function reduction of as much as  $\Delta\Phi = -2.9$  eV. The adsorption geometry, binding mechanism, and interface dipoles are studied for a variety of pyridine coverages using PES, TPD, and DFT. All DFT calculations and the resulting adsorption geometries together with the corresponding images were provided by Oliver Hofmann in the course of a joint experimental and theoretical work. Extensive details regarding the computational methods can be found in the corresponding paper [HDX<sup>+</sup>13].<sup>17</sup>

### 4.1.1 Pyridine Layer Preparation and Characterization of the Adsorption Geometry

Pyridine (*Sigma Aldrich*, 99.8% purity) was first cleaned from exhalable contaminants by freeze-pump-thaw cycles (see Section 2.4.2 of Chapter III) and then dosed onto the freshly prepared, hydrogen-free ZnO(10 $\bar{1}$ 0) surface via the pinhole doser (see Fig. C.6). The work function of the ZnO(10 $\bar{1}$ 0) surface was routinely measured before adsorption and a value of  $\Phi_{\text{pristine}} = 4.52(5)$  eV was determined for the pristine surface. The sample temperature was held at  $\approx 100$  K during dosing to prevent unintentional desorption.

The thickness of the pyridine layers was monitored by thermally programmed desorption (TPD), with the QMS tuned to the mass of the pyridine molecule of 79 u (see Section 2.5.1 of Chapter III). The heating rates during desorption were between 8 K min<sup>-1</sup> to 60 K min<sup>-1</sup>. An exemplary TPD trace is shown in Fig. IV.36(a). The central feature is the pronounced and sharp adsorption onset at  $\approx 130$  K which is caused by desorption of the multilayer. The rest of the TPD trace consists of a broad continuum which extends up to  $\approx 450$  K. Within the continuum,

<sup>17</sup>In brief, the calculations were performed using the Perdew-Burke-Ernzerhof (PBE) generalized gradient functional and the Heyd-Scuseria-Ernzerhof (HSE) hybrid functional together with the van der Waals scheme of Tkatchenko and Scheffler.

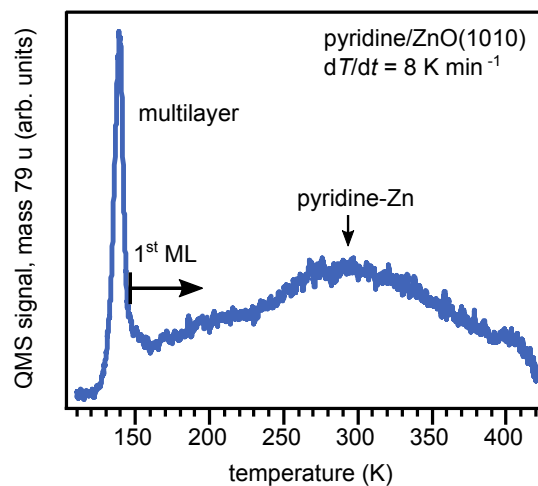


**Figure IV.36:** TPD trace of the pyridine adsorbed at the  $\text{ZnO}(10\bar{1}0)$  surface. The TPD signal shows a characteristic peak at  $\approx 140$  K which is indicative of multilayer desorption. At  $\approx 300$  K the supposed broad peak originating from pyridine–Zn bonds is indicated [HKW<sup>+</sup>00]. The integral of the signal is used for adlayer thickness calibration.

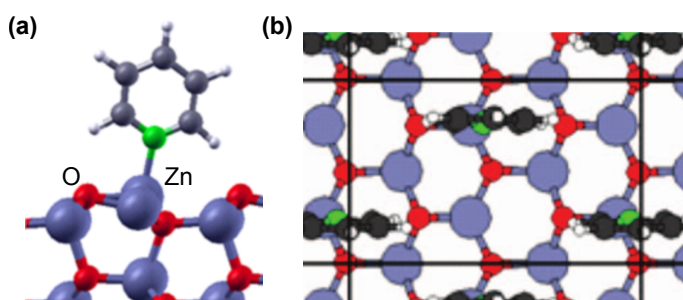


**Figure IV.37:** Pyridine adsorption geometry on the  $\text{ZnO}(10\bar{1}0)$  surface resulting from PBE+van der Waals (vdW) calculations: (a) Side view showing the bond between N and surface Zn atoms, and (b) top view of the unit cell at full coverage. Image provided by O. Hofmann

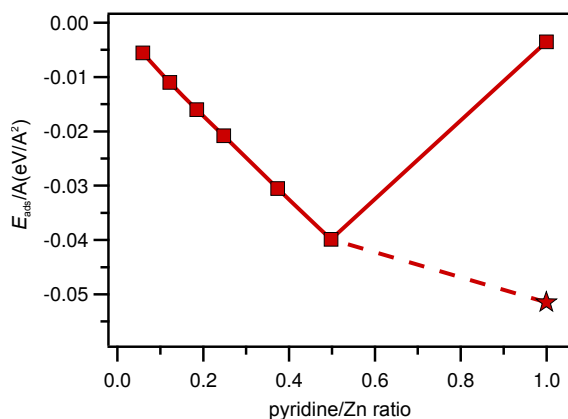


**Figure IV.38:** Calculated absorption energy (PBE+vdW) per unit area as a function of the ratio between pyridine and surface Zn atoms resulting from Eq. IV.11. Dashed line and open star denote the formation of an amorphous layer on top of the ordered first layer. An amorphous layer is most likely to form as every *second* surface Zn atom is covered with a pyridine molecule. Data courtesy of O. Hofmann.

two broad signatures can be identified, one comparably weak at  $\approx 200$  K and one dominating at  $\approx 300$  K. An identification of these two features is possible, when one compares the TPD trace with those measured at the two polar surfaces by Hövel et al. [HKW<sup>+</sup>00]. The authors assign a broad adsorption peak at approximately 365 K to the pyridine–Zn bond and a peak at 225 K is assigned to the pyridine–O bond.<sup>18</sup>

The dominance of the signature of the pyridine–Zn bond in our data indicates the prevalent occurrence of this bond at the mixed-terminated surface, which is further corroborated by the higher binding energy of the pyridine–Zn bond found by Hövel et al.: In that work the bond energies were determined by a Redhead analysis (see Ref. [Kin75]) of the TPD traces, which yielded  $57 \text{ kJ mol}^{-1}$  for the O-terminated surface and  $112 \text{ kJ mol}^{-1}$  for the Zn-terminated surface.

Further insight into the atomic structure of the pyridine/ZnO( $10\bar{1}0$ ) interface can be gained from the DFT calculations provided by Oliver Hofmann. It is found that, at low coverage, single molecules can only adsorb in one stable geometry, which is in contrast to metals, where often several different structures are observed [NR92]. The structure resulting from the calculations is displayed in Fig. IV.37. In (a) it shows the bond of the pyridine molecule to a surface Zn atom via the nitrogen electron lone pair and the molecule stands upright with a small tilt angle of  $15^\circ$ , which is independent of coverage. The top view in (b) shows the orientation of the aromatic plane along the (1120) crystal direction. This geometry is in excellent agreement with the NEXAFS study by Walsh et al. for a coverage of  $0.10(5)$  ML [WDM<sup>+</sup>93], who found a tilt angle of  $10^\circ$ .

More information on the adsorption geometry and the strength of the pyridine–Zn bond can be deduced from the coverage-dependent binding energy which was calculated as

$$E_{\text{ads}} = (E_{\text{sys}} - E_{\text{mol}} - E_{\text{ZnO}}), \quad (\text{IV.11})$$

<sup>18</sup>Please note, that temperature comparisons between different TPD experiments may vary, especially when different heating rates are used.

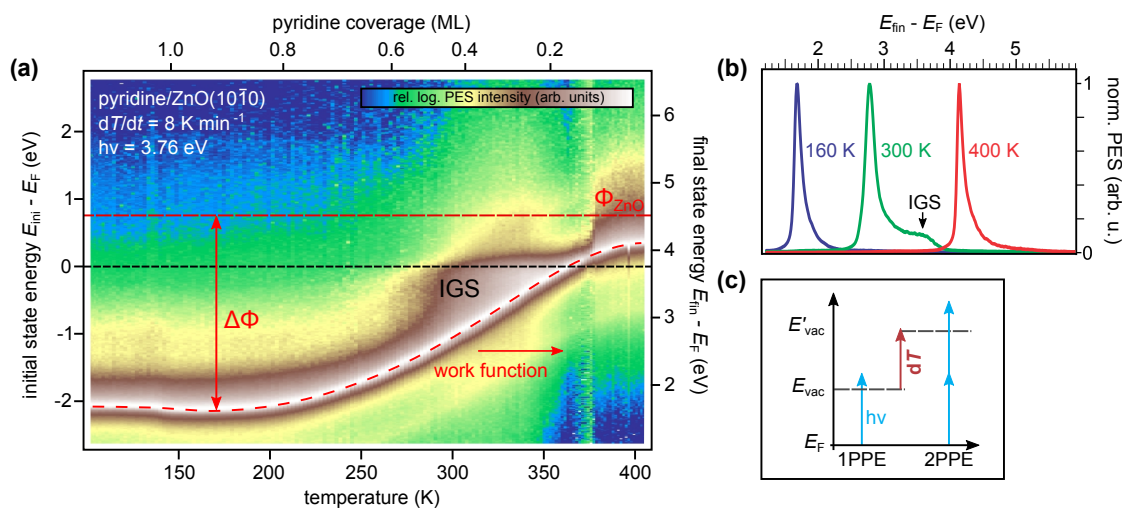


**Figure IV.39:** Plot of the PES signal of pyridine/ZnO(10 $\bar{1}$ 0) during sample heating and, thus, evaporating of the pyridine adlayer. (a) Two-dimensional false color representation of the measurement showing the essential features of the PES spectra. Most importantly, the drastic shift of the secondary electron cutoff which indicates the work function shift  $\Delta\Phi$ . The work function can be directly read from the position of the cutoff relative to the final state energy axis. For coverages from 0.6 ML to 0.2 ML an IGS is clearly visible. (b) Exemplary spectra taken at different temperatures showing predominantly the secondary electron signal and, for 300 K the IGS signature. (c) Excitation scheme depicting the transition from a 1PPE to a 2PPE process due to the increase of  $\Phi$  in the course of the measurement.

with  $E_{\text{mol}}$  the energy of the free molecule,  $E_{\text{ZnO}}$  the energy of the isolated ZnO(10 $\bar{1}$ 0) crystal, and  $E_{\text{sys}}$  the energy of the combined system. For the energetically favorable structure shown in Fig. IV.37, and divided by the area  $A$  per molecule, the binding energies are shown in Fig. IV.38. There is a pronounced minimum found at a coverage where pyridine is adsorbed at every *second* surface Zn atom. This geometry is shown in Fig. IV.37(b). Note that an increase of the density of pyridine molecules with the same geometry destabilizes the adlayer as the binding energy is greatly reduced. Instead, the calculations hint at the formation of an amorphous pyridine layer which is not connected to the substrate surface, shown as star symbol in Fig. IV.38. It is henceforth well-justified to assign the full monolayer coverage  $\Theta = 1.0$  to the adsorption geometry shown in Fig. IV.37(b), where every second Zn atom is covered by a pyridine molecule. This finding is consistent with the apparently zeroth order desorption peak at low temperature shown in the TPD trace, which is indicative of the desorption of an amorphous bulk layer. Furthermore, it should be noted that an amorphous multilayer does not add to the net dipole moment at the surface, which means that no changes to the work function are expected. This allows a precise assignment of pyridine coverage to surface work function as will be demonstrated in the next section.

#### 4.1.2 Giant Work Function Reduction

The work function changes induced by formation of ordered pyridine overlayers were measured by PES using a photon energy of  $h\nu = 3.76$  eV. In order to gather data for a high number of

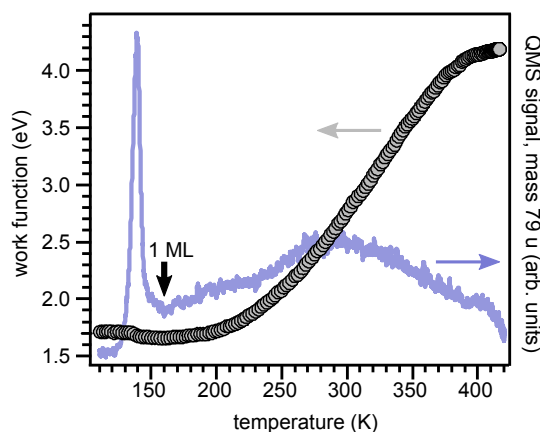


**Figure IV.40:** Work function of the pyridine/ZnO( $10\bar{1}0$ ) surface as a function of temperature, as derived from the spectra shown in Fig. IV.39. The overlying TPD trace shows that the minimum work function corresponds to the full single monolayer (black arrow).

different coverages up to  $\approx 1$  ML, first a multilayer pyridine coverage was prepared. Photoelectron spectra were then continuously recorded while pyridine was heated off at a slow rate of  $8 \text{ K min}^{-1}$ . Figure IV.39(a) shows the resulting spectra as a two-dimensional plot where the PES intensity is represented by the logarithmic colorscale. The most prominent feature of the spectra is the secondary electron cutoff, which is marked by the red dashed line. During desorption, the cutoff shifts by an energy of  $\Delta\Phi \approx 2.7 \text{ eV}$  towards higher energies. The corresponding work function  $\Phi$  can be directly read from the cutoff position relative to the final state energy axis on the right. Apart from the secondary electron signal there is one more discernible feature, which is an occupied initial state below  $E_F$ , denoted *in-gap state (IGS)*, for coverages from approximately 0.2 ML to 0.6 ML, which will be discussed in detail in Section 4.1.3. Exemplary spectra that illustrate these features, taken at different temperatures, are shown in Fig. IV.39(b). Note that during the course of the experiment the work function increase was sufficiently strong to cause a transition from a 1PPE to a 2PPE excitation scheme, which is schematically shown in (c). The resulting drastic reduction of PES signal intensity was compensated by an increase of the laser intensity in the course of the experiment. For the sake of clarity, these changes were normalized.

The values of the work function that result from the measurement shown in Fig. IV.39 are plotted as a function of sample temperature in Fig. IV.40. The comparison with the TPD trace which was measured for an identical coverage and at the same heating rate is the key for an assignment of the work function to a pyridine coverage  $\Theta$ . Remarkably, the minimum of the work function occurs at  $\approx 150 \text{ K}$ , which is exactly the temperature at which the multilayer has just desorbed. Thus, this coverage can be assigned to the complete first monolayer. Since TPD trace and sample work function are precisely aligned and the assignment of the full monolayer to a temperature is possible, the integral of the TPD trace can be used to assign every temperature value to a coverage [see, e.g., top axis in Fig. IV.39(a)]. On the other hand, the comparison between work function and TPD trace also indicates clearly, that the broad desorption peak corresponds to desorption of the first monolayer of pyridine.

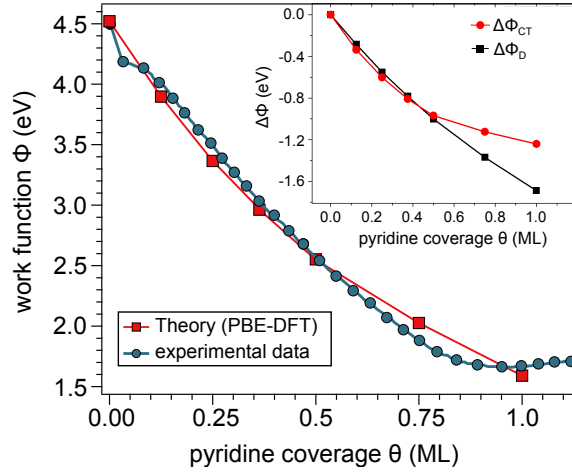


**Figure IV.41:** Comparison of the experimental and calculated work function shift  $\Delta\Phi$  at the pyridine/ZnO(10 $\bar{1}0$ ) surface, showing an excellent agreement of the values. The inset shows the coverage-dependent contributions to  $\Delta\Phi$ . Static dipole ( $\Delta\Phi_D$ ) and bond-induced charge transfer ( $\Delta\Phi_{CT}$ ) are collectively causing the large work function reduction.

Because the DFT calculations yield the work function change  $\Delta\Phi$  as a function of coverage  $\Theta$ , it is now possible to directly compare the theoretical and experimental results. Figure IV.41 displays a plot of the sample work function as a function of pyridine coverage. The experimentally determined work function of the pristine ZnO(10 $\bar{1}0$ ) surface of  $\Phi_{\text{pristine}} = 4.52(5)$  eV is used as reference point for the calculated change  $\Delta\Phi$  (red squares).

The measured work function at full monolayer coverage is  $\Phi(\Theta = 1) = 1.66(5)$  eV which amounts to a giant work function reduction of  $\Delta\Phi_{\text{max}} = -2.86(8)$  eV. Within the experimental error this is identical to the calculated value of  $\Delta\Phi_{\text{calc}} = -2.9$  eV. For intermediate coverage, there is also excellent agreement between experiment and theory, which further validates the computational approach to treat such hybrid interfaces. Any deviations between experimental and calculated values are within the experimental error of the coverage which is  $\pm 0.05$  ML.

Theory is also able to determine whether the extraordinarily large interface dipole originates from the intrinsic molecular dipole or from charge transfer to the substrate upon bond formation. For this purpose the total shift can be divided into a dipole part  $\Delta\Phi_D$  and a charge transfer-induced shift  $\Delta\Phi_{CT}$ :

$$\Delta\Phi = \Delta\Phi_D + \Delta\Phi_{CT}. \quad (\text{IV.12})$$

In this case,  $\Delta\Phi_D$  can be computed by considering a hypothetical free standing pyridine layer in vacuum, while  $\Delta\Phi_{CT}$  follows from Eq. IV.12, because  $\Delta\Phi$  is known. As a consequence,  $\Delta\Phi_{CT}$  describes the complete electronic response also of the substrate upon adsorption, which includes the possible formation of image dipoles. The results, which are depicted in the inset of Fig. IV.41, show that both the molecular dipole and the CT dipole act cooperatively and contribute equally to the overall  $\Delta\Phi$  up to a coverage of roughly  $\Theta = 0.5$ . For larger  $\Theta$ , the charge transfer-induced shift acts less strongly compared to the static dipole, indicating increased repulsive interactions through the ZnO substrate. Both components show depolarization for

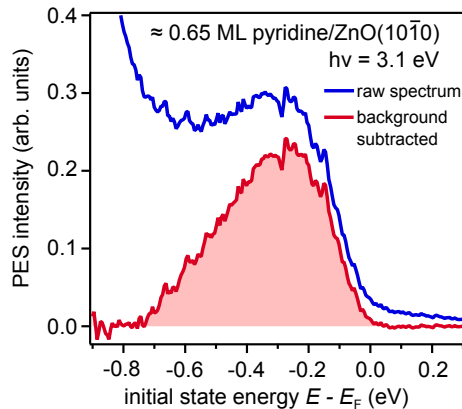


**Figure IV.42:** PES signature of the pyridine IGS measured with for a 0.65 ML coverage on the ZnO( $10\bar{1}0$ ) surface. After subtraction of the secondary electron background, the IGS signature (red curve) appears at broad peak with a maximum at 0.3 eV below  $E_F$ .

large coverages. Comparing the effect of the static dipole  $\Delta\Phi_D$  with that calculated using the simple Helmholtz equation II.4, the depolarization effect reduces  $\Delta\Phi_D$  by  $\approx 30\%$ .

#### 4.1.3 Modifications to the Electronic Structure: The In-Gap State

It was shown in detail in the previous sections that pyridine can drastically change the surface properties of ZnO( $10\bar{1}0$ ), possibly leading to lower energy barriers. The electronic structure of pyridine itself was not discussed so far, because the energetic location of its HOMO more than 9 eV below the vacuum level [AY84] mean that there are no electronic states accessible with the photon energies available in our laboratory. However, as shown in the coverage-dependent photoelectron spectra in Fig. IV.39, there is an occupied electronic state occurring for certain coverages. For coverages between approximately 0.2 ML and 0.6 ML this *in-gap state* (IGS) appears right below the Fermi level (see Section 4.3 of Chapter II for an introduction to IGS). An explanation for this vanishing of the IGS for higher coverages than 0.6 ML requires further investigations. It might be possible that the mechanism behind IGS formation and vanishing is similar for IGS and CAL, where the complete filling of all surface atoms at the ZnO( $10\bar{1}0$ ) surface resulted in the disappearance of the occupied electronic state (see Section 2).

A more detailed spectrum of the IGS measured with a photon energy of 3.1 eV and at a comparably high coverage of  $\approx 0.65$  ML is shown in Fig. IV.42. The state appears as a broad peak with an FWHM of  $\approx 0.4$  eV and with a maximum at  $\approx 0.3$  eV below  $E_F$ . Thus, it resembles the hydrogen-induced CAL signature, shifted to lower energies (see, e.g., Fig. IV.14). These kinds of IGS have recently been observed in a number of hybrid interfaces and their important role in energy level alignment at those interfaces has lately been recognized (see, e.g., Refs. [WSC<sup>+</sup>14, RKM15]). In the following section, where the pyridine molecule is replaced by a more complex relative 5P-Py, it will be shown that the IGS is most probably intrinsic to the N-Zn bond at the interface and that this state may serve as an initial state in a CT excitation experiment.

#### 4.1.4 Conclusion

The hybrid interface between pyridine and the ZnO(10 $\bar{1}0$ ) surface was characterized using TPD and photoelectron spectroscopy in conjunction with DFT calculations which were provided by Oliver Hofmann. Pyridine was chosen as model  $\pi$ -conjugated molecule with strong static dipole moment, and it was found that the ordered pyridine monolayer is capable of reducing the surface work function by the remarkable amount of 2.9 eV. The maximum work function shift occurs for an adsorption geometry where the molecules stand upright and every second surface Zn atom is covered with a pyridine molecule which binds to the Zn via the nitrogen lone-pair electrons. As a result the shift of  $\Phi$  can be traced back to the cooperative effect of the static molecular dipole and the dipole induced by electron transfer from the molecule into the substrate upon bond formation. A crucial factor that enables the very low work function is the negative electron affinity of pyridine. The energetic location of the LUMO above the vacuum level prevents Fermi level pinning. This principle of using strongly dipolar molecules with negative electron affinity may – in principle – allow work functions close to zero. As an example, hypothetically packing the pyridine molecules on the ZnO(10 $\bar{1}0$ ) surface more densely, so that every surface Zn atom is covered by a pyridine molecule, would lead to an overall work function of mere 0.3 eV. Further, the combination of hydrogen, which predominantly binds to surface O atoms, and pyridine on the ZnO(10 $\bar{1}0$ ) surface is a promising candidate for extremely low work functions.

Remarkably, the experimentally determined work function of 1.66(5) eV is already sufficiently small so that electron injection barriers should be lowered substantially. At the same time, pyridine is expected to improve the hole blocking abilities of the interface with ZnO, because the pyridine HOMO is strongly hybridized and exhibits only little DOS in the ZnO band gap (see Ref. [HDX<sup>+</sup>13] for details).

The drawback of using pyridine as an adsorbate on ZnO, which impedes its use in realistic devices, is its thermal instability. At room temperature, most of the pyridine will have evaporated, so that similar molecules, which exhibit stronger bonds to the substrate surface or among each other, have to be found.

What remains to be explored is the microscopic effect of pyridine or similar molecules on the electronic properties at the interface. Similar to the established description of the CAL, the effect of functional interfaces is usually described as an average over a certain area. However, the full understanding of such interfaces requires microscopic knowledge of the electronic properties exactly at the binding site of the functional molecule. For the case of hydrogen in Section 2 it was shown that these properties can vary strongly, even on an atomic scale. Tackling this issue in the future is desirable, but also very challenging for both experiment and theory.

## 4.2 The 5-Phenyl-Pyridine/ZnO(10 $\bar{1}$ 0) Interface – Level Alignment and Ultrafast Charge Transfer Dynamics

As a next step, following the rationale of increasing interface complexity, the interface between a *novel* organic adsorbate – 5-phenyl-pyridine (5P-Py) – and the ZnO(10 $\bar{1}$ 0) surface is analyzed. The 5P-Py molecule itself is a nonsymmetric derivative of the established and well-known chromophore *p*-sexiphenyl (*p*-6P) where one of the end carbon atoms is replaced with a nitrogen atom (see Fig. IV.43). The idea behind using this molecule is to maintain the ordered adsorption properties of pyridine, while achieving stability of the adlayer also at elevated temperatures. Further, the increase of the molecular chain length is expected to drastically reduce the optical gap of the molecule, so that above-band gap excitation becomes possible with visible or near-UV light pulses which are available in our experiment. This shrinking of the gap between molecular levels is analogous to the shrinking of energy intervals in a one-dimensional quantum well with increased well size [PAD08].

In this section, first experiments on the 5P-Py/ZnO(10 $\bar{1}$ 0) interface will be presented, which focus on the geometric structure of the interface, modifications to the interfacial electronic structure and resulting interfacial charge carrier dynamics. Due to the novel character of this interface, many details on the systematic experimental approach towards understanding the interface will be given, and the properties of the *p*-6P/ZnO(10 $\bar{1}$ 0) interface will be used as reference.

The growth of 5P-Py on ZnO and the resulting interfacial electronic structure are examined using both 1PPE and single-color 2PPE methods. It is found that the molecular layer can be prepared in a way that leads to an upright standing molecular orientation, which is accompanied by work function reduction by up to  $\Delta\Phi = -1.9$  eV, which is large but significantly smaller than the reduction achieved by pyridine adsorption. The resulting interfacial electronic structure is found to be more complex than that of the pyridine/ZnO interface. Apart from intense final state signatures, an unoccupied state below the vacuum level can be detected, which is attributed to the molecular LUMO, meaning that 5P-Py exhibits a positive electron affinity. In analogy to the pyridine/ZnO interface, an occupied IGS can be identified, which is energetically located below  $E_F$ .

The gained knowledge about the interfacial alignment of electronic levels is used to examine the charge transfer dynamics across the hybrid interface in a 2PPE experiment. By injecting electrons from the interface into the unoccupied molecular LUMO, the characteristics of this excited state can be monitored which reveals relevant details on interfacial electronic coupling and charge transfer processes at this interface. The resulting ultrashort lifetimes of the excited state indicate that in an excitation scheme where the hole is not located in the molecular layer, but in the interfacial IGS, no stable long-lived charge transfer (CT) exciton is formed.

### 4.2.1 Preparation and Thickness Characterization of 5P-Py Adlayers

The 5P-Py molecules, despite being chemically almost identical to *p*-6P, have not been produced on a larger scale before. We were provided with sample molecules by the group of Stefan Hecht at the Humboldt University in Berlin who recently succeeded in developing a route to synthesize such nonsymmetrical, terminally substituted *p*-6P derivatives [GSH<sup>+</sup> 14].

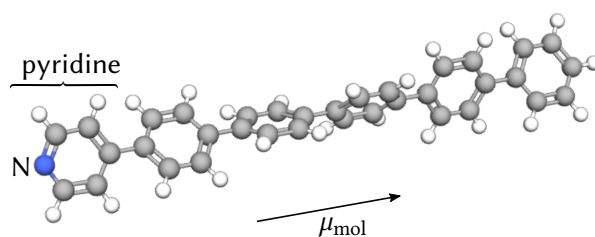


**Figure IV.43:** Representation of an isolated 5P-Py molecule with the terminally substituted end on the left and indicated dipole moment  $\mu_{\text{mol}}$ .

In contrast to pyridine, which is a liquid under standard conditions, 5P-Py is a slightly yellow powder. As a consequence, it could not be dosed onto the sample via the gas system, but had to be evaporated under UHV conditions using a Knudsen cell (see Section 2.4.2 of Chapter III). The evaporation temperature was on the order of 530 K and the layer thickness was monitored during the evaporation process using a quartz crystal microbalance (QCM) (see Section 2.5.2 of Chapter III). During the evaporation process the sample temperature was held constant at a temperature of 100 K. Before adsorption the ZnO crystal was freshly prepared, so that the surface did not exhibit metallic character.

To calibrate the thickness measurement, the mass density of *p*-6P of 1.102 g cm<sup>-3</sup> was assigned to the 5P-Py layer, as a value for 5P-Py was not available. This evaporation procedure led to highly controlled and reproducible adlayer growth with rates on the order of 1 nm min<sup>-1</sup>, because of the high precision of the QCM method.

The desorption of 5P-Py molecules from the ZnO(10 $\bar{1}0$ ) surface was monitored by thermally programmed desorption (TPD), which gives some insight into adsorption energies (see Section 2.5.1 of Chapter III). An exemplary TPD trace for a multilayer coverage of  $\approx 10$  nm 5P-Py on ZnO(10 $\bar{1}0$ ), which was recorded with a heating rate of 0.5 K min<sup>-1</sup> is shown in Fig. IV.44. The monitored signature corresponds to the molecular fragment with a mass of 80 u, which yielded a comparably strong signal compared to other expected fragments. The overall signal, however, was comparably weak, so that for (sub-)monolayer coverages barely any molecules were detected by the QMS.

For the thicker adlayer there is there is a signature at  $T \approx 520$  K which can be assigned to the desorption of bulk, i.e., multilayer 5P-Py, as it corresponds to the desorption temperature of bulk molecules in the Knudsen cell. The prominent desorption peak starting at 650 K remains present also at lower coverages, albeit at very low intensity. For this reason it can be assigned to the desorption of the first monolayer which is apparently strongly bound to the ZnO surface. Thus, compared to pyridine, a thermally highly stable interface could be produced.

#### 4.2.2 Complex Adsorption Geometry, Work Function Changes and In-Gap State

A model of an isolated 5P-Py molecule is shown in Fig. IV.43. The molecule is comparably flexible due to the C–C single bonds between the phenyl rings, which allows rotation. The twist angle between adjacent phenyl rings can be estimated from the angle in *p*-6P, which is on the

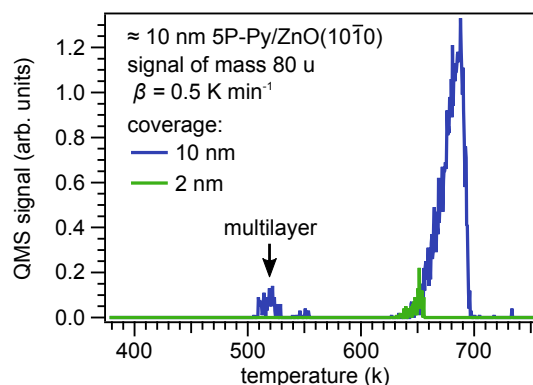


**Figure IV.44:** Representative TPD traces of  $\approx 10$  nm and  $\approx 2$  nm 5P-Py on ZnO( $10\bar{1}0$ ) recorded with a heating rate of  $\beta = 0.5$  K  $\text{min}^{-1}$  for a molecular fragment with a mass of 80 u. The peak at  $\approx 520$  K is assigned to the desorption of bulk 5P-Py, while the main peak can be assigned to the first layer.

order of  $35^\circ$  according to DFT calculations [PHHD14]. This is expected to cause a large Stokes shift, as it is observed in *p*-6P (cf. Section 4.2.3). Despite the commonalities between 5P-Py and *p*-6P the key difference – the nitrogen end atom – can be expected to cause significant differences in the interaction with the ZnO( $10\bar{1}0$ ) surface, because of static dipole of the 5P-Py molecule and the possible bond of the nitrogen end atom with the surface.

For *p*-6P adlayers on inorganic substrates several adsorption geometries have been found experimentally. As an example, *p*-6P is oriented with its long axis (*c*-axis) perpendicular to the surface after evaporation on a heated Ag substrate [NIE<sup>+</sup>95]. A recent study of *p*-6P on different ZnO surfaces showed that the molecules also form upright standing layers on the Zn-terminated ZnO(0001) surface, irrespective of the substrate temperature (for 290 K to 450 K) [BGS<sup>+</sup>10]. For the mixed-terminated ZnO( $10\bar{1}0$ ) surface, however, a flat-lying structure is formed, i.e., the *c*-axis is oriented parallel to the substrate surface, indicating a markedly stronger molecule–substrate interaction compared to the Zn-terminated surface.

Naturally, the question now is whether the adsorption geometry of 5P-Py on ZnO( $10\bar{1}0$ ) is governed by the pyridine-like character of the chain end, or whether it behaves like *p*-6P on the surface. Answering this question is complicated due to the fact that photoemission methods can only give indirect insight into surface morphology. For this study, a film with a thickness of 2 nm was prepared, which is analogous to the thickness of an upright standing layer of *p*-6P (see Ref. [BGS<sup>+</sup>10]) and the PES signal was measured using laser pulses with a photon energy of  $h\nu = 6.2$  eV.

Figure IV.45(a) shows a logarithmically scaled comparison of two photoelectron spectra of this 5P-Py/ZnO( $10\bar{1}0$ ) interface. The first spectrum (blue curve) shows the PES signal after dosing the 2 nm thick layer onto the cold (100 K) ZnO surface. The single discernible feature of this spectrum is the secondary electron cutoff at low energies. From the energetic position of the cutoff, the surface work function can be calculated as  $\Phi_{\text{cold}} = 3.4(1)$  eV, which is a slightly stronger shift than the  $\Phi_{\text{6P}} = 3.60$  eV observed for the *p*-6P/ZnO( $10\bar{1}0$ ) surface [BGS<sup>+</sup>10]. For higher 5P-Py coverages no further shift of the work function is observed, which indicates that the nominally 2 nm thick layer completely covers the surface so that there are no remaining

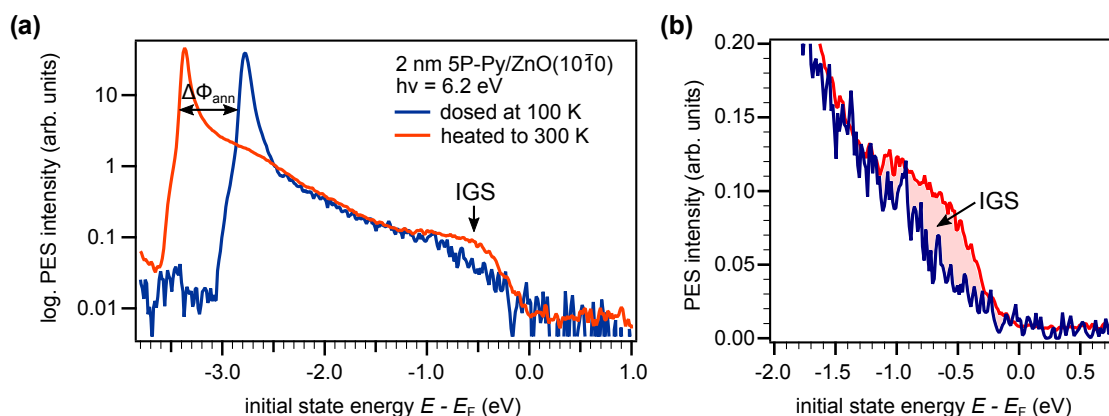


**Figure IV.45:** Photoelectron spectrum of the 5P-Py/ZnO(10 $\bar{1}$ 0) interface measured with  $h\nu = 6.2$  eV photons showing the change of the spectrum with temperature. (a) The spectrum right after dosing the molecules onto the cold (100 K) sample (blue curve) shows no distinct features apart from the secondary electron cutoff. After heating the sample to 300 K (red curve) the secondary cutoff has shifted to lower energies. Further, an occupied electronic state appears below  $E_F$ . (b) Close-up of the occupied IGS  $\approx 0.7$  eV below  $E_F$ .

uncovered portions of the ZnO surface. Regarding the weak TPD signal from the monolayer for such coverages (see Fig. IV.44), the complete covering of the ZnO surface seems slightly surprising. However, there might be complex reordering of the molecules during heating as will be discussed in the following.

Towards higher energies the photoemission (PE) spectrum consists of a broad and weak featureless tail extending toward  $E_F$  which mainly originates from the secondary electron background and possibly a number of occupied defect states. At  $E_F$  there is no PES signal, showing that the interface exhibits semiconducting character. Apparently, this measurement does not yield a clear information about the energetic location of any occupied states, such as the HOMO.

The second spectrum shown in red corresponds to the interface after an annealing process to  $T = 300$  K for a few minutes. Please remember, that at this relatively low temperature no desorption occurs, so that the number of molecules on the ZnO surface remains unchanged. However, the annealing process leads to significant changes to the photoelectron signature: The secondary electron cutoff has shifted to lower energies, which means that the surface work function has been lowered to a value of  $\Phi_{\text{ann}} = 2.8(1)$  eV. Further, an occupied electronic state appears  $\approx 0.7$  eV below  $E_F$ , which is shown in detail in Fig. IV.45(b). This state closely resembles the interfacial IGS that was found at the pyridine/ZnO(10 $\bar{1}$ 0) interface (see Fig. IV.42). In addition to the IGS, there appears to be a weak signature at an initial state energy of  $\approx -2.8$  eV that does not belong to the secondary electron background, which will be discussed in detail in the next section.

This behavior strongly suggests that during annealing the adsorption geometry of the molecules must have changed. The work function reduction, which is now  $\Delta\Phi = -1.7$  eV relative to the pristine ZnO(10 $\bar{1}$ 0) surface, suggests that the static dipoles of the 5P-Py molecules are

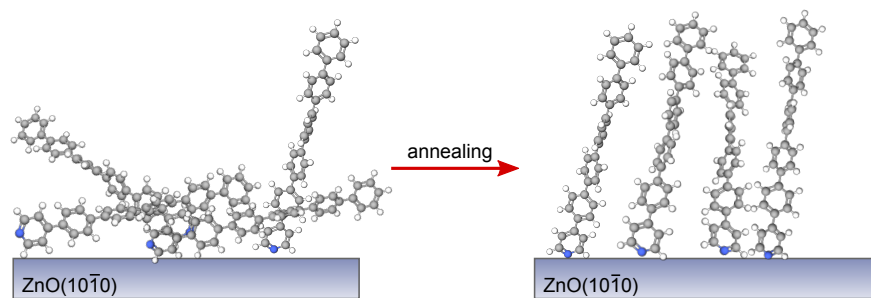


**Figure IV.46:** Artistic representation of the heat-induced ordering of the 5P-Py molecules on the ZnO(10 $\bar{1}$ 0) surface. Annealing leads to a morphology in which the molecules preferentially bind to the ZnO surface via the pyridine end group, resulting in an upright standing geometry. The absolute degree of order before and after annealing is not known so far.

aligned more closely along the surface normal, with the pyridine end pointing towards the substrate. In addition to the alignment of the static molecular dipole perpendicular to the substrate surface, any change in the bond between ZnO and molecules may also lead to an adsorption-induced dipole caused by charge transfer, as it occurred in case of the pyridine/ZnO(10 $\bar{1}$ 0) interface. The measured work function shift is still substantially lower than that caused by pyridine adsorption, which was on the order of  $\Delta\Phi = -2.9$  eV. This may be due to the probably positive electron affinity which allows pinning of the Fermi level as soon as the LUMO gets in resonance with  $E_F$ , or there might be different reasons, such as a lower degree of order or a larger adsorption angle.

In addition, the occurrence of the IGS, which was related to the bond between nitrogen and a surface Zn atom in case of pyridine adsorption (see Section 4.1.3), further supports the interpretation that the annealing of the interface leads to an ordered upright standing adsorption geometry of the 5P-Py molecules on the ZnO(10 $\bar{1}$ 0) surface. Figure IV.46 schematically shows this heat-induced reordering of the molecular layer. So far, it is not clear whether the achieved interface morphology cannot be changed further by varying the adsorption or annealing process. The reproducibility of surface work function and spectral features using the same annealing procedure in different experiments and at different coverages hints at a comparably stable morphology, though.

As a consequence, all photoemission experiments at the 5P-Py/ZnO(10 $\bar{1}$ 0) interface described in the following were conducted after sample annealing to 300 K to ensure a sufficiently ordered adlayer and reproducible conditions. The photoemission experiments were then all carried out after the sample had reached a temperature of  $\approx 100$  K again.

### 4.2.3 Optical Properties and Electronic Structure of 5P-Py

After this first characterization of the occupied electronic band structure at the interface, which bears some resemblance to that of the pyridine/ZnO interface, this section will focus on the *unoccupied* electronic states, which can be explored using 2PPE. As mentioned above, the chain

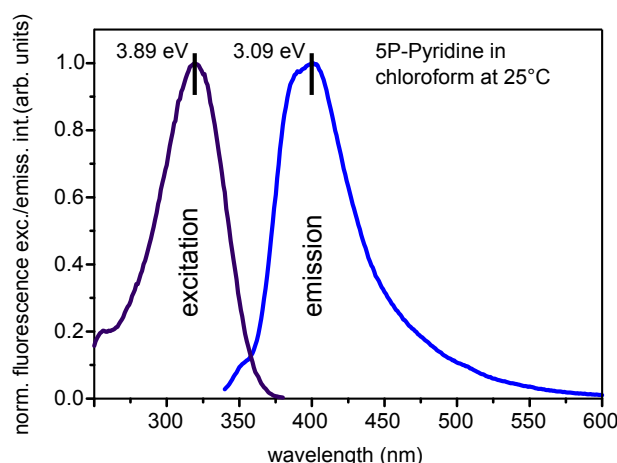


**Figure IV.47:** Normalized fluorescence excitation and emission spectrum of 5P-Py in chloroform at 25 °C. Data courtesy of Y. Garmshausen, HU Berlin.

of phenyl rings is expected to drastically reduce the optical gap in 5P-Py compared to pyridine, which may also lead to a shift of the LUMO below the vacuum level, as it is the case in *p*-6P.

As a starting point, the optical properties of the 5P-Py molecules in chloroform (CHCl<sub>3</sub>) solution at 25 °C are shown in Fig. IV.47, which was provided to us by Y. Garmshausen, HU Berlin. The highly emissive molecules exhibit a maximum in the fluorescence emission intensity at 401 nm (3.09 eV) and the fluorescence excitation spectrum, which corresponds to the optical gap of the molecules, shows a maximum at 319 nm (3.89 eV).<sup>19</sup> Compared to *p*-6P, the emission spectrum is red shifted by  $\approx 0.2$  eV, i.e., the 5P-Py molecule shows an even stronger Stokes shift which might be detrimental to the exciton migration efficiency [KGB<sup>+</sup>12], but limits the possibility of fluorescence reabsorption by the molecular layer itself.

Nevertheless, the increase of the molecular length has drastically reduced the optical band gap of the molecule compared to pyridine. How do the molecular electronic levels of 5P-Py align at the ZnO surface and is there a modification of the optical gap compared to the molecules in solution?

As a comparison, the optical gap of *p*-6P is on the order of 3.1 eV, and considering the exciton binding energy of  $\approx 0.4$  eV the transport gap has a size of  $\approx 3.5$  eV [BGS<sup>+</sup>10].<sup>20</sup> From UPS measurements it was then concluded that at the interface of flat-lying *p*-6P on the ZnO(10 $\bar{1}$ 0) surface the bands align in a so-called type-II way, i.e., the VBM–HOMO and CBM–LUMO energy offsets both have the same sign. This type of alignment is favorable for photovoltaic applications, as holes and electrons are driven away from the interface in different directions, comparable to a *p*–*n* junction. This is illustrated in the energy level diagram in Fig. IV.48 which was adapted from Ref. [BGS<sup>+</sup>10]. Please note that the positions of the unoccupied bands were not measured directly but calculated from the absorption spectra in that work.

In contrast to UPS measurements we can access the unoccupied band structure directly with

<sup>19</sup>Absorption spectra could not be obtained because of the low solubility and the resulting insufficient optical density of the molecules.

<sup>20</sup>See Section 3 of Chapter II for a discussion of energy level and gap assignments.

**Figure IV.48:** Energy level alignment at the  $p$ -6P/ZnO( $10\bar{1}0$ ) interface as determined in Ref. [BGS<sup>+</sup>10]. The positions of the occupied states were determined by UPS experiments and energy values for unoccupied states were obtained from absorption data and show a type-II alignment. Please note that the quoted energy values for the ZnO levels differ slightly from the values determined in this work.

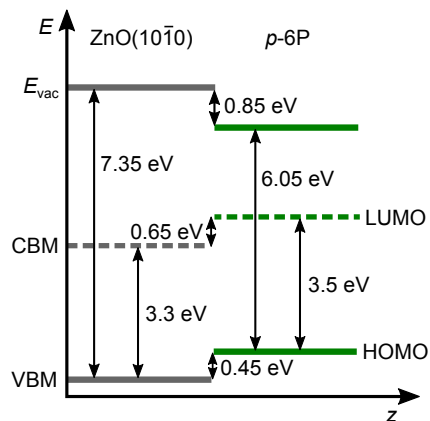
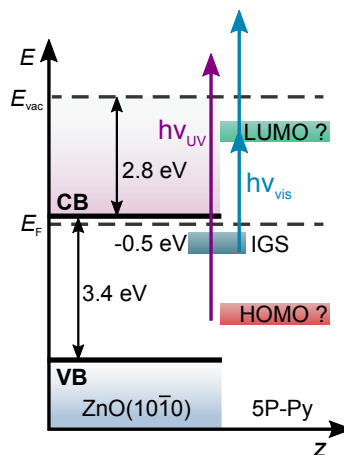


**Figure IV.49:** Energy levels and excitation scheme for single-color 2PPE experiments at the 5P-Py/ZnO( $10\bar{1}0$ ) interface.



the 2PPE excitation scheme (see Section 1.4 of Chapter III). Figure IV.49 displays the electronic levels at the 5P-Py/ZnO(10 $\bar{1}$ 0) interface as deduced from the experiments described previously. It also shows the different excitation pathways, 1PPE with  $h\nu_{UV} = 6.2$  eV, and single-color 2PPE with  $h\nu_{vis} \approx 2.3$ – $2.7$  eV, which are used to analyze the interfacial electronic structure.

Figure IV.50(a) shows a detailed 1PPE spectrum of a 2 nm ( $\approx 1$  ML) thin film of 5P-Py on ZnO(10 $\bar{1}$ 0) measured with  $h\nu = 6.2$  eV [cf. Fig. IV.45(a)]. The molecules were dosed onto the 100 K cold sample and then annealed to 300 K, as described above. The spectrum can be reproduced by a fit that combines the secondary electron background (double exponential shape) with two Gaussian peaks A and B. The peak positions resulting from the fit correspond to final state energies of 3.4 eV and 3.9 eV above  $E_F$ , respectively.

In order to make a clear assignment of the energies of these signatures, which might be occupied initial states or final states above  $E_{vac}$ , the photon energies were varied, as indicated in Fig. IV.49. By varying the photon energies and by using a 2PPE excitation scheme, it is possible to clearly distinguish between (i) occupied initial, (ii) bound intermediate, or (iii) final states above the vacuum level: When the kinetic energy of the photoelectrons is plotted as a function of photon energy, the peak positions shift with (i)  $2 \cdot \Delta h\nu$ , (ii)  $\Delta h\nu$ , or (iii) are independent of photon energy. This procedure is explained in detail in Section 1.4 of Chapter III.

In Fig. IV.50(b) an exemplary spectrum recorded with a photon energy of  $h\nu_{vis} = 2.51$  eV is shown. For this experiment, the thickness of the 5P-Py layer was increased to 7 nm ( $\approx 3.5$  ML) in order to increase the sensitivity for purely molecular electronic states, e.g., the LUMO. The work function of  $\Phi = 2.79$  eV is identical to that of the thin layer, indicating that second and third 5P-Py layer do not add to the overall surface dipole as described above, most possibly due to amorphous multilayer growth. In the high energy region, the 2PPE spectrum in (b) is subtly different from that shown in (a), because an additional signature C appears. Using the same fitting procedure which includes all three peaks, a final state energy of  $\approx 4.7$  eV can be deduced for signature C. Interestingly, signatures A and B are located at approximately the same final state energy, as that found in the 1PPE experiment: at 3.3 eV and 4.0 eV, respectively.

This fitting procedure was carried out for single-color 2PPE spectra with photon energies from 2.3 eV to 2.7 eV, the results of which are plotted in Fig. IV.50(c). The positions of signatures A and B show indeed no variation in their final state energy, which strongly suggests that these signatures belong to final electronic states above  $E_{vac}$ .

In contrast to that, signature C clearly varies as a function of photon energy. This variation can be approximated by a linear dependence  $\Delta E_C \approx \Delta h\nu$  which clearly suggests that C originates from a bound unoccupied state. The corresponding intermediate state energy that can be deduced from these measurements is 2.1(2) eV relative to  $E_F$ . Considering the work function of  $\Phi = 2.8$  eV, this results in a vertical binding energy (VBE) of  $\approx 0.7$  eV (cf. Section 3 of Chapter II).

Assuming that signature C originates from the molecular LUMO, it is possible to roughly estimate the energetic position of the HOMO from the optical data (Fig IV.47). With an optical gap of 3.9 eV and the LUMO VBE of  $\approx 0.7$  eV, the ionization energy of the HOMO can be expected to be on the order of  $E_{ion} = 4.6$  eV. The corresponding initial state energy would then be  $E - E_F = 1.8$  eV. This would mean that the HOMO signature overlaps with the prominent final state peaks (see Fig. IV.50), which might be a reason, why it is not resolved in our experiment. The above estimate of the energetic position of the HOMO neglects both the exciton binding

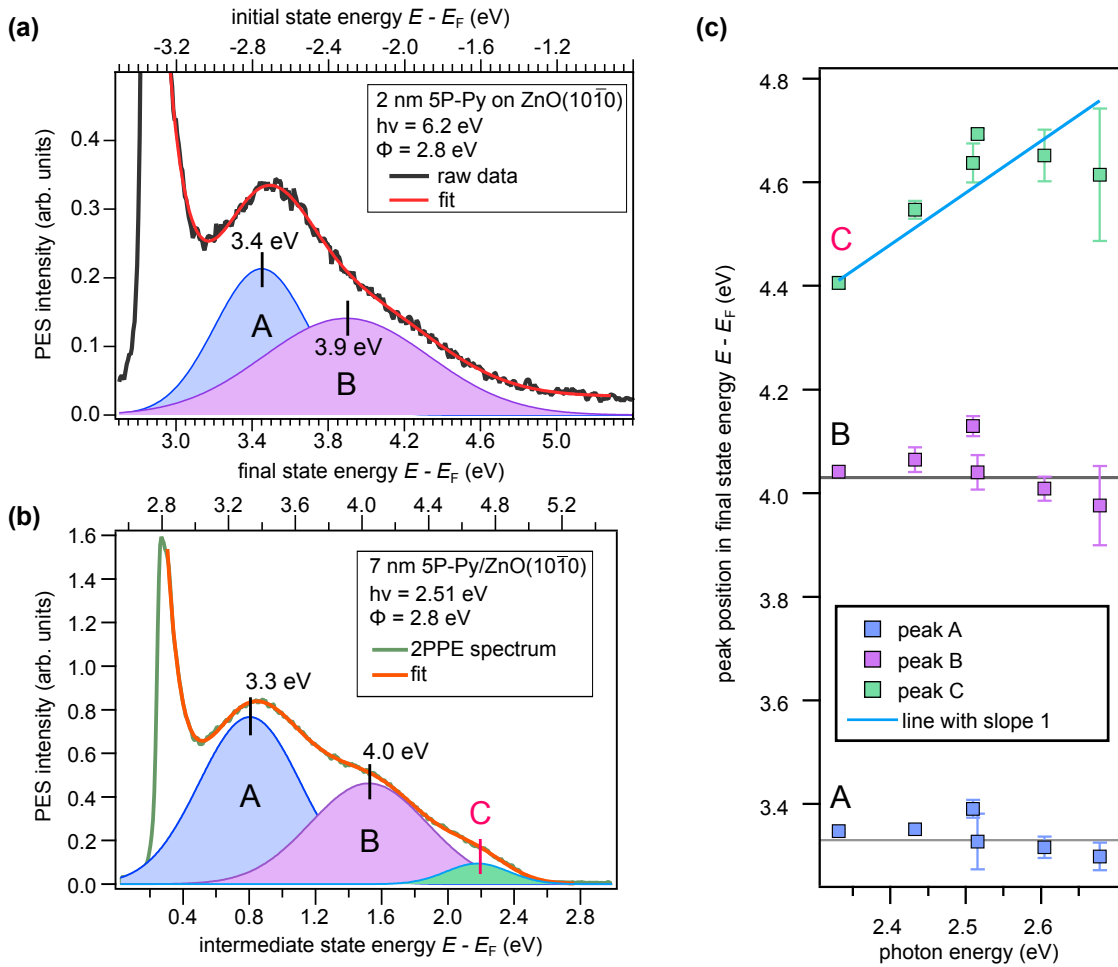


**Figure IV.50:** Photoelectron signatures of 5P-Py on ZnO(10 $\bar{1}0$ ) measured with 6.2 eV and 2.5 eV photon energy. (a) The 1PPE spectrum measured with 6.2 eV photons exhibits two comparably broad peaks which have final state energies of 3.4 eV and 3.9 eV, respectively. (b) The 2PPE spectrum measured with 2.51 eV photons on a 7 nm thick 5P-Py layer shows an additional signature C located at  $\approx 4.7$  eV final state energy. (c) The variation of the peak position with photon energy shows the character of the electronic states associated with the signatures. Peak A and B show no variation with photon energy while peak C exhibits a linear shift with  $\Delta h\nu$ . Thus, A and B belong to final electronic states and C originates from an unoccupied intermediate state located  $\approx 2$  eV above  $E_F$ .

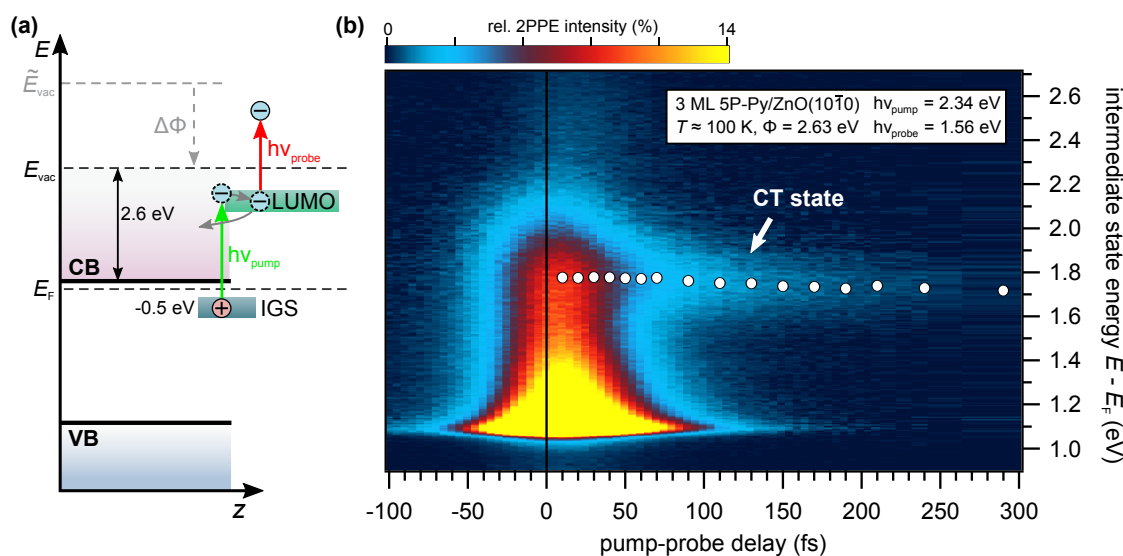


**Figure IV.51:** 2PPE excitation scheme and resulting 2D plot of the charge carrier dynamics at the 5P-Py/ZnO(10 $\bar{1}$ 0) interface. (a) The scheme shows the initial excitation of electrons originating from the occupied IGS into the unoccupied molecular LUMO with 2.34 eV photons. The transient population of the intermediate state is then probed with varying time delay, which results in the two-dimensional false color representation shown in (b). The background-subtracted plot clearly shows a comparably long-lived intermediate state at an energy of  $\approx 1.8$  eV above  $E_F$ . Circular markers show the energetic position of the peak maximum (for details, see text).

energy and the band gap renormalization that occurs upon adsorption [NHL06, GLRRT09]. These corrections have opposite signs and, thus, might cancel each other to some extent. As a consequence, further experiments that tackle the above-mentioned questions are highly desirable.

With this knowledge about the electronic structure of the interface, is it possible to learn something about the elementary processes, such as charge transfer, at this interface? A look at the preliminary energy level diagram in Fig. IV.49 reveals, that the energetic distance between the IGS and the LUMO is approximately 2.5 eV. This means the LUMO is populated nearly resonantly by absorption of a photon  $h\nu_{\text{vis}}$  from an electron in the IGS. It can be assumed that the IGS is spatially localized directly at the interface while the LUMO is a purely molecular feature, which means that electron and hole are spatially separated during the 2PPE process. Thus, it would be highly interesting to monitor the dynamics of the intermediate state, i.e., the additional electron in the molecular LUMO. Thereby, it might be shown whether bound charge transfer (CT) excitons form due to the separation of electron and hole (see Section 5.3.3 of Chapter II) or whether this is prevented due to screening or other effects.

#### 4.2.4 Charge Transfer Excitation and Electronic Coupling Across the Hybrid Interface

To identify the functionality of a hybrid interface, it is necessary to understand the dynamics of the elementary interfacial processes, as discussed in Section 5.3 of Chapter II. The 5P-Py/ZnO(10 $\bar{1}0$ ) interface is a particularly interesting system, because it is possible to monitor the dynamics of an additional electron in the molecular LUMO while the hole is located at the interface, i.e., the IGS. The resulting dynamics could be compared to those of excited organic layers where the hole is located in the molecular HOMO, which is the case when the molecular layer is directly excited. As discussed in Section 5.3.3 of Chapter II, the latter has been found to lead to the formation of a stable, long-lived CT exciton in various systems [SPN<sup>+</sup>14, VBG12]. The lifetimes on the order of hundreds of picoseconds of this bound interfacial state, which is a supposedly intrinsic feature of hybrid molecule/ZnO interfaces, is considered as the reason for the generally poor performance of ZnO-based photovoltaic cells [SPN<sup>+</sup>14]. The detailed understanding and character of these states and alternative interfacial processes is far from complete.

In this section, a first TR-2PPE experiment at the 5P-Py/ZnO(10 $\bar{1}0$ ) interface is presented, where electrons are injected nearly resonantly from the IGS into the unoccupied molecular LUMO using a pump photon energy of 2.34 eV, as depicted in Fig. IV.51(a) (cf. Section 1.4.2 of Chapter III). Please note that this photon energy is too low to directly excite excitons in the molecular layer. The population of the intermediate state is then probed with  $h\nu_{\text{probe}} = 1.56$  eV pulses. To determine the duration of the pulses and to set the zero delay  $\Delta t = 0$ , an XC experiment on a GaAs sample was carried out. As a result, an upper limit for the pulse duration of 39 fs could be determined, and the zero delay was fixed to  $\pm 10$  fs which was used as a starting point for the XC fitting procedure described in the following.

For this TR-2PPE experiment, a  $\approx 3$  ML thin 5P-Py film on ZnO(10 $\bar{1}0$ ) was prepared analogous to the single-color experiment discussed in the previous section. Interestingly, the work function of  $\Phi = 2.63$  eV is now  $\approx 0.2$  eV lower than in previous experiments. Since no desorption may have taken place, this can only be attributed to a reduction of molecular disorder. The reason for this might have been the comparably intense IR probe beam with which the sample is irradiated for several minutes before the start of the experiments. The fluence of the IR beam of  $86 \mu\text{J cm}^{-2}$  is an order of magnitude higher than the fluence of the visible beam, which is  $6.5 \mu\text{J cm}^{-2}$ . As discussed above, the understanding of the exact interface morphology and the influence of different preparation parameters is not yet complete and further experiments as well as insights from theory are needed. During the experiment no further changes to the work function or any spectral signatures were observed. This means that there was no indication of sample degradation and the stability of the surface surpassed that of the pristine or hydrogen-covered ZnO surface.

Figure IV.51(b) shows the result of the TR-2PPE experiment: the pump-induced changes to the photoelectron intensity after subtraction of the static background signal. The energies of the intermediate states are given with respect to  $E_{\text{F}}$ . The dominating signal is a continuum of states which extends from the secondary cutoff to energies of  $\approx 2$  eV above  $E_{\text{F}}$  and exhibits a comparably short lifetime. A comparison of this signature with the experiment on the hydrogen-covered ZnO(10 $\bar{1}0$ ) surface (Section 3.1) shows that this continuum can be attributed

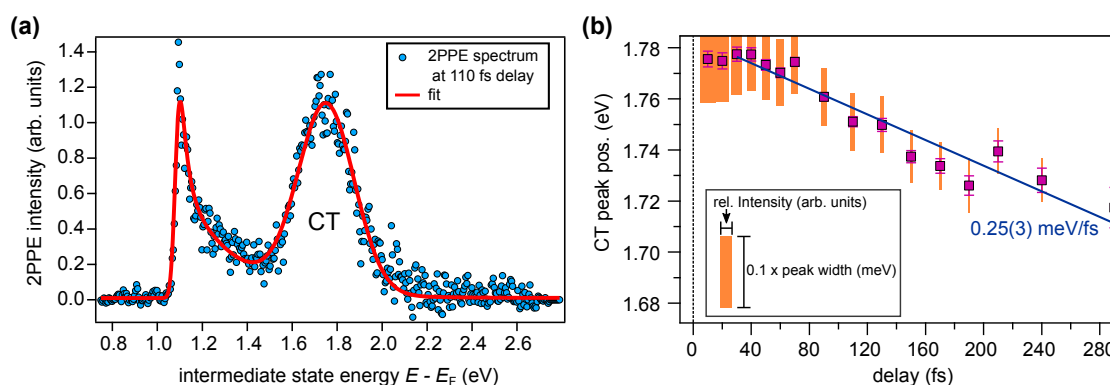


**Figure IV.52:** 2PPE spectrum of the transient CT state and its energetic position with respect to the pump-probe delay. (a) The exemplary spectrum at a delay of 110 fs shows a clear peak at 1.76 eV above  $E_F$ . A fit to the spectra at different delays reveals the exact energetic position of the CT peak, as shown in (b). There is a slight energetic relaxation of the CT state of  $\approx 60$  meV during 300 fs which yields a rate of 0.25(3) meV/fs. Orange bars illustrate the peak amplitude (horizontal) and width (vertical) at the respective delay.

to electrons that were excited from the IGS into the ZnO CB where they exhibit a characteristic decay constant on the order of ten femtoseconds.

The TR-2PPE signal also shows a signature which strikingly differs from previous experiments: At an intermediate state energy of  $\approx 1.8$  eV there is a clear comparably long-lived signature. From the work function of 2.63 eV one can deduce a VBE of 0.8(1) eV which exactly corresponds to the energetic position of the molecular LUMO that was determined in the previous section. Thus, the results presented in Fig. IV.51(b) strongly suggest that it is indeed possible to inject electrons from the interfacial IGS into the molecular LUMO and then monitor the decay of this electronic population back into the substrate. The comparably short femtosecond lifetime of this state further indicates that this process does *not* involve the formation of a long-lived bound excitonic state, so that the term CT excitation, instead of exciton, will be used in the following. In addition, the energetic position of the LUMO shows that at this interface Anderson's rule applies (see Section 2 of Chapter II), i.e., the LUMO is pinned to the vacuum level.

The finding that the electron located in the molecular LUMO relaxes back, supposedly into the isoenergetic states of the ZnO CB before an exciton can form shows that the LUMO is electronically strongly coupled to the substrate. The fact that the hole in the IGS appears not to play a decisive role in the process also means that the energetic position of the LUMO is possibly very close to the actual transport level. This makes the CT excitation an interesting experimental scheme to explore the interfacial energy level alignment, maybe also at different materials.

To learn more about the characteristics of the CT excitation process its exact binding energy as a function of time is analyzed, which allows to identify any energetic relaxation processes within the excited state. Figure IV.52(a) displays a background-subtracted 2PPE spectrum at a delay of 110 fs taken from the data in Fig. IV.51. The energetic position of the prominent CT state is deduced by fitting a Gaussian on a single exponential background (red curve) to the

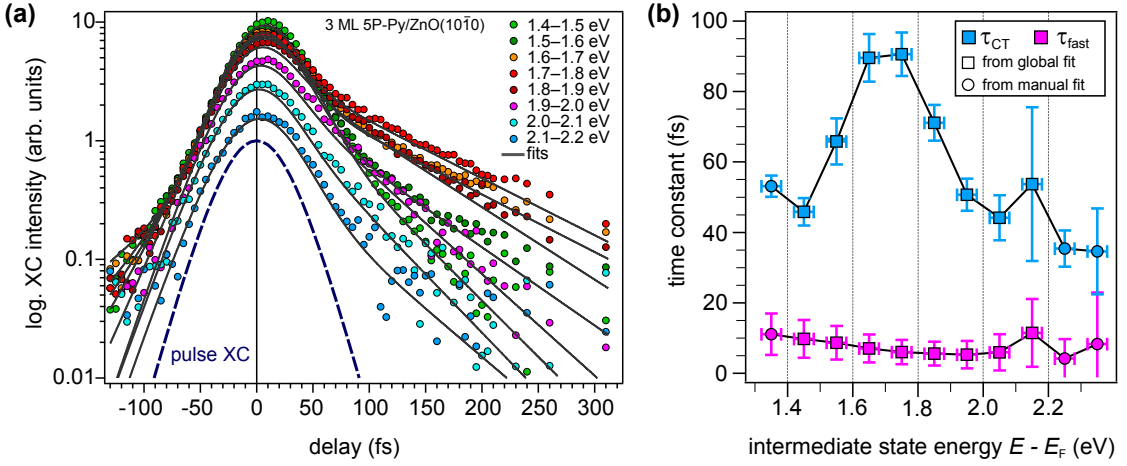


**Figure IV.53:** Relaxation dynamics of the CT exciton at the 5P-Py/ZnO(10 $\bar{1}0$ ) interface. (a) XC traces of the excited state dynamics taken from the measurement shown in Fig. IV.51. The dashed lines show the result of the global fitting procedure which accurately reproduces the dynamics. (b) The resulting time constants for the interfacial charge transfer ( $\tau_{CT}$ , slow component) and the intra-CB decay ( $\tau_{fast}$ , fast component). For the CT excitation a characteristic time constant of  $\tau_{CT} = 90(7)$  fs is found.

data. The resulting energetic positions relative to  $E_F$  are plotted in Fig. IV.52(b). There is a slight energetic shift of the CT state with time. During the first 300 fs after excitation the peak shifts by  $\approx -60$  meV, from approximately 1.78 eV to 1.72 eV above  $E_F$ , which yields a rate of 0.25(3) meV/fs. In addition, the orange bars illustrate the evolution of the width of the CT state peak and the amplitude. Both are decreasing exponentially with time; whereas the FWHM of the peak is reduced from 0.45 eV to 0.23 eV during the 300 fs after pumping, the peak amplitude is reduced by a factor of  $\approx 25$ .

Interestingly, the rate of the energetic shift is nearly identical to the rate of energetic relaxation of excess electrons in amorphous ice layers on a metal substrate, which was determined as 0.27 meV/fs in a similarly setup TR-2PPE experiment [GBFW02, SDW<sup>+</sup>15]. In case of the ice, the shift was attributed to the dynamical rearrangement of water molecules in the surroundings of the excess electron, thereby lowering its energy. This type of relaxation process, which involves a change in the nuclear coordinates in the surroundings of the excess electron, might also occur in the 5P-Py adlayer. As introduced in Section 3 of Chapter II, this means that the observed shift is most probably a signature of the *polaron* formation process in the molecular layer. As a comparison, the polaron formation process was characterized in a TR-2PPE experiment at the dihexyl-sexithiophene (DH6T)/Ag(111) interface [JMFH10]. The authors found a relaxation rate of 0.2 meV/fs for an upright standing DH6T layer and attributed this to the formation of a self-localizing small polaron. This process is linked to the increase in spatial localization of the electronic wave function with time, which can be measured in TR-2PPE by analyzing the dispersion of the intermediate state (see, e.g., Ref. [SBMW08]). Thus, it would be highly interesting to further examine the dispersion of the time-resolved data from the gls5P-Py/ZnO(10 $\bar{1}0$ ) interface, for which a strongly improved signal-to-noise ratio is necessary.

The charge carrier dynamics at the interface are analyzed quantitatively by fitting the XC

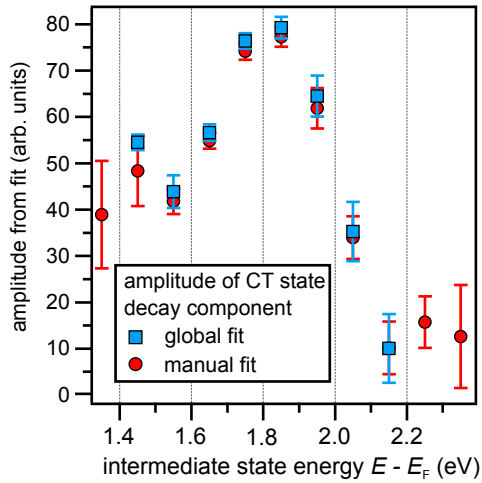


**Figure IV.54:** Amplitudes of the slow decay component associated with the CT state as a function of excess energy. The amplitudes of the exponential decay reflect the energetic position of the CT state.

traces to an appropriate model, analogous to the analysis of the TR-2PPE data on the hydrogen-covered ZnO surface (see Section 3). Since both signatures that are observed in this experiment, the hot electrons in the ZnO CB and the CT excitation are populated instantaneously by the pump pulse, the overall decay of the electronic population is modeled as double exponential. The fit function additionally includes the decay of hot electrons with an inverted pump-probe scheme to negative delays and the laser XC which is convolved with the exponential decays. To assign the resulting decay constants to intermediate state energies, the TR-2PPE data was integrated over energy windows with a width of 0.1 eV. The resulting energy-resolved XC traces are plotted in Fig. IV.53(a).

To reduce the above-mentioned uncertainties of laser pulse duration and zero delay, a fit routine was used that changed both of these values simultaneously for all traces at once.<sup>21</sup> By iterative variation of both zero delay and pulse duration, a robust and consistent fit to the data could be found, which is displayed as solid lines in Fig. IV.53(a). In addition, all traces were also fitted manually and the variations of the resulting decay constants were used to estimate the error due to the uncertainties in pulse duration and  $\Delta t = 0$  position.<sup>22</sup>

The resulting decay time constants of both exponential processes are displayed in Fig. IV.53(b) as a function of the intermediate state energy. For the fast component,  $\tau_{\text{fast}}$  is on the order of 10 fs (violet markers). This is identical to the ultrafast relaxation timescales that were determined for hot electron relaxation in the ZnO(10 $\bar{1}0$ ) CB, as discussed in Section 3.1. As it was observed before for these hot electrons in the CB, lifetimes become shorter with higher excess energy.

The slow component  $\tau_{\text{CT}}$  (blue markers) clearly corresponds to the CT state, as it shows the exact same energy dependence. The resulting characteristic time constant of this state is  $\tau_{\text{CT}} = 90(7)$  fs for the energy of the CT state maximum intensity. This ultrafast decay of the CT excitation supposedly precedes any exciton formation process, so that the observed signature corresponds to the single electron, and the interaction between electron and hole is negligible.

<sup>21</sup>This is the global fit routine which is part of the Igor Pro data analysis software.

<sup>22</sup>The error of the decay constants was then calculated as a sum of the error of the least squares fit and an additional error due to the uncertainties. For the fast decay constant this error was estimated to be 20%, while for the slow component it amounts to 5%.

It hints at a large wave function overlap between the CT state, presumably a polaron in the molecular LUMO and the accepting states in the ZnO CB. The behavior of the 5P-Py/ZnO(10 $\bar{1}$ 0) interface strongly resembles that of the DH6T/metal interface described in Ref. [JMFH10] where the measured decay time constant was 80(30) fs. In that work, the mechanism of charge transfer was a tunneling process, which could be altered by changing the morphology of the molecular adlayer.

The fit procedure further gives the amplitude of the respective decay components as a function of energy, which is plotted in Fig. IV.54 for the slow component. The amplitude distribution exhibits a maximum at  $\approx 1.8$  eV. Thus, it clearly shows the energetic position of the CT state, however, the maximum amplitude occurs at a slightly higher energy compared to the maximum decay constant [cf. Fig. IV.53(b)]. This is a consequence of the energetic relaxation process which reduces the apparent lifetime of electrons that are excited to higher energies. At these energies, the population of excited electrons is not only reduced by the transfer back into the substrate, but also by the increase of binding energy due to the supposed polaron formation.

#### 4.2.5 Conclusion

In a first series of measurements at the 5P-Py/ZnO(10 $\bar{1}$ 0) interface this novel system has already revealed a wealth of interesting physical features. In contrast to the related *p*-6P molecule, thermal activation leads to an increase in the degree of order molecular layer on the ZnO(10 $\bar{1}$ 0) surface, presumably resulting in upright standing molecules that are bound to the ZnO surface via their nitrogen atom. The static molecular dipole moment leads to a sizable reduction of the work function by up to 1.9 eV. It could be shown that the molecular levels supposedly shift with the interface dipole, i.e., the work function, which confirm the validity of Anderson's rule at this interface and might be a pathway to precisely adjust the electronic level alignment at hybrid interfaces.

An IGS is formed presumably by the interfacial bond via the nitrogen atom, comparable to the pyridine/ZnO(10 $\bar{1}$ 0) interface. This occupied state enables the direct injection of electrons into an unoccupied molecular state, supposedly the molecular LUMO, which exhibits a VBE of  $\approx 0.8$  eV. The subsequent decay of this transient CT state, where the hole is retained at the interface, while the electron is located in the organic adlayer, is examined in a TR-2PPE experiment. It is found that the CT state has an ultrashort lifetime with a characteristic decay constant of  $\tau_{CT} = 90(7)$  fs. At the same time there is an energetic shift of the CT state at a rate of 0.25 meV/fs, which strongly indicates that the excited electron becomes trapped and localized by the rearrangement of the surrounding molecules. This supposedly polaronic state, which would correspond to the transport LUMO level of the molecules at the interface, apparently strongly couples electronically to the substrate. Exciton formation is either prevented by the rapidness of the decay process, or the screening of the hole at the interface. Figure IV.55 summarizes these findings on the interfacial electronic structure and the interfacial charge transfer dynamics.

The dynamics observed in this work are in stark contrast to the initially described formation of hybrid CT excitons which are bound at the interface and show lifetimes on the order of hundreds of picoseconds [SPN<sup>+</sup>14]. The essential difference between these dissimilar intermediate states, the CT exciton and the CT state, is the spatial location of the hole. Apparently, the direct excitation of an exciton in the molecule leads to a decisively stronger electron hole interaction

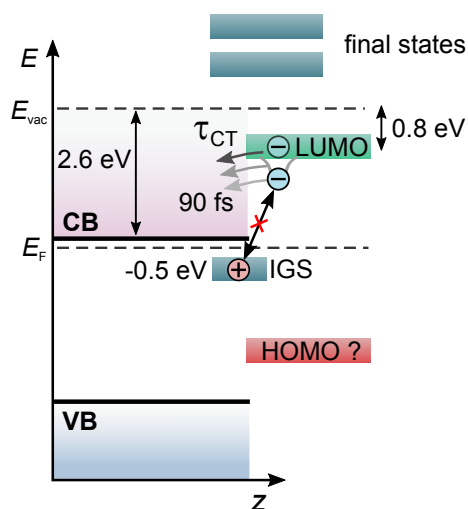


**Figure IV.55:** Overview of the experimental results regarding the 5P-Py/ZnO(10 $\bar{1}0$ ) interface showing the energetic positions of the molecular and interfacial electronic states.

that allows the formation of a bound interfacial state. The exact mechanism behind the formation of CT excitons at ZnO-based interfaces is not fully clear yet, and it would be worthwhile to conduct a corresponding experiment also on the 5P-Py/ZnO(10 $\bar{1}0$ ) interface. In addition, by exploiting the possibilities of interface modifications, i.e., via hydrogen adsorption or by varying molecular orientation, further insights into interfacial electronic coupling and localization of charges could be gained. Thus, the 5P-Py/ZnO(10 $\bar{1}0$ ) interface might prove an interesting model system and playground for learning more about fundamental electronic processes at hybrid semiconductor interfaces.



## V Conclusion and Outlook

The aim of this dissertation was to shed light on elementary electronic processes at model zinc oxide-based hybrid interfaces which hold great promise as novel optoelectronic devices. This work in particular discusses *why* these systems are so complicated and demonstrates how these complications can be tackled by offering fundamental insights into (i) the hydrogen-induced semiconductor-to-metal transition at ZnO surfaces and (ii) the characteristics of the ZnO surface exciton. Organic molecules were then used to (iii) examine the possibility of strong work function shifts by adsorbing dipolar molecules, and (iv) to conduct first experiments on charge transfer states and interfacial electronic coupling at a model hybrid interface.

To reach a deep understanding of hybrid systems and the relevant dynamics of various quasiparticle states, it is necessary to learn, and ideally control, the microscopic electronic properties of the substrate and the interface. This is presumably only possible by starting with a comparably simple model system, the pristine ZnO surface, and continuing with a successive increase of system complexity.

The experimental method of choice to examine such increasingly complex interfaces was ultrafast time-resolved two-photon photoelectron spectroscopy which was complemented with a number of surface science techniques and theoretical work carried out by our collaborators. A summary of the essential findings regarding the above-mentioned questions is given in the following.

**The local aspects of hydrogen-induced metallization of the ZnO(10 $\bar{1}$ 0) and (000 $\bar{1}$ ) surfaces** It is well-known that the ZnO(10 $\bar{1}$ 0) and ZnO(000 $\bar{1}$ ) surfaces can exhibit a thin surface layer of high electron density, the CAL, which can easily be induced by the adsorption of hydrogen atoms. This formation of O–H bonds is accompanied by a significant increase in charge carrier density at the surface and a reduction of the work function by up to  $\approx 0.7$  eV. At the mixed-terminated ZnO(10 $\bar{1}$ 0) surface, it was possible to demonstrate how the two different surface atom species, O and Zn, play diametrically different roles when hydrogen is adsorbed. It was found that for coverages well below saturation, O–H bond formation dominates due to its energetic advantage, leading to laterally highly localized potential wells at the adsorption site. At coverages exceeding  $\approx 18\%$  Zn–H bonds become energetically favorable, which eventually leads to a reduction in surface charge carrier density. The oppositional role of O–H and Zn–H bonds is confirmed by adsorption experiments on the O-terminated surface, where the hydrogen-induced work function shift is  $\approx -1.8$  eV and a reduction of charge carrier density for high coverages is *not* observed, which means that only effects due to O–H bonds occur.

This work expands on the previous description of the hydrogen-induced CAL at the ZnO surface by providing a fundamental microscopic description of the observed changes to the surface electronic structure. This description underlines the complexity of ZnO surfaces. Addi-

tionally, it also shows how surface properties can be tuned precisely in order to, e.g., modify the screening of the Coulomb interaction between excited carriers, which is important for hot electron relaxation and exciton formation processes.

Eventually, these findings are not only the basis for our further experiments on more complex surfaces and interfaces, but they may also stimulate further studies on the surface electronic structure of TCOs materials and the associated microscopic surface properties. In particular, this work stresses the crucial influence of adsorbed hydrogen as ubiquitous contaminant in vacuum environments, which has often been overlooked.

**Ultrafast electron relaxation and exciton formation at the zinc oxide surface** This work presents an extensive and systematic investigation of the excited charge carrier dynamics at the ZnO(10 $\bar{1}$ 0) surface, precisely (i) the **electron–phonon (e–ph)** scattering and (ii) formation and subsequent decay of subsurface-bound excitons (**SX**), which exhibit timescales that span several orders of magnitude. The strong coupling of electrons to **LO** phonons in ZnO results in relaxation times of few ten femtoseconds for electrons with excess energies more than 0.2 eV above the bulk **conduction band minimum (CBM)**. Additionally, the **SX** form within 200 fs after optical excitation, which demonstrates that, other than previously thought, excitonic populations can form on such ultrafast timescales. The **SX** exhibits a remarkable stability also due to its very large binding energy with respect to the bulk **CBM**, leading to lifetimes on the order of nanoseconds.

Further, it was demonstrated how these relaxation dynamics can be influenced by static or transient changes to the carrier density at the surface. By increasing the electron density in the **CAL**, the screening of the Coulomb interaction reduces the **e–ph** coupling strength and leads to a slowing down of the hot electron relaxation dynamics. Similarly, the formation probability of the **SX** is reduced for sufficiently high charge carrier densities. The same effect is observed due to the creation of a dense electron–hole plasma by an adequately high excitation density, which leads to an excitonic Mott transition.

The study thus offers a novel picture of the quasiparticle relaxation at the ZnO(10 $\bar{1}$ 0) surface and illustrates the role of complex many-body effects that occur in such systems. The existence of a stable subsurface excitonic species is highly relevant for applications of ZnO that, e.g., involve interfacial energy transfer via **FRET**. The **SX** may dominate this dipole-dipole coupling process due to its adjacency to the interface and its persistence even under non-**UHV** conditions.

**Strong vacuum level shift by adsorption of a molecule with negative electron affinity: Pyridine on ZnO(10 $\bar{1}$ 0)** The tuning of the energy levels and the associated energetic barriers at hybrid interfaces requires control of the *interface dipole*. Using the model interface pyridine/ZnO(10 $\bar{1}$ 0) it was shown how dipolar molecular layers with negative electron affinity can lead to remarkably strong interface dipoles that manifest themselves in huge work function shifts:  $\Delta\Phi = -2.9$  eV in this particular case. In collaboration with theory it could be shown that this strong reduction of  $\Phi$  is rendered possible by (i) a well-ordered adsorption geometry with all molecular dipoles aligned normal to the substrate surface and (ii) the cooperative effect of these intrinsic dipoles with the dipole induced by charge transfer upon adsorption.

This work gives an example how the mechanism of preventing Fermi level pinning by choosing

---

materials with negative electron affinity can be exploited to reduce energy injection barriers at organic/ZnO systems. It might be interesting to combine pyridine with the different surface terminations of ZnO and also with hydrogen to get further insight into the possibilities of ZnO surface modifications. Since pyridine was shown to bind to surface Zn atoms, additional O–H bonds at the mixed terminated surface may lead to an even lower work function. Alternatively, at the Zn-terminated surface, a denser packing of the molecules may have the same effect. This shows, how well-defined TCO surfaces can be used as a “playground” for drastic surface modifications induced by adsorption using the understanding that is provided in this work.

**Charge transfer excitation and ultrafast interfacial electron transfer across the 5-Phenyl-Pyridine/ZnO(10 $\bar{1}$ 0) interface** The 5P-Py/ZnO(10 $\bar{1}$ 0) interface was chosen as a first step towards functional hybrid interfaces because it builds on previous findings with the advantage that the molecular adlayer is thermally stable and optically active, in contrast to pyridine.

The commonalities to pyridine, formation of a presumably ordered first layer and the associated occurrence of an occupied interface state proved to be crucial for the excitation of a charge transfer state with the electron located in a normally unoccupied molecular state and the hole located at the interface. The transfer of the excited electron back into the ZnO CB happens with a characteristic time constant of 90(7) fs, which illustrates the strong electronic coupling across the interface. In addition, the intermediate state exhibit an energetic shift to higher binding energies at a rate of 0.25 meV/fs which is highly indicative of a polaron formation process. Thus, the experiment gives insight into the competition between the localization and stabilization of an excess electron in the molecular layer and the back-transfer into the inorganic substrate through an ultrafast tunneling process.

This charge transfer process shows strikingly different characteristics compared to the charge separation process at ZnO interfaces where the hole is not located at the interface, but in the organic layer. The resulting charge transfer excitons show lifetimes on the order of hundreds of picoseconds, which is highly detrimental for photovoltaics applications that rely on fast charge separation. Further experiments at the 5P-Py/ZnO(10 $\bar{1}$ 0) under varied conditions, i.e., which include molecular excitons or a hydrogenated, metallic ZnO substrate, may shed more light on the elusive charge transfer and separation processes at this model interface which help understanding hybrid interfaces in general.

The studies presented in this dissertation provide a novel detailed view on model zinc oxide-based interfaces, which is enabled by a combination of state-of-the-art experimental and theoretical methods. By focusing on the microscopic electronic properties and their interplay with surface morphology and adsorbate geometries, it was possible to gain a comprehensive understanding of a number of relevant model systems. These microscopic properties were found to be highly complex, e.g., the drastic hydrogen-induced surface modifications can only be understood by considering the precise adsorption site. Thus, the influence of hydrogen on ZnO surfaces, which is highly relevant for both fundamental science and device design, cannot be described by an area-averaged model. The importance of considering microscopic effects was further corroborated in the experiments on surface exciton dynamics at the ZnO surface, where an intricate interplay between exciton formation probability, surface metallicity

and screening effects was found. At the inorganic/organic interfaces, a precise explanation of a huge work function modification could be given. The fundamental principle behind this surface modification might be of general interest for the intentional energy level alignment at interfaces. Following the rationale of increasing interface complexity, the 5P-Py/ZnO(10 $\bar{1}$ 0) has proven to be a highly interesting hybrid interface which combines the potential of strong surface modifications and the possibility of observing elementary interfacial processes, in particular polaron formation and charge transfer. By further exploiting the gained knowledge about controlling the interface properties, the 5P-Py/ZnO(10 $\bar{1}$ 0) interface may be used as versatile model system to study various fundamental processes that are relevant for the understanding of hybrid systems in general.





# Appendices

## A Data Analysis for 2PPE

### A.1 How Electron Energies Are Determined

In photoelectron spectroscopy (PES) the accurate knowledge about the kinetic energies of the nascent photoelectrons is obviously crucial (also see Ref. [CK03]). The hemispherical analyzer that is used in experiment always measures these kinetic energies relative to its own vacuum level, which is defined by the analyzer work function of  $\Phi_{\text{an}} = 4.32$  eV (see Fig. A.1). Obviously, this is generally different from the sample work function, and usually a bias voltage  $U_b$  is applied between sample and analyzer which further shifts the photoelectron energies, as shown in Fig. A.1(b). As a result, the kinetic energy of the photoelectron with respect to the sample is given by

$$E_{\text{kin}}^s = E_{\text{kin}}^{\text{an}} - (\Delta\Phi + U_b). \quad (.1)$$

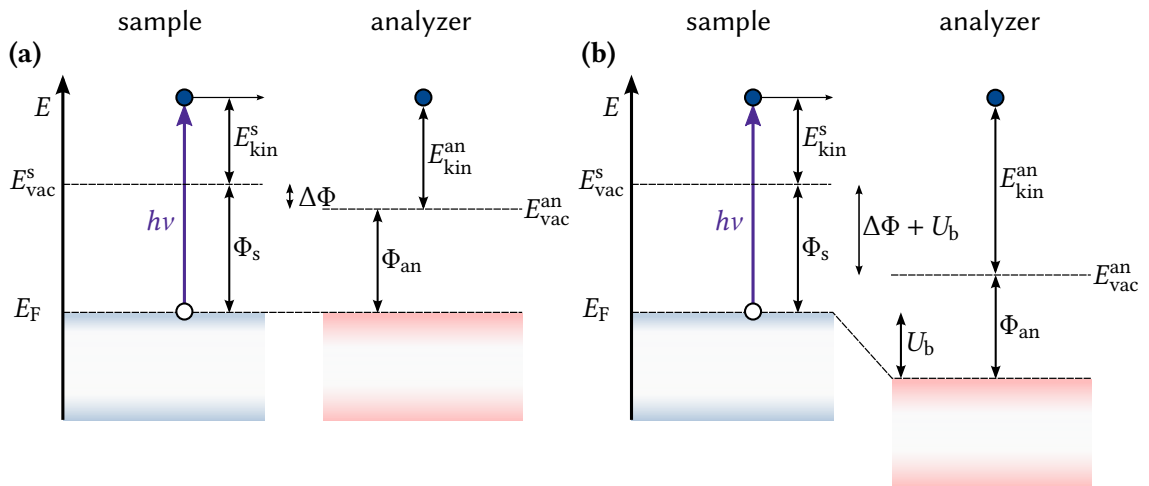
Thus, for determining all photoelectron energies with respect to the sample,  $\Delta\Phi$  and  $U_b$  have to be known. Alternatively, an energy reference can be used, which is usually the Fermi level of the sample, or, in case of semiconducting samples, the metallic sample holder. Knowing to which analyzer kinetic energy  $E_{\text{kin}}^{\text{an}}$  the sample Fermi level is mapped then allows to accordingly relate all measured photoelectron kinetic energies. Generally, the Fermi energy is defined as zero in this work, which yields the initial state energy scale in the photoelectron spectra. By adding the photon energy to the energy scale, intermediate or final state energy axes are defined, depending on the type of photoemission process.

The bias voltage  $U_b$  was usually chosen as the minimum voltage, at which the secondary electron edge is mapped completely to the detector screen. It is, in principle, possible to use higher voltages, however, this can lead to distortions of the spectra, especially when the mapped state shows a strong angular dispersion. In Ref. [Dei11] this effect is discussed using the strongly dispersing surface state on the Cu(111) surface as an example.

For the pristine ZnO surface,  $U_b$  was chosen as 1.5 V, and for surfaces with lower work function the value was increased accordingly.

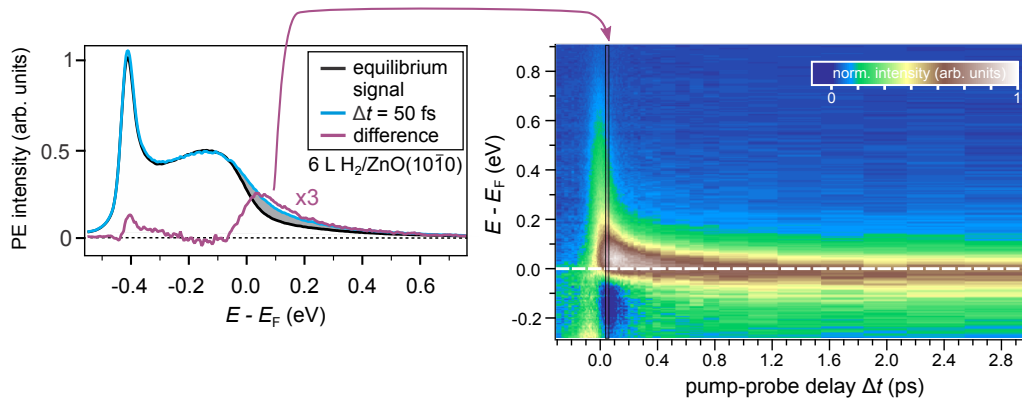
### A.2 How 2PPE Spectra are Generated

Figure A.2 illustrates, how the pump-induced changes to the photoelectron signal are extracted from the raw spectra. The black curve corresponds to an exemplary equilibrium signal which almost completely consists of the 1PPE signal of the hydrogenated ZnO(10 $\bar{1}$ 0) surface probed with  $h\nu = 4.64$  eV photons. The addition of the pump pulses and the resulting above-band gap excitation leads to a slight modification of the spectrum (blue curve). The difference of the two spectra is the pump-induced change to the photoelectron signal (violet curve), which can be



**Figure A.1:** Scheme of the determination of photoelectron kinetic energies with the hemispheric analyzer. The measured quantity is always the kinetic energy of the photoelectrons  $E_{kin}^{an}$ . (a) The Fermi levels of sample and analyzer are aligned due to their electrical contact. The difference in vacuum levels between sample and analyzer  $\Delta\Phi$  leads to a difference in kinetic energies. (b) The sample is usually energetically offset by a bias voltage  $U_b$ , which leads to a further shift between the kinetic energies.

determined at various delays. Assembling these spectra finally yields the two-dimensional plot on the right, which represents the complete energy- and time-resolved pump-induced dynamics in the examined system.



**Figure A.2:** Exemplary 2PPE spectra demonstrating the extraction of the pump-induced changes to the photoelectron signal. The black curve shows the equilibrium background spectrum, where the intensity below  $E_F$  results from the CAL. Above band gap excitation results in additional 2PPE intensity at energies around  $E_F$ , shown for a delay of  $\Delta t = 50$  fs (blue). Subtraction of the equilibrium background signal yields the pump-induced changes to the spectrum (violet). These spectra are then arranged for different delays to yield the false-color 2D plot presented on the right.

## B Time-Resolved 2PPE on ZnO – Technical Details and Challenges

2PPE experiments on ZnO surfaces have proven to be challenging compared to experiments on metal surfaces, such as gold or copper. This is due to the high reactivity and especially the sensitivity of ZnO with respect to hydrogen, which may lead to instabilities (see Section 1.1.3 of Chapter II). As a consequence, we typically observe a continuous slow shift of the sample work function which is reduced by a few ten meV per hour. This shift is accompanied by an increase of the photoelectron signal at the secondary secondary edge.

Another complication when probing intermediate state energies which are located below  $E_F$  is the constant one-photon photoemission (1PPE) background as shown in Fig. A.2, which imposes limitations on the pump intensity because the saturation of the analyzer screen has to be avoided. At the same time, the DOS of initial states in ZnO is relatively low regarding the low photon energies that are available in our setup (cf. Fig. III.9 of Chapter III) with the VB peaking at  $\approx 3.7$  eV below  $E_F$  [SSO<sup>+</sup>04]. In conjunction with the strong secondary electron signal this results in a signal-to-noise ratio which is generally lower compared to measurements on metal substrates. Thus, time-resolved measurements require an extended number of delay scans and a meticulously optimized setup in order to generate sufficiently clear data. In order to be certain that exciton formation is not suppressed by excitation densities above the exciton Mott density (see Section 5.2.1 of Chapter II), laser intensities which are below that level are generally chosen, unless stated otherwise. The calculated excitation densities given in this work are the upper limit which is only reached at the very surface of the sample, whereas the light intensity gradually reduces with a characteristic absorption depth of  $\approx 50$  nm.

In order to stabilize the photoemission signal, the freshly-prepared ZnO surfaces were usually exposed to a low dose of 6 L of hydrogen. This has another advantageous effect, namely the

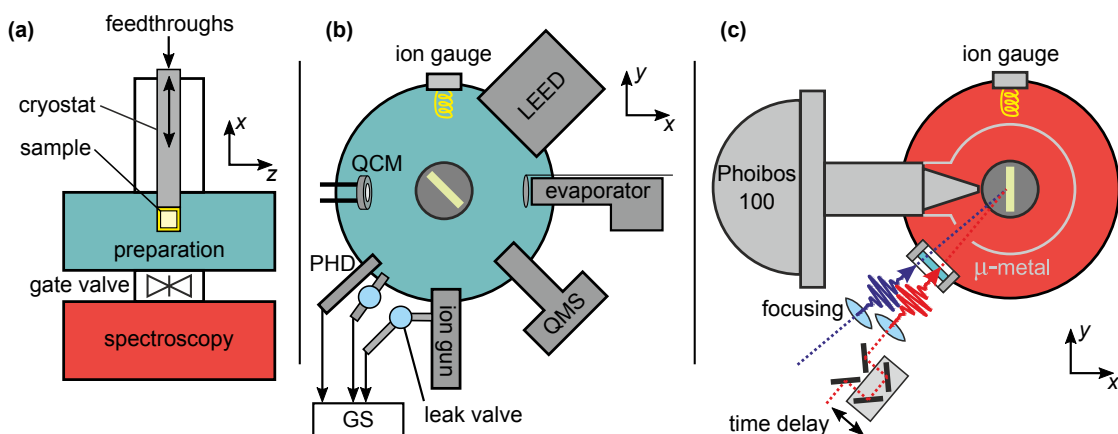


**Figure C.3:** Detailed overview of the UHV setup. (a) The side view shows the separation between preparation and spectrometer chamber. The sample can be moved between the two sections by variation of its  $z$ -position. (b) Top view of the preparation section showing the devices used for adlayer preparation and characterization (for details, see text). (c) Top view of the spectrometer section of the system. There is an additional  $\mu$ -metal shield to screen any magnetic fields. Laser light enters the spectrometer section to a  $\text{MgF}_2$  window. Modified from Ref. [Weg15].

lowering of the work function to values of  $\Phi \approx 4.2$  eV, which enables access to occupied states  $\approx 0.4$  eV below  $E_F$  with the probe photon energy of 4.64 eV. The charge density in the CAL for such low hydrogen dosages is on the order of  $1 \times 10^{18} \text{ cm}^{-3}$ , according to Ref. [OM11]. The calculations presented in Section 2.3 of Chapter IV show that only a few percent of the surface oxygen atoms are covered with hydrogen in that case. In order to compensate for any intensity shifts due to slow hydrogen adsorption during the typically few hour long measurements the direction of the delay scans is alternated. A scan from positive to negative pump-probe delays is followed by a reverse scan. For analysis, several of these scans are averaged to exclude any signal contributions that are due to a stoichiometric change of the sample surface.

## C The UHV System in Detail

### C.1 UHV Chamber

Photoelectron spectroscopy on pristine and well defined sample surface requires ultrahigh vacuum conditions with pressures below  $10^{-7}$  mbar to prevent any unwanted surface contamination (see Section 2.3 of Chapter III). In contrast to that, surface preparation and adlayer deposition requires much higher partial pressures of the desired gas molecules at the sample surface. As a consequence, sample preparation usually leads to non-UHV conditions and a contamination of the chamber walls which should be avoided when base pressures on the order of  $p_{\text{base}} < 10^{-11}$  mbar preferable. For this reason, the UHV system can be split into two parts, as shown in Fig. C.3(a): (top) A preparation section where adsorbates can be introduced into the UHV system, and (bottom) a spectrometer section which can be separated from the top by a gate valve during sample preparation. This results in base pressures of spectrometer and

preparation chamber which differ by approximately one order of magnitude: In the preparation chamber the base pressure is on the order of  $p_{\text{base}} < 5 \times 10^{-11}$  mbar, while the preparation chamber a base pressure of  $p_{\text{prep}} < 1 \times 10^{-10}$  mbar is reached. These pressures are monitored using Bayard-Alpert ionization gauges in each of the sections.

The sample is attached to a flow cryostat (*Cryovac GmbH*) which in turn is mounted on a motorized manipulator that can be moved linearly along  $x$ -,  $y$ -, and  $z$ -direction as well as rotated around the  $z$ -axis. Cooling of the sample was routinely done with liquid nitrogen which allowed sample temperatures as low as 100 K. Using liquid helium, sample temperatures of  $\lesssim 50$  K could be reached.

Figure C.3(b) shows a scheme of the top view of the preparation chamber which includes all vacuum components that are needed for sample preparation and basic surface characterization. For  $\text{Ar}^+$ -ion sputtering, the ion gun (*SPECS GmbH*) is used which is supplied with argon via the gas system. Gaseous substances for adlayer preparation can be introduced either by the home-built **pinhole doser (PHD)** which essentially consists of a pinhole with a diameter of 5 micrometer and a 22 cm long metal tube [Dei11]. By positioning the sample in front of the **PHD** at a few millimeters distance, a highly directed adsorbate flow onto the sample surface is ensured. Alternatively, gases can be introduced by backfilling the chamber through a leak valve, which was done for hydrogen dosing. For solid substances, such as **5P-Py** molecules, a Knudsen cell (*Dr. Eberl MBE-Komponenten GmbH*) is used to evaporate the molecules and the molecular flow can then be monitored using a **QCM** (*INFICON AG*) (see Section 2.5.2 of Chapter III). The evaporator contains the molecules in the form of solid powder inside a quartz crucible. Heating the crucible to the sublimation temperature then created a molecular beam with a cross section of  $\approx 4$  cm at the sample position.

For surface and adlayer analysis, the preparation chamber is equipped with a **LEED** apparatus (*SPECS GmbH*) that is used to characterize the geometric structure of the sample surface. For residual gas analysis and to conduct **TPD** experiments, a **QMS** (*MKS satellite*) is used.

The spectrometer section, which is schematically depicted in Fig. C.3(c), only houses the entrance to the photoelectron analyzer and a  $\mu$ -metal shield which screens any magnetic fields that might influence the photoelectron trajectories. The laser light is coupled into the chamber non-collinearly through a  $\text{MgF}_2$  window with high transmittance in the **UV** regime. Focusing and beam steering occurs on an optical breadboard which is connected to the **UHV** chamber. This breadboard is equipped with a beam profiler for analysis of the beams' cross sections.

## C.2 Sample Holder

The sample holder, which is depicted in Fig. C.4, enables the control and measurement of the sample temperature. It consists of a fixed part which is directly attached to the cryostat, and a transferable sample "schiffchen". The fixed part, as shown in (a), mainly consists of the copper cold finger and two copper halves which are electrically insulated by sapphire plates. The removable part consists of two electrically insulated halves made of molybdenum. It holds two tantalum wires which are connected to the sample. Connecting these two halves with a power supply outside of the chamber allows the resistive heating of the sample. To measure the temperature of the sample, it is connected to type-K **thermocouple (TC)** wires. The connection of the **TC** wires to the outside of the chamber is established using connector pins at the top

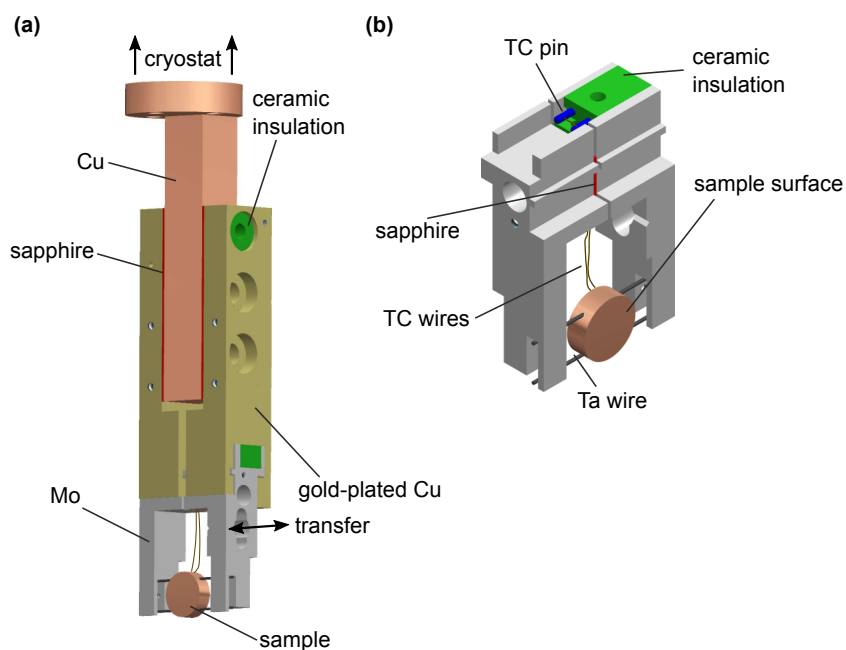


**Figure C.4:** Drawing of the sample holder. (a) overview of the custom-built sample holder. Its top is directly connected to the cryostat. The sample (here, a generic copper sample is shown) is mounted between two tantalum wires in a detachable part (“schiffchen”). (b) The sample “schiffchen”, which can be transferred separately, is equipped with **thermocouple (TC)** connector pins, which enables sample temperature measurements. The two halves of the sample holder are electrically insulated with sapphire plates. Modified from Ref. [Weg15].

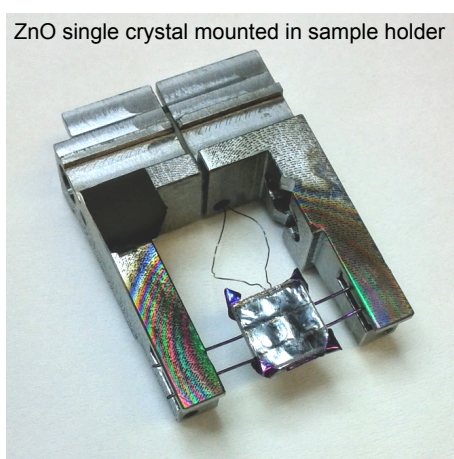


**Figure C.5:** Photograph of the ZnO sample mounted in the sample holder.

of the “schiffchen” which are plugged into their respective counterparts at the fixed part of the sample holder. As a result, the sample temperature can be set precisely to values between approximately 50 K to 1000 K with a PID controller (*Lake Shore Cryotronics, Inc.*).

Figure C.5 shows a photograph of the clear ZnO(10 $\bar{1}$ 0) sample mounted in the “schiffchen”. The colored rings on the sides of the holder originate from the evaporating of molecules from the Knudsen cell. They clearly show that the sample is well-centered in the molecular beam.

### C.3 The Gas System and Pump Setup

The gas system, as introduced in Section 2.3.1 in Chapter III, is depicted in Fig. C.6. It is designed in a way that allows the connection of desired gas bottles or sealed glass tubes to each of the inlets into the UHV chamber that were described above. The system is constructed from stainless steel tubes, fittings and valves (*Dockweiler AG* and *Swagelok Company*).

Pumping of the gas system is performed by a combination of membrane and turbomolecular pump. The pressure in the gas system can be as low as  $10^{-7}$  mbar after bakeout. The very high surface to volume ratio of the gas system, however, leads to base pressures which are two to three orders of magnitude higher while it is in use. It provides connections for numerous gas bottles and two detachable sealed test tubes for liquid substances.

Figure C.6 also shows the layout of the pumps used to ensure UHV conditions inside the chamber. The preparation section is pumped by two consecutive turbomolecular pumps and a membrane pump. At the lower end of the spectrometer chamber, an ion pump is used to improve the base pressure as well as to serve as sole pump for the spectrometer section while the gate valve between the chamber parts is closed. Additionally, a titanium sublimation pump is used to chemisorb reactive gaseous residues to the wall of the lower part of the spectrometer chamber. This pump is only run for a few cycles after the bakeout of the chamber.

The figure also indicates the location of the transfer system which is used to introduce samples into the UHV system without the need to open the preparation chamber. The transfer system is separated from the main chamber by a gate valve. Samples can be inserted linearly into the fixed part of the sample holder using a magnetically driven transfer rod.

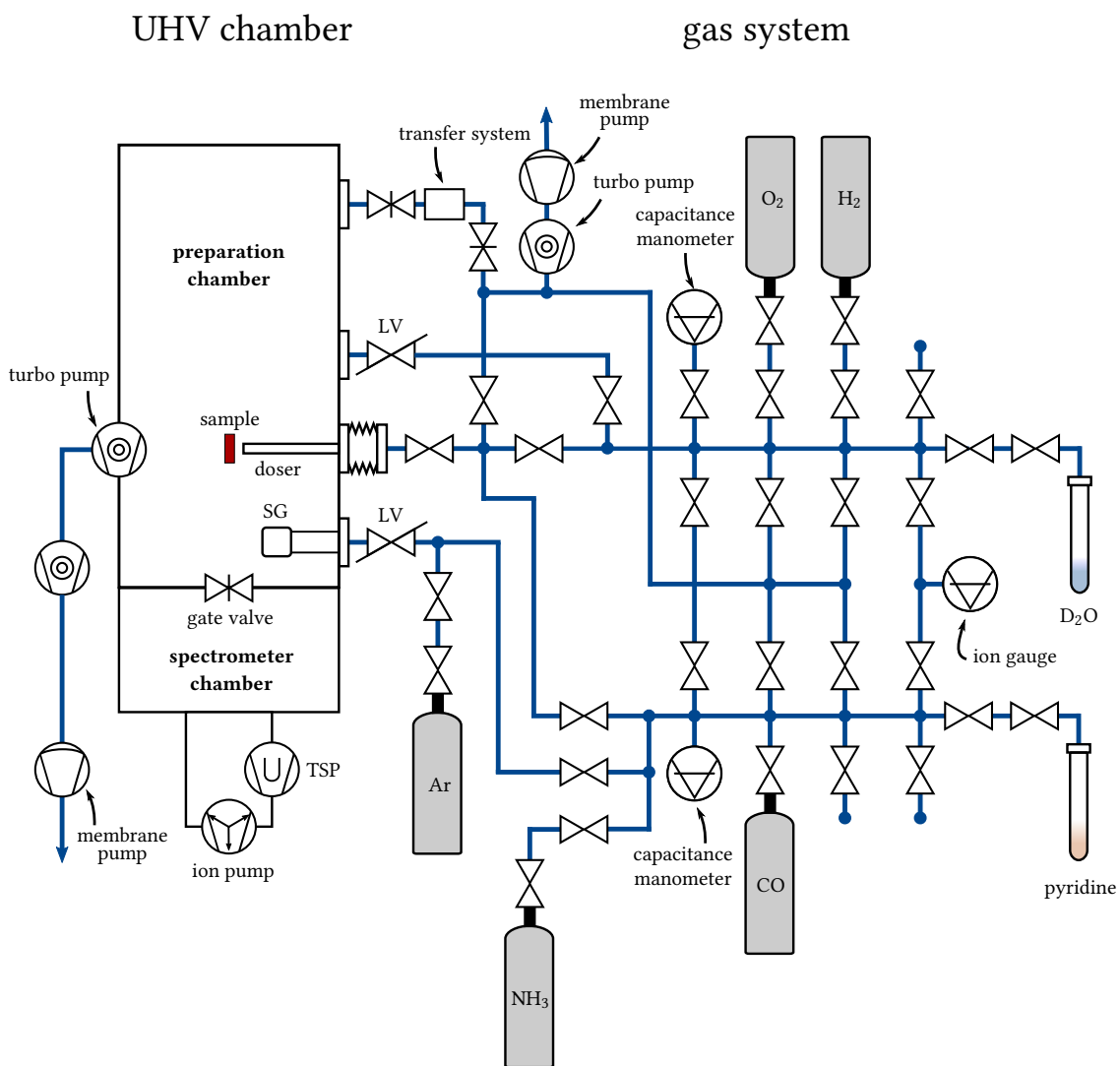


**Figure C.6:** Scheme of the gas system and attached vacuum parts. There are two separate pumping circuits, one for the UHV chamber (left), and one for the gas system (right). The Knudsen cell for evaporation of solids and the differential pumping of the manipulator are omitted in this scheme.

## Bibliography

- [ABL<sup>+</sup>14] M. Alloing, M. Beian, M. Lewenstein, D. Fuster, Y. González, L. González, R. Combescot, M. Combescot, and F. Dubin. Evidence for a Bose-Einstein condensate of excitons. *EPL*, 107(1):10012, jul 2014. 24
- [ACH90] M. Alonso, R. Cimino, and K. Horn. Surface photovoltage effects in photoemission from metal-GaP(110) interfaces: Importance for band bending evaluation. *Phys. Rev. Lett.*, 64:1947–1950, Apr 1990. 73, 111
- [AHB03] V. I. Arkhipov, P. Heremans, and H. Bässler. Why is exciton dissociation so efficient at the interface between a conjugated polymer and an electron acceptor? *Appl. Phys. Lett.*, 82(25):4605, 2003. 28
- [And60] R. L. Anderson. Germanium-gallium arsenide heterojunctions. *IBM Journal of Research and Development*, 4(3):283–287, jul 1960. 9
- [ASM<sup>+</sup>10] M. W. Allen, C. H. Swartz, T. H. Myers, T. D. Veal, C. F. McConville, and S. M. Durbin. Bulk transport measurements in ZnO: The effect of surface electron layers. *Phys. Rev. B*, 81(7):075211, feb 2010. 36
- [AT04] C. Adachi and T. Tsutsui. Molecular LED: Design concept of molecular materials for high-performance OLED. In *Organic Light-Emitting Devices*, pages 43–69. Springer Science + Business Media, 2004. 26
- [AY84] M. Arimura and Y. Yoshikawa. Ionization efficiency and ionization energy of cyclic compounds by electron impact. *J. Mass Spectrom. Soc. Jpn.*, 32(5):375–380, 1984. 136
- [BGS<sup>+</sup>10] S. Blumstengel, H. Glowatzki, S. Sadofev, N. Koch, S. Kowarik, J. P. Rabe, and F. Henneberger. Band-offset engineering in organic/inorganic semiconductor hybrid structures. *Phys. Chem. Chem. Phys.*, 12(37):11642, 2010. 1, 140, 143, 144
- [BH91] M. Baeumler and R. Haight. Ultrafast electron dynamics at the Ge(111)2×1 surface. *Phys. Rev. Lett.*, 67:1153–1156, Aug 1991. 22
- [BHK<sup>+</sup>01] Th. Becker, St. Hövel, M. Kunat, Ch. Boas, U. Burghaus, and Ch. Wöll. Interaction of hydrogen with metal oxides: the case of the polar ZnO(0001) surface. *Surf. Sci.*, 486(3):L502–L506, jul 2001. 38, 86, 95
- [BJK<sup>+</sup>11] M. Biswas, Y. S. Jung, H. K. Kim, K. Kumar, G. J. Hughes, S. Newcomb, M. O. Henry, and E. McGlynn. Microscopic origins of the surface exciton photoluminescence peak in ZnO nanostructures. *Phys. Rev. B*, 83(23):235320, jun 2011. 43

- [BM15] K. Bandopadhyay and J. Mitra. Zn interstitials and O vacancies responsible for n-type ZnO: What do the emission spectra reveal? *RSC Adv.*, 5(30):23540–23547, 2015. [43](#)
- [BMA15] M. Bauer, A. Marienfeld, and M. Aeschlimann. Hot electron lifetimes in metals probed by time-resolved two-photon photoemission. *Prog. Surf. Sci.*, 90(3):319–376, aug 2015. [2](#), [19](#), [20](#), [21](#), [22](#)
- [BNF<sup>+</sup>06] F. Bisio, M. Nývlt, J. Franta, H. Petek, and J. Kirschner. Mechanisms of high-order perturbative photoemission from Cu(001). *Phys. Rev. Lett.*, 96:087601, Feb 2006. [52](#)
- [Bog15] L. Bogner. *Ultrafast Relaxation Processes After Optical Excitation of Hybrid Inorganic/Organic Systems*. PhD thesis, Freie Universität Berlin, 2015. [101](#)
- [Bov05] U. Bovensiepen. Ultrafast electron transfer, localization and solvation at ice–metal interfaces: Correlation of structure and dynamics. *Prog. Surf. Sci.*, 78(3-4):87–100, jan 2005. [57](#)
- [BPZ<sup>+</sup>13] E. M. Bothschafter, A. Paarmann, E. S. Zijlstra, N. Karpowicz, M. E. Garcia, Reinhard K., and R. Ernstorfer. Ultrafast evolution of the excited-state potential energy surface of  $\text{TiO}_2$  single crystals induced by carrier cooling. *Phys. Rev. Lett.*, 110:067402, Feb 2013. [42](#)
- [Bre99] Kevin F. Brennan. *The Physics of Semiconductors*. Cambridge University Press, 1999. [22](#)
- [Bré14] J.-L. Brédas. Mind the gap! *Mater. Horiz.*, 1(1):17–19, 2014. [11](#), [12](#)
- [BRP<sup>+</sup>12] A. A. Bakulin, A. Rao, V. G. Pavelyev, P. H. M. van Loosdrecht, M. S. Pshenichnikov, D. Niedzialek, J. Cornil, D. Beljonne, and R. H. Friend. The role of driving energy and delocalized states for charge separation in organic semiconductors. *Science*, 335(6074):1340–1344, feb 2012. [16](#), [28](#)
- [BSX<sup>+</sup>06] S. Blumstengel, S. Sadofev, C. Xu, J. Puls, and F. Henneberger. Converting Wannier into Frenkel excitons in an inorganic/organic hybrid semiconductor nanostructure. *Phys. Rev. Lett.*, 97:237401, Dec 2006. [27](#)
- [BvHS<sup>+</sup>93] P. W. M. Blom, P. J. van Hall, C. Smit, J. P. Cuypers, and J. H. Wolter. Selective exciton formation in thin GaAs/ $\text{Al}_x\text{Ga}_{1-x}\text{As}$  quantum wells. *Phys. Rev. Lett.*, 71:3878–3881, Dec 1993. [114](#)
- [CEM<sup>+</sup>04] S. Chatterjee, C. Ell, S. Mosor, G. Khitrova, H. M. Gibbs, W. Hoyer, M. Kira, S. W. Koch, J. P. Prineas, and H. Stolz. Excitonic photoluminescence in semiconductor quantum wells: Plasma versus excitons. *Phys. Rev. Lett.*, 92:067402, Feb 2004. [115](#)
- [CGC<sup>+</sup>02] X. Crispin, V. Geskin, A. Crispin, J. Cornil, R. Lazzaroni, W. R. Salaneck, and J.-L. Brédas. Characterization of the interface dipole at organic/ metal interfaces. *J. Am. Chem. Soc.*, 124(27):8131–8141, jul 2002. [9](#), [10](#), [14](#)

- [CGLI<sup>+</sup>10] L. Chiodo, J. M. García-Lastra, A. Iacomino, S. Ossicini, J. Zhao, H. Petek, and A. Rubio. Self-energy and excitonic effects in the electronic and optical properties of TiO<sub>2</sub> crystalline phases. *Phys. Rev. B*, 82:045207, Jul 2010. 13, 42
- [CK03] D. Cahen and A. Kahn. Electron energetics at surfaces and interfaces: Concepts and experiments. *Adv. Mater.*, 15(4):271–277, feb 2003. 161
- [CLJ<sup>+</sup>11] W.-L. Chan, M. Ligges, A. Jailaubekov, L. Kaake, L. Miaja-Avila, and X.-Y. Zhu. Observing the multiexciton state in singlet fission and ensuing ultrafast multielectron transfer. *Science*, 334(6062):1541–1545, dec 2011. 13, 24
- [CNS<sup>+</sup>89] Y. Chen, S. Nannarone, J. Schaefer, J. C. Hermanson, and G. J. Lapeyre. Coupled plasmon and phonon excitations in the space-charge layer on GaAs(110) surfaces. *Phys. Rev. B*, 39:7653–7658, Apr 1989. 89
- [CRZ<sup>+</sup>96] I. H. Campbell, S. Rubin, T. A. Zawodzinski, J. D. Kress, R. L. Martin, D. L. Smith, N. N. Barashkov, and J. P. Ferraris. Controlling schottky energy barriers in organic electronic devices using self-assembled monolayers. *Phys. Rev. B*, 54:R14321–R14324, Nov 1996. 10
- [CS01] D. S. Chemla and J. Shah. Many-body and correlation effects in semiconductors. *Nature*, 411(6837):549–557, May 2001. 114
- [CWA<sup>+</sup>14] Xuefeng Cui, Cong Wang, Adam Argondizzo, Sean Garrett-Roe, Branko Gumhalter, and Hrvoje Petek. Transient excitons at metal surfaces. *Nature Physics*, 10(7):505–509, jun 2014. 20, 56
- [CZH<sup>+</sup>99] H. Cao, Y. G. Zhao, S. T. Ho, E. W. Seelig, Q. H. Wang, and R. P. H. Chang. Random laser action in semiconductor powder. *Phys. Rev. Lett.*, 82:2278–2281, Mar 1999. 29
- [DBD02] O. Dulub, L. A. Boatner, and U. Diebold. STM study of the geometric and electronic structure of ZnO(0001)-Zn, (000 $\bar{1}$ )-O, (10 $\bar{1}$ 0), and (11 $\bar{2}$ 0) surfaces. *Surf. Sci.*, 519(3):201–217, nov 2002. 33, 66, 73, 77, 78
- [DDK03] O. Dulub, U. Diebold, and G. Kresse. Novel stabilization mechanism on polar surfaces: ZnO(0001)-Zn. *Phys. Rev. Lett.*, 90:016102, Jan 2003. 95
- [Dei11] J.-C. Deinert. Zeit- und winkelaufgelöste Zweiphotonen-Photoemissionsspektroskopie: Aufbau und Charakterisierung des Experiments anhand der Cu(111)- und der D<sub>2</sub>O/Cu(111)-Oberfläche. Master’s thesis, Freie Universität Berlin, 2011. 61, 62, 68, 76, 161, 165
- [DHH14] T.-F. Dai, W.-C. Hsu, and H.-C. Hsu. Improvement of photoluminescence and lasing properties in ZnO submicron spheres by elimination of surface-trapped state. *Opt. Express*, 22(22):27169, October 2014. 29
- [DHM<sup>+</sup>15] J.-C. Deinert, O. T. Hofmann, M. Meyer, P. Rinke, and J. Stähler. Local aspects of hydrogen-induced metallization of the ZnO(10 $\bar{1}$ 0) surface. *Phys. Rev. B*, 91:235313, Jun 2015. 81, 84

- [DKD04] U. Diebold, L. V. Koplitz, and O. Dulub. Atomic-scale properties of low-index ZnO surfaces. *Appl. Surf. Sci.*, 237(1-4):336–342, October 2004. 33, 66, 73
- [DPT66] T. C. Damen, S. P. S. Porto, and B. Tell. Raman effect in zinc oxide. *Phys. Rev.*, 142:570–574, Feb 1966. 21
- [DQLZ05] Gregory Dutton, Daniel P. Quinn, C. D. Lindstrom, and X.-Y. Zhu. Exciton dynamics at molecule-metal interfaces: C<sub>60</sub>/Au(111). *Phys. Rev. B*, 72:045441, Jul 2005. 13
- [Dru00] P. Drude. Zur Elektronentheorie der Metalle. *Ann. Phys.*, 306(3):566–613, 1900. 36
- [DSO<sup>+</sup>90] T. C. Damen, J. Shah, D. Y. Oberli, D. S. Chemla, J. E. Cunningham, and J. M. Kuo. Dynamics of exciton formation and relaxation in GaAs quantum wells. *Phys. Rev. B*, 42:7434–7438, Oct 1990. 2, 115, 125
- [Duk67] C. B. Duke. Optical absorption due to space-charge-induced localized states. *Phys. Rev.*, 159:632–644, Jul 1967. 36
- [DWG54] Billy B. DeMore, W. S. Wilcox, and J. H. Goldstein. Microwave spectrum and dipole moment of pyridine. *J. Chem. Phys.*, 22(5):876, 1954. 17, 130
- [DWM<sup>+</sup>14] J.-C. Deinert, D. Wegkamp, M. Meyer, C. Richter, M. Wolf, and J. Stähler. Ultrafast exciton formation at the ZnO(10 $\bar{1}$ 0) surface. *Phys. Rev. Lett.*, 113:057602, Jul 2014. 101
- [Ein05] A. Einstein. Über einen die Erzeugung und Verwandlung des Lichtes betreffenden heuristischen Gesichtspunkt. *Annalen der Physik*, 322(6):132–148, 1905. 48
- [EKR08] K. Ellmer, A. Klein, and B. Rech, editors. *Transparent Conductive Zinc Oxide*. Springer Berlin Heidelberg, 2008. 31
- [Ell01] K. Ellmer. Resistivity of polycrystalline zinc oxide films: current status and physical limit. *J. Phys. D: Appl. Phys.*, 34(21):3097–3108, oct 2001. 94
- [EMG76] D. Eger, A. Many, and Y. Goldstein. Quantum properties of strong accumulation layers on ZnO surfaces. *Surf. Sci.*, 58(1):18–24, aug 1976. 2, 89
- [ERR<sup>+</sup>10] D. A. Egger, F. Rissner, G. M. Rangger, O. T. Hofmann, L. Wittwer, G. Heimel, and E. Zojer. Self-assembled monolayers of polar molecules on Au(111) surfaces: Distributing the dipoles. *Phys. Chem. Chem. Phys.*, 12(17):4291, 2010. 17
- [Fau94] Th. Fauster. Two-photon photoemission. *Prog. Surf. Sci.*, 46(2-3):177–186, jun 1994. 54
- [FDG83] E. De Frésart, J. Darville, and J.M. Gilles. Surface properties of tin dioxide single crystals. *Surf. Sci.*, 126(1-3):518–522, mar 1983. 36

- [Fin06] K. Fink. Ab initio cluster calculations on the electronic structure of oxygen vacancies at the polar ZnO(000 $\bar{1}$ ) surface and on the adsorption of H<sub>2</sub>, CO, and CO<sub>2</sub> at these sites. *Phys. Chem. Chem. Phys.*, 8(13):1482, 2006. 97
- [FKK<sup>+</sup>07] H. Fukagawa, S. Kera, T. Kataoka, S. Hosoumi, Y. Watanabe, K. Kudo, and N. Ueno. The role of the ionization potential in vacuum-level alignment at organic semiconductor interfaces. *Adv. Mater.*, 19(5):665–668, mar 2007. 10
- [Fog15] L. Foglia. *Ultrafast Dynamics and Energy Loss Channels at a Hybrid Inorganic Organic Interface*. PhD thesis, Technische Universität Berlin, 2015. 106, 125, 128
- [För48] Th. Förster. Zwischenmolekulare Energiewanderung und Fluoreszenz. *Ann. Phys.*, 437(1-2):55–75, 1948. 27
- [Frö37] H. Fröhlich. Theory of electrical breakdown in ionic crystals. *Proceedings of the Royal Society A: Mathematical, Physical and Engineering Sciences*, 160(901):230–241, may 1937. 21
- [FSTB92] W. S. Fann, R. Storz, H. W. K. Tom, and J. Bokor. Direct measurement of nonequilibrium electron-energy distributions in subpicosecond laser-heated gold films. *Phys. Rev. Lett.*, 68:2834–2837, May 1992. 55
- [GBFW02] C. Gahl, U. Bovensiepen, C. Frischkorn, and M. Wolf. Ultrafast dynamics of electron localization and solvation in ice layers on Cu(111). *Phys. Rev. Lett.*, 89:107402, Aug 2002. 150
- [GHP11] D. S. Ginley, H. Hosono, and D. C. Paine, editors. *Handbook of Transparent Conductors*, volume 1. Springer US, 2011. 29, 31
- [GLRRT09] J. M. Garcia-Lastra, C. Rostgaard, A. Rubio, and K. S. Thygesen. Polarization-induced renormalization of molecular levels at metallic and semiconducting surfaces. *Phys. Rev. B*, 80(24):245427, dec 2009. 147
- [GMM01] D. Gust, Th. A. Moore, and A. L. Moore. Mimicking photosynthetic solar energy transduction. *Acc. Chem. Res.*, 34(1):40–48, jan 2001. 28
- [Göp85] W. Göpel. Chemisorption and charge transfer at ionic semiconductor surfaces: Implications in designing gas sensors. *Progress in Surface Science*, 20(1):9 – 103, 1985. 29
- [GPIR82] W. Göpel, J. Pollmann, I. Ivanov, and B. Reihl. Angle-resolved photoemission from polar and nonpolar zinc oxide surfaces. *Phys. Rev. B*, 26:3144–3150, Sep 1982. 30
- [Gri80] G Grimwall. *The Electron-Phonon Interaction in Metals*. North-Holland, 1980. 21
- [GS73] J. L. Gland and G. A. Somorjai. Low energy electron diffraction and work function studies of benzene, naphthalene and pyridine adsorbed on Pt(111) and Pt(100) single crystal surfaces. *Surf. Sci.*, 38(1):157–186, jul 1973. 17

- [GSH<sup>+</sup>14] Y. Garmshausen, J. Schwarz, J. Hildebrandt, B. Kobin, M. Pätzelt, and S. Hecht. Making nonsymmetrical bricks: Synthesis of insoluble dipolar sexiphenyls. *Org. Lett.*, 16(11):2838–2841, jun 2014. 4, 138
- [GWH00] Nien-Hui Ge, Chung M. Wong, and Charles B. Harris. Femtosecond studies of electron dynamics at interfaces. *Acc. Chem. Res.*, 33(2):111–118, February 2000. 57
- [Hai95] R. Haight. Electron dynamics at surfaces. *Surf. Sci. Rep.*, 21:275–325, 1995. 19, 21
- [HDX<sup>+</sup>13] O. T. Hofmann, J.-C. Deinert, Y. Xu, P. Rinke, J. Stähler, M. Wolf, and M. Scheffler. Large work function reduction by adsorption of a molecule with a negative electron affinity: Pyridine on ZnO(10 $\bar{1}$ 0). *J. Chem. Phys.*, 139(17):174701, nov 2013. 15, 129, 130, 137
- [HG94] M. Henzler and W. Göpel. *Oberflächenphysik des Festkörpers*. Vieweg+Teubner Verlag, 1994. 48, 64, 65
- [HGB00] K. Hannewald, S. Glutsch, and F. Bechstedt. Theory of photoluminescence in semiconductors. *Phys. Rev. B*, 62:4519–4525, Aug 2000. 115
- [HH04] H.-C. Hsu and W.-F. Hsieh. Excitonic polaron and phonon assisted photoluminescence of ZnO nanowires. *Solid State Commun.*, 131(6):371–375, aug 2004. 42
- [HHL<sup>+</sup>02] D. M. Hofmann, A. Hofstaetter, . Leiter, H. Zhou, F. Henecker, B. K. Meyer, S. B. Orlinskii, J. Schmidt, and P. G. Baranov. Hydrogen: A relevant shallow donor in zinc oxide. *Phys. Rev. Lett.*, 88:045504, Jan 2002. 38
- [HIM<sup>+</sup>06] G. Heliotis, G. Itskos, R. Murray, M. D. Dawson, I. M. Watson, and D. D. C. Bradley. Hybrid inorganic/organic semiconductor heterostructures with efficient non-radiative energy transfer. *Adv. Mater.*, 18(3):334–338, feb 2006. 27
- [HK69] G. Heiland and P. Kunstmann. Polar surfaces of zinc oxide crystals. *Surf. Sci.*, 13(1):72–84, jan 1969. 37
- [HKB07] E. Hendry, M. Koeberg, and M. Bonn. Exciton and electron–hole plasma formation dynamics in ZnO. *Phys. Rev. B*, 76(4):045214, jul 2007. 2, 25, 112, 124
- [HKW<sup>+</sup>00] St. Hövel, C. Kolczewski, M. Wühn, J. Albers, K. Weiss, V. Staemmler, and Ch. Wöll. Pyridine adsorption on the polar ZnO(0001) surface: Zn termination versus O termination. *J. Chem. Phys.*, 112(8):3909, 2000. 131, 132
- [HKWE96] T. Hertel, E. Knoesel, M. Wolf, and G. Ertl. Ultrafast electron dynamics at Cu(111): Response of an electron gas to optical excitation. *Phys. Rev. Lett.*, 76:535–538, Jan 1996. 52
- [HMG<sup>+</sup>11] T. Hosokai, H. Machida, A. Gerlach, S. Kera, F. Schreiber, and N. Ueno. Impact of structural imperfections on the energy-level alignment in organic films. *Phys. Rev. B*, 83:195310, May 2011. 18

- [HRMBK09] S. Hellmann, K. Rossnagel, M. Marczyński-Bühlow, and L. Kipp. Vacuum space-charge effects in solid-state photoemission. *Phys. Rev. B*, 79:035402, Jan 2009. 114
- [HRZB07] G. Heimel, L. Romaner, E. Zojer, and J.-L. Brédas. Toward control of the metal-organic interfacial electronic structure in molecular electronics: A first-principles study on self-assembled monolayers of  $\pi$ -conjugated molecules on noble metals. *Nano Lett.*, 7(4):932–940, apr 2007. 17, 129
- [HSR<sup>+</sup>97] U. Höfer, I. L. Shumay, Ch. Reuß, U. Thomann, W. Wallauer, and Th. Fauster. Time-resolved coherent photoelectron spectroscopy of quantized electronic states on metal surfaces. *Science*, 277(5331):1480–1482, September 1997. 52
- [Hüf96] S. Hüfner. *Photoelectron Spectroscopy*. Springer Berlin Heidelberg, 1996. 50, 52
- [IOH<sup>+</sup>01] E. Ito, H. Oji, N. Hayashi, H. Ishii, Y. Ouchi, and K. Seki. Electronic structures of TPD/metal interfaces studied by photoemission and Kelvin probe method. *Appl. Surf. Sci.*, 175-176:407–411, may 2001. 15
- [ISIS99] H. Ishii, K. Sugiyama, E. Ito, and K. Seki. Energy level alignment and interfacial electronic structures at organic/metal and organic/organic interfaces. *Adv. Mater.*, 11(8):605–625, 1999. 3, 9, 10, 14, 16
- [JdW05] A. Janotti and C. G. Van de Walle. Oxygen vacancies in ZnO. *Appl. Phys. Lett.*, 87(12):122102, 2005. 31
- [JdW06] A. Janotti and C. G. Van de Walle. Hydrogen multicentre bonds. *Nat. Mater.*, 6(1):44–47, dec 2006. 38
- [JMFH10] J. E. Johns, E. A. Muller, J. M. J. Frechet, and C. B. Harris. The origin of charge localization observed in organic photovoltaic materials. *J. Am. Chem. Soc.*, 132(44):15720–15725, November 2010. 11, 150, 152
- [JZG84] K. Jacobi, G. Zwicker, and A. Gutmann. Work function, electron affinity and band bending of zinc oxide surfaces. *Surf. Sci.*, 141(1):109–125, jun 1984. 2, 3, 40, 73, 76, 77, 78, 81
- [KAV<sup>+</sup>96] D. Kovalev, B. Averboux, D. Volm, B. K. Meyer, H. Amano, and I. Akasaki. Free exciton emission in GaN. *Phys. Rev. B*, 54:2518–2522, Jul 1996. 117, 124
- [KBH<sup>+</sup>14] N. Kedem, S. Blumstengel, F. Henneberger, H. Cohen, G. Hodes, and D. Cahen. Morphology-, synthesis- and doping-independent tuning of ZnO work function using phenylphosphonates. *Phys. Chem. Chem. Phys.*, 16(18):8310, 2014. 3, 15, 73
- [KFS<sup>+</sup>13] S. Kuehn, S. Friede, S. Sadofev, S. Blumstengel, F. Henneberger, and T. Elsaesser. Surface excitons on a ZnO (000-1) thin film. *Appl. Phys. Lett.*, 103(19):191909, 2013. 42, 43, 110

- [KFZ<sup>+</sup>10] C. Klingshirn, J. Fallert, H. Zhou, J. Sartor, C. Thiele, F. Maier-Flaig, D. Schneider, and H. Kalt. 65 years of ZnO research – old and very recent results. *physica status solidi (b)*, 247(6):1424–1447, apr 2010. 1, 29, 42
- [KGB<sup>+</sup>12] B. Kobin, L. Grubert, S. Blumstengel, F. Henneberger, and S. Hecht. Vacuum-processable ladder-type oligophenylenes for organic–inorganic hybrid structures: Synthesis, optical and electrochemical properties upon increasing planarization as well as thin film growth. *J. Mater. Chem.*, 22(10):4383, 2012. 143
- [KGGB<sup>+</sup>02] M. Kunat, St. Gil Girol, Th. Becker, U. Burghaus, and Ch. Wöll. Stability of the polar surfaces of ZnO: A reinvestigation using He-atom scattering. *Phys. Rev. B*, 66:081402, Aug 2002. 34, 77
- [KHFK07] C. Klingshirn, R. Hauschild, J. Fallert, and H. Kalt. Room-temperature stimulated emission of ZnO: Alternatives to excitonic lasing. *Phys. Rev. B*, 75(11):115203, mar 2007. 25
- [KIA<sup>+</sup>05] R. Khanna, K. Ip, K. K. Allums, K. Baik, C. R. Abernathy, S. J. Pearton, Y. W. Heo, D. P. Norton, F. Ren, S. Shojah-Ardalan, and R. Wilkins. Proton irradiation of ZnO schottky diodes. *J. Electron. Mater.*, 34(4):395–398, apr 2005. 29
- [Kin75] D. A. King. Thermal desorption from metal surfaces: A review. *Surf. Sci.*, 47(1):384–402, December 1975. 68, 132
- [Kir08] P. S. Kirchmann. *Ultrafast Electron Dynamics in Low-Dimensional Materials*. PhD thesis, Freie Universität Berlin, feb 2008. 22, 53
- [Kit05] C. Kittel. *Introduction to Solid State Physics*, volume 8. John Wiley & Sons Ltd, 2005. 103
- [KKK76] P. Kneschaurek, Avid Kamgar, and J. F. Koch. Electronic levels in surface space charge layers on Si(100). *Phys. Rev. B*, 14:1610–1622, Aug 1976. 89
- [KKKG06] S. W. Koch, M. Kira, G. Khitrova, and H. M. Gibbs. Semiconductor excitons in new light. *Nat. Mater.*, 5(7):523–531, jul 2006. 2, 24, 25
- [KLI04] J. Kröger, S. Lehwald, and H. Ibach. Estimation of the electron–phonon coupling parameter of Mo(110)–H and W(110)–H. *Phys. Rev. B*, 69:201404, May 2004. 22
- [Kli07] C. Klingshirn. ZnO: Material, physics and applications. *ChemPhysChem*, 8(6):782–803, apr 2007. 29, 44
- [Koc07] N. Koch. Organic electronic devices and their functional interfaces. *ChemPhysChem*, 8(10):1438–1455, jul 2007. 1, 8, 9, 10
- [Koc12] N. Koch. *Electronic Structure of Interfaces with Conjugated Organic Materials*, chapter 2, pages 35–64. Wiley-VCH Verlag GmbH & Co. KGaA, 2012. 9

- [KPD<sup>+</sup>05] C. Klingshirn, H. Priller, M. Decker, J. Brückner, H. Kalt, R. Hauschild, J. Zeller, A. Waag, A. Bakin, H. Wehmann, K. Thonke, R. Sauer, R. Kling, F. Reuss, and Ch. Kirchner. Excitonic properties of ZnO. In *Advances in Solid State Physics*, pages 275–287. Springer Science + Business Media, 2005. 29
- [KV11] P. D. C. King and T. D. Veal. Conductivity in transparent oxide semiconductors. *J. Phys.: Condens. Matter*, 23(33):334214, aug 2011. 29, 32
- [KVJ<sup>+</sup>09] P. D. C. King, T. D. Veal, P. H. Jefferson, J. Zúñiga Pérez, V. Muñoz Sanjosé, and C. F. McConville. Unification of the electrical behavior of defects, impurities, and surface states in semiconductors: Virtual gap states in CdO. *Phys. Rev. B*, 79:035203, Jan 2009. 32, 36
- [KVM<sup>+</sup>10] P. D. C. King, T. D. Veal, C. F. McConville, J. Zúñiga-Pérez, V. Muñoz-Sanjosé, M. Hopkinson, E. D. L. Rienks, M. Fuglsang Jensen, and Ph. Hofmann. Surface band-gap narrowing in quantized electron accumulation layers. *Phys. Rev. Lett.*, 104(25):256803, jun 2010. 1, 20, 36
- [KYY<sup>+</sup>04] S. Kera, Y. Yabuuchi, H. Yamane, H. Setoyama, K. K. Okudaira, A. Kahn, and N. Ueno. Impact of an interface dipole layer on molecular level alignment at an organic-conductor interface studied by ultraviolet photoemission spectroscopy. *Phys. Rev. B*, 70:085304, Aug 2004. 10
- [Lia70] W. Y. Liang. Excitons. *Physics Education*, 5(4):226–228, jul 1970. 22, 23
- [LK71] N. D. Lang and W. Kohn. Theory of metal surfaces: Work function. *Phys. Rev. B*, 3:1215–1223, Feb 1971. 14
- [Loo08] D. C. Look. Two-layer Hall-effect model with arbitrary surface-donor profiles: Application to ZnO. *J. Appl. Phys.*, 104(6):063718, 2008. 36, 39
- [LPTT14] L. L. C. Lem, M. R. Phillips, and C. Ton-That. Controlling the visible luminescence in hydrothermal ZnO. *J. Lumin.*, 154:387–391, oct 2014. 42
- [LRP<sup>+</sup>14] I. Lange, S. Reiter, M. Pätzel, A. Zykov, A. Nefedov, J. Hildebrandt, S. Hecht, S. Kowarik, Ch. Wöll, G. Heimel, and D. Neher. Tuning the work function of polar zinc oxide surfaces using modified phosphonic acid self-assembled monolayers. *Adv. Funct. Mater.*, 24(44):7014–7024, sep 2014. 15
- [Lüt10] H. Lüth. *Solid Surfaces, Interfaces and Thin Films*. Graduate Texts in Physics. Springer Berlin Heidelberg, 5th edition, 2010. 2, 15, 18, 33, 34, 35, 36, 91, 93
- [LW77] L. D. Laude and M. Wautelet. Double-beam photoemission and the electronic structure of tellurium. *Il Nuovo Cimento B*, 39(2):734–738, jun 1977. 54
- [LZ07] S. Lany and A. Zunger. Dopability, intrinsic conductivity, and nonstoichiometry of transparent conducting oxides. *Phys. Rev. Lett.*, 98(4):045501, jan 2007. 41

- [LZR<sup>+</sup>08] A. Liu, S. Zhao, S.-B. Rim, J. Wu, M. Könemann, P. Erk, and P. Peumans. Control of electric field strength and orientation at the donor–acceptor interface in organic solar cells. *Adv. Mater.*, 20(5):1065–1070, mar 2008. [28](#)
- [Mah67] G. D. Mahan. Excitons in degenerate semiconductors. *Phys. Rev.*, 153(3):882–889, January 1967. [25](#)
- [Mah70] G. D. Mahan. Theory of photoemission in simple metals. *Phys. Rev. B*, 2:4334–4350, Dec 1970. [51](#)
- [MAH<sup>+</sup>04] B. K. Meyer, H. Alves, D. M. Hofmann, W. Kriegseis, D. Forster, F. Bertram, J. Christen, A. Hoffmann, M. Straßburg, M. Dworzak, U. Haboeck, and A. V. Rodina. Bound exciton and donor–acceptor pair recombinations in ZnO. *physica status solidi (b)*, 241(2):231–260, feb 2004. [42](#)
- [MBJ95] B. A. McDougall, T. Balasubramanian, and E. Jensen. Phonon contribution to quasiparticle lifetimes in Cu measured by angle-resolved photoemission. *Phys. Rev. B*, 51:13891–13894, May 1995. [22](#)
- [Mey04] B. Meyer. First-principles study of the polar O-terminated ZnO surface in thermodynamic equilibrium with oxygen and hydrogen. *Phys. Rev. B*, 69:045416, Jan 2004. [34](#)
- [MJ09] M. D. McCluskey and S. J. Jokela. Defects in ZnO. *J. Appl. Phys.*, 106(7):071101, 2009. [31](#)
- [MKH79] H. Moormann, D. Kohl, and G. Heiland. Work function and band bending on clean cleaved zinc oxide surfaces. *Surf. Sci.*, 80:261–264, feb 1979. [40](#)
- [MKH80] H. Moormann, D. Kohl, and G. Heiland. Variations of work function and surface conductivity on clean cleaved zinc oxide surfaces by annealing and by hydrogen adsorption. *Surf. Sci.*, 100(2):302–314, nov 1980. [75](#), [76](#), [77](#)
- [MMC96] T. Miller, W. E. McMahon, and T.-C. Chiang. Interference between bulk and surface photoemission transitions in Ag(111). *Phys. Rev. Lett.*, 77:1167–1170, Aug 1996. [52](#)
- [MMD<sup>+</sup>04] B. Meyer, D. Marx, O. Dulub, U. Diebold, M. Kunat, D. Langenberg, and Ch. Wöll. Partial dissociation of water leads to stable superstructures on the surface of zinc oxide. *Angew. Chem. Int. Ed.*, 43(48):6641–6645, dec 2004. [33](#)
- [MMG93] R. Matzdorf, G. Meister, and A. Goldmann. Influence of electron–phonon interactions on angle-resolved photoelectron spectra from metals. *Surf. Sci.*, 296(2):241–250, oct 1993. [22](#)
- [MOI99] Y. Mi, H. Odaka, and S. Iwata. Electronic structures and optical properties of ZnO, SnO<sub>2</sub> and In<sub>2</sub>O<sub>3</sub>. *Jpn. J. Appl. Phys.*, 38(Part 1, No. 6A):3453–3458, jun 1999. [30](#)

- [Mön01] W. Mönch. *Semiconductor Surfaces and Interfaces*, volume 26 of *Springer Series in Surface Sciences*. Springer Berlin Heidelberg, Berlin, Heidelberg, third edition, 2001. [34](#)
- [MS85] R.A. Marcus and N. Sutin. Electron transfers in chemistry and biology. *Biochimica et Biophysica Acta (BBA) - Reviews on Bioenergetics*, 811(3):265–322, aug 1985. [26](#)
- [MSKL11] W. Melitz, J. Shen, A. C. Kummel, and S. Lee. Kelvin probe force microscopy and its application. *Surf. Sci. Rep.*, 66(1):1–27, jan 2011. [15](#)
- [MYTZ08] M. Muntwiler, Q. Yang, W. A. Tisdale, and X.-Y. Zhu. Coulomb barrier for charge separation at an organic semiconductor interface. *Phys. Rev. Lett.*, 101(19):196403, nov 2008. [27](#), [28](#)
- [MZ10] M. Muntwiler and X.-Y. Zhu. *Dynamics at Solid State Surfaces and Interfaces*, volume 1: Current Developments, chapter Exciton Formation and decay at Surfaces and Interfaces, pages 325–358. Wiley-Blackwell, oct 2010. [11](#), [12](#), [13](#)
- [NBW<sup>+</sup>10] T. Nagata, O. Bierwagen, M. E. White, M.-Y. Tsai, and J. S. Speck. Study of the Au Schottky contact formation on oxygen plasma treated *n*-type SnO<sub>2</sub> (101) thin films. *J. Appl. Phys.*, 107(3):033707, 2010. [36](#)
- [Nen75] I. Nenner. Temporary negative ions and electron affinities of benzene and *n*-heterocyclic molecules: Pyridine, pyridazine, pyrimidine, pyrazine, and *s*-triazine. *J. Chem. Phys.*, 62(5):1747, 1975. [17](#), [130](#)
- [NF03] N. H. Nickel and K. Fleischer. Hydrogen local vibrational modes in zinc oxide. *Phys. Rev. Lett.*, 90:197402, May 2003. [66](#)
- [NHF<sup>+</sup>14] H. Nakanotani, T. Higuchi, T. Furukawa, K. Masui, K. Morimoto, M. Numata, H. Tanaka, Y. Sagara, T. Yasuda, and C. Adachi. High-efficiency organic light-emitting diodes with fluorescent emitters. *Nature Communications*, 5:4016, may 2014. [27](#)
- [NHL06] J. B. Neaton, Mark S. Hybertsen, and Steven G. Louie. Renormalization of molecular electronic levels at metal-molecule interfaces. *Phys. Rev. Lett.*, 97:216405, Nov 2006. [147](#)
- [NIE<sup>+</sup>95] S. Narioka, H. Ishii, K. Edamatsu, K. Kamiya, S. Hasegawa, T. Ohta, N. Ueno, and K. Seki. Angle-resolved photoelectron spectroscopic study of oriented *p*-sexiphenyl: Wave-number conservation and blurring in a short model compound of poly(*p*-phenylene). *Phys. Rev. B*, 52(4):2362–2373, jul 1995. [140](#)
- [NKHT07] A. Natan, L. Kronik, H. Haick, and R. T. Tung. Electrostatic properties of ideal and non-ideal polar organic monolayers: Implications for electronic devices. *Adv. Mater.*, 19(23):4103–4117, dec 2007. [11](#)

- [Noz01] A. J. Nozik. Spectroscopy and hot electron relaxation dynamics in semiconductor quantum wells and quantum dots. *Annu. Rev. Phys. Chem.*, 52(1):193–231, oct 2001. [103](#)
- [NR92] F. P. Netzer and M. G. Ramsey. Structure and orientation of organic molecules on metal surfaces. *Crit. Rev. Solid State Mater. Sci.*, 17(5):397–475, jan 1992. [132](#)
- [ÖAL<sup>+</sup>05] Ü. Özgür, Ya. I. Alivov, C. Liu, A. Teke, M. A. Reshchikov, S. Doğan, V. Avrutin, S.-J. Cho, and H. Morkoç. A comprehensive review of ZnO materials and devices. *J. Appl. Phys.*, 98(4):041301, 2005. [29](#)
- [OM10] K. Ozawa and K. Mase. Metallization of ZnO(101 $\bar{1}$ 0) by adsorption of hydrogen, methanol, and water: Angle-resolved photoelectron spectroscopy. *Phys. Rev. B*, 81(20):1–6, May 2010. [36](#), [37](#), [38](#), [66](#), [76](#)
- [OM11] K. Ozawa and K. Mase. Comparison of the surface electronic structures of H adsorbed ZnO surfaces: An angle-resolved photoelectron spectroscopy study. *Phys. Rev. B*, 83(12):1–8, March 2011. [2](#), [20](#), [21](#), [38](#), [40](#), [74](#), [77](#), [78](#), [79](#), [80](#), [81](#), [83](#), [95](#), [96](#), [103](#), [109](#), [119](#), [164](#)
- [OOE<sup>+</sup>09] K. Ozawa, Y. Oba, K. Edamoto, M. Higashiguchi, Y. Miura, K. Tanaka, K. Shimada, H. Namatame, and M. Taniguchi. Valence-band structure of the polar ZnO surfaces studied by angle-resolved photoelectron spectroscopy. *Phys. Rev. B*, 79(7):075314, feb 2009. [75](#)
- [OSS<sup>+</sup>03] K. Ozawa, K. Sawada, Y. Shirotori, K. Edamoto, and M. Nakatake. Angle-resolved photoelectron spectroscopy study of the anion-derived dangling-bond band on ZnO (10 $\bar{1}$ 0). *Phys. Rev. B*, 68(12):125417, sep 2003. [75](#)
- [PAD08] P. Puschnig and C. Ambrosch-Draxl. First-principles approach to the understanding of  $\pi$ -conjugated organic semiconductors. *Monatshefte für Chemie - Chemical Monthly*, 139(4):389–399, mar 2008. [138](#)
- [Pen76] J.B. Pendry. Theory of photoemission. *Surf. Sci.*, 57(2):679–705, jul 1976. [51](#)
- [Per75] S. Permogorov. Hot excitons in semiconductors. *physica status solidi (b)*, 68(1):9–42, mar 1975. [24](#)
- [Per02] I. E. Perakis. Condensed-matter physics: Exciton developments. *Nature*, 417(6884):33–35, may 2002. [24](#)
- [PHHD14] K. Palczynski, G. Heimel, J. Heyda, and J. Dzubiella. Growth and characterization of molecular crystals of para-sexiphenyl by all-atom computer simulations. *Crystal Growth & Design*, 14(8):3791–3799, aug 2014. [140](#)
- [PLL<sup>+</sup>06] L. Perfetti, P. A. Loukakos, M. Lisowski, U. Bovensiepen, H. Berger, S. Biermann, P. S. Cornaglia, A. Georges, and M. Wolf. Time evolution of the electronic structure of 1T-TaS<sub>2</sub> through the insulator-metal transition. *Phys. Rev. Lett.*, 97:067402, Aug 2006. [55](#)

- [PO97] H. Petek and S. Ogawa. Femtosecond time-resolved two-photon photoemission studies of electron dynamics in metals. *Prog. Surf. Sci.*, 56(4):239–310, dec 1997. [56](#)
- [PZK<sup>+</sup>04] J. M. Pitarke, V. P. Zhukov, R. Keyling, E. V. Chulkov, and P. M. Echenique. Ultrafast electron dynamics in metals. *ChemPhysChem*, 5(9):1284–1300, 2004. [20](#)
- [QF58] J. J. Quinn and R. A. Ferrell. Electron self-energy approach to correlation in a degenerate electron gas. *Phys. Rev.*, 112:812–827, Nov 1958. [21](#)
- [Red03] P. A. Redhead. Hydrogen in vacuum systems: An overview. In *AIP Conference Proceedings*, volume 671, pages 243–254. AIP, 2003. [38](#)
- [RGK<sup>+</sup>14] J. Reimann, J. Gdde, K. Kuroda, E. V. Chulkov, and U. Hfer. Spectroscopy and dynamics of unoccupied electronic states of the topological insulators Sb<sub>2</sub>Te<sub>3</sub> and Sb<sub>2</sub>Te<sub>2</sub>S. *Phys. Rev. B*, 90:081106, Aug 2014. [52](#)
- [RGW92] U. Rau, H. H. Gttler, and J. H. Werner. The ideality of spatially inhomogeneous schottky contacts. *MRS Proc.*, 260, jan 1992. [11](#)
- [Ric14] C. Richter. Electron and exciton dynamics at ZnO surfaces. Master’s thesis, Freie Universitt Berlin, 2014. [79](#), [97](#), [98](#), [101](#), [114](#)
- [RKK<sup>+</sup>15] D. A. Racke, L. L. Kelly, H. Kim, P. Schulz, A. Sigdel, J. J. Berry, S. Graham, D. Nordlund, and O. L. A. Monti. Disrupted attosecond charge carrier delocalization at a hybrid organic/inorganic semiconductor interface. *The Journal of Physical Chemistry Letters*, 6(10):1935–1941, 2015. PMID: 26263273. [28](#)
- [RKM15] D. A. Racke, L. L. Kelly, and O. L. A. Monti. The importance of gap states for energy level alignment at hybrid interfaces. *J. Electron Spectrosc. Relat. Phenom.*, 204:132–139, oct 2015. [4](#), [9](#), [18](#), [136](#)
- [RL96] L. J. Rothberg and A. J. Lovinger. Status of and prospects for organic electroluminescence. *J. Mater. Res.*, 11(12):3174–3187, dec 1996. [9](#)
- [RSA<sup>+</sup>12] G. Ren, C. W. Schlenker, E. Ahmed, S. Subramaniyan, S. Olthof, A. Kahn, D. S. Ginger, and S. A. Jenekhe. Photoinduced hole transfer becomes suppressed with diminished driving force in polymer-fullerene solar cells while electron transfer remains active. *Adv. Funct. Mater.*, 23(10):1238–1249, oct 2012. [12](#)
- [RWKP03] M. Rhlfing, N.-P. Wang, P. Krger, and J. Pollmann. Image states and excitons at insulator surfaces with negative electron affinity. *Phys. Rev. Lett.*, 91:256802, Dec 2003. [119](#)
- [Sam73] S. Samson. Defect structure and electronic donor levels in stannic oxide crystals. *J. Appl. Phys.*, 44(10):4618, 1973. [31](#)
- [Sau59] G. Sauerbrey. Verwendung von Schwingquarzen zur Wgung dnner Schichten und zur Mikrowgung. *Zeitschrift fr Physik*, 155(2):206–222, 1959. [69](#)

- [SBB<sup>+</sup>15] R. Schlesinger, F. Bianchi, S. Blumstengel, C. Christodoulou, R. Ovsyannikov, B. Kobin, K. Moudgil, S. Barlow, S. Hecht, S.R. Marder, F. Henneberger, and N. Koch. Efficient light emission from inorganic and organic semiconductor hybrid structures by energy-level tuning. *Nature Communications*, 6:6754, apr 2015. 3, 9, 10, 73
- [SBMW08] J. Stähler, U. Bovensiepen, M. Meyer, and M. Wolf. A surface science approach to ultrafast electron transfer and solvation dynamics at interfaces. *Chem. Soc. Rev.*, 37(10):2180, 2008. 150
- [SBP<sup>+</sup>02] J. Schnadt, P. A. Brühwiler, L. Patthey, J. N. O’Shea, S. Södergren, M. Odelius, R. Ahuja, O. Karis, M. Bässler, P. Persson, H. Siegbahn, S. Lunell, and N. Mårtensson. Experimental evidence for sub-3-fs charge transfer from an aromatic adsorbate to a semiconductor. *Nature*, 418(6898):620–623, aug 2002. 28
- [SBS<sup>+</sup>13] Ch. Strothkämper, A. Bartelt, P. Sippel, Th. Hannappel, R. Schütz, and R. Eichberger. Delayed electron transfer through interface states in hybrid ZnO/organic-dye nanostructures. *J. Phys. Chem. C*, 117(35):17901–17908, sep 2013. 28
- [SBW10] J. Stähler, U. Bovensiepen, and M. Wolf. Electron dynamics at polar molecule-metal interfaces: Competition between localization, solvation, and transfer. In *Dynamics at Solid State Surfaces and Interfaces*, pages 359–379. Wiley-Blackwell, oct 2010. 58
- [SC94] E. A. Silinsh and V. Čápek. *Organic Molecular Crystals: Interaction, Localization, and Transport Phenomena*. AIP Press, Woodbury, NY, 1994. 11
- [Sco03] J. Campbell Scott. Metal–organic interface and charge injection in organic electronic devices. *Journal of Vacuum Science & Technology A: Vacuum, Surfaces, and Films*, 21(3):521, 2003. 26
- [SDW<sup>+</sup>15] J. Stähler, J.-C. Deinert, D. Wegkamp, S. Hagen, and M. Wolf. Real-time measurement of the vertical binding energy during the birth of a solvated electron. *J. Am. Chem. Soc.*, 137(10):3520–3524, mar 2015. 150
- [SFR<sup>+</sup>09] A. Schleife, F. Fuchs, C. Rödl, J. Furthmüller, and F. Bechstedt. Branch-point energies and band discontinuities of III-nitrides and III-/II-oxides from quasiparticle band-structure calculations. *Appl. Phys. Lett.*, 94(1):012104, 2009. 32
- [SG71] J.R. Schrieffer and R. Gomer. Induced covalent bond mechanism of chemisorption. *Surf. Sci.*, 25(2):315–320, apr 1971. 14
- [SGH<sup>+</sup>13] B. F. Spencer, D. M. Graham, S. J. O. Hardman, E. A. Seddon, M. J. Cliffe, K. L. Syres, A. G. Thomas, S. K. Stubbs, F. Sirotti, M. G. Silly, P. F. Kirkham, A. R. Kumarasinghe, G. J. Hirst, A. J. Moss, S. F. Hill, D. A. Shaw, S. Chattopadhyay, and W. R. Flavell. Time-resolved surface photovoltage measurements at n-type photovoltaic surfaces: Si(111) and ZnO(10 $\bar{1}$ 0). *Phys. Rev. B*, 88(19):195301, nov 2013. 37

- [SKB<sup>+</sup>04] J. Szczytko, L. Kappei, J. Berney, F. Morier-Genoud, M. T. Portella-Oberli, and B. Deveaud. Determination of the exciton formation in quantum wells from time-resolved interband luminescence. *Phys. Rev. Lett.*, 93(13):137401, sep 2004. [2](#), [25](#), [114](#), [115](#)
- [SKdW<sup>+</sup>05] O. Schmidt, P. Kiesel, C. G. Van de Walle, N. M. Johnson, J. Nause, and G. H. Döhler. Effects of an electrically conducting layer at the zinc oxide surface. *Jpn. J. Appl. Phys.*, 44(10):7271–7274, oct 2005. [36](#), [37](#)
- [Ski88] J. L. Skinner. Theory of pure dephasing in crystals. *Annu. Rev. Phys. Chem.*, 39(1):463–478, oct 1988. [22](#)
- [SLMF14] M. Slootsky, X. Liu, V. M. Menon, and S. R. Forrest. Room temperature frenkel-wannier-mott hybridization of degenerate excitons in a strongly coupled microcavity. *Phys. Rev. Lett.*, 112:076401, Feb 2014. [110](#)
- [SOOK95] A. Sutoh, Y. Okada, S. Ohta, and M. Kawabe. Cracking efficiency of hydrogen with tungsten filament in molecular beam epitaxy. *Jpn. J. Appl. Phys.*, 34(Part 2, No. 10B):L1379–L1382, oct 1995. [81](#)
- [SPD98] Th. Sjödin, H. Petek, and H.-L. Dai. Ultrafast carrier dynamics in silicon: A two-color transient reflection grating study on a (111) surface. *Phys. Rev. Lett.*, 81:5664–5667, Dec 1998. [107](#)
- [SPN<sup>+</sup>14] K. R. Siefertmann, C. D. Pemmaraju, S. Nepll, A. Shavorskiy, A. A. Cordones, J. Vura-Weis, D. S. Slaughter, F. P. Sturm, F. Weise, H. Bluhm, M. L. Strader, H. Cho, M.F. Lin, C. Bacellar, C. Khurmi, J. Guo, G. Coslovich, J. S. Robinson, R. A. Kaindl, R. W. Schoenlein, A. Belkacem, D. M. Neumark, S. R. Leone, D. Nordlund, H. Ogasawara, O. Krupin, J. J. Turner, W. F. Schlotter, M. R. Holmes, M. Messerschmidt, M. P. Minitti, S. Gul, J. Z. Zhang, N. Huse, D. Prendergast, and O. Gessner. Atomic-scale perspective of ultrafast charge transfer at a dye–semiconductor interface. *J. Phys. Chem. Lett.*, 5(15):2753–2759, aug 2014. [2](#), [4](#), [26](#), [28](#), [148](#), [152](#)
- [SPSZ12] D. Sanchez-Portal, J. Stähler, and X.-Y. Zhu. Basic theory of heterogeneous electron transfer. In *Dynamics at Solid State Surfaces and Interfaces*, volume 2, chapter 4, pages 155–180. Wiley-Blackwell, apr 2012. [26](#)
- [SR92] H. L. Skriver and N. M. Rosengaard. Surface energy and work function of elemental metals. *Phys. Rev. B*, 46:7157–7168, Sep 1992. [16](#)
- [SRF<sup>+</sup>11] A. Schleife, C. Rödl, F. Fuchs, K. Hannewald, and F. Bechstedt. Optical absorption in degenerately doped semiconductors: Mott transition or Mahan excitons? *Phys. Rev. Lett.*, 107(23):236405, November 2011. [25](#)
- [SS05] B. Sun and H. Sirringhaus. Solution-processed zinc oxide field-effect transistors based on self-assembly of colloidal nanorods. *Nano Lett.*, 5(12):2408–2413, dec 2005. [29](#)

- [SS14] S. Suga and A. Sekiyama. *Photoelectron Spectroscopy*, volume 176 of *Springer Series in Optical Sciences*. Springer Berlin Heidelberg, 1st edition, 2014. [48](#), [50](#), [51](#)
- [SSO<sup>+</sup>04] K. Sawada, Y. Shirotori, K. Ozawa, K. Edamoto, and M. Nakatake. Valence band structure of the ZnO surface studied by angle-resolved photoemission spectroscopy. *Appl. Surf. Sci.*, 237(1-4):343–347, oct 2004. [163](#)
- [ST11] C. W. Schlenker and M. E. Thompson. Current challenges in organic photovoltaic solar energy conversion. In *Unimolecular and Supramolecular Electronics I*, pages 175–212. Springer Science + Business Media, 2011. [12](#)
- [SWSL07] F. A. Selim, M. H. Weber, D. Solodovnikov, and K. G. Lynn. Nature of native defects in ZnO. *Phys. Rev. Lett.*, 99(8):085502, aug 2007. [31](#), [38](#)
- [TFS90] V. V. Travnikov, A. Freiberg, and S. F. Savikhin. Surface excitons in ZnO crystals. *J. Lumin.*, 47(3):107–112, oct 1990. [43](#), [110](#)
- [Tho60] D. G. Thomas. The exciton spectrum of zinc oxide. *J. Phys. Chem. Solids*, 15(1-2):86–96, aug 1960. [29](#), [42](#)
- [TKK<sup>+</sup>15] A. V. Trifonov, S. N. Korotan, A. S. Kurdyubov, I. Ya. Gerlovin, I. V. Ignatiev, Yu. P. Efimov, S. A. Eliseev, V. V. Petrov, Yu. K. Dolgikh, V. V. Ovsyankin, and A. V. Kavokin. Nontrivial relaxation dynamics of excitons in high-quality InGaAs/GaAs quantum wells. *Phys. Rev. B*, 91:115307, Mar 2015. [125](#)
- [TL56] D. G. Thomas and J. J. Lander. Hydrogen as a donor in zinc oxide. *J. Chem. Phys.*, 25(6):1136, 1956. [38](#)
- [TMN<sup>+</sup>08] W. A. Tisdale, M. Muntwiler, D. J. Norris, E. S. Aydil, and X.-Y. Zhu. Electron dynamics at the ZnO (10 $\bar{1}0$ ) surface. *J. Phys. Chem. C*, 112(37):14682–14692, sep 2008. [2](#), [3](#), [37](#), [40](#), [44](#), [74](#), [75](#), [76](#), [77](#), [101](#), [103](#), [105](#), [106](#), [107](#), [125](#), [127](#)
- [TNK<sup>+</sup>14] M. Timpel, M. V. Nardi, S. Krause, G. Ligorio, Ch. Christodoulou, L. Pasquali, A. Giglia, J. Frisch, B. Wegner, P. Moras, and N. Koch. Surface modification of ZnO(0001)–Zn with phosphonate-based self-assembled monolayers: Binding modes, orientation, and work function. *Chem. Mater.*, 26(17):5042–5050, sep 2014. [73](#)
- [TOO<sup>+</sup>04] A. Tsukazaki, A. Ohtomo, T. Onuma, M. Ohtani, T. Makino, M. Sumiya, K. Ohtani, S. F. Chichibu, S. Fuke, Y. Segawa, H. Ohno, H. Koinuma, and M. Kawasaki. Repeated temperature modulation epitaxy for p-type doping and light-emitting diode based on ZnO. *Nat. Mater.*, 4(1):42–46, dec 2004. [31](#)
- [TPP11] S. Tanuma, C. J. Powell, and D. R. Penn. Calculations of electron inelastic mean free paths. IX. data for 41 elemental solids over the 50 eV to 30 keV range. *Surf. Interface Anal.*, 43(3):689–713, feb 2011. [52](#)

- [Tun92] R. T. Tung. Electron transport at metal-semiconductor interfaces: General theory. *Phys. Rev. B*, 45:13509–13523, Jun 1992. 11
- [Van00] C. G. Van de Walle. Hydrogen as a cause of doping in zinc oxide. *Phys. Rev. Lett.*, 85(5):1012–1015, jul 2000. 38
- [VBGF12] Y. Vaynzof, A. A. Bakulin, S. Gélinas, and R. H. Friend. Direct observation of photoinduced bound charge-pair states at an organic-inorganic semiconductor interface. *Phys. Rev. Lett.*, 108:246605, Jun 2012. 28, 148
- [vGDGS94] R. van Grondelle, J. P. Dekker, T. Gillbro, and V. Sundstrom. Energy transfer and trapping in photosynthesis. *Biochimica et Biophysica Acta (BBA) - Bioenergetics*, 1187(1):1–65, aug 1994. 27
- [VN03] C. G. Van De Walle and J. Neugebauer. Universal alignment of hydrogen levels in semiconductors, insulators and solutions. *Nature*, 423(6940):626–628, 2003. 38
- [VW05] L. S. Vlasenko and G. D. Watkins. Optical detection of electron paramagnetic resonance in room-temperature electron-irradiated ZnO. *Phys. Rev. B*, 71:125210, Mar 2005. 31
- [WBB<sup>+</sup>09] C. Wang, A. S. Batsanov, M. R. Bryce, S. Martín, R. J. Nichols, S. J. Higgins, V. M. García-Suárez, and C. J. Lambert. Oligoynne single molecule wires. *J. Am. Chem. Soc.*, 131(43):15647–15654, nov 2009. 17, 129
- [WDM<sup>+</sup>93] J. F. Walsh, R. Davis, C. A. Muryn, G. Thornton, V. R. Dhanak, and K. C. Prince. Orientation of benzene and pyridine on zno(1010). *Phys. Rev. B*, 48:14749–14752, Nov 1993. 17, 132
- [Weg15] D. Wegkamp. *Ultrafast Electron Dynamics and the Role of Screening*. Phd thesis, Freie Universität Berlin, 2015. 60, 61, 62, 164, 166
- [WGB06] M. G. Wardle, J. P. Goss, and P. R. Briddon. First-principles study of the diffusion of hydrogen in zno. *Phys. Rev. Lett.*, 96:205504, May 2006. 38, 95
- [WHKV99] M. Wolf, A. Hotzel, E. Knoesel, and D. Velic. Direct and indirect excitation mechanisms in two-photon photoemission spectroscopy of Cu(111) and CO/Cu(111). *Phys. Rev. B*, 59:5926–5935, Feb 1999. 58
- [WKFR04] M. Weinelt, M. Kutschera, Th. Fauster, and M. Rohlfiing. Dynamics of exciton formation at the Si(100)  $c(4 \times 2)$  surface. *Phys. Rev. Lett.*, 92:126801, Mar 2004. 13, 110
- [WKS<sup>+</sup>05] M. Weinelt, M. Kutschera, R. Schmidt, C. Orth, Th. Fauster, and M. Rohlfiing. Electronic structure and electron dynamics at Si(100). *Applied Physics A*, 80(5):995–1003, 2005. 101
- [WL77] M. Wautelet and L. D. Laude. Laser-modulated photoemission in semiconductors. *Phys. Rev. Lett.*, 38:40–43, Jan 1977. 54

- [WMY<sup>+</sup>05] Y. Wang, B. Meyer, X. Yin, M. Kunat, D. Langenberg, F. Traeger, A. Birkner, and Ch. Wöll. Hydrogen induced metallicity on the ZnO (10 $\bar{1}$ 0) surface. *Phys. Rev. Lett.*, 95(26):266104, dec 2005. [2](#), [38](#), [40](#), [81](#), [84](#), [85](#), [96](#)
- [Wöl07] Ch. Wöll. The chemistry and physics of zinc oxide surfaces. *Prog. Surf. Sci.*, 82(2-3):55–120, 2007. [2](#), [34](#), [40](#), [95](#)
- [WSC<sup>+</sup>14] P. Winget, L. K. Schirra, D. Cornil, H. Li, V. Coropceanu, P. F. Ndione, A. K. Sigdel, D. S. Ginley, J. J. Berry, J. Shim, H. Kim, B. Kippelen, J.-L. Brédas, and O. L. A. Monti. Defect-driven interfacial electronic structures at an organic/metal-oxide semiconductor heterojunction. *Adv. Mater.*, 26(27):4711–4716, may 2014. [4](#), [18](#), [136](#)
- [WVR<sup>+</sup>06] L. Wischmeier, T. Voss, I. Rückmann, J. Gutowski, A. C. Mofor, A. Bakin, and A. Waag. Dynamics of surface-excitonic emission in ZnO nanowires. *Phys. Rev. B*, 74:195333, Nov 2006. [42](#), [43](#), [110](#), [115](#), [117](#), [125](#), [126](#)
- [YBH<sup>+</sup>06] X.-L. Yin, A. Birkner, K. Hänel, Th. Löber, U. Köhler, and Ch. Wöll. Adsorption of atomic hydrogen on ZnO(10 $\bar{1}$ 0): STM study. *Phys. Chem. Chem. Phys.*, 8(13):1477, 2006. [33](#)
- [YC10] P. Y. Yu and M. Cardona. *Fundamentals of Semiconductors*. Graduate Texts in Physics. Springer Berlin Heidelberg, fourth edition edition, 2010. [21](#)
- [YJLH<sup>+</sup>12] C. K. Yong, H. J. Joyce, J. Lloyd-Hughes, Q. Gao, H. Hoe Tan, C. Jagadish, M. B. Johnston, and L. M. Herz. Ultrafast dynamics of exciton formation in semiconductor nanowires. *Small*, 8(11):1725–1731, mar 2012. [114](#), [125](#)
- [Yof80] E. J. Yoffa. Dynamics of dense laser-induced plasmas. *Phys. Rev. B*, 21:2415–2425, Mar 1980. [107](#)
- [Yof81] E. J. Yoffa. Screening of hot-carrier relaxation in highly photoexcited semiconductors. *Phys. Rev. B*, 23:1909–1919, Feb 1981. [107](#)
- [YOY<sup>+</sup>15] R. Yukawa, K. Ozawa, S. Yamamoto, R.-Y. Liu, and I. Matsuda. Anisotropic effective mass approximation model to calculate multiple subband structures at wide-gap semiconductor surfaces: Application to accumulation layers of SrTiO<sub>3</sub> and ZnO. *Surf. Sci.*, 641:224–230, jul 2015. [34](#), [36](#), [39](#), [40](#)
- [YYO<sup>+</sup>14] R. Yukawa, S. Yamamoto, K. Ozawa, M. Emori, M. Ogawa, Sh. Yamamoto, K. Fujikawa, R. Hobara, S. Kitagawa, H. Daimon, H. Sakama, and I. Matsuda. Electron-hole recombination on ZnO(0001) single-crystal surface studied by time-resolved soft x-ray photoelectron spectroscopy. *Appl. Phys. Lett.*, 105(15):151602, oct 2014. [79](#)
- [ZDL<sup>+</sup>10] H. Zeng, G. Duan, Y. Li, S. Yang, X. Xu, and W. Cai. Blue luminescence of ZnO nanoparticles based on non-equilibrium processes: Defect origins and emission controls. *Adv. Funct. Mater.*, 20(4):561–572, feb 2010. [43](#)

- [ZEC10] V. P. Zhukov, P. M. Echenique, and E. V. Chulkov. Two types of excited electron dynamics in zinc oxide. *Phys. Rev. B*, 82:094302, Sep 2010. [42](#), [44](#), [45](#), [101](#), [109](#), [116](#)
- [ZEO<sup>+</sup>13] K. H. L. Zhang, R. G. Egdell, F. Offi, S. Iacobucci, L. Petaccia, S. Gorovikov, and P. D. C. King. Microscopic Origin of Electron Accumulation in In<sub>2</sub>O<sub>3</sub>. *Phys. Rev. Lett.*, 110:056803, Jan 2013. [36](#)
- [ZFHS<sup>+</sup>12] Y. Zhou, C. Fuentes-Hernandez, J. Shim, J. Meyer, A. J. Giordano, H. Li, P. Winget, T. Papadopoulos, H. Cheun, J. Kim, M. Fenoll, A. Dindar, W. Haske, E. Najafabadi, T. M. Khan, H. Sojoudi, S. Barlow, S. Graham, J.-L. Bredas, S. R. Marder, A. Kahn, and B. Kippelen. A universal method to produce low-work function electrodes for organic electronics. *Science*, 336(6079):327–332, apr 2012. [16](#), [129](#)
- [ZGW02] Q. Zhong, C. Gahl, and M. Wolf. Two-photon photoemission spectroscopy of pyridine adsorbed on Cu(111). *Surf. Sci.*, 496(1-2):21–32, jan 2002. [17](#)
- [Zhu04a] X.-Y. Zhu. Charge transport at metal-molecule interfaces: A spectroscopic view. *The Journal of Physical Chemistry B*, 108(26):8778–8793, jul 2004. [26](#)
- [Zhu04b] X.-Y. Zhu. Electronic structure and electron dynamics at molecule–metal interfaces: Implications for molecule-based electronics. *Surf. Sci. Rep.*, 56(1-2):1–83, nov 2004. [2](#), [19](#), [58](#), [59](#)
- [Zhu14] X.-Y. Zhu. How to draw energy level diagrams in excitonic solar cells. *Journal of Physical Chemistry Letters*, 5(13):2283–2288, 2014. [11](#), [12](#), [110](#)
- [ZMG<sup>+</sup>15] X.-Y. Zhu, N. R. Monahan, Z. Gong, H. Zhu, K. W. Williams, and C. A. Nelson. Charge transfer excitons at van der Waals interfaces. *J. Am. Chem. Soc.*, 137(26):8313–8320, jul 2015. [28](#)
- [ZT15] A. Zhugayevych and S. Tretiak. Theoretical description of structural and electronic properties of organic photovoltaic materials. *Annu. Rev. Phys. Chem.*, 66(1):305–330, apr 2015. [9](#), [19](#)
- [ZYM09] X.-Y. Zhu, Q. Yang, and M. Muntwiler. Charge-transfer excitons at organic semiconductor surfaces and interfaces. *Acc. Chem. Res.*, 42(11):1779–1787, nov 2009. [26](#), [28](#)

# Acronyms

***p*-6P** *p*-sexiphenyl. 138, 139, 140, 142, 143, 152

**1PPE** one-photon photoelectron spectroscopy. 48, 133, 138, 143, 145, 161

**1PPE** one-photon photoemission. 163

**2DEG** two-dimensional electron gas. 19, 25, 36, 39, 109

**2PPE** two-photon photoelectron spectroscopy. 2, 26, 44, 47, 48, 54, 55, 57, 58, 60, 71, 73, 75, 78, 101, 102, 103, 105, 108, 110, 111, 112, 115, 116, 119, 120, 121, 125, 127, 129, 133, 138, 142, 143, 145, 147, 149, 162, 163

**5P-Py** 5-phenyl-pyridine. 4, 129, 136, 138, 139, 140, 141, 142, 143, 145, 147, 148, 150, 151, 152, 157, 165

**AEA** anisotropic effective-mass approximation. 39

**ARPES** angle-resolved photoelectron spectroscopy. 36, 38, 39, 53, 54, 79, 80, 109

**BBO**  $\beta$ -Barium borate. 61, 62

**BEC** Bose–Einstein condensate. 24

**BGR** band gap renormalization. 112

**CAL** charge accumulation layer. 1, 2, 3, 7, 36, 37, 38, 39, 38, 39, 38, 41, 77, 79, 81, 82, 83, 89, 91, 92, 93, 94, 95, 96, 97, 98, 101, 102, 105, 108, 109, 110, 111, 112, 115, 117, 118, 119, 120, 121, 126, 127, 136, 137, 155, 156, 162, 163

**CB** conduction band. 3, 4, 11, 25, 27, 29, 31, 38, 44, 71, 92, 101, 102, 103, 105, 107, 108, 111, 112, 116, 126, 127, 129, 148, 149, 150, 151, 157

**CBM** conduction band minimum. 29, 31, 32, 35, 36, 37, 38, 39, 44, 73, 79, 82, 92, 93, 94, 96, 101, 102, 103, 105, 106, 110, 114, 116, 117, 143, 156

**CL** cathodoluminescence. 42

**CNL** charge neutrality level. 32, 35, 38, 85

**CT** charge transfer. 12, 15, 16, 25, 26, 25, 26, 27, 28, 129, 135, 136, 138, 147, 149, 150, 149, 150, 151, 152

- 
- DFT** density functional theory. 2, 3, 15, 34, 38, 71, 80, 84, 93, 95, 96, 129, 130, 132, 134, 136, 139
- DH6T** dihexyl-sexithiophene. 150, 151
- DOS** density of states. 49, 83, 105, 112, 137, 163
- EDC** energy distribution curve. 94
- e-e** electron-electron. 21, 24
- e-h** electron-hole. 4, 7, 9, 20, 23, 27, 28, 42, 102, 110, 112, 114, 115, 120
- EIB** electron injection barrier. 9, 14
- e-ph** electron-phonon. 3, 19, 21, 22, 24, 44, 101, 106, 107, 108, 127, 156
- eSFG** electronic sum frequency generation. 125
- ET** electron transfer. 12
- FHG** fourth harmonic generation. 60, 61, 62
- FHI** Fritz Haber Institute. 2, 71, 80
- FLT** Fermi-liquid theory. 21
- FRET** Förster resonant energy transfer. 3, 23, 26, 27, 42, 101, 121, 156
- FWHM** full width at half maximum. 92, 136, 149
- GVD** group velocity dispersion. 61
- HAS** helium atom scattering. 39
- HIB** hole injection barrier. 9, 14
- HIOS** hybrid inorganic/organic system. 1, 2, 7, 8, 9, 13, 14, 16, 19, 25, 26, 29, 43, 54, 80, 101, 109, 121, 126
- HOMO** highest occupied molecular orbital. 9, 11, 12, 16, 18, 136, 137, 141, 143, 145, 147
- IGS** in-gap state. 18, 133, 136, 138, 140, 141, 142, 147, 148, 149, 152
- IR** infrared. 28, 148
- ITO** Sn-doped In<sub>2</sub>O<sub>3</sub>. 16, 28
- LED** light emitting diode. 7
- LEED** low-energy electron diffraction. 33, 34, 39, 48, 51, 66, 73, 77, 78, 165

- LO** longitudinal optical. 3, 21, 22, 43, 44, 101, 103, 105, 106, 107, 124, 127, 156
- LUMO** lowest unoccupied molecular orbital. 4, 9, 11, 16, 17, 27, 71, 129, 130, 136, 138, 141, 142, 143, 145, 147, 148, 149, 151, 152
- LV** leak valve. 67
- MCP** micro-channel plate. 62
- ML** monolayer. 130
- MTFA** modified Thomas–Fermi approximation. 39
- NEXAFS** near edge X-ray absorption fine structure. 17, 132
- OLED** organic light emitting diode. 1, 9, 26
- OPA** optical parametric amplifier. 60, 61
- OPVC** organic photovoltaic cell. 1
- PBE** Perdew-Burke-Ernzerhof. 130, 132
- PE** photoemission. 141
- PES** photoelectron spectroscopy. 9, 11, 14, 40, 48, 49, 51, 62, 66, 67, 75, 77, 81, 96, 123, 130, 133, 136, 140, 141, 161
- PHD** pinhole doser. 165
- PL** photoluminescence. 24, 42, 43, 110, 114, 115, 117, 124, 125
- QCM** quartz crystal microbalance. 68, 138, 139, 165
- QMS** quadrupole mass spectrometer. 67, 68, 67, 78, 130, 139, 165
- RegA** regenerative amplifier. 60, 61
- SBB** surface band bending. 36, 38, 73, 79, 105, 110, 112, 114, 120
- SE** singlet exciton. 9
- SFG** sum frequency generation. 62
- SHG** second harmonic generation. 61, 62
- SPV** surface photovoltage. 111, 112, 114
- STM** scanning tunneling microscopy. 33, 39, 73, 77, 84

- STS** scanning tunneling spectroscopy. 39
- SX** surface exciton. 3, 43, 71, 92, 101, 110, 111, 110, 111, 112, 114, 115, 116, 117, 118, 119, 118, 119, 120, 121, 123, 124, 125, 126, 127, 128, 127, 156
- TC** thermocouple. 165
- TCO** transparent conductive oxide. 1, 7, 8, 10, 16, 19, 26, 29, 31, 32, 31, 32, 34, 35, 36, 37, 38, 40, 73, 127, 128, 156
- THG** third harmonic generation. 60, 61
- TPD** thermally programmed desorption. 48, 64, 67, 68, 130, 132, 130, 132, 134, 136, 139, 140, 165
- TR-2PPE** time-resolved 2PPE. 2, 3, 7, 11, 12, 13, 56, 57, 58, 101, 102, 121, 123, 126, 148, 149, 150, 152
- UHV** ultrahigh vacuum. 2, 36, 40, 47, 48, 64, 65, 67, 75, 77, 78, 96, 110, 121, 138, 156, 164, 165, 167
- UPS** ultraviolet photoelectron spectroscopy. 2, 9, 11, 12, 83, 95, 143
- UV** ultraviolet. 37, 57, 138, 165
- VB** valence band. 11, 12, 25, 29, 55, 73, 75, 76, 78, 163
- VBE** vertical binding energy. 145, 149, 152
- VBM** valence band maximum. 32, 73, 75, 76, 77, 78, 79, 143
- vdW** van der Waals. 130, 132
- XC** cross correlation. 103, 108, 109, 115, 116, 117, 121, 123, 125, 148, 150



# Acknowledgements

Mein erster Dank gilt Martin Wolf, als Gutachter meiner Arbeit und als Direktor der Abteilung Physikalische Chemie hat er für ein Arbeitsumfeld gesorgt, in dem ich mich voll auf meine Arbeit konzentrieren konnte und in der es gleichzeitig nicht an interessanten Seminaren, Veranstaltungen und dem Austausch mit exzellenten Gästen und Kollegen mangelte. Die Diskussionen über die anfangs sehr überraschenden Daten waren hilfreich und ermutigend.

Julia Stähler danke ich zuerst dafür, dass Sie mich durchweg mit hohem Einsatz unterstützt hat. Damit hat Sie den Weg bereitet, auf dem die Messungen an einem manchmal sehr schwierigen System zu diesem erfreulichen Abschluss gebracht wurden. Ich habe unglaublich viel gelernt und werde die Erfahrungen, die ich in der Arbeitsgruppe gemacht habe wohl nie vergessen. Und zum Abschluss sage ich jetzt auch gar nichts Kitschiges mehr.

Mario Dähne danke ich für seine Bereitschaft, meine Arbeit zu begutachten. Das Seminar in seiner Arbeitsgruppe, sein Interesse an meiner Arbeit und die vielen interessanten Fragen waren sehr hilfreich.

Den Organisatoren des Sfb 951 *HIOS* danke ich für die Möglichkeiten, mich mit interdisziplinären Ansätzen und über die Institutsgrenzen hinweg mit dem Thema Hybridsysteme zu beschäftigen. Insbesondere die *Young Researcher Workshops* waren eine willkommene Gelegenheit, sich mit anderen Doktoranden auszutauschen und neue Sichtweisen kennenzulernen. Die Diskussionen und vor allem die Zusammenarbeit mit Oliver Hofmann und Patrick Rinke waren entscheidend dafür, das ich viele Teile meine experimentellen Ergebnisse erst wirklich verstehen und erfolgreich publizieren konnte.

Ein sehr wichtiger Teil meiner Zeit am FHI ist auch die Teilnahme an der IMPRS *Functional Interfaces in Materials Science*, die exzellent durch Niklas Nilus und nachfolgend Tobias Kampfrath koordiniert wurde. Besonderer Dank gilt hier auch Bettina Menzel. Unter den vielen herausragenden Mitdoktoranden, mit denen ich die Zeit, insbesondere beim Workshop in Ringberg, teilen durfte möchte ich hier insbesondere Felix, Steffi und Bo-Hong hervorheben. Jenga ist seit Ringberg auch nicht mehr das gleiche.

Die Menschen, die mir aus dieser Zeit am Institut persönlich am wichtigsten sind, und zwar nicht nur, weil ich die meiste Zeit mit ihnen verbracht habe, sind die Mitglieder der *electron dynamix group*. Und da ich so ziemlich von Anfang an dabei war, sind das gar nicht so wenige. Ich danke Sebastian für seine Starthilfe im Labor (und beim Skifahren). Daniel, mit dem ich fast den gesamten Wahnsinn hier durchgemacht habe, inklusive der Hochzeiten. Laura, die ebenfalls von Anfang an dabei war, und mit der es nie Stress wegen der Konkurrenz um den Laser gab. Das mit dem Arm tut mir immer noch sehr Leid. Mit Lea hat unsere Gruppe die wahrscheinlich coolste und am schwärzesten angezogene Extradoktorandin adoptiert, die man sich vorstellen kann. Clemens, mit dem ich am meisten mitgefiebert habe bei seinen Messungen. Auch ich ihnen durch bloße Auflistung nicht wirklich gerecht werde: Danke Simon, Micha, Marc, Selene, Lukas, Sessa, und Sarah. Unter unseren Labornachbarn müssen zweifellos Melanie und vor

allem Lutz erwähnt werden. Allein die Rettung des Stücks Käse, was jetzt rein gar nichts mit der Doktorarbeit zu tun hat, verdient höchste Anerkennung.

Ich hoffe, dass ich die vielen kleinen verrückten Dinge, die wir alle innerhalb und außerhalb des Labors neben den großen verrückten Dingen unternommen habe, nie vergessen werde.

Alex und insbesondere Ralph gilt der Dank, was ganz allgemeine Diskussionen im Vorbeigehen und beim leider eingeschlafenen Literaturclub betrifft. Was die technische und administrative Unterstützung in der Abteilung PC angeht, danke ich Sven, Manuel, Marcel, Albrecht und Daria. Bei praktisch allen weiteren Mitarbeitern des FHI möchte ich mich für die entspannte, produktive und angenehme Arbeitsatmosphäre bedanken.

Zuletzt gilt mein großer Dank meiner Familie. Meinen Eltern, die mich durch das ganze Studium hindurch bedingungslos unterstützt haben und Isabell, für all die Stabilisierung, das Auffangen und das Aushalten der letzten Jahre.





# List of Publications

## Publications related to this thesis

---

O. T. Hofmann, J.-C. Deinert, Y. Xu, P. Rinke, J. Stähler, M. Wolf, and M. Scheffler. Large work function reduction by adsorption of a molecule with negative electron affinity: Pyridine on ZnO(10 $\bar{1}$ 0). *J. Chem. Phys.* **139**(17):174701 (2013)

J.-C. Deinert, D. Wegkamp, M. Meyer, C. Richter, M. Wolf, and J. Stähler. Ultrafast exciton formation at the ZnO(10 $\bar{1}$ 0) surface. *Phys. Rev. Lett.* **113**:057602 (2014)

J.-C. Deinert, O. T. Hofmann, M. Meyer, P. Rinke, and J. Stähler. Local aspects of hydrogen-induced metallisation of the ZnO(10 $\bar{1}$ 0) surface. *Phys. Rev. B* **91**:235313 (2015)

## Additional publications concerning other topics

---

J. Stähler, J.-C. Deinert, D. Wegkamp, S. Hagen, and M. Wolf. Real-time measurement of the vertical binding energy during the birth of a solvated electron. *J. Am. Chem. Soc.* **137**(10):3520 (2015)



# Academic Curriculum Vitae

Jan-Christoph Deinert  
born July 9, 1985 in Dannenberg (Elbe), Germany

---

<b>06.2004</b>	<b>Abitur</b> , Gymnasium Lüchow, Lüchow (Wendland), Germany
<b>07.2004–03.2005</b>	<b>Alternative civilian service</b> , HVHS Bildungszentrum Jagdschloss Göhrde e.V., Göhrde, Germany
<b>04.2005–03.2011</b>	<b>Diploma studies in Physics, minor in Chemistry</b> Freie Universität Berlin
<b>10.2009–1.2011</b>	<b>Diploma thesis</b> Fritz Haber Institute of the Max Planck Society, Berlin
Thesis title:	<i>Zeit- und winkelaufgelöste Zweiphotonen-Photoemissionsspektroskopie: Aufbau und Charakterisierung des Experiments anhand der Cu(111) und der D<sub>2</sub>O/Cu(111)-Oberfläche</i>
Supervised by:	Dr. Julia Stähler and Prof. Martin Wolf
<b>03.2011–today</b>	<b>Doctoral studies</b> Fritz Haber Institute of the Max Planck Society, Berlin, and Technische Universität Berlin
Thesis title:	<i>Zinc Oxide Surfaces and Interfaces: Electronic Structure and Dynamics of Excited States</i>
Supervised by:	Dr. Julia Stähler and Prof. Dr. Martin Wolf



# Eidstattliche Versicherung

Hiermit versichere ich, Jan-Christoph Deinert, geboren am 9.7.1985 in Dannenberg (Elbe), an Eides statt die vorliegende Dissertation selbstständig verfasst zu haben. Sämtliche verwendeten Hilfsmittel, Hilfen und Quellen sind an der entsprechenden Stelle angegeben. Diese Arbeit wurde bisher weder in gleicher noch ähnlicher Form einer anderen Prüfungskommission vorgelegt oder veröffentlicht. Die Angaben über meinen Eigenanteil an den Veröffentlichungen in meiner Erklärung sind zutreffend.

Jan-Christoph Deinert

Berlin, den 27. Januar 2016